INVESTIGATION OF RARE EARTH-DOPED CERAMICS AS THERMAL BARRIER COATING MATERIALS

JING WANG, MPhil

Thesis submitted

for the degree of Doctor of Philosophy

Department of Mechanical, Materials and Manufacturing Engineering

Faculty of Engineering

University of Nottingham

July 2016

Abstract

Increasing operating temperatures of gas engines is an effective approach to further improve thermal efficiency. But the ceramic top-coat (conventional 7-8 wt% yttria-stabilised zirconia, 7-8YSZ) in thermal barrier coatings (TBCs) cannot afford application temperatures above 1250 ^{o}C, the main reason of which is the accelerated phase transformation, due to quick cation diffusion. In addition, 7-8YSZ has relatively large thermal conductivity, small coefficient of thermal expansion (CTE) and large oxygen ion diffusivity. The relatively small CTE could create the mismatch between ceramic top-coat and metallic bond coat in thermal barrier coatings (TBCs), which can generate strain or stress at the interface to cause the spallation of TBCs. The oxygen atoms for the formation of thermally grown oxides (TGO) in TBCs come from ceramic top-coat, but the thickness of TGO cannot exceed 10 μm in order to avoid the spallation of TBCs. Therefore, it is extremely important to find new ceramic candidates to replace 7-8YSZ and to be used at elevated temperatures.

According to these critical criteria of ceramic top-coat, three ceramic candidates were chosen and studied, which are stannate with pyrochlore crystal structure, erbia-based oxides stabilised zirconia and yttrium aluminium garnet. All candidates were synthesised using a sol-gel method. Crystalline phases of all as-synthesised powders were characterised by X-ray diffraction (XRD). Thermal conductivity, coefficient of thermal expansion

(CTE), phase stability, chemical compatibility were also studied. Furthermore, molecular dynamics (MD) simulations were used to calculate thermal conductivity and CTE, and to analyse and explain experimental results.

Pyrochlore has excellent phase stability and relatively low thermal conductivity, but relatively small CTE. From the consideration of crystal structure and ion radius, La^{3+} doped $Yb_2Sn_2O_7$ ceramics with pyrochlore crystal structures are investigated as one TBCs candidate material. As La^{3+} and Yb^{3+} ions have the largest radius difference in lanthanide group, La^{3+} ions are expected to produce significant disorders by replacing Yb^{3+} ions in cation layers of $Yb_2Sn_2O_7$. Both experimental and computational XRD data and phase analysis are carried out and good agreement has been obtained. The lattice constants of solid solution $(La_xYb_{1-x})_2Sn_2O_7$ (x=0.3, 0.5, 0.7) increase linearly when the content of La^{3+} is increased. The thermal properties (thermal conductivity and coefficients of thermal expansion) have been compared with the traditional 8 wt% yttria-stabilised zirconia (8YSZ) and $La_2Zr_2O_7$ (LZ). La^{3+} doped $Yb_2Sn_2O_7$ exhibits lower thermal conductivities than un-doped stannates and thermal conductivity deceases with the increase of doping concentration, but it reaches a minimum value when x=0.5 then increases again. Thus among $(La_xYb_{1-x})_2Sn_2O_7$ compositions, $(La_{0.5}Yb_{0.5})_2Sn_2O_7$ exhibits the lowest thermal conductivity (0.851 $W{\cdot}m^{-1}{\cdot}K^{-1}$ at room temperature), which is much lower than that of 8YSZ (1.353 $W{\cdot}m^{-1}{\cdot}K^{-1}$). Moreover, it possesses a high coefficient of thermal expansion (13.530×10^{-6} K^{-1} at 950 ^{o}C). In addition, the

simulation results obtained from the MD simulations, indicate that the variation of thermal conductivity with increasing doping concentration in solid solution $(La_xYb_{1-x})_2Sn_2O_7$ (x=0.3, 0.5, 0.7) is independent of external effects, like porosity, grain size and grain boundary.

Stabilised zirconia is still one of the most popular TBCs top-coat systems, but new stabilisers are still under-seeking. For stabilised zirconia, to improve thermal phase stability and further reduce thermal conductivity are the most urgent challenges. Erbia-based rare earth oxides stabilised zirconia is studied at 1400 ^oC. XRD patterns confirmed that erbia-stabilised zirconia have the non-transformable phase. Thermal conductivity decreases and thermal phase stability is improved with the increase of the erbia content.

Mono- or bi-rare earth oxides doped erbia-stabilised zirconia is studied to further reduce thermal conductivity due to creating cluster defects. The influences on thermal phase stability produced by different dopants are also analysed. The chemical formulas of Mono- or bi-rare earth oxides doped erbia stabilised zirconia are $Er_{0.05}R_{0.05}Zr_{0.9}O_{1.95}$ (R=Yb, Gd and Dy) and $Er_{0.04}R_{0.04}$ $R^*_{0.04}Zr_{0.88}O_{1.94}$ (R+R*=Yb+Dy, Yb+Gd and Dy+Gd), respectively. Thermal conductivities of $Er_{0.05}R_{0.05}Zr_{0.9}O_{1.95}$ (R=Yb, Gd and Dy) and $Er_{0.04}R_{0.04}$ $R^*_{0.04}Zr_{0.88}O_{1.94}$ (R+R*=Yb+Dy, Yb+Gd and Dy+Gd) are lower than that of conventional 8YSZ and also they exhibit comparable CTEs to 8YSZ. Importantly, it is found that the thermal phase stability is dependent on the tetragonality, $c/a\sqrt{2}$ ratio. When the $c/a\sqrt{2}$ ratio decreases from 1.010 to 1.006

for mono- or bi-rare earth oxides doped erbia, the thermal phase stability is better.

Yttrium aluminium garnet (YAG) is also an attractive candidate as thermal barrier material, due to its relatively low thermal conductivity, low oxygen diffusivity and good phase stability at elevated temperatures. YAG has a complex crystal structure, in which Y^{3+} ions locate in dodecahedra and Al^{3+} ions in octahedra and tetrahedra. Replacing the host cations with rare earth elements can cause the distortion of polyhedrons which influences the thermal properties of YAG. Because the space inside the octahedra are relatively small, Yb^{3+} ions which have the smallest ionic radial sizes in the lanthanide series, have been selected and doped on dodecahedral and octahedral sites to investigate the effects on thermal conductivity and thermal expansion. The variation of lattice constant indicates that Yb^{3+} ions are located on the dodecahedra or octahedra.

In addition, when Yb^{3+} ions replace Al^{3+} ions on octahedral sites, thermal conductivity at room temperature is dramatically reduced and the coefficient of thermal expansion is over 10×10^{-6} K^{-1} at high temperatures, which results from the expansion of octahedra due to Yb^{3+} ions with much larger radii compared with the host cations (Al^{3+} ions). On the contrary, replacing Y^{3+} ions with Yb^{3+} ions in dodecahedra, thermal conductivity gradually reduces but the coefficient of thermal expansion is smaller, due to the relatively small ionic radii of Yb^{3+} ions causing the contraction of the dodecahedra. Additionally, it is found that the largest decrease in thermal conductivity results from phonon scattering caused by the

large atomic mass difference rather than the relatively small difference in ionic radius.

Acknowledgments

I greatly appreciate all the people who have provided me with tremendous help, support, and inspiration throughout my PhD studies. Their supports are undoubtedly invaluable.

First and foremost, I would like to thank my supervisors, Dr. Xianghui Hou and Dr. Richard Wheatley, for their support, guidance, inspiration, invaluable suggestions and especially their patience throughout my research period. Moreover, I would like to thank all the researchers in the group for their helps. They are Dr. Fang Xu, Dr. Ming Li, Dr. Junpeng Liu, Lingyi Qian, Siwen Ding, Tianhui Liu, Bo Tan and Tamal Barman. I am also grateful to all staff and researchers in Advanced Materials Research Group for their helps and all technicians in Wolfson Building for the equipment training and technical support. Special thanks to Mr.Keith Dinsdale and Dr. Nigel Neate for their constant help and expertise using a range of characterisation techniques.

Finally, I want to thank my family for their unconditional love, encouragement and support. Special thanks are given to my grandfather and grandmother. Without their sacrifices and efforts, I could never have been able to complete my study.

This work is funded by the University of Nottingham and ACAE and thanks for their sponsorship.

Publications

Publications of Journal

1. **Jing Wang**, Fang Xu, Richard J. Wheatley, Kwang-Leong Choy, Nigel Neate, and Xianghui Hou. Investigation of La^{3+} Doped $Yb_2Sn_2O_7$ as new thermal barrier materials. *Materials & Design* 85 (2015): 423-430.

2. Pengrong Ren, Qian Wang, Xin Wang, Lu Wang, **Jing Wang**, Huiqing Fan, and Gaoyang Zhao. Effects of doping sites on electrical properties of yttrium doped $BaTiO_3$. *Materials Letters* 174 (2016): 197-200.

3. **Jing Wang**, Fang Xu, Richard J. Wheatley, Nigel Neate, and Xianghui Hou. Yb^{3+} doping effects on thermal conductivity and thermal expansion of Yttrium aluminium garnet. *Ceramics International* 42 (2016): 14228-14235

4. **Jing Wang,** Fang Xu, Richard J. Wheatley, Nigel Neate, and Xianghui Hou. Improved Thermal Stability at 1400 ^oC of Zirconia Stabilised with Erbia-based Oxides (In Preparation**)**

Table of Contents

List of Figures

List of Tables

List of Abbreviations

Symbols

γ	Grüneisen parameter
θ	Bragg angle
2θ	2-theta
λ	X-ray wavelength
ρ	Mass density
ρ'	Measured density
ρ_{th}	Theoretical density
τ	Phonon relaxation time
τ_U	Relaxation time of Umklapp phonon-phonon scattering
τ_{gb}	Relaxation time of grain boundary
ϕ	Diameter
$\emptyset$	Estimated fractional porosity of a specimen
$\emptyset(r)$	Buckingham potential
ω	Phonon frequency
a'	Average lattice parameter obtained from simulation
a_V	Volume coefficient of thermal expansion
a_l	Linear coefficient of thermal expansion
a, *b*, *c*	Lattice parameters
A_a	Cross section area
A, *B* and *C*	Buckingham parameters
C_p	Heat capacity

d	Perpendicular distance between pairs of adjacent planes in crystal structure
d'	Grain size
$d_{h^*k^*l^*}$	Distance between the lattice planes
E	Total energy of potential energy and kinetic energy
E'	Young's modulus
E_q	Quantum energies of atom vibration wave
f_i	Fraction of atoms with atomic mass (m_i) and ionic radius (r_i) that resides on a site with average atomic mass ($\bar{m}$) and ionic radius ($\bar{r}$)
h	Planck constant
h^*, k^*, l^*	Miller indices of the Bragg plane
J	Thermal powder
k	Simulated thermal conductivity
k'	Measured thermal conductivity
k^*	Thermal conductivity
k_B	Boltzmann constant
k_c	Thermal conductivity reduction by cluster defect scattering
k_d	Thermal conductivity reduction by substituting defect scattering
KE_{avg}	Average kinetic energy
k_{gb}	Thermal conductivity reduction by gain boundary in nanostructured materials
k_i	Intrinsic thermal conductivity
k_L	Thermal conductivity of lattice vibrations
k_m	Thermal conductivities reduction by the difference of atomic mass

k_{min}	Minimum thermal conductivity
k_o	Corrected thermal conductivity
k_r	Thermal conductivities reduction by the difference of ionic radius
k_U	Thermal conductivity reduction by Umklapp phonon-phonon scattering
k_v	Thermal conductivity reduction by oxygen vacancy scattering
l	Phonon mean free path
l_f	Final length of a sample at final temperature
l_{gb}	Mean free path of grain boundaries
l_i	Mean free path of interstitials
l_o	Initial length of a sample at initial temperature
l_s	Mean free path of strain
l_v	Mean free path of vacancies (usually oxygen vacancies)
$\overline{m}$	Average atomic mass
m_i	Atomic mass
M_m	Amount of monoclinic phase
M_t	Amount of tetragonal and cubic phase
MW	Molecular weight
N	Number of atoms
N_A	Avogadro constant
$NA_m(11\bar{1})$	Net area of $(11\bar{1})$ peak in monoclinic phase
$NA_m(111)$	Net area of (111) peak in monoclinic phase
$NA_t(111)$	Net area of (111) peak in tetragonal/cubic phases
P	Simulation pressure

q	Heat flux
$\vec{q}$	Local heat flux density
$\bar{r}$	Average ionic radius
r_i	Ionic radius
T	Temperature
T_f	Final temperature
T_o	Initial temperature
ΔT	Temperature gradient
t	Simulation time
t^*	Time
V	Simulation system volume
V	Volume per atom
V_a	Average volume per atom
V_{cell}	Volume of a unit cell
V_f	Final volume of a sample at the final temperature
V_o	Initial volume of a sample at initial temperature
v	Phonon velocity
v'	Frequency of vibration wave
v_g	Phonon group velocity (ω/w)
v_p	Phonon phase velocity ($d\omega/dw$)
w	Wave vector
x, *y*, *z*	Doping mole percentage
Z	Formula number per unit cell

Abbreviations

α-Al_2O_3	Alfha phase of Al_2O_3
A1	$(Yb_{0.05}Y_{0.95})_3Al_2Al_3O_{12}$
A2	$(Yb_{0.15}Y_{0.85})_3Al_2Al_3O_{12}$
A3	$(Yb_{0.20}Y_{0.80})_3Al_2Al_3O_{12}$
APS	Air plasma spray
B1	$Y_3(Yb_{0.005}Al_{0.995})_2Al_3O_{12}$
B2	$Y_3(Yb_{0.015}Al_{0.985})_2Al_3O_{12}$
B3	$Y_3(Yb_{0.020}Al_{0.980})_2Al_3O_{12}$
BC	Bond coat
Calc	Calculated
c-phase	Cubic phase
CTE	Coefficient of thermal expansion
Diff	Difference
EB-PVD	Electron beam physical vapour deposition
Eq.	Equation
E2.5D2.5Z	2.5 mol% Er_2O_3, 2.5 mol% Dy_2O_3 stabilised zirconia
E2.5G2.5Z	2.5 mol% Er_2O_3, 2.5 mol% Gd_2O_3 stabilised zirconia
E2Y2D2Z	2 mol% Er_2O_3, 2 mol% Yb_2O_3, 2 mol% Dy_2O_3 stabilised zirconia
E2Y2G2Z	2 mol% Er_2O_3, 2 mol% Yb_2O_3, 2 mol% Gd_2O_3 stabilised zirconia
E2.5Y2.5Z	2.5 mol% Er_2O_3, 2.5 mol% Yb_2O_3 stabilised zirconia
E4Z	4 mol% erbia-stabilised zirconia

E5Z	5 mol% erbia-stabilised zirconia
E6Z	6 mol% erbia-stabilised zirconia
GSAS	General structure analysis aystem
LZ	$La_2Zr_2O_7$
m or *m*-phase	Monoclinic phase
M	The total doping concentration of La^{3+} ions (mol%)
M´	The total residual percentage of Al^{3+} ions after forming YAG (mol%)
M´´	The residual percentage of Al^{3+} ions after forming YAG forming YAG and $LaAlO_3$ (mol%)
MD	Molecular dynamics
MTPS	Modified transient plane source
Obs	Observed
PDF	Powder diffraction file
SEM	Scanning electron microscopy
$T_o^{t'-t''}$	Boundary of non-transformable tetragonal to second metastable tetragonal phase transformation
$T_o^{t'-c}$	Boundary of non-transformable tetragonal to cubic phase transformation
T_o^{t-m}	Boundary of tetragonal to monoclinic phase transformation
t-phase	First metastable tetragonal phase
t′-phase	Non-transformable tetragonal phase
t′′-phase	Second metastable tetragonal phase
TBCs	Thermal barrier coatings
TC	Ceramic top-coat

TCA	Thermal conductivity analyser
TEM	Transmission electron microscopy
TG-DSC	Thermogravimetry and differential scanning calorimetry
TGO	Thermally grown oxides
TMA	Thermal mechanical analysis
U-process	Umklapp process
wt	Weight
XRD	X-ray diffraction
YAG	$Y_3Al(1)_2Al(2)_3O_{12}$
7-8YSZ	7-8 wt% Y_2O_3-stabilised ZrO_2

Chapter 1. Introduction

1.1 Development of Thermal Barrier Coatings in Gas Engines

Thermal barrier coatings (TBCs) are defined as a kind of thermal insulating material applied to the surface of metal substrates, to protect them from the higher temperature environments, improve their thermal fatigue assistance and reduce the oxidation [1]. Figure 1-1 **(a)** exhibits the relationship between thermal efficiency and turbine inlet temperature, where the thermal efficiency can be improved by increasing the inlet temperature. Around 3% thermal efficiency can be achieved if the inlet temperature is increased every 100 ^{o}C [2].

Figure 1-1 **(b)** shows the development of TBCs materials and substrates to satisfy the requirement of the increasing turbine inlet temperature [3]. At the beginning, the operation temperature was very low, so there was no conventional TBCs applied on the substrate [4]. To improve thermal efficiency, TBCs have been investigated and applied on the surface of substrates due to increasing the operating temperature. Generally, the capability temperature of turbine blades can be increased by 150~250 ^{o}C after applying TBCs [5].

In TBCs, there are two important layers, bond coat and ceramic top-coat. The compositions of both layers have been continuously developed to meet the increasing temperature. The first

generation of bond coat was Ni-Al and the coating was deposited on a super-alloy nickel based substrate by the flamed-spray technique. Moreover, the composition of bond coats was modified by adding more elements (Co, Cr, Al, Y or Ni) to enhance its mechanical properties and chemical stability. Meanwhile, the deposition technology was changed to air plasma spray (APS) [6]. For ceramic top-coat, the initial ceramic materials were magnesia or calcia-stabilised zirconia, but both of them showed the disastrous destabilisations and also relatively low application temperatures, below 1000 ^{o}C [7]. Then it was found that 7-8 wt% yttria-stabilised zirconia (7-8YSZ) can dramatically improve the durability of TBCs about four times more than that of calcia-stabilised zirconia and 7-8YSZ became the most popular solution for TBCs top-coat [8]. Additionally, improved APS and electron beam physical vapour deposition (EB-PVD) techniques have been developed for coating deposition and both of them are still used nowadays. However, 7-8YSZ as a ceramic coat has the limitation that it cannot be used above 1250 ^{o}C, due to the accelerated phase transformations [9]. In addition, the mismatch of thermal expansion between YSZ ceramic top-coat and bond coat can also cause the spallation of TBCs. Thus, with the high demand on increasing engine operation temperature, there is always a strong requirement to develop new TBCs top-coat materials.

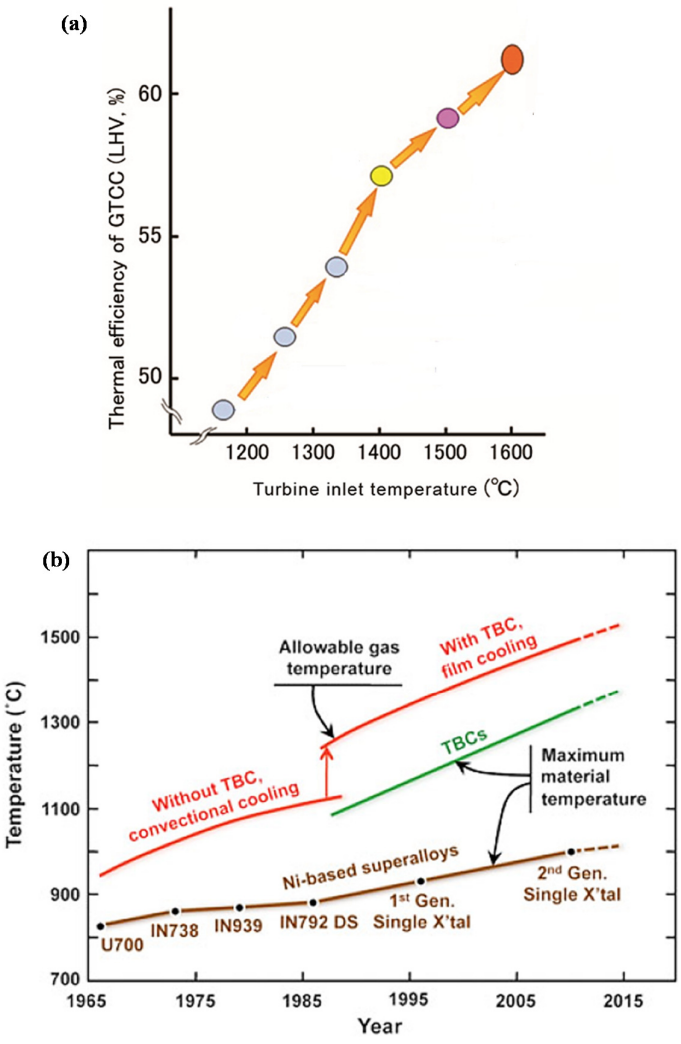

Figure 1-1: **(a)** The improvement of thermal efficiency with increasing the turbine inlet temperature; **(b)** The development of TBCs materials and substrates over the past 50 years [2, 3].

1.2 Current Thermal Barrier Coatings

Currently, the conventional TBCs system consists of three typical layers, including metallic bond coat (BC), thermally grown oxide (TGO) and ceramic top-coat (TC). The cross section of TBCs

extracted from a small area of turbine blade is shown in Figure 1-2 [4]. Moreover, the functions of each layer are also presented in the bottom of the graph.

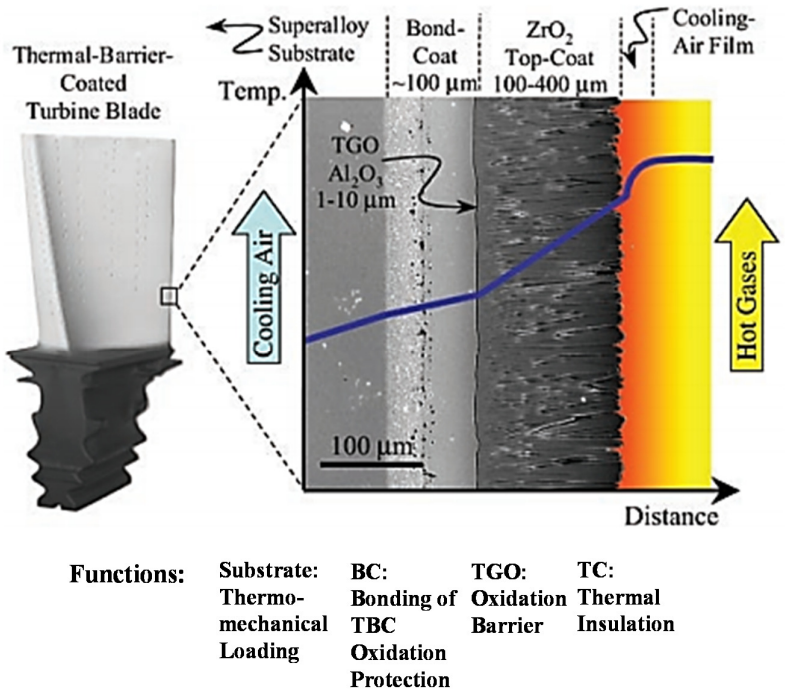

Figure 1-2: TBCs layered structure including ceramic top-coat, thermally grown oxide, metallic bond coat and super-alloy substrate; scanning electron microscopy (SEM) image showing a cross-sectional structure enlarged from a small area of a blade, adapted from ref [4, 10].

Ni-based single crystal components are usually used as substrates, which mainly support the thermo-mechanical loading. NiAl-based alloys are applied as metallic bond coats to improve the mismatch of coefficient of thermal expansion between ceramic top-coat and

substrate, and also to resist oxidation at high temperatures. Thermally grown oxide mainly consists of α-Al_2O_3 phase, which is formed between TC and BC and influences further oxidation. The typical function of 7-8YSZ is for thermal insulation as the outer layer of TBCs [11].

1.3 The Challenge of Top-Coat in TBCs

The top-coat of TBCs is a key limiting factor for further increase of operation temperature of gas engines, in the pursuit of higher engine efficiency and power output. 7-8YSZ has been well studied and applied as top-coat for a long time, but its application temperature is limited below 1250 ^{o}C, due to the quick phase transformations above this temperature [12-15]. Once above 1250 ^{o}C, non-transformable tetragonal phase (*t'*) in 7-8YSZ can quickly transform into first metastable tetragonal (*t*) and cubic phases (*c*), due to the accelerated diffusion of Y^{3+} ions. Then *t*-phase transforms to monoclinic phase (*m*) when it is close to room temperature. The volume difference of tetragonal and monoclinic phases can result in 3.5% volume change and also cause serious strain in the ceramic [16], leading to the failure of ceramic coating.

Additionally, the coefficient of thermal expansion (CTE) of 7-8YSZ is relatively small, about 11×10^{-6} K^{-1}, compared with CTE of BC (around 14×10^{-6} K^{-1}) [10]. This CTE mismatch can generate stress at the interface between ceramic top-coat and bond coat, which can also cause the spallation of TBCs. Meanwhile, if the operating temperature increase, more temperature reduction is expected by

the ceramic top-coat, which means that ceramic candidates must have very low thermal conductivity.

Furthermore, there is a strict requirement on the thickness of TGO, which cannot exceed 10 μm in order to avoid the spallation of TBCs [7]. Meanwhile, ceramic top-coat is the main oxygen source for the growth of TGO layer. The oxygen ionic diffusivity in 7-8YSZ is around 10^{-10}-10^{-11} $m^2 \cdot s^{-1}$ [17]. Therefore, lower oxygen ionic diffusivity is one more requirement for the ceramic candidates.

1.4 Aims and Objectives of the Dissertation

Since the increase of operating temperature of turbine blades is highly important for improving thermal efficiency of gas engines, it would be desirable to increase the operating temperature above 1250 ^{o}C, which means that conventional YSZ cannot be used [12-15]. Therefore, it is an urgent need to investigate new ceramic materials with low thermal conductivity, good phase stability, high coefficient of thermal expansion and low oxygen diffusivity to replace the current 7-8YSZ. The main aims of this research are to explore different ceramic materials for potential high temperature application as ceramic top-coat.

As there is no ceramic material that can satisfy the above severe requirements, the objectives of this thesis can be summarised as follow.

According to literature review, by considering thermal phase stability, thermal conductivity, coefficient of thermal expansion

and oxygen diffusivity, stannate, erbia-stabilised zirconia and yttrium aluminium garnet are studied;

Synthesis of the selected new ceramic candidates;

Microstructural characterisation and measurement of properties, such as crystalline phase, thermal conductivity, coefficient of thermal expansion, thermal phase stability;

Calculation of thermal conductivity and coefficient of thermal expansion by molecular dynamics simulations to better understand the influence from crystal structure modification;

Analysis and interpretation of the relationship between crystal structure and material properties.

The literature review in Chapter 2 provides background on TBCs materials and molecular dynamics simulations and also presents a critical comparison of typical potential ceramic candidates. The basic theory of thermal conductivity and coefficient of thermal expansion of ceramic materials are also explained.

The sol-gel method has been used for synthesizing ceramic powder of all candidate materials to obtain nano-sized powders (Chapter 3). Various characterization techniques and testing conditions are used to measure crystalline phase, thermal conductivity, coefficient of thermal expansion, thermal phase stability and microstructure of the synthesised ceramic candidates. Furthermore, Molecular Dynamics (MD) theories are used to calculate thermal conductivity and coefficient of thermal expansion

from room temperature to around 1400 ^{o}C, in order to better understand influences derived from the crystal structure changes.

Chapter 4 studies thermal properties of the stannate system, which has the pyrochlore crystal structure. The disorders of the cation layers can dramatically reduce thermal conductivity, which is also verified by MD simulations. Erbia-stabilised zirconia with and without rare earth oxides are investigated in Chapter 5. Good thermal phase stability is found due to relatively slow cation diffusion through the crystal structure. Furthermore, the relationship between phase stability and crystal structure is investigated. Furthermore, doping on different polyhedrons in yttrium aluminium garnet changes the crystal structure and has different influences on thermal conductivity and coefficient of thermal expansion (Chapter 6). The influences mainly come from the different atomic mass and ionic radius between dopants and host atoms. Finally, the thesis closes with conclusions and the suggestions for future work in Chapter 7.

Chapter 2. Literature Review

2.1 Critical Criteria for TBCs Top-Coat Materials

Due to the extremely complicated and rigorous operating environment of gas engines, there are strict requirements for selecting new ceramic candidates to improve the efficiency of gas engines. So far, there are several criteria for selecting potential materials as TBCs top-coat materials. Several important properties are discussed in the following.

Low thermal conductivity is essential to significantly reduce heat transmission from the surface of the top-coat to the interface between top-coat and bond coat. Normally, it should be below 2.2~2.6 $W \cdot m^{-1} \cdot K^{-1}$ which is the typical range for conventional bulk 8 wt% yttria stabilised zirconia (8YSZ) [18].

In addition to low thermal conductivity, high coefficient of thermal expansion (CTE) would be required for ceramic candidates. As the CTE mismatch between the ceramic top-coat and bond coat can lead to the formation of strain or stress at their interface and cause TBCs failure at this interface [19], the desired CTE value for ceramic top-coat is about $14\text{-}17 \times 10^{-6}$ K^{-1}, which is compatible with the CTE value of bond coat.

Good thermal phase stability is another important property for new ceramic materials, which are exposed to high temperatures after long thermal cycling times. The maximum application temperature of conventional 8YSZ is around 1250 ^{o}C, thus the candidate

materials should be capable to stabilise above 1250 ^{o}C, like 1400 ^{o}C or even higher [15, 20].

In order to avoid the instability between top-coat and thermally grown oxide, it is required that the ceramic materials do not chemically react with the main phase (α-Al_2O_3) in thermally grown oxide. Good chemical compatibility with α-Al_2O_3 can avoid the instability produced at their interface, which can maintain the long life times of gas engines [12].

Oxidation resistance, which means lower oxygen diffusion rate, can reduce the growth rate of the TGO. Because one of the major failure mechanisms of TBCs is related to the thickness of the TGO layer, which cannot exceed 6 μm [7]. Thus, high oxygen resistance of top-coat materials can extend the life time of turbine blades.

2.1.1 Thermal Conductivity of Solid Materials

Thermal conductivity of a material refers to the diffusivity of heat flow, which is usually temperature dependent. For ceramic materials, the values of thermal conductivity are between those of metals and glasses. For TBCs application, low thermal conductivity is required to effectively reduce temperature from outer atmosphere to the interface between the top-coat and bond coat. In order to achieve low thermal conductivity of ceramic material, it is necessary to understand the heat transfer mechanisms.

2.1.1.1 Heat Transfer and Thermal Conductivity in Solid

Heat transfer in a solid is often through the transport of the phonons (lattice vibrations), electrons and photons (radiation) [21]. As most ceramic materials are electrical insulators or semi-conductors, electrons and photons have little contribution to the thermal conductivity [22]. Therefore, phonons play the most important role in thermal transmission to affect the thermal conductivity in ceramics. In a unit cell, atoms vibrate but not independently from each other, so the lattice waves can be created from the atomic displacement when coupling with their nearest atoms. The quantum energies of these waves (E_q) can be given by hv' as shown in Eq. (2-1) [23]:

$$E_q = hv' \qquad \text{Eq. (2-1)}$$

where h is Planck constant and v' is the frequency of a lattice wave and the smallest quantum energy is named phonon.

The thermal conductivity (k^*) is used to indicate how quickly the thermal energy can be transferred through a material, and also, it can be defined in an equilibrium state based on classical thermodynamic theory, which is described in Eq. (2-2) based on Fourier law [24];

$$q = -k^* \Delta T \qquad \text{Eq. (2-2)}$$

where q is heat flux and ΔT is temperature gradient. Assuming no mass transfer, the partial differential equation can be expressed in Eq. (2-3) [24]:

$$k^*\Delta^2 T = \rho C_v \frac{\partial T}{\partial t^*} \quad \text{Eq. (2-3)}$$

where T is a temperature; ρ is the mass density; t^* is time.

2.1.1.2 Phonon Scattering

The magnitude of thermal conductivity is usually determined by the phonon scattering. Moreover, for a ceramic material, the phonon scattering are mainly dependent on defects (including oxygen vacancies or substitutional cations), the atomic mass, ionic radius and valence of the substitutional cations [25]. There are four main mechanisms used to describe the process of phonon scattering [26]: phonon-phonon scattering (also named Umklapp process or U-process), atomic mass (or ionic radius)-difference scattering, grain boundary scattering and phonon-electron scattering. Among these phonon scattering mechanisms, grain boundary scattering usually contributes in low-dimensional nanostructures [27-29]. Besides these internal effects, porosity of bulk materials is also a main factor to influence thermal conductivity.

Thermal conductivity of lattice vibrations k_L is usually described by heat capacity (C_p), phonon velocity (v) and phonon mean free path (l), so Eq. (2-4) is considered for calculating thermal conductivity [30]:

$$k_L = \frac{1}{3} C_p v l = \frac{1}{3} C_p v^2 \tau \quad \text{Eq. (2-4)}$$

$$v = {}^{l}/_{\tau} \qquad \text{Eq. (2-5)}$$

where τ is the phonon relaxation time, which is related to phonon mean free path and phonon velocity as shown in Eq. (2-5).

Additionally, the minimum thermal conductivity (k_{min}) is deduced and expressed in Eq. (2-6) [31, 32]:

$$k_{min} \sim 0.87 k_B V_a^{-2/3} \left(\frac{E'}{\rho}\right)^{1/2} \qquad \text{Eq. (2-6)}$$

where ρ is the mass density; E' is the Young's modulus and V_a is the average volume per atom.

The phonon mean free path (l) can be defined by Eq. (2-7) [33]:

$${}^{1}/_{l} = {}^{1}/_{l_v} + {}^{1}/_{l_i} + {}^{1}/_{l_{gb}} + {}^{1}/_{l_s} \qquad \text{Eq. (2-7)}$$

where l_v, l_i, l_{gb}, and l_s are the mean free path of vacancies (usually oxygen vacancy), interstitials, grain boundaries, and strain, respectively. The strain is usually found in doped ceramic materials, which is usually caused by the differences of radial sizes or atomic masses between atoms. These differences can cause distortion of the bond length which creates strain fields within the lattice to produce phonon scattering.

In addition, thermal conductivity is typically limited by a combination of phonon-phonon scattering, point defect scattering and grain boundary scattering (in nanostructured materials), so the phonon relaxation time can be summarised according to Eq. (2-8):

$$\tau^{-1} = \sum_i \tau_i^{-1} \quad \text{Eq. (2-8)}$$

For Umklapp phonon-phonon scattering, it is often strongly dependent on the anharmonicity of the bonding, the average atomic mass ($\bar{m}$) and temperature (T), where the anharmonicity of the bonding is usually described by the Grüneisen parameter (γ) [34, 35]. So the relaxation time of Umklapp phonon-phonon scattering is described in Eq. (2-9) [30, 36-38]:

$$\tau_U \propto \frac{\bar{m}v^3}{V^{1/3}\omega^2\gamma^2 T} \quad \text{Eq. (2-9)}$$

where V is the volume per atom and ω is the frequency of a phonon.

The grain boundary scattering is usually related with nanostructured polycrystalline materials, in which the relaxation time can be estimated by Eq. (2-10) [39]:

$$\tau_{gb} = \frac{d'}{v} \quad \text{Eq. (2-10)}$$

where d' is the grain size.

Point defect scattering arises from strain contrast caused by the difference in atomic mass or radius in the lattice, so the relaxation time is given by Eq. (2-11):

$$\tau_{pd}^{-1} = \frac{Vw^4}{4\pi v_p^2 v_g}\left[\sum_i f_i\left(1-\frac{m_i}{\bar{m}}\right)^2 + f_i\left(1-\frac{r_i}{\bar{r}}\right)^2\right. \quad \text{Eq. (2-11)}$$

where v_p and v_g are phonon phase velocity ($d\omega/dw$) and group velocity (ω/w), respectively; w is the wave vector; f_i is the fraction of atoms with atomic mass (m_i) and ionic radius (r_i) that resides on a site with average atomic mass ($\overline{m}$) and ionic radius ($\bar{r}$), respectively [40-42].

The discussed scattering mechanisms correspond to the different frequencies of phonons. Umklapp and point defect scattering are usually connected with phonons with high frequency and the boundary scattering is often dominant for phonons with low frequency. The interactions between lattice waves are shown in Figure 2-1, which are due to anharmonic interactions, point defects and grain boundaries, respectively.

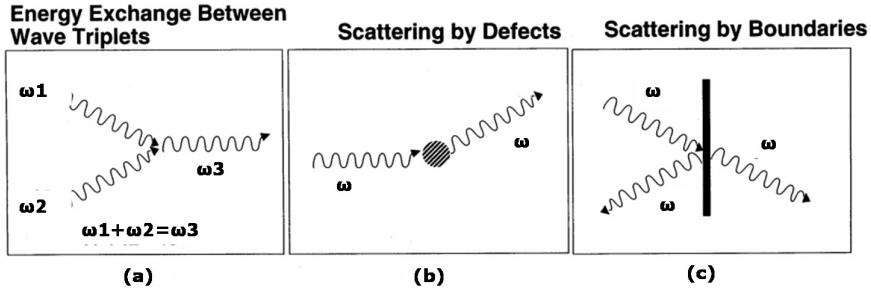

Figure 2-1: The interactions between lattice waves, which are due to **(a)** anharmonic interaction, **(b)** point defect and **(c)** grain boundaries.

Figure 2-2 shows a brief summary of some TBCs candidates, the thermal conductivity of which varies with temperature or is independent of temperature [43]. Ideally, if a material has very

low thermal conductivity that is almost independent of temperature, it could be applied as the TBCs material. A material with independent thermal conductivity can reduce the thermal strains during the rapid cooling process, which would provide long thermal cycling life time of the blade.

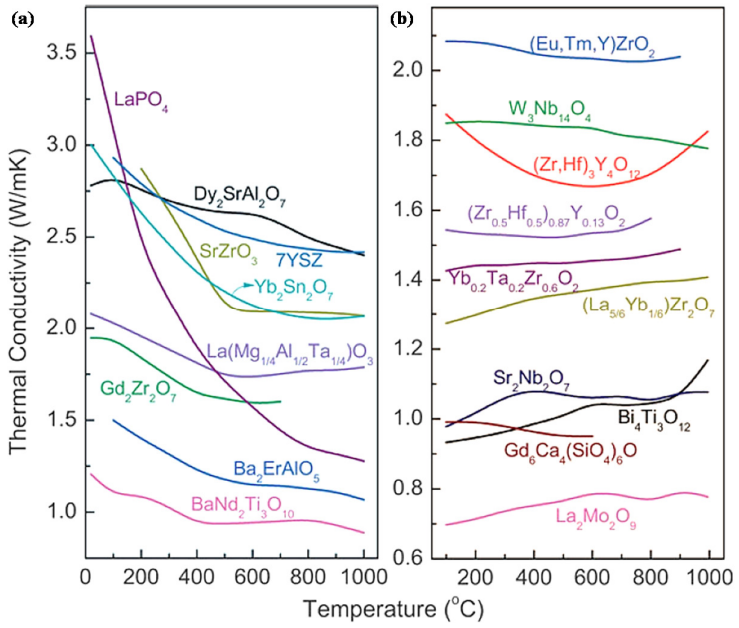

Figure 2-2: Summary of thermal conductivity of some ceramic materials for TBCs applications: **(a)** thermal conductivity varies with temperature; **(b)** thermal conductivity is almost independent on temperature [43].

2.1.2 Coefficient of Thermal Expansion of Solid Materials

The coefficient of thermal expansion (CTE) is also a very important parameter for TBCs application, because most TBCs failures result from the strains caused by the CTE mismatch between the ceramic coating and bond coating.

Thermal expansion of a material is related to its asymmetry and the strength of bonding in the material as shown in Figure 2-3. Normally, the average separation of atoms is a specific value, but this distance changes with rising temperature. In Figure 2-3 **(a)**, the thermal expansion occurs, if a material presents the weak bonding, in which the average value of interatomic distance dramatically increases. Otherwise, if the average value of interatomic distance slightly increases when the bonding is strong, the thermal expansion is smaller to happen as indicated in Figure 2-3 **(b)** [44]. According to this theory, the thermal expansion of ceramics is proportional to the average distance between atoms among the lattice and related to the strength of the bonding of constituent atoms in their crystals [45].

Therefore, materials with stronger interatomic bonding have small coefficient of thermal expansion and correspondingly, large coefficient of thermal expansion can be obtained in material with weak bonding. This can explain why ceramic materials (top-coats) have smaller CTE values than metal alloy (bond coat).

Generally, there are two definitions for the coefficient of thermal expansion: Linear coefficient of thermal expansion and volume

coefficient of thermal expansion [44]. The linear coefficient of thermal expansion expressed by Eq. (2-12):

$$\frac{l_f - l_o}{l_o} = \frac{\Delta l}{l_o} = a_l\left(T_f - T_o\right) = a_l \Delta T \qquad \text{Eq. (2-12)}$$

where a_l is the linear coefficient of thermal expansion, l_o is the initial length of sample at initial temperature T_o and l_f is the final length at final temperature T_f.

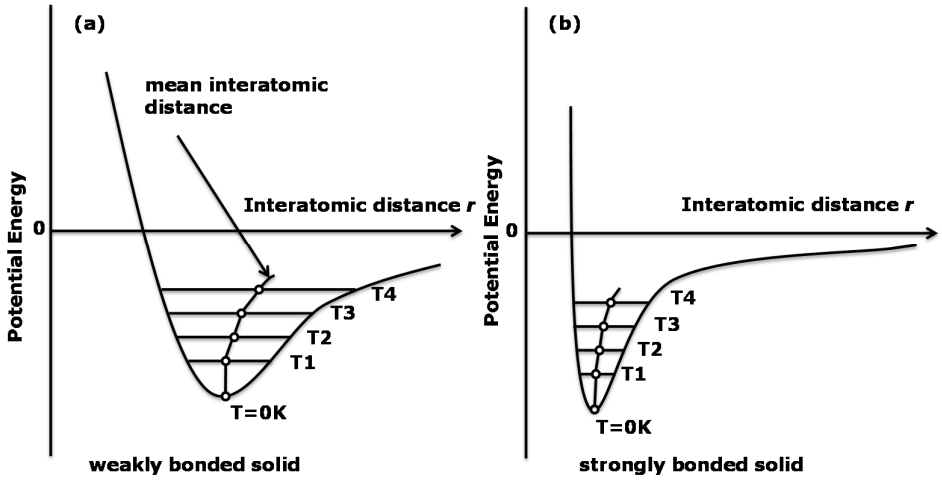

Figure 2-3: The plots of mean interatomic distance in a solid varying with the increase of temperature; **(a)** a solid with weak bonding; **(b)** a solid with very strong bonding.

The volume coefficient of thermal expansion expressed by Eq. (2-13):

$$\frac{V_f - V_o}{V_o} = \frac{\Delta V}{V_o} = a_V\left(T_f - T_o\right) = a_V \Delta T \qquad \text{Eq. (2-13)}$$

where a_V is the volume coefficient of thermal expansion, V_o is initial volume of sample at initial temperature T_o and V_f is final volume at the final temperature T_f.

Ceramic materials usually have high elastic modulus, high melting point, but low coefficient of thermal expansion. Therefore, if high CTE is required for TBCs application, one effective strategy is to properly weaken the bonding in the materials. Furthermore, it is found that CTE would be increased by introducing atoms with high radial size [46], which will be studied in this project.

2.2 7-8 wt% Yttria-Stabilised Zirconia (7-8YSZ) as Typical Ceramic Top-Coat

2.2.1 Background of Conventional 7-8YSZ

Pure zirconia (ZrO_2) has a high melting point of 2690 ^oC and has two phase transformations during cooling. At 2370 ^oC, zirconia can transform from a cubic (*c*-phase) to a tetragonal (*t*-phase) phase; when cooling down to 1170 ^oC, the *t*-phase changes to a monoclinic phase (*m*-phase) [7]. During the phase transformations, the volume difference between the *t*-phase and *m*-phase can produce the disastrous strains, which result in the failure of TBCs.

In order to avoid phase transformations for TBCs application, yttrium oxide with cubic phase can be used to stabilise zirconia, the phase diagram of which is shown in Figure 2-4. When the doping content of yttria is 5-10 wt% (2.2-6.3 mol%), the stabilised

zirconia exhibits non-transformable tetragonal phase (*t´*-phase). The *t´*-phase can present good phase stability. [47]. Moreover, when the doping content is above 10 wt% (6.3 mol%), cubic phase is observed but can still occur phase transformations [13, 48, 49].

Figure 2-5 shows the crystal structure of yttria stabilised zirconia. Because the charges of Y ion and Zr ion are 3+ and 4+, respectively, the oxygen vacancy is generated for the charge compensation. According to the defect chemistry and Kroger-Vink notation, the formation of Y^{3+} substitution defect can be expressed in Eq. (2-14).

$$\mathrm{xY_2O_3} \xrightarrow{\mathrm{ZrO_2}} 2\mathrm{xY'_{Zr}} + 3\mathrm{xO_O^X} + \mathrm{xV_{\ddot{O}}} \qquad \text{Eq. (2-14)}$$

7-8 wt% ytrria stabilised zirconia (7-8YSZ) has been well studied and popularly applied as a TBCs material for several decades. From the Zr_2O_3-Y_2O_3 phase diagram in Figure 2-4, the non-transferable metastable phase can be obtained via displacive transformation by quenching liquid or cubic phases from high temperatures [50]. The space group of *t´*-phase is $P4_2/nmc$, where oxygen displacement is in *c*-direction and lattice parameter *c* is larger than lattice parameter *a* (*a*=*b*) (Figure 2-6) [51].

A critical way to distinguish the tetragonal and non-tetragonal phase is using tetragonality, $^{c}/_{a\sqrt{2}}$. When the value of $^{c}/_{a\sqrt{2}}$ is close to 1.010, the crystal phase is indicated as *t'*-phase for 7-8YSZ [48].

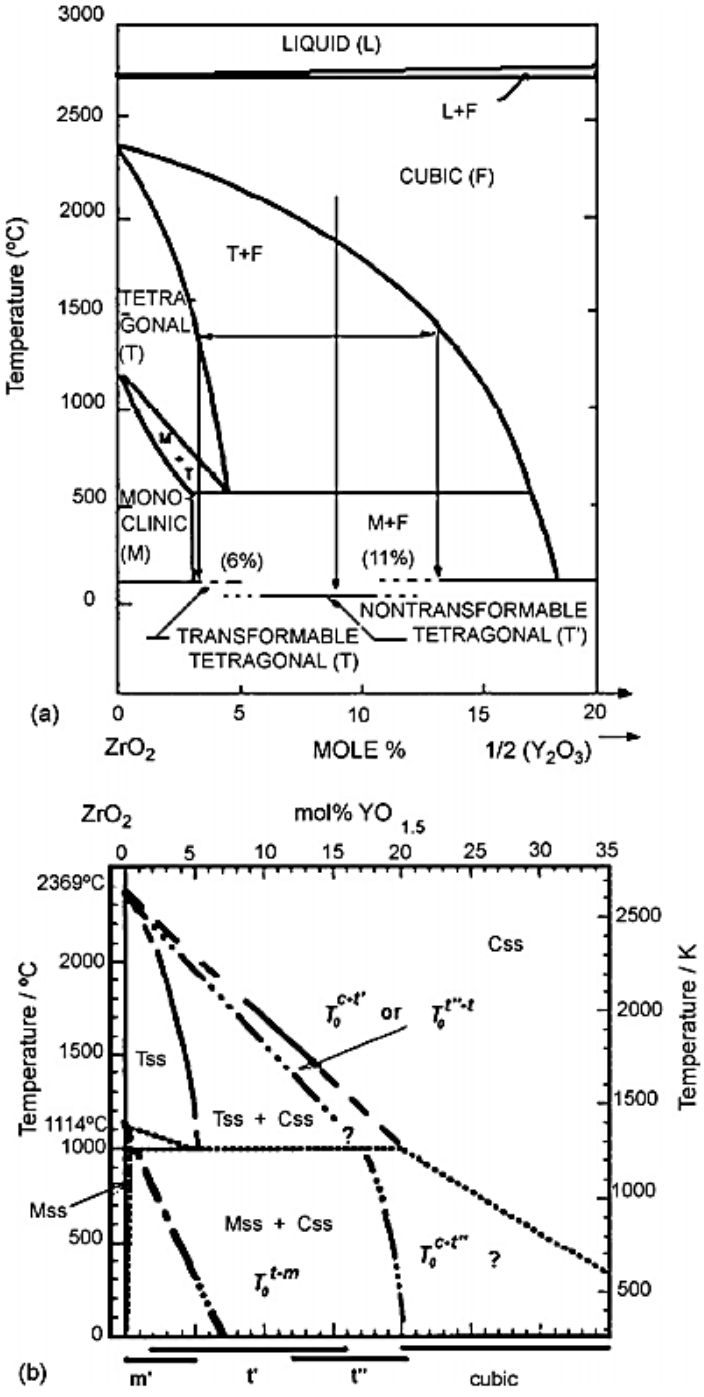

Figure 2-4: **(a)** Phase diagram of Y_2O_3-ZrO_2 in the zirconia rich region; **(b)** Stable-metastable boundary lines are presented by the dash lines [50].

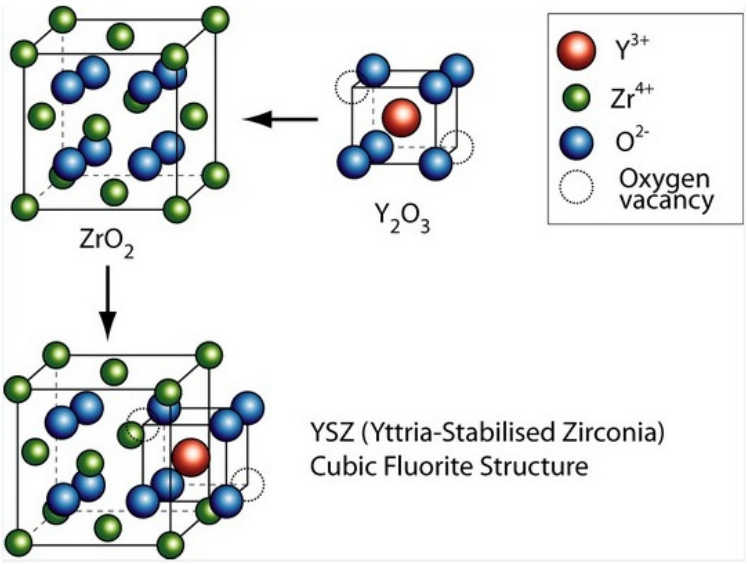

Figure 2-5: The crystal structure of yttria stabilised zirconia with oxygen vacancies [52].

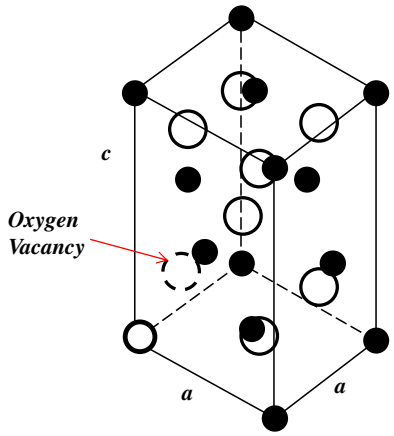

Figure 2-6: The non-transformable tetragonal structure of stabilised zirconia, where the oxygen vacancy is presented inside the unit cell.

2.2.2 Limitations of Conventional 7-8YSZ

Even though 7-8YSZ with *t'*-phase has remarkable resistance to phase transformation, the phase transformations can still occur after the long-time thermal cycling, generating a cubic phase, a yttria-rich tetragonal phase and a yttria-poor tetragonal phase due to yttrium diffusion [47]. Furthermore, 7-8YSZ cannot be applied at higher temperatures (above 1250 ^{o}C), because the *t'*-phase can quickly transform into tetragonal and cubic phases, and then the tetragonal phase convers to monoclinic phase when temperature is close to room temperature. The volume difference of tetragonal and monoclinic phases would result in 3.5% volume change and also cause strain, which could lead to spallation of ceramic coating [16]. Therefore, the phase transformation rate is mainly dependent on the diffusivity of Y^{3+} ions, which is dramatically increased with the increase of temperature.

In addition, if the operation temperature increase, more temperature reduction is needed from the ceramic top-coat, which means that new TBCs materials must have extremely low thermal conductivity. But the thermal conductivity of bulk 8YSZ is 2.1-2.9 $W \cdot m^{-1} \cdot K^{-1}$, which is still relatively high for future gas engines [7, 53]. Furthermore, 8YSZ does not match very well with bond coats, due to its relatively small coefficient of thermal expansion, 11×10^{-6} K^{-1}. The CTE of bond coat is usually around 14×10^{-6} K^{-1} [10]. This CTE mismatch causes strains at the interface between ceramic top-coat and bond coat, which is one of the failure mechanisms of TBCs.

The thickness of TGO in TBCs cannot exceed 6 μm [7], the growth rate of which is dependent on the oxygen ionic diffusivity from ceramic top-coat. The oxygen ionic diffusivity of 7-8YSZ is about 10^{-10}-10^{-11} $m^2 \cdot s^{-1}$ [17], which is still relatively large for oxygen resistance. A material with much lower value would be expected in the future.

2.3 Deposition of Ceramic Top-Coat

Up to now, there are two common techniques for top-coat deposition in thermal barrier coatings (TBCs), Air Plasma Spray (APS) and Electron Beam Physical Vapour Deposition (EB-PVD). The comparison of both technologies is listed in Table 2-1. In addition, the deposition process does not have significant effect on CTE values of 7-8YSZ [12].

Table 2-1: The comparison of bulk 7-8YSZ and materials deposited by APS and EB-PVD techniques.

Deposition Process	Thermal Conductivity	Microstructure
APS	0.8~1.7 [54]	Laminated structure and column within the splats [55]
EB-PVD	1.3~2.0 [12]	Columnar structure and feather-like within the columns [56]
Bulk	2.1~2.9	-

2.3.1 Air Plasma Spray

The APS technique has been well developed for ceramic top-coat deposition for TBCs application. Figure 2-7 presents the schematics of APS manufacturing facility and APS spray process [57, 58]. A high current arc is generated by high frequency voltage. When the plasma gas flows through the gap between the electrodes, it can be ionised by current arc. Powdered feedstock material is injected into the plasma jet, which will be melted and propelled to the surface of the substrate.

Due to the very high temperature of the plasma spray gun, powder materials usually are melted or partially melted. When a molten or semi-molten droplet is deposited on the substrate surface, it spreads into a 'splat' as shown in Figure 2-8 **(a)** [59]. Individual splats are usually very thin, around 1 to 20 μm [60]. The typical microstructure of top-coat by APS is a lamellar structure as shown in Figure 2-8 **(b)** [10]. Furthermore, column structure presents within one 'splat' [Figure 2-8 **(c)**] [60].

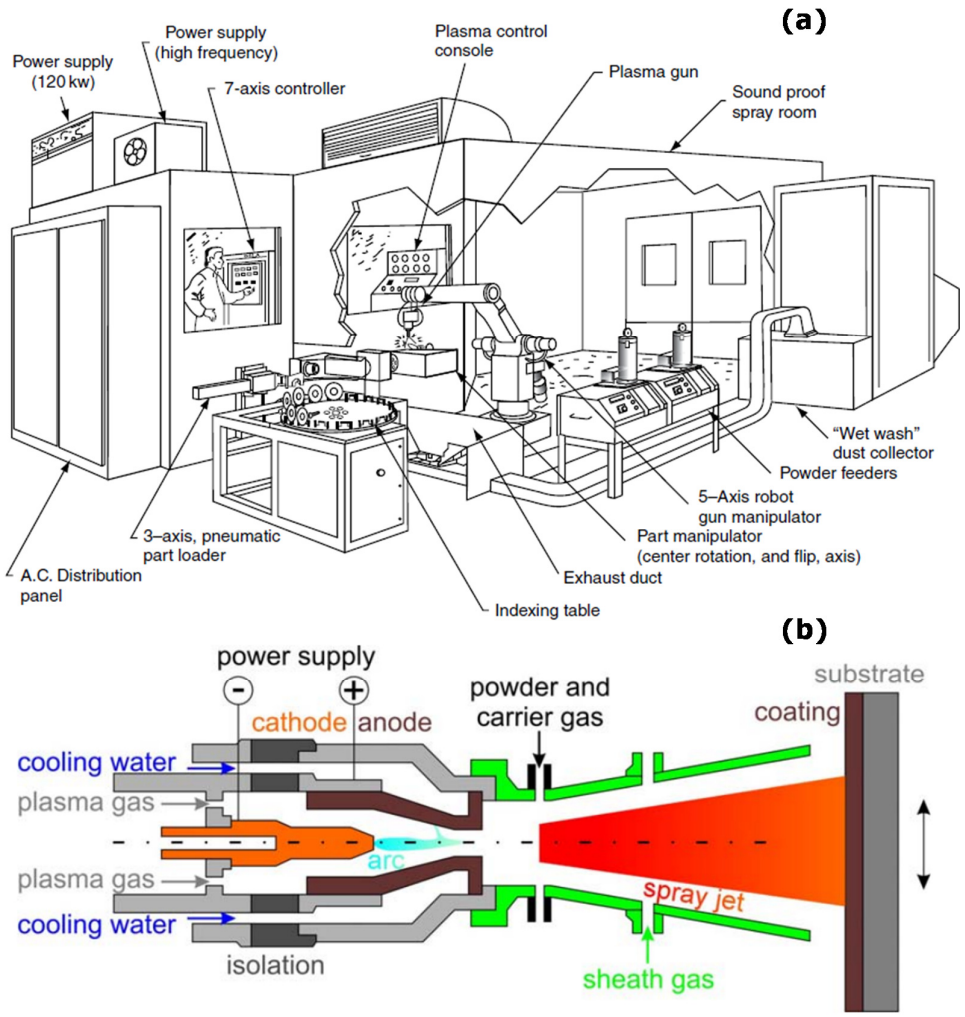

Figure 2-7: **(a)** Schematic of plasma spray manufacturing facility; **(b)** principle of the APS process [57, 58].

In Table 2-1, 7-8YSZ has much lower thermal conductivity than bulk material, which is mainly attributed to the presence of microcracks and porosity in the coatings deposited by APS and EB-PVD. The thermal conductivity of 7-8YSZ deposited by APS is 0.8-1.7 $W \cdot m^{-1} \cdot K^{-1}$, which is roughly half of the value of EB-PVD deposited 7-8YSZ [54]. A significant factor of this difference is due to different microstructure between the both coatings. For plasma

sprayed coating, network microcracks are randomly distributed, where the majority of the microcracks are parallel to the deposition surface, due to the poor contacting between the splats. Some microcracks are perpendicular to the deposition surface, which generated within the individual splats. These microcracks are caused by thermal stresses during cooling. The parallel microcracks are dominant on preventing heat transferring through the coating for reducing thermal conductivity, rather than the vertical microcracks [12].

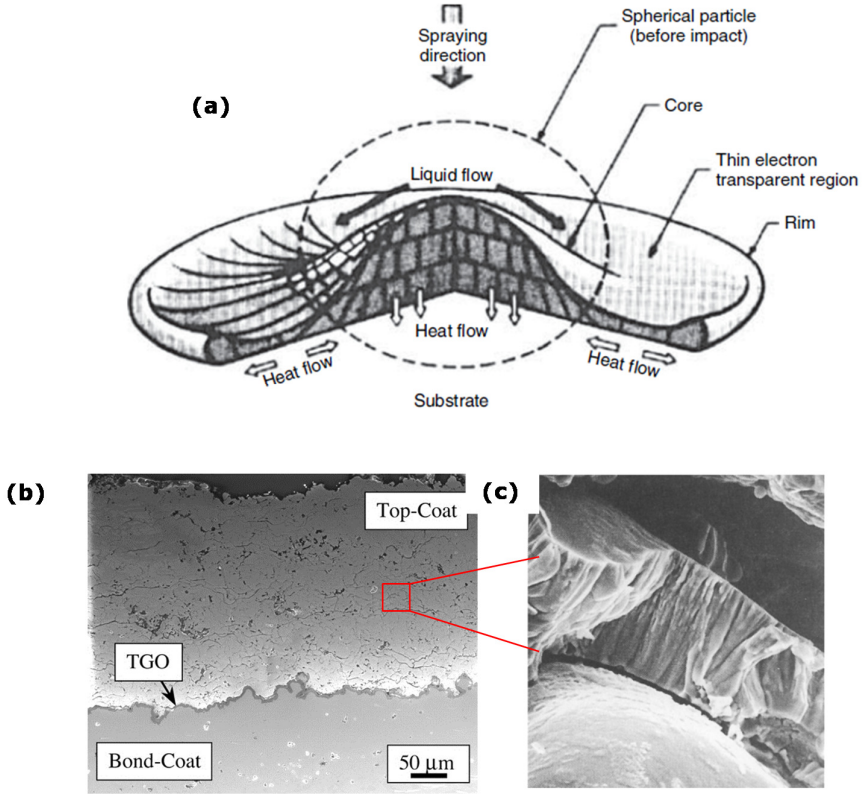

Figure 2-8: **(a)** The schematic of deformation of a APS droplet; **(b)** the typical lamellar microstructure of APS and **(c)** the columnar structure observed within enlarged a splat [10, 59, 60].

2.3.2 Electron Beam Physical Vapour Deposition (EB-PVD)

Because stabilised zirconia has very high melting point (3690 ^{o}C), the traditional methods are very hard to use for ordinary physical vapour deposition (PVD). 7-8YSZ coating can also be deposited by EB-PVD with high power of focused electrons. Figure 2-9 presents the schematic of deposition chamber of EB-PVD [7]. The raw coating materials for EB-PVD deposition are different to that used in APS process and can be in the form of either granules or cylindrical ingots. The electron beam heated raw materials are melted in an evacuated chamber and coated on the surface of the substrate. The position and distance between substrate and ingot can be adjusted by manipulator and substrate holder, to achieve uniform deposition coating. There are two ion beam assist units that can help changing internal tensile stress caused by CTE mismatch between substrate and coating [7].

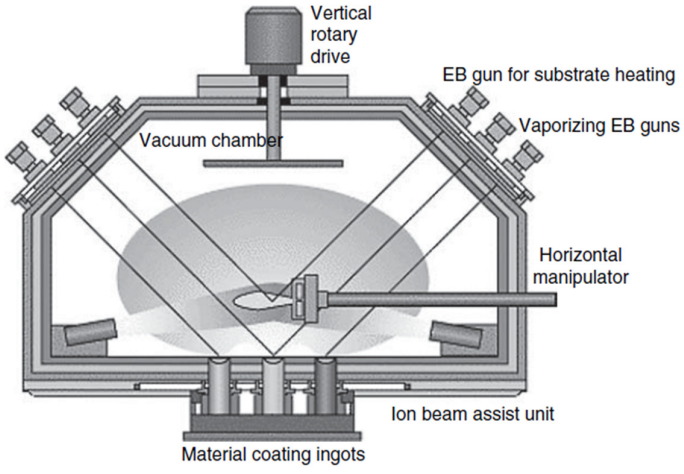

Figure 2-9: Schematic of EB-PVD deposition [7].

In Table 2-1, the thermal conductivity of 7-8YSZ coated by EB-PVD is between the values of plasma sprayed and bulk material. Variation of thermal conductivity of YSZ deposited by different techniques against temperature is exhibited in Figure 2-10 [61]. Compared the microstructure of the top-coat deposited by the plasma sprayed, ceramic coating deposited by EB-PVD shows columnar structure and feather-like shape is observed within columns, see Figure 2-11 [56, 62].

During EB-PVD deposition process, fine porosity is generated within the coating, including porosity within the columns and porosity between columns [7]. But there are no microcracks parallel to the substrate surface in plasma sprayed coating.

Overall, due to the different microstructure deposited by APS and EB-PVD, ceramic top-coat presents different thermal and physical properties. Each method has its own advantages and disadvantages. APS has relatively low cost, easy process flexibility and relatively low thermal conductivity [63, 64]. Even though EB-PVD has higher cost than APS and produces YSZ coating with higher thermal conductivity, the columnar structure of the coating can tolerate thermal expansion and contraction, reducing strain or stresses to improve lifetime [65].

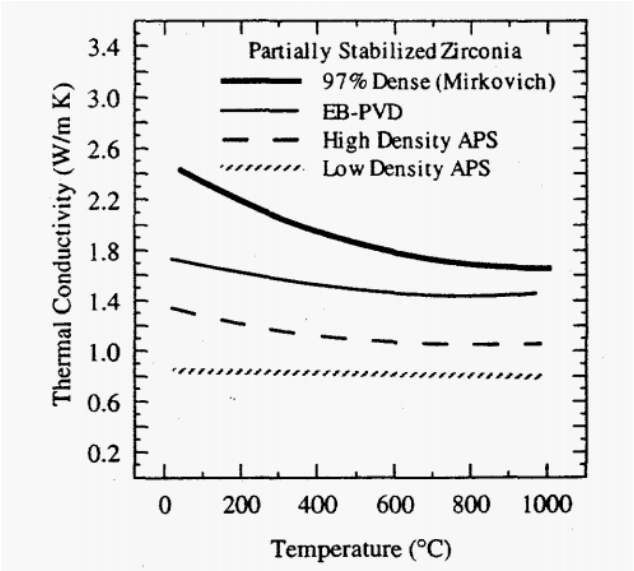

Figure 2-10: Thermal conductivity of yttria-stabilised zirconia deposited by APS, EB-PVD and bulk material [61].

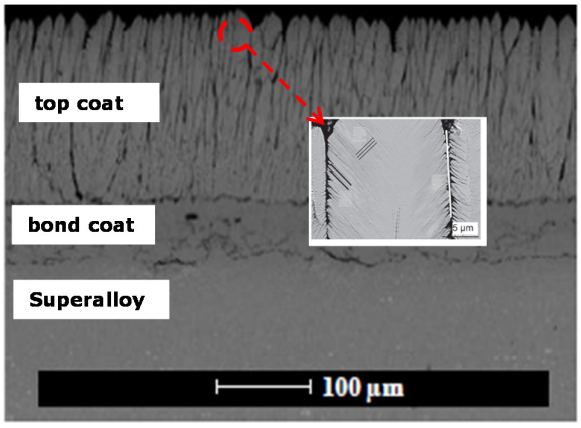

Figure 2-11: The cross-section of TBCs with ceramic coating deposited by EB-PVD, where the columnar structure is observed in top-coat and feather-like microstructure is formed within columns [56, 62].

2.4 Ceramic Systems Studied for TBCs Top-Coat Materials

By considering the criteria of TBCs top-coat materials in section 2.2, there is actually no material that can satisfy all these strict requirements. Currently, new TBCs candidates can be divided into several typical categories [66]:

(1) YSZ-M_xO

YSZ-M_xO group is based on conventional 7-8 wt% yttria stabilised zirconia (7-8YSZ) by adding other rare earth oxides to optimise its phase stability and further reduce the thermal conductivity. Ibegazene [67] *et al.* found that 4.53 mol% Y_2O_3 and HfO_2 co-doped ZrO_2 components can exhibit the non-transferable tetragonal phase without extra phases. Jones [14] reported that Sc_2O_3 can improve phase stability of YSZ up to 1400 ^oC, which was higher than that of 8YSZ (1250 ^oC). Moreover, different rare earth oxides doped YSZ [68] have also been studied, like Er_2O_3, NiO, Nd_2O_3, Gd_2O_3 and Yb_2O_3, for which thermal conductivity can be reduced to 1.0 $W{\cdot}m^{-1}{\cdot}K^{-1}$.

Moreover, Y^{3+} ions in 7-8YSZ show very high diffusivity above 1250 ^oC, which cause the poor thermal phase stability and short thermal cycling life time. Another motivation is to find a good stabiliser to replace Y^{3+} ions.

(2) Pyrochlore

Pyrochlore based materials have been widely investigated, due to high melting point, low thermal conductivity and good phase

stability up to the melting point. $Ln_2Zr_2O_7$ (Ln=Lanthanoides) has been well studied and considered as TBCs candidates [69]. $Ln_2Zr_2O_7$ has much lower thermal conductivity than YSZ, low elastic modulus, similar fracture toughness with YSZ and also better phase stability at higher temperatures. However, its coefficient of thermal expansion (CTE) is slightly smaller than YSZ. Meanwhile, $Ln_2Hf_2O_7$ and $Ln_2Sn_2O_7$ are also under investigation.

(3) Garnet

Garnet based materials have good phase stability and good mechanical properties until melting point. The most important advantage is that this type of materials have extremely low oxygen diffusivity, in which the oxygen diffusivity of $Y_3Al_5O_{12}$ is about 10 orders of magnitude lower than that in zirconia [70]. The small oxygen diffusivity can slow down the increasing thickness of the thermally grown oxide layer and extend the thermal cycling life time of turbine blade.

(4) $La(Mg/Ti)Al_{11}O_{19}$

$La(Mg/Ti)Al_{11}O_{19}$ has complex magnetoplumbite structure, and the phase stability can be maintained above 1400 ^oC [71, 72]. The advantage of this material is that the thermal cycling lifetime could be longer than YSZ if applied as TBCs material, because of its small shrinkage after a long time application at high temperatures. Also the thermal conductivity is smaller than that of YSZ.

(5) Other candidates

The other candidates are perovskite ($LaYbO_3$), perovskite-like materials [$BaLn_2Ti_3O_{10}$ (Ln=Nd and Sm)] and $LaPO_4$. $LaYbO_3$ is considered as TBCs candidate due to its high melting point, good phase stability even above 1300 ^oC, and low thermal conductivity [46].

$BaLn_2Ti_3O_{10}$ (Ln=Nd and Sm) has perovskite-like crystal structure, and belongs to Ruddlesden-Popper type [73]. Guo *et al.* [74] found that the thermal conductivity was lower than that of YSZ, with similar CTE value to YSZ. The monoclinic phase can be stable at 1500 ^oC for 110 h.

$LaPO_4$ [46] does not just have good phase stability at high temperatures, low thermal conductivity and high CTE, but also non-reactivity with α-Al_2O_3 (the main phase in thermally grown oxide layer), which means that $LaPO_4$ can have better stability with TGO. However, it has poor bonding capability with TGO, which is a disadvantage as TBCs candidate.

This thesis mainly focuses on the studies of pyrochlore (stannate), stabilised zirconia (erbia based rare earth oxides stabilised zirconia) and garnet (yttrium aluminium garnet) as new TBCs candidates.

2.4.1 Stannates with Pyrochlore Crystal Structure

Pyrochlore is the derivation of fluorite crystal structure, where a quarter part of pyrochlore has a similar structure to the fluorite

unit cell and the difference is vacancies at 8a sites created by oxygen missing in pyrochlore, as shown in Figure 2-12 [75]. The chemical formula is defined as $A_2B_2O_7$, where A site is 3+ cation from La to Lu and B site is 4+ cation like Zr, Ce, Hf, *etc.* [76-78]. Moreover, in pyrochlore, there are BO_6 units forming the network of corner-shared octahedra which create big space among them, so A atoms can stay in these spaces as shown in Figure 2-13 **(a)** and **(b)**. In 1983, Sunbramanian *et al.* reported that pyrochlore can be stabilised when the ratio of r_A/r_B is between 1.46 and 1.78 [79]. Therefore, there are two sites (A and B sites) of interest for optimising the necessary properties.

Because of this complex crystal structure, pyrochlore possesses more intrinsic defects (like oxygen vacancy) that decrease the mean free path for reducing thermal conductivity. However, this type of material has relatively small coefficient of thermal expansion. Because the thermal expansion is proportional to the mean interatomic distance, the relatively small CTE in pyrochlore is attributed to strong bonding of B-O [19]. For pyrochlore, there are a large number of oxygen vacancies, so both the strength of vibration and the transverse vibration motions can also control the thermal expansion of the crystal [80].

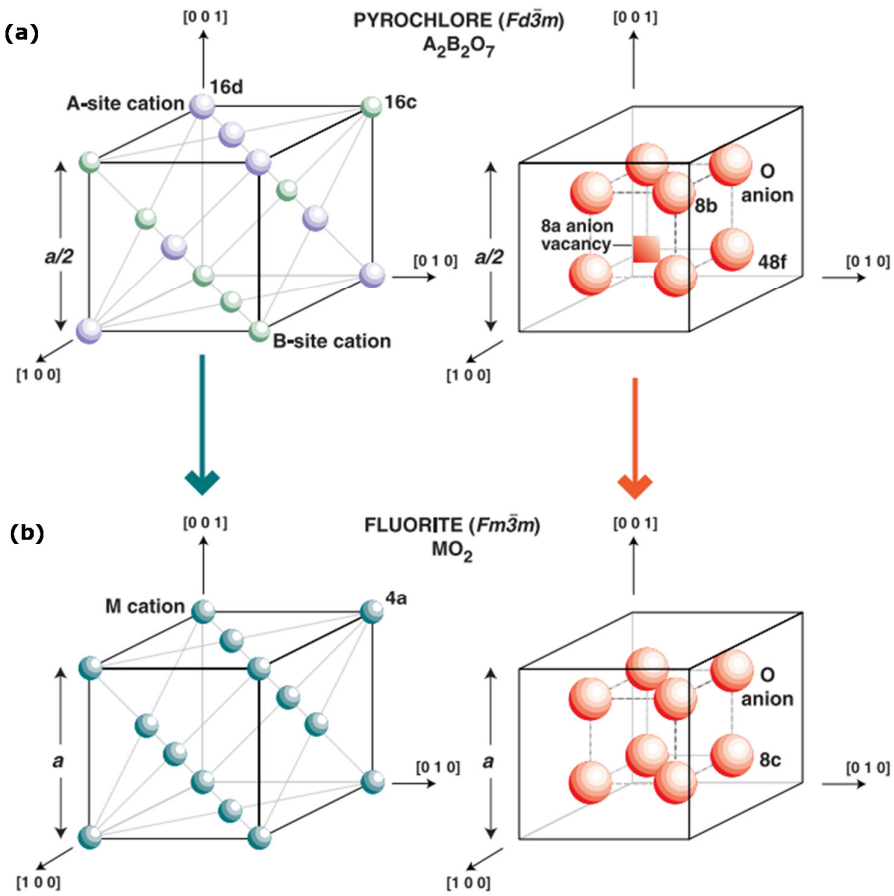

Figure 2-12: The difference of pyrochlore and fluorite crystal structure; **(a)** cations A and B in the unit cells of pyrochlore, **(b)** cations A and B in the unit cells of fluorite [75].

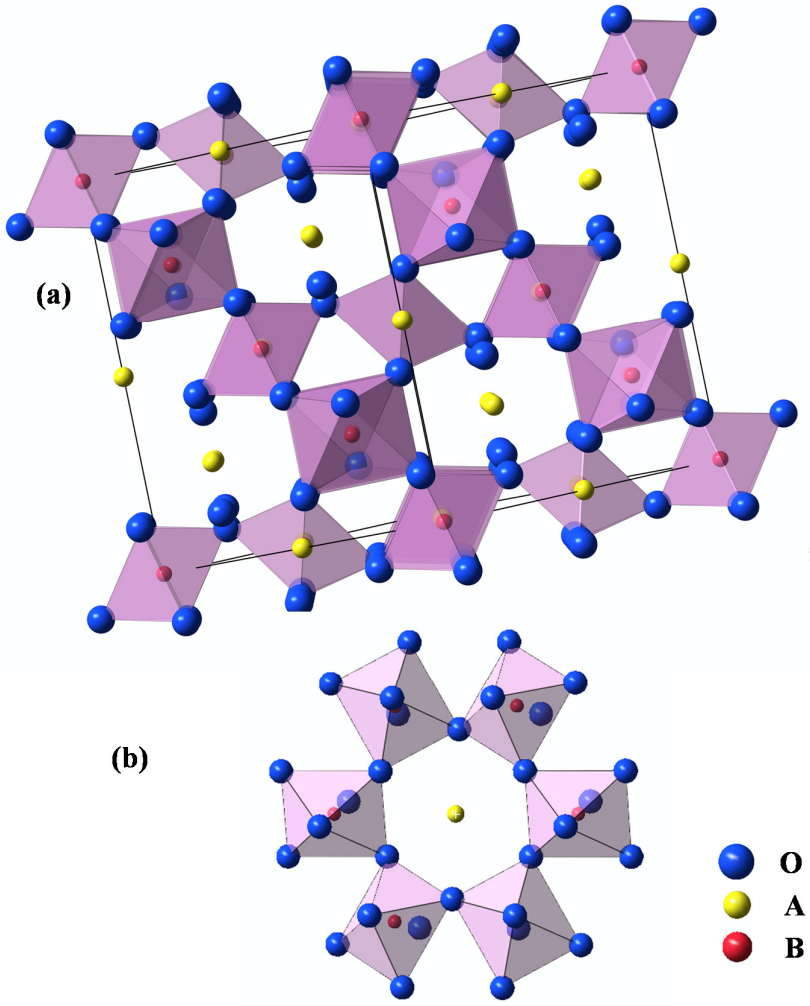

Figure 2-13: **(a)** BO6 units in pyrochlore crystal structure, **(b)** BO6 units forming the network of corner-shared octahedra, where A site stays in this new work.

The ceramic materials with pyrochlore crystal structure have been well studied for TBCs applications due to their low thermal conductivity and good phase stability. The well-known compositions are $Ln_2Zr_2O_7$ and doped $Ln_2Zr_2O_7$, Ln=La, Gd, Sm, Nd, Yb *etc.* in lanthanide group [9, 76, 81, 82]. For doped $Ln_2Zr_2O_7$,

there are three doping strategies to further reduce thermal conductivity and improve coefficient of thermal expansion, which are doping atoms in A sites, doping atoms in B sites and combined doping on both sites.

The properties of Zirconate $Ln_2Zr_2O_7$ (Ln=La, Nd, Sm, Gd *etc.*) have been well-investigated. A typical composition is $La_2Zr_2O_7$ (LZ), which has high melting point (2200 ^oC) and good phase stability up to the melting point as shown in the La_2O_3-ZrO_2 phase diagram in Figure 2-14 [79]. It is found that thermal conductivity of LZ (1.6 $W \cdot m^{-1} \cdot K^{-1}$) is much lower than that of conventional YSZ (2.2 $W \cdot m^{-1} \cdot K^{-1}$) at 1000 ^oC, but the coefficient of thermal expansion is in the range of $7 \sim 10 \times 10^{-6}$ K^{-1}, which is relatively smaller compared with that of YSZ (11×10^{-6} K^{-1}) [9, 76, 83, 84].

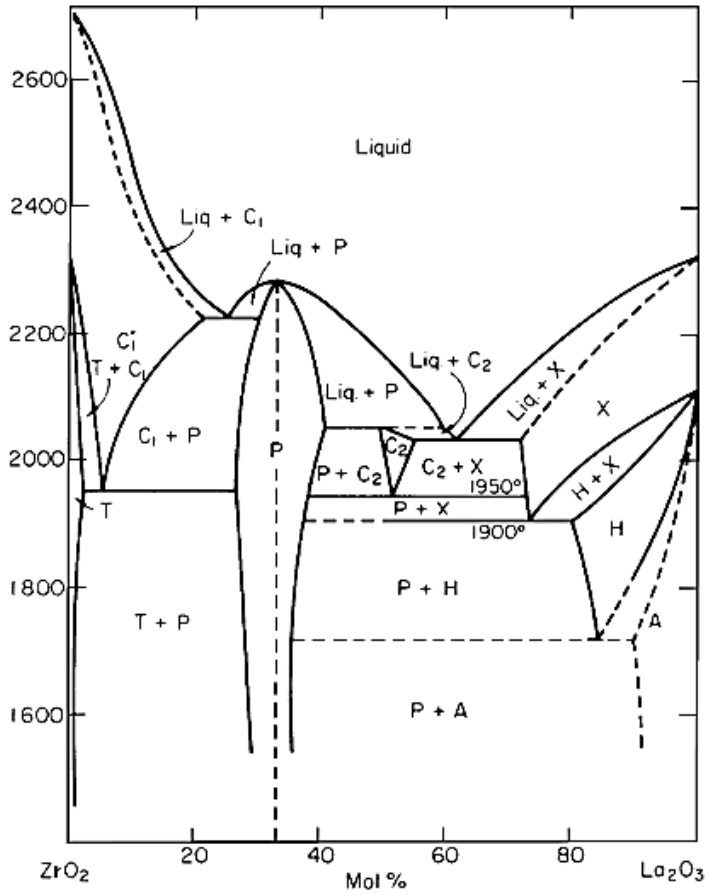

Figure 2-14: The phase diagram of La_2O_3-ZrO_2 system (Liq-Liquid; C-Cubic; T-Tetragonal; P-Pyrochlore; H-Hexagonal high-temperature structure; A-Hexagonal low-temperature structure; X-Another hexagonal high-temperature structure with various ZrO_2 contents) [83, 85].

In order to further reduce thermal conductivity and increase coefficient of thermal expansion, many works have been done on doped LZ. From previous report, by substituting La with Gd, Er, Yb, Sc, Y or Sm, thermal conductivity of doped LZ usually decreases with increasing the doping concentration and becomes

less dependent on the composition at high temperatures [86-90]. Furthermore, it is found that introducing Ce^{4+} ions to replace Zr^{4+} ions in LZ can increase coefficient of thermal expansion [9, 91-104], where the CTE of bulk materials $La_2(Zr_{0.7}Ce_{0.3})_2O_7$ is increased to 11~11.6×10^{-6} K^{-1} [Figure 2-15 **(a)**] [96]. The structure, phase stability and thermophysical properties produced by substituting both La and Zr have also been investigated [98, 105, 106]. The bulk material $(Sm_{0.5}La_{0.5})_2(Zr_{0.8}Ce_{0.2})_2O_7$ obtained by solid state reaction shows very low thermal conductivity [0.73 $W{\cdot}m^{-1}{\cdot}K^{-1}$ as shown in Figure 2-15 **(b)**] and similar coefficient of thermal expansion (10.4×10^{-6} K^{-1}) [98].

Stannate is one pyrochlore materials with a high melting point (> 2000 ^{o}C) [107]. In 2004, Shelling *et al.* did molecular dynamics simulations on optimizing thermal conductivity of pyrochlore, and found that stannates could exhibit the lowest thermal conductivity in pyrochlore, but the low coefficients of thermal expansion (CTEs) of stannates need further improvement for TBCs application [108]. Afterwards, the thermal properties of un-doped stannates were studied by Qu *et al.* [109]. $Ln_2Sn_2O_7$ (Ln = La, Nd, Sm, Gd, Er and Yb) samples prepared by a chemical co-precipitation method exhibited the pyrochlore crystal structure. However, the thermal conductivities are close to that of 7-8YSZ (around 2 $W{\cdot}m^{-1}{\cdot}K^{-1}$ at 1200 ^{o}C) and their CTEs (7~9×10^{-6} K^{-1}) are relatively lower. Furthermore, there is an interesting discovery that phonon scattering is mainly attributed from the strain field caused by the displacement of oxygen ions at 48*f* sites, rather than oxygen vacancies at 8*a* sites.

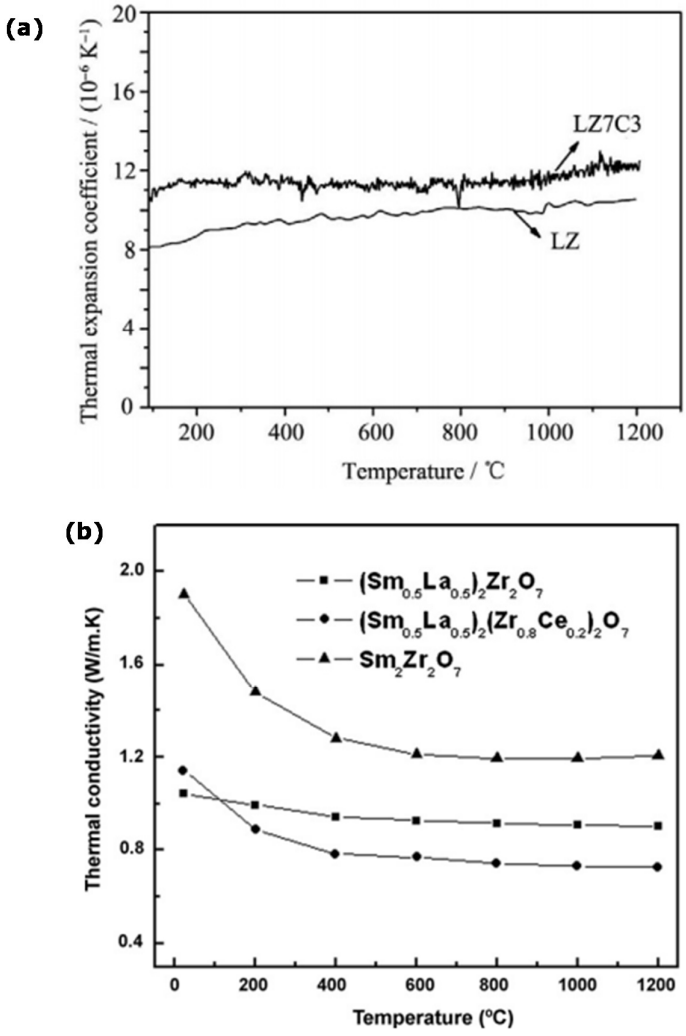

Figure 2-15: **(a)** Coefficient of thermal expansion of $La_2(Zr_{0.7}Ce_{0.3})_2O_7$ [96] **(b)** Thermal conductivity of $(Sm_{0.5}La_{0.5})_2(Zr_{0.8}Ce_{0.2})_2O_7$ [98].

2.4.2 Rare Earth Oxides Doped Zirconia

To further reduce thermal conductivity and improve thermal phase stability of stabilised zirconia is an important demand for future TBCs application. Based on conventional 7-8YSZ, most studies

focus on rare earth oxides doped 7-8YSZ. The doping approaches are proposed including one dopant or two dopants doped in 7-8YSZ. The dopants of the former approach are Ce_2O_3, Gd_2O_3, Dy_2O_3, Sc_2O_3, La_2O_3, HfO_2 and ThO_2 [67, 110-115]. Either Gd_2O_3 or La_2O_3 doped Y_2O_3 stabilised ZrO_2 can further reduce thermal conductivity [110, 111]. The thermal conductivity is made 25% lower than that of 7-8YSZ by introducing Hf^{4+} ions, the effect of which is attributed to mass disorder on the cation sub-lattice in stabilised zirconia [94].

Furthermore, an important discovery is that Sc_2O_3 doped yttria stabilised zirconia exhibits the non-transformable tetragonal phase and has better thermal phase stability at 1400 ^oC than the 7-8 YSZ [116, 117]. In Figure 2-16, the percentage of monoclinic phase increases after 140 h at 1400 ^oC as compared with the content in as-sprayed coat. The phase stability is improved with the increase of Sc_2O_3 content. The best composition (5.63 mol% Sc_2O_3 and 0.37 mol% Y_2O_3) has minimum monoclinic phase (around 7%). Moreover, thermal phase stability can be greatly improved with less content of Y_2O_3 in zirconia.

However, YSZ stabilised by two dopants is more interesting, due to the very low thermal conductivity resulting from the defect cluster. The defect cluster can further scatter phonons [118, 119]. For two dopants, one is usually the normal rare earth oxide (*e.g.* La_2O_3, Nd_2O_3, Gd_2O_3, Yb_2O_3 *etc.*) [120, 121] and the other could be either rare earth oxide or Ta_2O_5 or Nb_2O_5 [122]. Figure 2-17 **(a)** presents the thermal conductivity of 1RE1Yb–YSZ (RE=La, Nd, Gd, Yb), which is significantly lower than that of YSZ. Additionally,

2Yb-YSZ exhibits better phase stability than other specimens, the monoclinic phase is about 10% after 150 h heat treatment at 1400 °C.

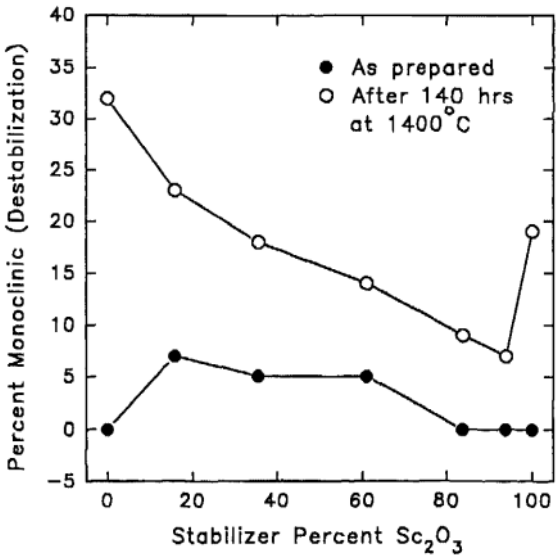

Figure 2-16: Percentage of monoclinic phase in as-plasma sprayed coating and after 140 h at 1400 °C as a function of Sc_2O_3 content (relative mol%) [116].

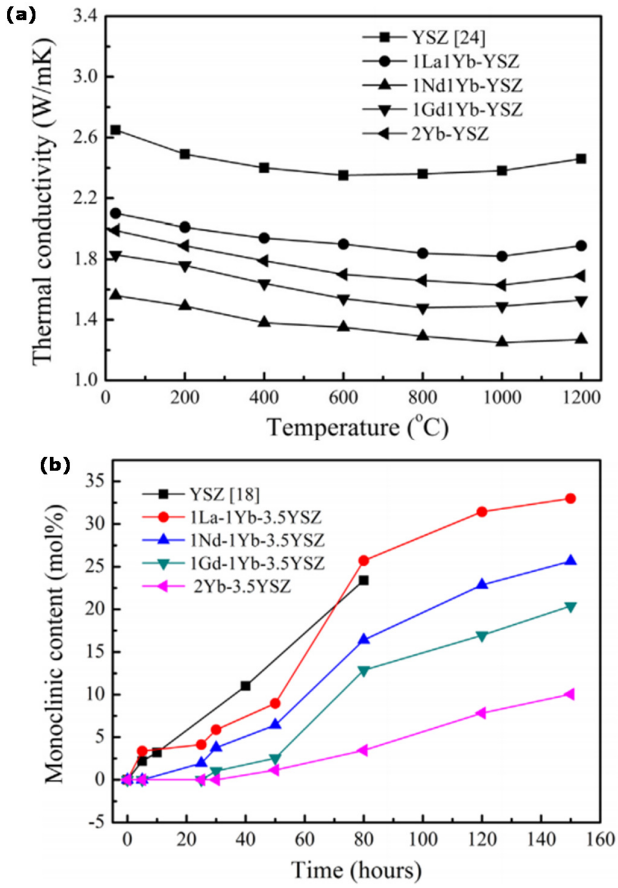

Figure 2-17: **(a)** Thermal conductivity of 1RE1Yb–YSZ (RE=La, Nd, Gd, Yb) as function of temperature; **(b)** monoclinic phase of 1RE1Yb–YSZ powders heat-treated at 1400 °C [120].

Nowadays, exploring new stabilisers for zirconia become an interesting strategy. It has been investigated on the thermal conductivity and phase stability of CeO_2, Nd_2O_3, Er_2O_3, Sm_2O_3, and Yb_2O_3 stabilised zirconia [123-131]. The most popular stabiliser is CeO_2, which can contribute to a relatively high coefficient of thermal expansion (12.5×10^{-6} K^{-1}) and also extremely low thermal conductivity (0.5 $W\cdot m^{-1}\cdot K^{-1}$) with high content of CeO_2 (Figure

2-18) [124].

Furthermore, 25 wt% CeO_2 stabilised ZrO_2 can maintain the tetragonal phase until 100 h annealed at 1600 ^oC [130]. Besides rare earth oxides stabilised zirconia, CaO, MgO, MoO_3, $TaO_{2.5}$ and $NbO_{2.5}$ doped ZrO_2 have also been studied, but most of them show very poor phase stability [132-134]. Khor and Yand [126] studied the lattice parameters, tetragonality and transformability of the tetragonal phase and predicted that Er_2O_3 would be a good phase stabiliser. However, there is little study on the thermal conductivity and the thermal phase stability of zirconia stabilised by Er_2O_3.

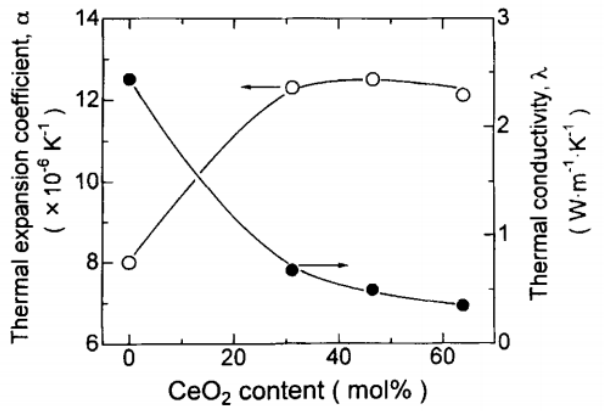

Figure 2-18: Variation of coefficient of thermal expansion and thermal conductivity as the function of CeO_2 content [124].

2.4.3 Yttrium Aluminium Garnet

Yttrium aluminium garnet $Y_3Al(1)_2Al(2)_3O_{12}$ ($A_3B_2C_3O_{12}$, YAG), is one of the garnet materials and has been considered as a promising thermal barrier material candidate, because it has a number of desirable properties, such as high temperature phase

stability, low density and relatively low thermal conductivity and very low oxygen diffusivity [17, 135-139]. The phase stability of YAG is up to the melting point, around 2000 °C from Y_2O_3-Al_2O_3 phase diagram [140]. The extremely low oxygen diffusivity of YAG is in the magnitude of about 10^{-25} $m^2 \cdot s^{-1}$, about 10 orders of magnitude lower than that in yttria stabilised zirconia (10^{-10}-10^{-11} $m^2 \cdot s^{-1}$) [17], which can slow down the growth rate of thermally grown oxides layer. Figure 2-19 shows the coefficient of thermal expansion against thermal conductivity of materials applied in TBCs system, in which YAG has similar thermal conductivity and only slightly lower coefficient of thermal expansion than those of conventional YSZ.

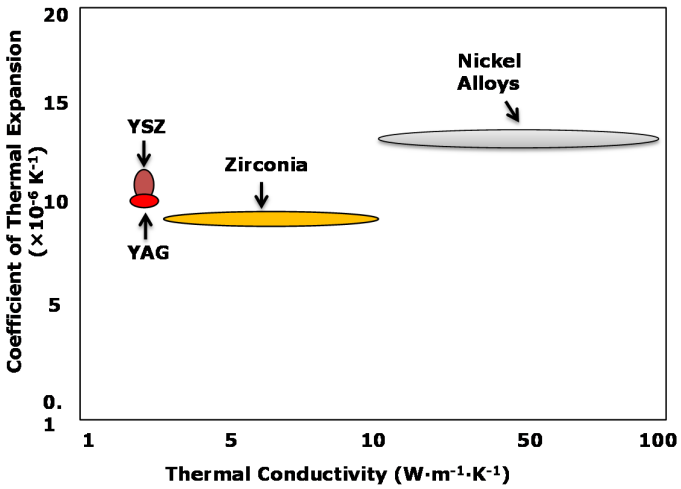

Figure 2-19: Coefficient of thermal expansion against thermal conductivity for materials applied on nickel based superalloys.

The space group of YAG is $Ia_3D(O_h)$ [141], in which it has three type polyhedrons, dodecahedra (YO_8 unit), octahedra (AlO_6 unit)

and tetrahedra (AlO_4 unit) as shown in Figure 2-20. Y^{3+} ions are located on dodecahedral sites (24c), $Al^{3+}(1)$ and $Al^{3+}(2)$ ions are on octahedral (16a) and tetrahedral sites (24d), respectively [142]. As a result of this complex crystal structure, YAG has low thermal conductivity which is only slightly higher than that of YSZ [136]. Therefore, YAG, in particular, is also being considered for future high-temperature structural applications due to its superior high-temperature mechanical properties [138, 139] and excellent phase/thermal stability up to the melting point [135].

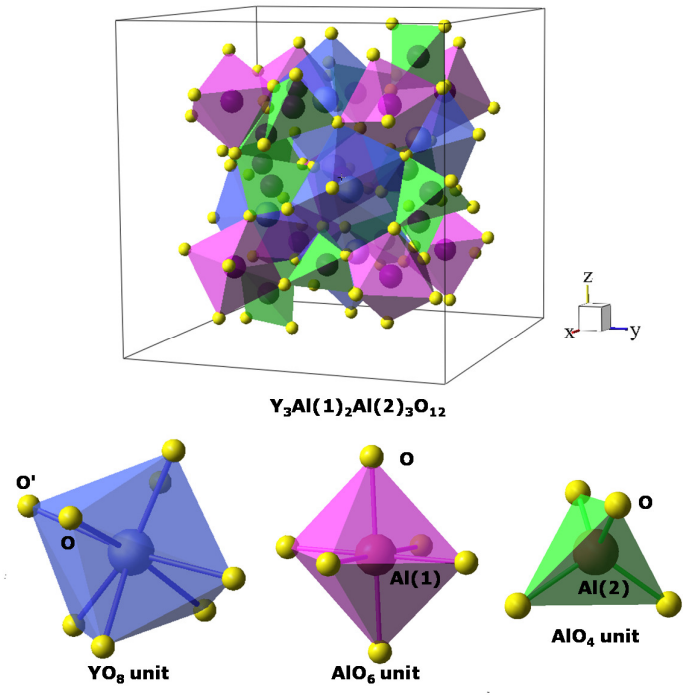

Figure 2-20: Crystal structure of $Y_3Al(1)_2Al(2)_3O_{12}$, which has three type polyhedrons, dodecahedra (YO_8 unit), octahedra (AlO_6 unit) and tetrahedra (AlO_4 unit).

Until now, there are few reports on YAG materials for TBCs application. Padture *et al.* investigated $Y_3Al_xFe_{(5-x)}O_{12}$ (x=0, 0.7, 1.4 and 5.0) solid solution and found its thermal conductivity was decreased by substituting Al^{3+} ions with Fe^{3+} ions. Recently, thermal conductivity can also be decreased by introducing Er on dodecahedral site in YAG, but also this doping mechanism decreases the coefficient of thermal expansion [143]. Other work focuses on designing multilayer TBCs, where YAG is deposited on the top of conventional YSZ layer. For as-sprayed YAG/YSZ coatings, it has been found that the top YAG layer can inhibit the outward diffusion of yttrium from high yttria stabilised *t*-zirconia, which can reduce the oxidation of bond coat [17, 137].

2.5 Methods of Synthesis of Ceramic Powders

Generally, various chemical synthesis methods can be used to prepare ceramic powders. In this section, three common methods are briefly introduced.

2.5.1 Solid State Reaction

Solid state reaction has been widely used to prepare polycrystalline solids. Starting materials are usually solid powders and mixed by stoichiometric ratio. Its typical principle is to keep mixed solid reactants at high temperatures and control the reaction at an appreciable rate to produce ceramic powders. The reaction process is dependent on area of contact between the solid

materials, the diffusion rate of atoms and the nucleation rate of the resultant [144].

The large contact area is desirable in solid state reaction, so starting materials with large surface area can maximise the contact between reactants. Additionally, the solid reactants are usually mixed and pelletised to intimate the contact area. The diffusion rate is one of the main factors to determine the reaction process. In order to increase diffusion rate of atoms, two approaches are generally applied, increasing the reaction temperature and introducing defects. The nucleation rate of the product is also required to be maximised. The strategy is to add mineralizing agent, which should have similar crystal structure as that of the final product [144, 145].

The general process of solid state reaction is shown in Figure 2-21. Some of the starting materials (like oxides) need to be heat-treated at around 600-800 ^{o}C for removing the water, which helps accurately weighing the amount of starting materials [16]. Moreover, ground ceramic powders may be further ball-milled and sieved to obtain fine product with uniform particle sizes [16].

For solid state reaction to synthesise TBCs materials, its advantage is that is easy to operate from the practical point. The drawbacks are relatively slow reaction rate, requiring high temperature and long reaction time, inhomogeneous product and bringing impurity during process.

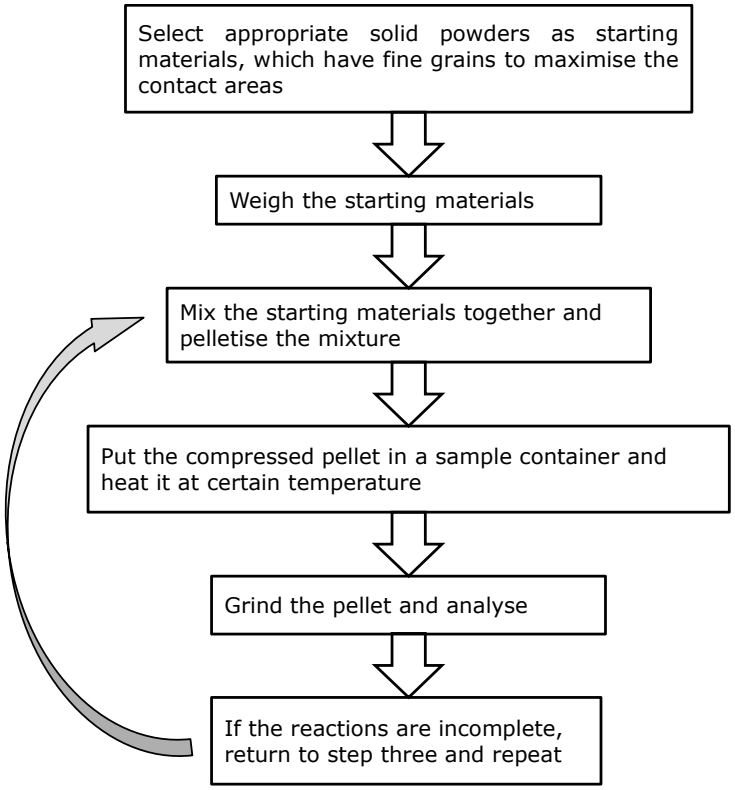

Figure 2-21: Flow-chart of solid state reaction.

2.5.2 Chemical Coprecipitation-Calcination Method

Chemical coprecipitation-calcination method is a technique for removing metal ions from solution, where the metal ions are co-precipited usually as hydroxides, carbonates, oxalates, formates and citrates [146, 147]. For a chemical reaction $AB \rightleftharpoons A^{+} + B^{-}$, it can reach solubility equilibrium when the rate of forward reaction equals the rate of the reverse reaction. By adding precipitate agent, the forward reaction continues and the metal ions are co-precipitated. The obtained precipitation is then calcined at an

appropriate temperature to finalise the products [148]. The general process route is presented in Figure 2-22.

The advantages of chemical co-precipitation are the very low reaction temperature and also simple operation for the synthesis of fine metal oxide powders [147]. However, this process is not suitable for the preparation of high purity and accurate stoichiometric phase. Moreover, if the reactants have very different solubility and precipitation rate, the process condition may not work very well [149]. Furthermore, the experimental condition is not universal, but varies with different materials.

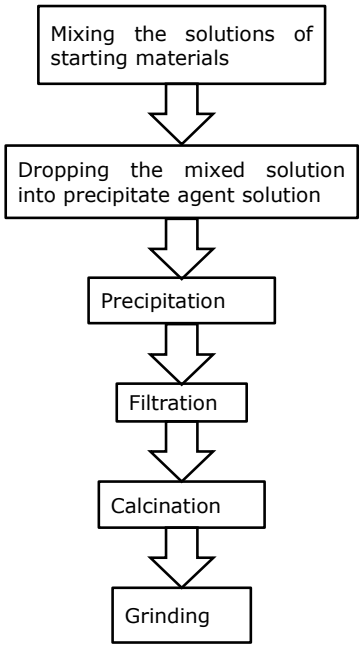

Figure 2-22: The preparation route of chemical coprecipitation-calcination method.

2.5.3 Sol-Gel Method

In recent years, the sol-gel method has become one of the most popular techniques to synthesise different types of materials, including powder, bulk, thin films, sheets and fibres *etc.* for various applications [150, 151]. The sol-gel process usually includes a series of steps of hydrolysis, gelation, condensation, drying and densification. The schematic diagram in Figure 2-23 shows the different sol-gel routes for various types of materials [152].

Starting materials in sol-gel are normally metal alkoxides or salts that can be dissolved in distilled water or solvents at room temperature or slightly higher temperature. After mixing the solutions together, controlling the pH value of the solution is very important [150]. A suitable pH environment can avoid the precipitation and also help to form homogeneous gel. Adjusting pH value is usually achieved by the additions of alkaline or acidic solutions. Furthermore, some organic compounds with hydrophilic functional group (such as citric acid and oxalic acid *etc.*) are used for bonding metal ions to form sol, which can also be used to control the particle size and produce uniform product [153, 154]. Then the process of gelation leads to homogeneous distribution of metal ions. Followed by evaporation, heat-treatment and grinding, the powder material can be obtained.

The advantages of sol-gel process can be summarised as follows: low temperature processing, small particle size, good homogeneity and phase purity compared to traditional ceramic methods. Its

disadvantage is difficulty in massively producing materials for industry application, which is not a serious problem for TBCs application.

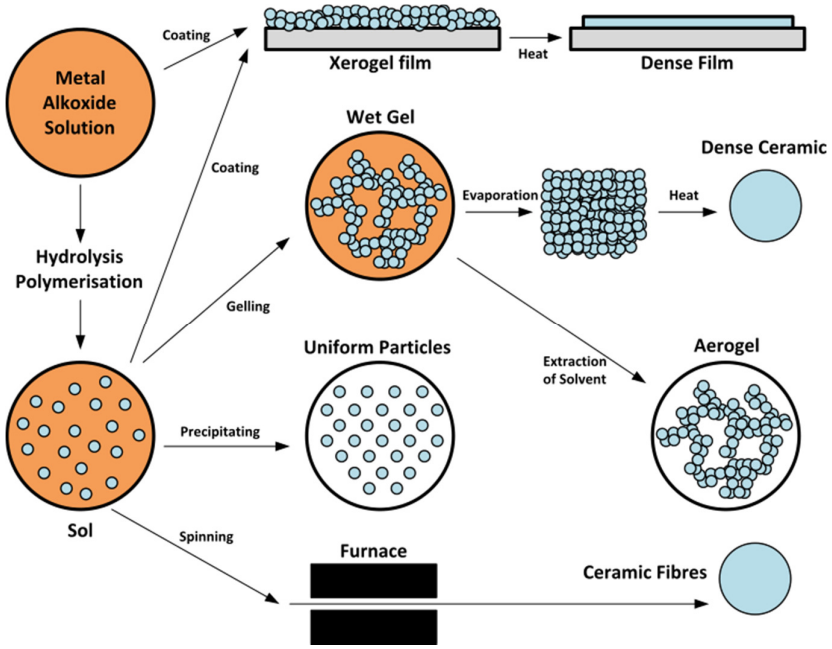

Figure 2-23: Schematic diagram of the different steps and routes of the sol-gel method for various types of materials [152].

2.6 Molecular Dynamics (MD) Simulations

Most studies focus on discovering new TBCs candidates using different experimental synthesis methods [100, 155-157], but thermal conductivity results in most cases cannot be properly explained due to many external affective factors, like porosity, grain boundary and grain size. Furthermore, some explanations cannot be supported by solid evidence. Therefore, it is necessary

and very important to investigate the materials from atomic level to better understand doping mechanisms and effects on thermal conductivity and thermal expansion.

2.6.1 The Motivation of Using MD Simulations

Molecular Dynamics (MD) is a method to study the physical movements of atoms and molecules and determine macroscopic thermodynamic properties of materials, which is based on the statistical ensemble averages when it is equal to time averages of the system [158]. There are two ensembles usually used to study thermal conductivity and thermal expansion in MD. These ensembles are NPT (constant number, pressure and temperature) and NVE (constant number, volume and energy). In a system, the number of atoms, N, is usually constant. If the integrator works, a MD code would preserve total energy (E), as the potential energy and kinetic energies are interchanged but the total remains constant. The simulation cell size of the periodic boundaries is fixed to obtain a constant volume (V) at different temperature (T). But for thermal expansion simulation, NPT ensemble is usually used. The pressure (P) is regulated, but the volume V should be unregulated for calculating thermal expansion [158-160].

Most importantly, MD simulations are a suitable approach to study the thermal conductivity and thermal expansion of materials in atomic level, MD simulations also allow anharmonic nature of atomic interactions which is important for thermal conductivity and

thermal expansion (especially at high temperature [160]) and MD can be used for handling a system with millions of atoms [24].

2.6.2 Thermal Conductivity and Thermal Expansion Simulation of TBCs Materials

The thermal conductivity of yttria stabilised zirconia has been calculated from low temperature up to 2000K by direct MD simulations. The thermal conductivity decreases with the increase of the defect concentration as shown in Figure 2-24 [161]. The simulations also indicate that it is very difficult to reduce thermal conductivity below minimum value by point defects, but the mass contrast might be able to reduce thermal conductivity below the minimum value.

Shelling *et al.* have investigated 40 pyrochlores ($A_2B_2O_7$, A=La, Pr, Nd, Sm, Eu, Gd, Y, Er or Lu; B=Ti, Mo, Sn, Zr or Pb) and low thermal conductivity is predicted by molecular dynamics simulations [108]. Thermal conductivity and coefficient of thermal expansion maps are shown in Figure 2-25 and Figure 2-26, as a function of radii of A and B ions. Figure 2-25 indicate that a Pb-based system has the lowest thermal conductivity due to the structural disorder which causes high level oxygen diffusion, but significant oxygen diffusivity can result in quick increase of TGO layer. However, this discovery cannot be adapted to other pyrochlore systems. In order to find compositions with minimum thermal conductivity, Sn-based systems are predicted to exhibit lower thermal conductivities than either Mo- or Zr-based systems.

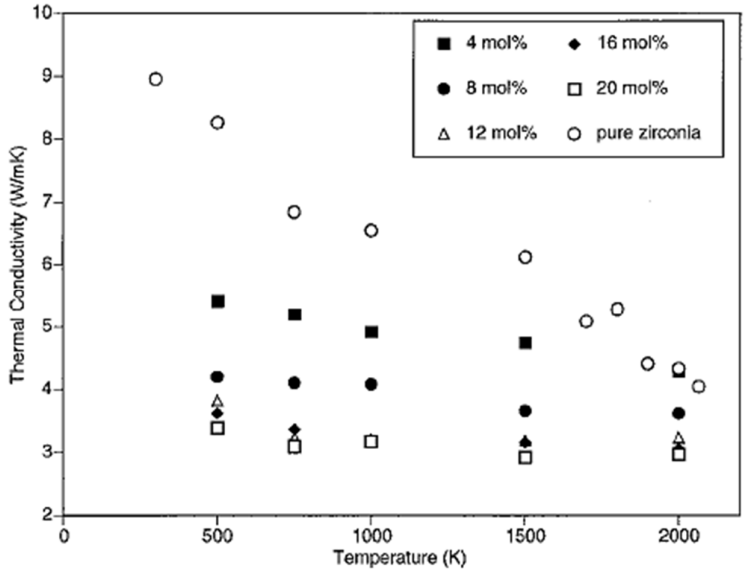

Figure 2-24: Thermal conductivity of yttria-stabilised zirconia obtained by MD simulations, which decreases with the increase of yttria contents and the increase of temperature.

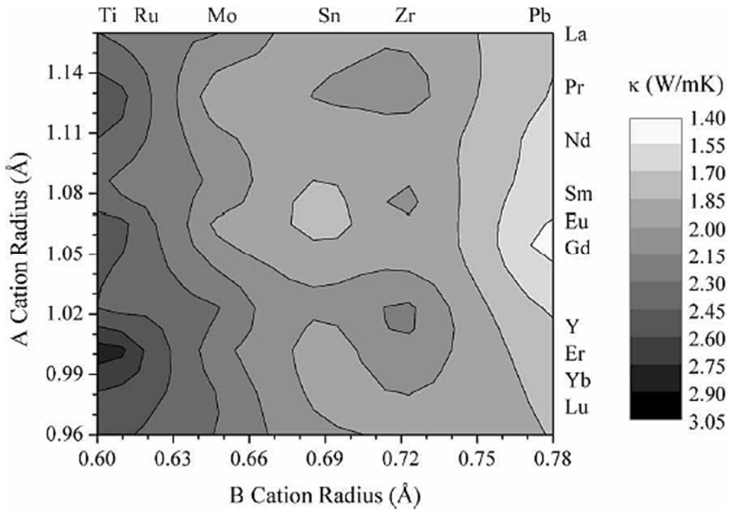

Figure 2-25: Thermal conductivity map of $A_2B_2O_7$ as a function of the radii of A and B ions at 1473K [108].

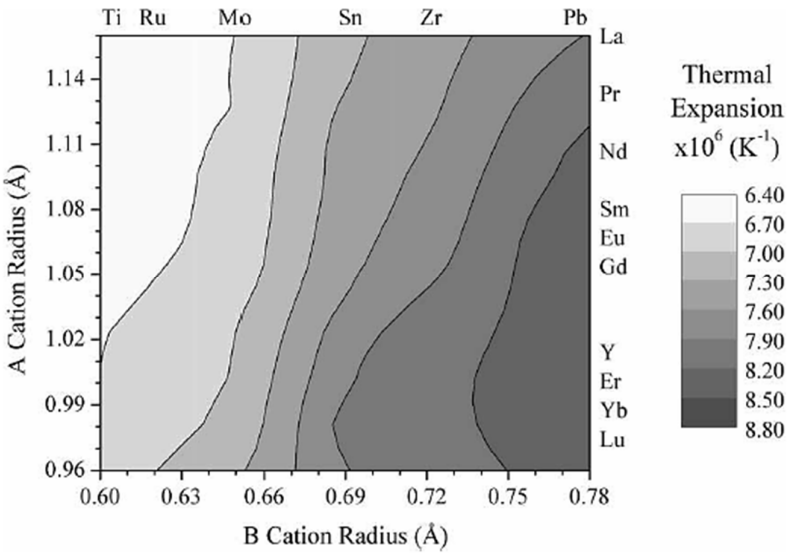

Figure 2-26: Coefficient of thermal expansion map of $A_2B_2O_7$ as a function of the radii of A and B ions at 1473K [108].

Chapter 3. Experimental Methodologies, Characterization and Simulation

This Chapter mainly introduces experimental methodologies and characterization methods for ceramic materials selected from literature review. Molecular Dynamics (MD) theory and methodology are also described to simulate thermal conductivity and coefficient of thermal expansion.

Section 3.1 studies the synthesis of ceramic powers using sol-gel method. Then the materials are characterised in terms of crystalline phase, lattice parameters, microstructures and thermal properties (section 3.2, 3.3 and 3.4). The MD simulation (section 3.5) is performed to study thermal conductivity and coefficient of thermal expansion without the influence of grain size, grain boundary and porosity. The overall experimental flow-chart is given in Figure 3-1.

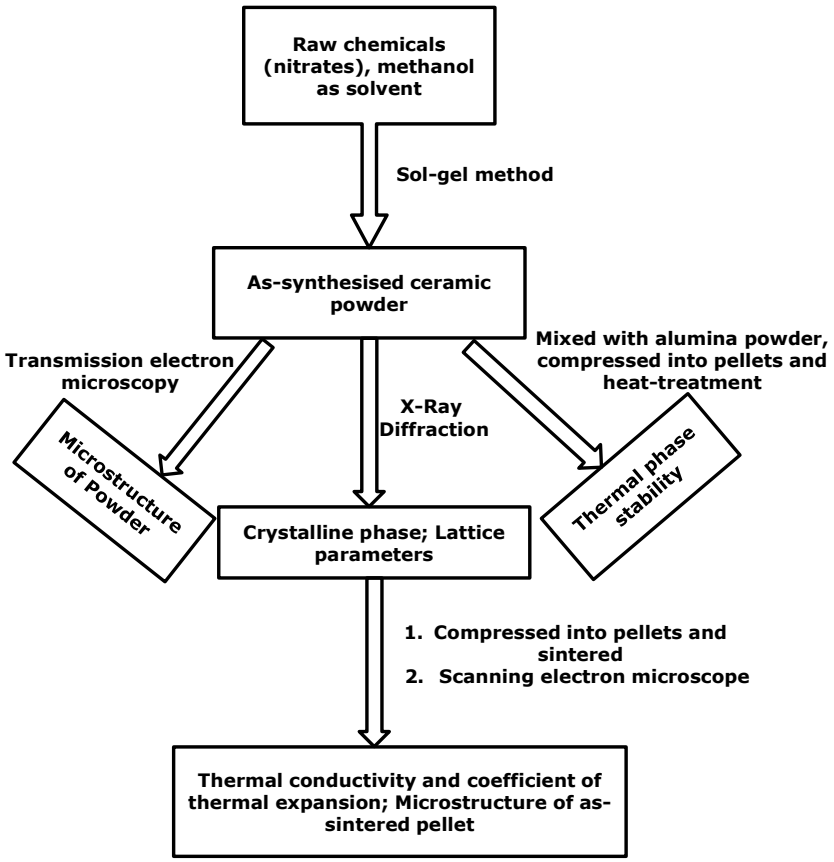

Figure 3-1: Experimental flow-chat of synthesis and characterizations of ceramic materials.

3.1 Materials Preparation

3.1.1 The Powder and Pellet Preparation of Un-Doped Stannate and $(La_xYb_{1-x})_2Sn_2O_7$ Solid Solution (x=0.3, 0.5 and 0.7)

Sol-gel method was used to synthesise ceramic powders as candidate materials. Lanthanum nitrate hexahydrate (Sigma-Aldrich, ≥ 99.0%), ytterbium nitrate pentahydrate (Sigma-Aldrich, 99.9%), and stannic chloride (Sigma-Aldrich, 98%) were selected as raw materials and citric acid (Sigma-Aldrich, 99%) as organic

complexing agent. Methanol (Sigma-Aldrich, ≥ 99.8%) was used as solvent. Firstly, a specific amount of stannic chloride determined by the different stoichiometric ratio of the ceramic was dissolved in methanol, followed by slowly dropping rare earth nitrate solutions under magnetic stirring. After stirring for 30 mins, citric acid was added at a molar ratio of citric acid/cation ions=1.2/1.0. The forerunner was stirred for 6 h at room temperature and then held under static condition at 50 ^{o}C for two days until gel formed. Then the gels were dried at 120 ^{o}C. Afterwards, dried gels were placed into an alumina crucible and kept at 500 ^{o}C for 5 h with a heating rate of 2 ^{o}C/min to remove organic compositions, then heated up to 950 ^{o}C with a rate of 5 ^{o}C/min, and held for 4 h, to completely remove other impurities, such as nitrate group. The next step was to further crystallise them at 1300 ^{o}C for 6 h, with heating rate of 10 ^{o}C/min and cooling rate of 15 ^{o}C/min. Finally, the obtained materials were ground to ceramic powders with a mortar.

The pellets with diameters of 20 mm and 5 mm, were separately compressed under fixed pressure (around 130 MPa for 20 mm and 32 MPa for 5 mm, respectively) by a Pellet Press (Specac, as shown in Figure 3-2) and sintered at 1300 ^{o}C for 6 h, at a heating rate of 10 ^{o}C/min and cooling rate of 15 ^{o}C/min. They were used for thermal conductivity (ϕ 20 mm pellets) and coefficient of thermal expansion measurement (ϕ 5 mm pellets).

8 wt% yttria stabilised zirconia (8YSZ) and $La_2Zr_2O_7$ were synthesised as reference material. Yttrium and lanthanum nitrates (Sigma-Aldrich, 99~99.8%) and zirconyl chloride octahydrate

(Sigma- Aldrich, 98%) were chosen as raw materials and citric acid as organic complexing agent. The difference was that the molar ratio of citric acid/cation ions for 8YSZ was 0.6:1.0. Then a similar process as the stannates was carried out to obtain powder material. Furthermore, the similar procedure was used to acquire pellets of 8YSZ and $La_2Zr_2O_7$ for thermal conductivity and coefficient of thermal expansion measurement. The only difference was that the sintering temperature for 8YSZ pellets was 1200 ^oC for 6 h.

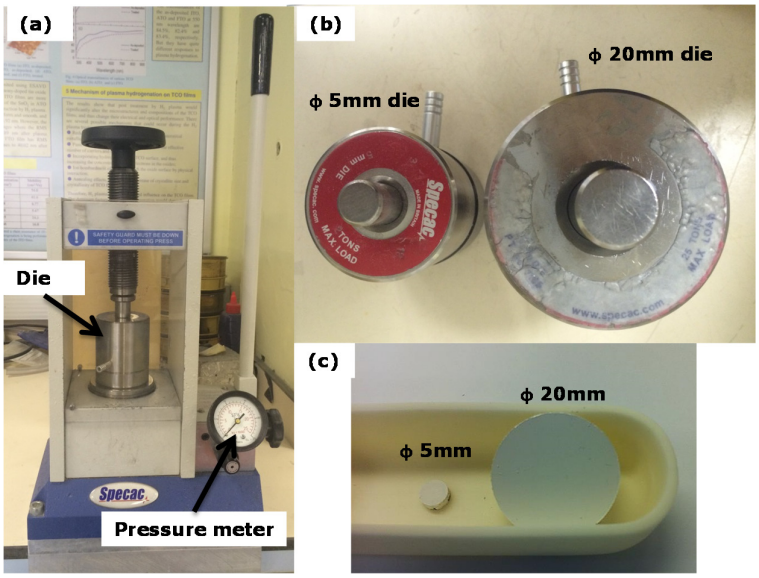

Figure 3-2: **(a)** The compressing equipment for compressing the pellets; **(b)** the dies used for powder compression; **(c)** the compressed pellets.

3.1.2 The Powder and Pellet Preparation of R_2O_3+Er_2O_3 Stabilised Zirconia (R_2O_3=Yb_2O_3, Gd_2O_3 and Dy_2O_3)

For synthesizing the rare earth oxides doped erbia-stabilised zirconias and 8YSZ (as the reference material), erbium(III) nitrate pentahydrate (Sigma-Aldrich, 99.9%), ytterbium(III) nitrate pentahydrate (Sigma-Aldrich, 99.9%), dysprosium(III) nitrate hydrate (Sigma-Aldrich, 99.9%), gadolinium(III) nitrate hexahydrate (Sigma-Aldrich, 99.9%) and zirconyl chloride octahydrate (Sigma-Aldrich, 98%) were chosen as raw materials and citric acid (Sigma-Aldrich, 99%) was selected as organic complexing agent. Methanol (Sigma-Aldrich, ≥ 99.8%) was used as solvent.

Firstly, certain amounts of raw materials determined by specific stoichiometric ratios were dissolved in methanol. The rare earth nitrates solutions were slowly dropped into zirconyl chloride octahydrate solution under magnetic stirring at 50 ^{o}C. After stirring for 30 min, citric acid solution was added, at a molar ratio of citric acid/cation ions = 0.6/1.0. Then the forerunner was stirred at 50 ^{o}C for 3 h, followed by heating at 80 ^{o}C until dried gel was obtained. The dried gel was placed into an alumina crucible and heated at 500 ^{o}C by 2 ^{o}C/min for 2 h to remove carbon contents from organic components, then heated up to 950 ^{o}C by 2 ^{o}C/min for 2 h to completely remove the remaining impurities, and cooled down with cooling rate of 10 ^{o}C/min to room temperature. Finally, the obtained materials were ground into ceramic powders using a mortar for phase analysis.

Pellets with diameter 20 mm and 5 mm were produced under the same condition as stannate system. The pellets were sintered at 1200 ^{o}C for 6 h, with heating and cooling rate of 10 ^{o}C/min for thermal conductivity and coefficient of thermal expansion measurement. The compositions of the specimens are listed in Table 3-1.

Table 3-1: Descriptions of R_2O_3+Er_2O_3 stabilised zirconia

Specimen	**Doping Concentration of R_2O_3 and Er_2O_3**
E5Z	5 mol% Er_2O_3 stabilised zirconia
E2.5Y2.5Z	2.5 mol% Er_2O_3, 2.5 mol% Yb_2O_3 stabilised zirconia
E2.5G2.5Z	2.5 mol %Er_2O_3, 2.5 mol% Gd_2O_3 stabilised zirconia
E2.5D2.5Z	2.5 mol% Er_2O_3, 2.5 mol% Dy_2O_3 stabilised zirconia
E6Z	6 mol% Er_2O_3 stabilised zirconia
E2Y2G2Z	2 mol% Er_2O_3, 2 mol% Yb_2O_3, 2 mol% Gd_2O_3 stabilised zirconia
E2Y2D2Z	2 mol% Er_2O_3, 2 mol% Yb_2O_3, 2 mol% Dy_2O_3 stabilised zirconia
E2D2G2Z	2 mol% Er_2O_3, 2 mol% Dy_2O_3, 2 mol% Gd_2O_3 stabilised zirconia

3.1.3 The Powder and Pellet Preparation of Un-Doped and Doped Yttrium Aluminium Garnet

To obtain un-doped and doped Yttrium aluminium garnet ($Y_3Al_5O_{12}$, YAG) powders, ytterbium nitrate pentahydrate (Sigma-Aldrich, 99.9%), erbium(III) nitrate pentahydrate (Sigma-Aldrich, 99.9%), lanthanum nitrate hexahydrate (Sigma-Aldrich, ≥ 99.0%), yttrium nitrate hexahydrate (Sigma-Aldrich, 99.8%) and aluminium nitrate nonahydrate (Sigma- Aldrich, 98%) were chosen as raw materials and citric acid (Sigma- Aldrich, 99%) as organic complexing agent. Methanol (Sigma- Aldrich, ≥ 99.8%) was used as solvent.

Firstly, certain amount of raw materials determined by different stoichiometric ratios for each sample was dissolved in methanol. Ytterbium nitrate pentahydrate and yttrium nitrate hexahydrate solutions were slowly dropped into aluminium nitrate nonahydrate solution under magnetic stirring at room temperature. After stirring for 30 mins, citric acid solution was dropped, where the molar ratio of citric acid/cation ions is 1.2/1.0. The forerunner was stirred for 3 h at room temperature. Then the mixed solution was moved into a furnace at 80 ^oC until the dried gel was obtained. The dried gel was placed into an alumina crucible and heat-treated at 500 ^oC by 2 ^oC/min for 4 h to remove carbon from organic components, then heating up to 950 ^oC with 2 ^oC/min for 2 h to completely remove the remaining impurities, and cooled down with cooling rate of 10 ^oC/min to room temperature. Finally, the obtained materials were ground into ceramic powders using a mortar.

The pellets of un-doped and doped YAG with diameters of 20 mm and 5 mm, were separately compressed under fixed pressure (130 MPa for 20 mm and 32 MPa for 5 mm, respectively), which were sintered at 1400 °C for 10 h, at a heating rate of 10 °C/min and cooling rate of 15 °C/min. The descriptions of Yb^{3+} ions doped in dodecahedra to replace host Y^{3+} ions or in octahedra to replace host Al^{3+} ions were listed in Table 3-2.

Table 3-2: The descriptions of YAG specimens.

Specimens	Specifications
A1	$(Yb_{0.05}Y_{0.95})_3Al_2Al_3O_{12}$
A2	$(Yb_{0.15}Y_{0.85})_3Al_2Al_3O_{12}$
A3	$(Yb_{0.20}Y_{0.80})_3Al_2Al_3O_{12}$
B1	$Y_3(Yb_{0.005}Al_{0.995})_2Al_3O_{12}$
B2	$Y_3(Yb_{0.015}Al_{0.985})_2Al_3O_{12}$
B3	$Y_3(Yb_{0.020}Al_{0.980})_2Al_3O_{12}$

3.1.4 Chemical Compatibility between Ceramic Material and Alumina

For un-doped stannate and $(La_xYb_{1-x})_2Sn_2O_7$ solid solution (x=0.3, 0.5 and 0.7), as synthesised powders were mixed with Al_2O_3 (Sigma-Aldrich, ≥ 98%) at 1:1 mole ratio, and the mixtures were pressed into pellets. The pellets were heat-treated at 1200 °C, 1250 °C, 1300 °C and 1350 °C for 6 h, respectively, and their X-Ray diffraction results were obtained after each heat treatment. Furthermore, Thermogravimetry and Differential Scanning Calorimetry (TG-DSC) was performed to further study the thermal

stability testing. The mixed powders were heated up to 1400 °C with 10 °C/min heating rate in air atmosphere. The TG-DSC data of pure Al_2O_3 was also measured and used as a reference material.

To evaluate the thermal phase stability and chemical compatibility of rare earth oxides stabilised zirconia with Al_2O_3, the as-synthesised stabilised zirconia powders were mixed with Al_2O_3 powder (Sigma-Aldrich, ≥ 98%) at the weight ratio of 1:1, and compressed into ϕ 13 mm pellets under fixed pressure (around 130 MPa). The pellets were heat-treated at 1400 °C for different durations with heating and cooling rate of 30 °C/min, and then the XRD patterns were collected after each heating duration for phase investigation and calculation.

3.2 Crystalline Phase Analysis

3.2.1 X-Ray Diffraction (XRD)

Overall, there are two XRD equipment used for crystalline phase and lattice parameter studying, Siemens D500 and Bruker D8 Advance. The scanning range of 2-theta (2θ) was different for stannate, stabilised zirconia and YAG. Bragg's law shown in Eq. (3-1) was used for analysing the relationship between peak shift and lattice parameters [162].

$$2d \sin\theta = n\lambda,\ n=1,\ 2,\ 3,\ etc. \qquad \text{Eq. (3-1)}$$

where d is the perpendicular distance between pairs of adjacent planes in crystal structure; θ is Bragg angle; λ is the X-ray wavelength.

For un-doped stannate and $(La_xYb_{1-x})_2Sn_2O_7$ solid solution (x=0.3, 0.5 and 0.7), X-Ray Diffraction (XRD, Siemens D500) using Cu *K*-alpha radiation as X-Ray source was used to analyse the crystalline phase of as-synthesised powder at room temperature, with scanning range of 2θ from 20^o to 90^o and scanning step of 0.02^o. The applied voltage and current were 40 kV and 25 mA, respectively. The XRD results were analysed by Eva software. The same XRD results were used for Rietveld refinement to obtain the lattice constant of $(La_xYb_{1-x})_2Sn_2O_7$ solid solution (x=0.3, 0.5 and 0.7).

For R_2O_3+Er_2O_3 stabilised zirconia (R_2O_3=Yb_2O_3, Gd_2O_3 and Dy_2O_3), D500 was performed on as-synthesised powder to identify the non-transformable phase, with 2θ from 20^o to 90^o and scanning step of 0.02^o. The applied voltage and current were 40 kV and 25 mA, respectively. Moreover, X-Ray Diffraction (XRD) (Bruker D8 Advance) using Cu *K*-alpha radiation as X-Ray source was used to analyse the lattice parameter at room temperature, with the scanning range of 2θ from 25^o to 150^o, at scanning step of 0.01^o. The voltage and current were 40 kV and 35 mA, respectively. The XRD results obtained from D8 were used for Rietveld refinement.

The crystalline phase of un-doped and doped YAG was studied from 20^o to 90^o with D500, with scanning step of 0.02^o. The applied voltage and current were 40 kV and 25 mA, respectively.

Meanwhile, the as-synthesised powder was also characterised at high 2θ from 85^{o} to 150^{o} for Rietveld refinement, with scanning step of 0.01^{o}. The voltage and current were 40 kV and 35 mA, respectively.

3.2.2 Rietveld Refinement

In order to better understand the change of crystal structure by introducing dopants, Rietveld refinement was applied to obtain the lattice constants. The lattice constants were also used to calculate the theoretical density then to obtain the porosity of pellet for correcting the thermal conductivity, which was described in section 3.5.2.

For $(La_xYb_{1-x})_2Sn_2O_7$ solid solution (x=0.3, 0.5, 0.7), the lattice constants of $(La_xYb_{1-x})_2Sn_2O_7$ (x=0.3, 0.5, 0.7) and the relative phase contents in $(La_xYb_{1-x})_2Sn_2O_7$ related with inhomogeneous distribution of dopants, were simulated by using the third Chu-Wan profile function of General Structure Analysis System (GSAS) software [163]. The calculative XRD database was referenced from pyrochlore $La_2Zr_2O_7$ [164].

For R_2O_3+Er_2O_3 stabilised zirconia (R_2O_3=Yb_2O_3, Gd_2O_3 and Dy_2O_3), their lattice constants were obtained from the same process as stannate system. The calculative XRD database was referenced from "Neutron Diffraction Study of Tetragonal Zirconias Containing Tetravalent Dopants" by Hunter [165].

Rietveld refinement was also applied to calculate the lattice constants of un-doped and doped YAG. The calculative XRD database was referenced from yttrium aluminium garnet [166].

3.2.3 Phase Evolution in New Stabilised Zirconia

To evaluate the thermal phase stability of R_2O_3+Er_2O_3 stabilised zirconia (R_2O_3=Yb_2O_3, Gd_2O_3 and Dy_2O_3), XRD results obtained from each heat treatment were used for calculating the content of each phase. The net area of peaks were applied for calculating the mole percentage of monoclinic phase and tetragonal phase after heat treatment, where Eq. (3-2) and (3-3) were used [101]:

$$\frac{M_m}{M_t} = 0.82 \frac{NA_m(11\bar{1})+NA_m(111)}{NA_t(111)} \quad \text{Eq. (3-2)}$$

$$M_m + M_t = 100 \quad \text{Eq. (3-3)}$$

where M_m is the amount of monoclinic phase; M_t is the amount of tetragonal phase; $NA_m(11\bar{1})$ is the net area of $(11\bar{1})$ peak in monoclinic phase; $NA_m(111)$ is the net area of (111) peak in monoclinic phase; and $NA_t(111)$ is the net area of (111) peak in tetragonal phases.

3.3 Microscopy Characterization

3.3.1 Transmission Electron Microscopy (TEM)

The microstructures of as-synthesised powders were studied by Transmission Electron Microscopy (TEM, JEOL 2000FX). The TEM specimens were prepared by dispersing small amount of ceramic powders in pure alcohol in an ultrasonic generator, and placing a drop of the dispersion on a copper mesh covered with a 'holey' carbon film. Conventional TEM images and electron diffraction patterns were obtained when the equipment was operated at 200 kV.

3.3.2 Scanning Electron Microscope (SEM)

The surface of as-sintered pellets was observed using a XL30 ESEM-FEG scanning electron microscope (SEM) with an accelerating voltage of 15 kV. The SEM samples were carbon coated before observation. The grain sizes were analysed using the software ImageJ based on SEM images, with average size calculated.

3.4 Measurements of Thermal Properties

3.4.1 Thermogravimetry and Differential Scanning Calorimetry (TG-DSC)

Thermogravimetry and Differential Scanning Calorimetry (TG-DSC, TA Instruments SDT-Q600 shown in Figure 3-3) was performed. For stannate system, DSC curves indicated the chemical reaction temperature between $(La_{0.5}Yb_{0.5})_2Sn_2O_7$ and Al_2O_3. The mixed powder of synthesised powder and alumina powder was heated from 200 ^oC to 1400 ^oC with heating rate, 5 ^oC/min in air atmosphere. For YAG system (Chapter 6), TG-DSC was performed on the dried precursor from room temperature to 1400 ^oC with heating rate of 5 ^oC/min in air atmosphere.

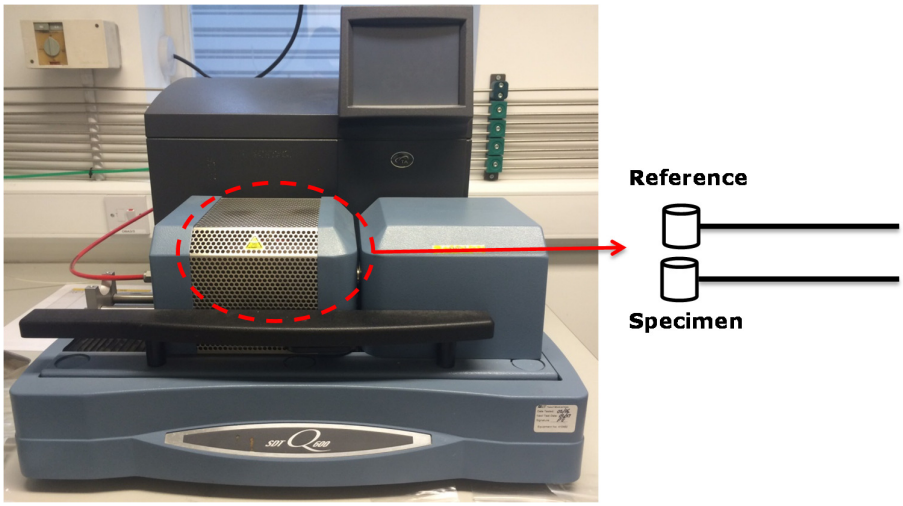

Figure 3-3: TG-DSC equipment used for detecting the variation of mass and heat flow.

3.4.2 Thermal Conductivity

Thermal Conductivity Analyser (TCA, C-THERM Tci™) uses the Modified Transient Plane Source (MTPS) technique. Interfacial heat reflectance on one side can apply a momentary constant heat source to the placed specimen shown in Figure 3-4. This heat results in a rise in temperature at the interface between sensor and specimen. Then this temperature rise induces a change in the voltage drop of the sensor element. The rate of increase in the sensor voltage is used to determine the thermal conductivity of the specimen, because the thermal property is inversely proportional to the rate of increase in the sensor voltage.

The thermal conductivities of ceramic pellets with 20 mm diameters and minimum thickness of 3 mm were measured at room temperature. Wakefield solution of T120 silicone was applied between the ceramic pellet and a sensor as thermal joint compound for good contact. The thermal conductivities of all pellets were corrected from the measured thermal conductivities and their porosities by Eq. (3-4) [21]:

$$\frac{k\prime}{k_o} = 1 - \frac{4}{3}\emptyset \qquad \text{Eq. (3-4)}$$

where k' is the value of measured thermal conductivity using TCA equipment; k_o is the corrected value of ceramic material and $\emptyset$ is the estimated fractional porosity of specimen.

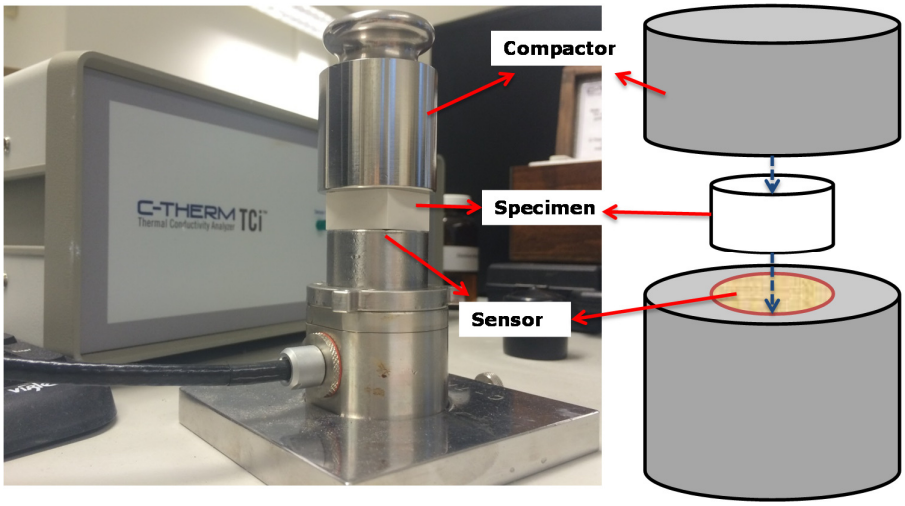

Figure 3-4: C-THERM Tci™ equipment and schematic of thermal conductivity measurement on pellets with ϕ20 mm.

The porosities of pellets were obtained from the relative density calculated by Eq. (3-5). The measured density (ρ') of each pellet was calculated by the weight and the volume. The theoretical density (ρ_{th}) of each pellet was calculated using Eq. (3-6) [22]. The volume of the unit cell was calculated from lattice parameters as obtained from Rietveld refinement.

$$\emptyset = 1 - \frac{\rho}{\rho_{th}} \qquad \text{Eq. (3-5)}$$

$$\rho_{th} = \frac{(MW)(Z)}{V_{cell}N_A} \times 10^{27} \qquad \text{Eq. (3-6)}$$

where MW is molecular weight;Z is formula number per unit cell; V_{cell} is volume of the unit cell ; N_A is Avogadro constant, 6.022×10^{23}. Therefore, all thermal conductivities discussed in this work are the corrected values.

3.4.3 Coefficients of Thermal Expansion

Thermal Mechanical Analysis (TMA, TA Instruments Q400 as shown in Figure 3-5) was used to measure the coefficient of thermal expansion (CTE) of the as-sintered pellets with diameter of 5 mm. The quartz glass probe was used in macro-expansion mode. The preload was 0.05 N and the applied force was 0.02 N. The measurement was carried out in nitrogen atmosphere with a flow rate of 50 mL/min from room temperature to 900 ^{o}C. The data was analysed by using TA Universal Analysis software.

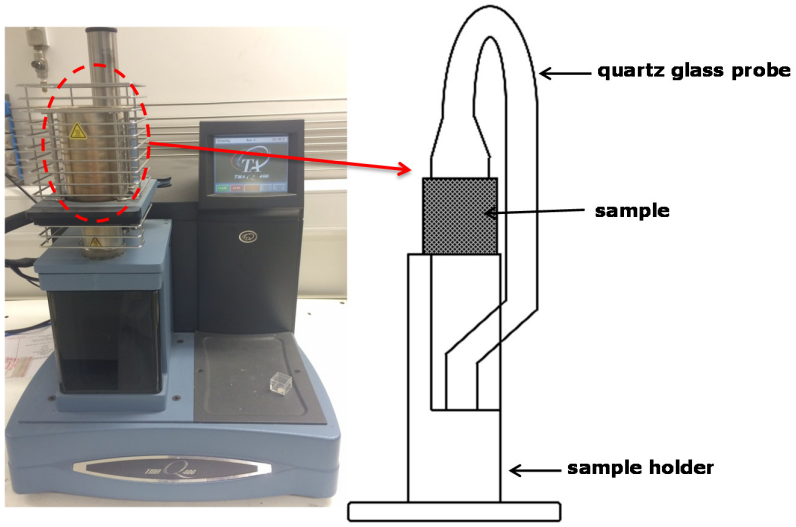

Figure 3-5: TMA machine and the schematic diagram of sample placement and quartz glass probe in TMA machine.

3.5 Molecular Dynamics Simulations

3.5.1 Buckingham Potential and Parameters

An in-house Molecular Dynamics (MD) program was used to conduct all simulations. To describe the interionic interaction in $Yb_2Sn_2O_7$, $La_2Sn_2O_7$ and $(La_xYb_{1-x})_2Sn_2O_7$ Solid Solution (x=0.3, 0.5 and 0.7), Wolf method was used for long–range coulomb interactions and a 6.0 Å cut-off was used for van der Waals forces [167]. Coulomb interactions between the ions used q_{La}=+3, q_{Yb}=+3, q_{Sn}=+4 and q_O=-2. The Buckingham potential $\emptyset(r)$ was used for the short ranged interactions:

$$\emptyset(r) = A\exp\left(-\frac{r}{B}\right) - \frac{C}{r^6} \qquad \text{Eq. (3-7)}$$

where *A*, *B* and *C* are Buckingham parameters.

The parameters for La-O, Yb-O and O-O were taken from previous reports [168-170], where the values of potential parameters were obtained by a lattice parameter fitting approach. The parameters for Sn-O were referred from Minervini *et al.* [169] and modified for this study. The basic idea was to observe the influence on lattice constant of the material by adjusting *A*, *B* and *C* parameters. The lattice constant *a* of $Yb_2Sn_2O_7$ at room temperature was used for this parameter modification. For input data, the simulation box was contained 3 × 3 × 3 unit cells. The calculation was performed with 50,000 equilibrium steps for NPT and 100,000 for simulation.

The parameters of Yb-O, La-O, Sn-O and O-O for the Buckingham potential are listed in Table 3-3. All the input lattice constants of

$Yb_2Sn_2O_7$, $La_2Sn_2O_7$ and $(La_xYb_{1-x})_2Sn_2O_7$ Solid Solution (x=0.3, 0.5 and 0.7) are shown in Table 3-4.

Table 3-3: Buckingham potential parameters used for La^{3+} doped $Yb_2Sn_2O_7$ and un-doped stannates.

Pairs	*A* (eV)	*B* (Å)	*C* (eVÅ^6)
Yb-O	1649.80	0.3386	16.57
La-O	2088.79	0.3460	23.25
Sn-O	1200.00	0.3592	13.66
O-O	9547.96	0.2192	32.0

Table 3-4: The initial lattice parameters [15] of La^{3+} doped $Yb_2Sn_2O_7$ and un-doped stannates used in simulation programs, which were obtained from the experimental results.

Ceramics	Lattice Constant a=b=c (Å)
$Yb_2Sn_2O_7$	10.276
$(La_{0.3}Yb_{0.7})_2Sn_2O_7$	10.432
$(La_{0.5}Yb_{0.5})_2Sn_2O_7$	10.483
$(La_{0.7}Yb_{0.3})_2Sn_2O_7$	10.585
$La_2Sn_2O_7$	10.631

3.5.2 Thermal Conductivity Simulation

In order to calculate the thermal conductivity, the method reported by Stackhouse *et al.* [159, 171] and Schelling *et al.* [161]

was applied. The simulation cell consisted of 3 × 3 × 20 ($x \times y \times z$) unit cells and the heat transfers along the *z*-direction. Before the program started to calculate the thermal conductivity, the unit cell was equilibrated in the NPT ensemble with 80,000 equilibrium steps and 120,000 calculation steps. Then the thermal conductivity simulation was performed in microcanonical ensemble (NVE), with 80,000 equilibrium steps and 500,000 steps for calculating the temperature gradient.

In order to impose a heat flux and to calculate a temperature profile, the simulation box was divided into 20 slabs perpendicular to the *z*-direction. To rescale the velocities of atoms at each time step, heat $\Delta\varepsilon$ was added in a thin slab of thickness δ around $Z=-L_z/4$ and removed from $Z=L_z/4$, where the simulation box extended from $-L_z/2$ to $+L_z/2$ (as seen in Figure 3-6). The purpose was to keep the energy current (J) constant during the simulation.

The temperature T was calculated from the average kinetic energy for a series of 20 slices, along the *z*-direction:

$$T = \frac{2}{3k_B} KE_{avg} \qquad \text{Eq. (3-8)}$$

where KE_{avg} is the average kinetic energy. k_B is the Boltzmann constant. 20 average temperatures in the parallel slices of the system were obtained. There was a maximum at the "hot plate" and a minimum at the "cold plate" as shown by plotting 20 average temperatures of the parallel slices (see Figure 3-7). The two average temperature differences between the slices were

calculated from zone 1 and zone 2, respectively. Then the temperature gradient (ΔT) was calculated:

$$\Delta T = \frac{\text{The average temperature differences}}{\text{The thickness of the slices}} \quad \text{Eq. (3-9)}$$

Fourier's law is used to calculate the thermal conductivity (k).

$$\vec{q} = -k\Delta T \quad \text{Eq. (3-10)}$$

So

$$k = -\frac{\vec{q}}{\Delta T} = -\frac{J}{A_a \Delta T} \quad \text{Eq. (3-11)}$$

where $\vec{q}$ is the local heat flux density; k is the thermal conductivity; ΔT is the temperature gradient. J is thermal powder. A_a is the cross section area. The temperature gradient became non-linear around the hot and cold sections at high temperatures (as seen in Figure 3-7) due to the non-Newtonian nature of the heat transfer, so the temperature gradient calculation avoided this area.

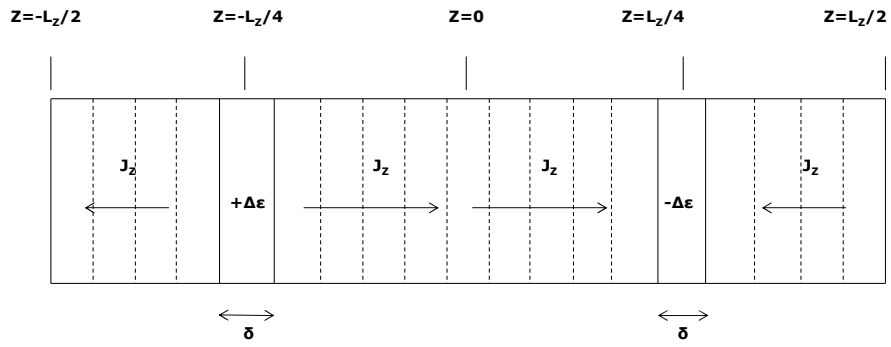

Figure 3-6: The schematic of the three-dimensional simulation cells; the total length L_z and the heat transfer in *z*-direction; the heat Δε added in a thin slab of thickness δ around $Z=-L_z/4$ and removed from $Z=L_z/4$.

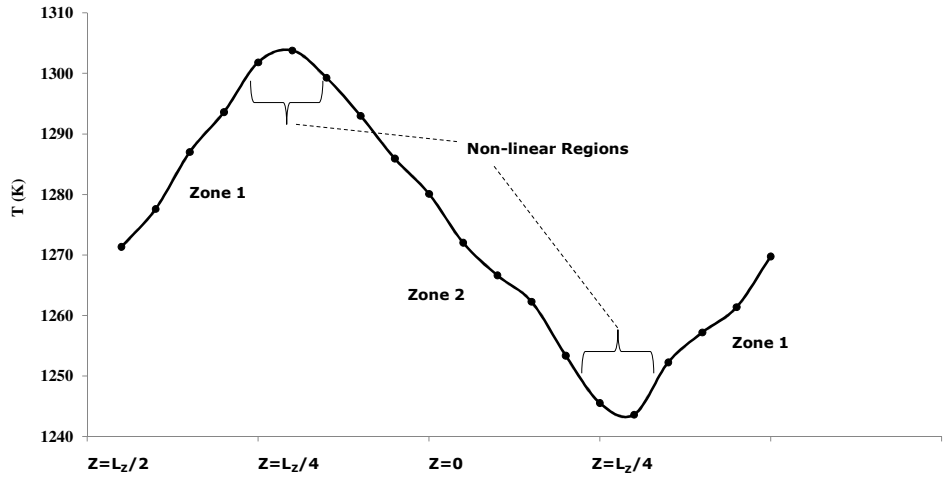

Figure 3-7: A representative temperature profile from a simulation of $Yb_2Sn_2O_7$ at 1273K. Only the linear part of the temperature gradient is used for the thermal conductivity calculation.

3.5.3 Linear Coefficient of Thermal Expansion Simulation

Thermal expansion was simulated between 20 °C and 1500 °C by using 5 × 5 × 5 unit cells. There were 88 atoms in a unit cell. The used time step was 0.5 fs. 60,000 steps of the isothermal-isochoric (NPT) static ensemble were used for equilibrium and the pressure is 1 bar. 120,000 steps were used for the calculation of the average lattice parameter. The initial lattice parameter was taken from Table 3-4.

The linear CTE was then calculated using [172]:

$$\mathrm{CTE} = \frac{1}{a'}\frac{da'}{dT} = \frac{d\,ln(a')}{dT} \qquad \text{Eq. (3-12)}$$

where a' is the average lattice parameter obtained from the simulation result. The first derivative of $ln(a')$ with respect to dT was calculated by using the cubic spline interpolation method.

Chapter 4. Experimental and Simulative Investigations of La^{3+} Doped $Yb_2Sn_2O_7$

4.1 Introduction

Stannates with pyrochlore structure have good phase stability up to the melting point (> 2000 ^oC) [107], which is much higher than that of 8YSZ (about 1250 ^oC). Recently, Schelling *et al.* found that pyrochlore might have much lower thermal conductivity than other systems [108]. From their simulation results, stannates were predicted to have the lowest thermal conductivity in pyrochlores, though the low coefficients of thermal expansion (CTEs) of stannates need further improvement for TBCs application.

Furthermore, the thermal properties of un-doped stannates were studied by Qu *et al.* [109]. $Ln_2Sn_2O_7$ (Ln = La, Nd, Sm, Gd, Er and Yb) samples prepared by a chemical co-precipitation method exhibit the pyrochlore crystal structure. However, their thermal conductivities are above 2 $W \cdot m^{-1} \cdot K^{-1}$ at 1200 ^oC, and their CTEs ($7 \sim 9 \times 10^{-6}$ K^{-1}) are slightly lower than YSZ. These lower thermal conductivity values were explained in terms of scattering the phonons by the strain field caused by the displacement of oxygen ions at 48*f* sites in the pyrochlore crystal structure, rather than oxygen vacancies at 8*a* sites.

Bansal *et al.* [156] found that small amount of rare earth doped pyrochlore had relatively low thermal conductivity, but it was still above 1 $W \cdot m^{-1} \cdot K^{-1}$. In ceramic materials, phonons carry heat

energy due to thermal motion of atoms (vibrations in different directions), which plays a main role in thermal conductivity [173]. In a perfect and simple crystal, the vibrations of atoms are monotonous and independent of each other, so thermal conductivity can be infinite. But in the real case, there are defects, distortions, and strain in crystals, which have significant effects on thermal conductivity due to scattering phonons.

In the past, most studies were based on un-doped stannates. In the present work, based on the consideration of crystal structure and the relative ion radius, La^{3+} Doped $Yb_2Sn_2O_7$ materials will be systematically investigated. As La^{3+} ions (0.118 nm) have larger radius than Yb^{3+} (0.098 nm) [174], the replacements are expected to produce significant disorders by replacing Yb^{3+} ions on cation layers. These disorders could have huge effects on the thermal properties of the materials. The main content of Section 4.2 involves the experimental study of crystalline phase and thermal properties of La^{3+} Doped $Yb_2Sn_2O_7$. Additionally, molecular dynamics simulations are applied to better understand the experimental results.

4.2 Experimental Results and Discussions

4.2.1 Pyrochlore Structure and Doping Mechanism

Pyrochlore is a derivative of fluorite structure [75], where a quarter part of pyrochlore has similar structure to fluorite unit cell and the difference is 8a vacancies created by missing oxygen

atoms in pyrochlore. Pyrochlore has cubic crystal structure, and it can be stable from room temperature up to its melting point [9, 175]. This property is the key advantage for gas engine application at high temperatures. As shown in Figure 4-1 **(a)**, oxygen atoms locate between cation layers but some of them are displaced from their centre positions due to the nearby oxygen vacancies at 8*a* sites. The sub-lattice of cations [Figure 4-1 **(b)**] shows layered-crystal structure that is more helpful for scattering phonons. If substitutional defects of cations and disorders are created between these layers, it could be a useful strategy to further reduce thermal conductivity of pyrochlore material. In lanthanoids group, La^{3+} and Yb^{3+} ions have the biggest radius difference, so by doping La^{3+} to replace Yb^{3+}, the most significant disorders would be produced in cation layers of crystal $Yb_2Sn_2O_7$.

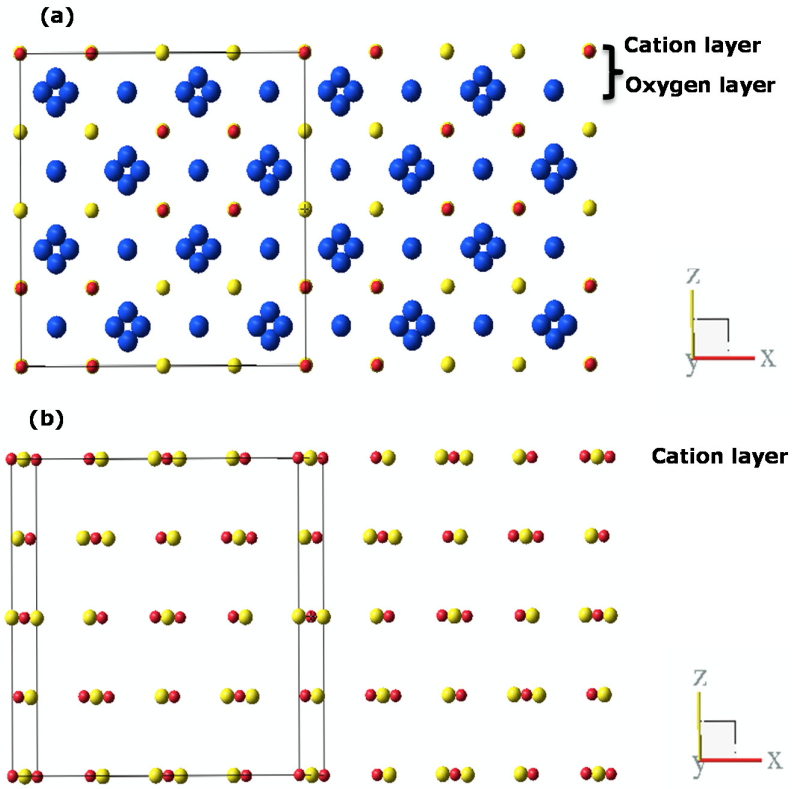

Figure 4-1: **(a)** Complex pyrochlore crystal structure of $A_2B_2O_7$ ($A=La^{3+}$, Yb^{3+} or La^{3+} and Yb^{3+} mixed together; $B=Zr^{4+}$) if observed from [0,1,0] direction; **(b)** Cationic sub-lattice of pyrochlore, where atom A is in yellow colour, atom B in red colour and atom O in blue colour.

4.2.2 Phase Analysis

4.2.2.1 XRD Results

In Figure 4-2, XRD patterns of $La_2Zr_2O_7$, $La_2Sn_2O_7$, $(La_{0.7}Yb_{0.3})_2Sn_2O_7$, $(La_{0.5}Yb_{0.5})_2Sn_2O_7$, $(La_{0.3}Yb_{0.7})_2Sn_2O_7$ and $Yb_2Sn_2O_7$ indicate their crystal structure. Figure 4-2 **(a)** presents pyrochlore crystal structures, distinguished from fluorite by (3,3,1)

and (5,1,1) peaks, which is in good agreement with the previous report by Brisse and Knop [176]. A minor second phase La_2O_3 is detected in $La_2Sn_2O_7$, $(La_{0.7}Yb_{0.3})_2Sn_2O_7$ and $(La_{0.5}Yb_{0.5})_2Sn_2O_7$ powders.

In Figure 4-2 **(b)**, by increasing the doping contents of Yb^{3+} dopants to replace La^{3+} ions, the lattice parameters are continuously decreasing [46], which can be observed from (2,2,2), (4,0,0), (4,4,0) and (6,2,2) peaks that are shifting from low 2θ. In addition, it is found that there are two compositions in solid solution $(La_xYb_{1-x})_2Sn_2O_7$ (x = 0.3, 0.5 and 0.7) by distinguishing the overlapped two peaks, (4,4,0) and (6,2,2). In order to identify these compositions, C1 and C2 $[(La_{0.7}Yb_{0.3})_2Sn_2O_7]$, C3 and C4 $[(La_{0.5}Yb_{0.5})_2Sn_2O_7]$, C5 and C6 $[(La_{0.3}Yb_{0.7})_2Sn_2O_7]$, are introduced to represent these different compositions, which also have a pyrochlore crystal structure.

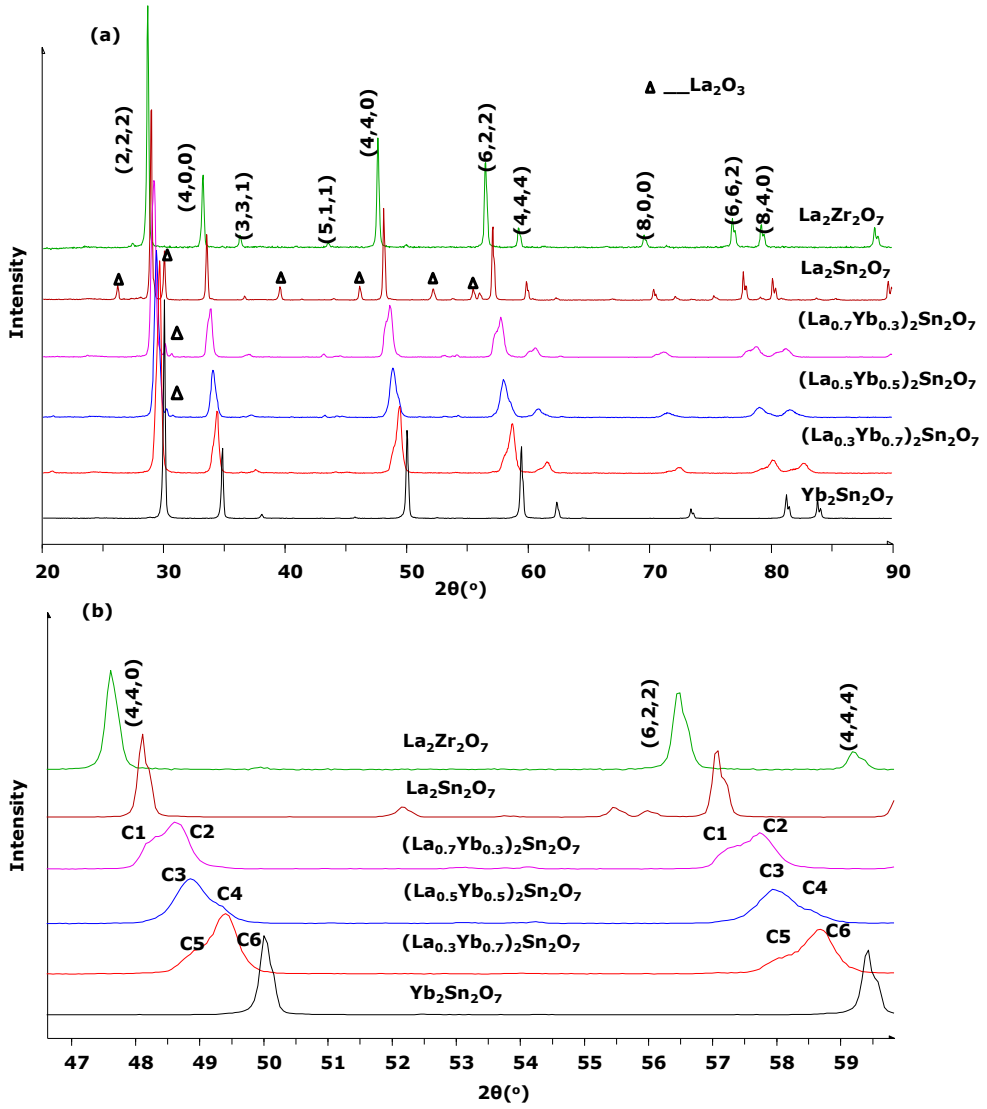

Figure 4-2: **(a)**: XRD patterns of ceramic $La_2Zr_2O_7$, $La_2Sn_2O_7$, $(La_{0.7}Yb_{0.3})_2Sn_2O_7$, $(La_{0.5}Yb_{0.5})_2Sn_2O_7$, $(La_{0.3}Yb_{0.7})_2Sn_2O_7$, and $Yb_2Sn_2O_7$ powders detected at room temperature. Graphs **(b)** enlarged from **(a)**, where solid solutions $(La_xYb_{1-x})_2Sn_2O_7$ (x = 0.3, 0.5 and 0.7) have two similar compositions identified from the widen peaks, (4,4,0) and (6,2,2).

4.2.2.2 Rietveld Refinement

After the Rietveld refinement, Figure 4-3 **(a)-(c)** demonstrates that calculative XRD patterns of samples $(La_{0.7}Yb_{0.3})_2Sn_2O_7$, $(La_{0.5}Yb_{0.5})_2Sn_2O_7$ and $(La_{0.3}Yb_{0.7})_2Sn_2O_7$ have good fitting agreement with their experimental XRD results, especially at high 2θ. The lattice constants and relative phase contents of C1, C2, C3, C4, C5 and C6 obtained from the simulations are listed in Table 4-1. It is observed that the contents of different compositions in $(La_{0.5}Yb_{0.5})_2Sn_2O_7$ and $(La_{0.3}Yb_{0.7})_2Sn_2O_7$ are slightly different from those in $(La_{0.7}Yb_{0.3})_2Sn_2O_7$. The relative phase contents of C3 (10.570 Å) and C5 (10.525 Å) are 28.10% and 21.72%, so C4 (10.483 Å) and C6 (10.432 Å) are 71.90% and 78.28%, respectively. But in sample $(La_{0.7}Yb_{0.3})_2Sn_2O_7$, the relative phase contents of C1 and C2 are 73.77% and 26.23% with lattice constants 10.655 Å and 10.585 Å, respectively. Apparently, the relative phase contents of the compositions with larger lattice constants decrease with the decreasing doping level of La^{3+} ions. But when larger ion La^{3+} ions dominate in solid solution $(La_{0.7}Yb_{0.3})_2Sn_2O_7$, the relative phase content of composition C1 with rich La^{3+} ions is higher than that of composition C2.

Table 4-1: The lattice constants and relative phase contents of different compositions in $(La_xYb_{1-x})_2Sn_2O_7$ (x = 0.3, 0.5 and 0.7) solid solutions.

Sample ID	Composition	Lattice Constant (Å)	Relative Phase Content (mol%)
$(La_{0.7}Yb_{0.3})_2Sn_2O_7$	C1	10.655	73.77%
	C2	10.585	26.23%
$(La_{0.5}Yb_{0.5})_2Sn_2O_7$	C3	10.570	28.10%
	C4	10.483	71.90%
$(La_{0.3}Yb_{0.7})_2Sn_2O_7$	C5	10.525	21.72%
	C6	10.432	78.28%

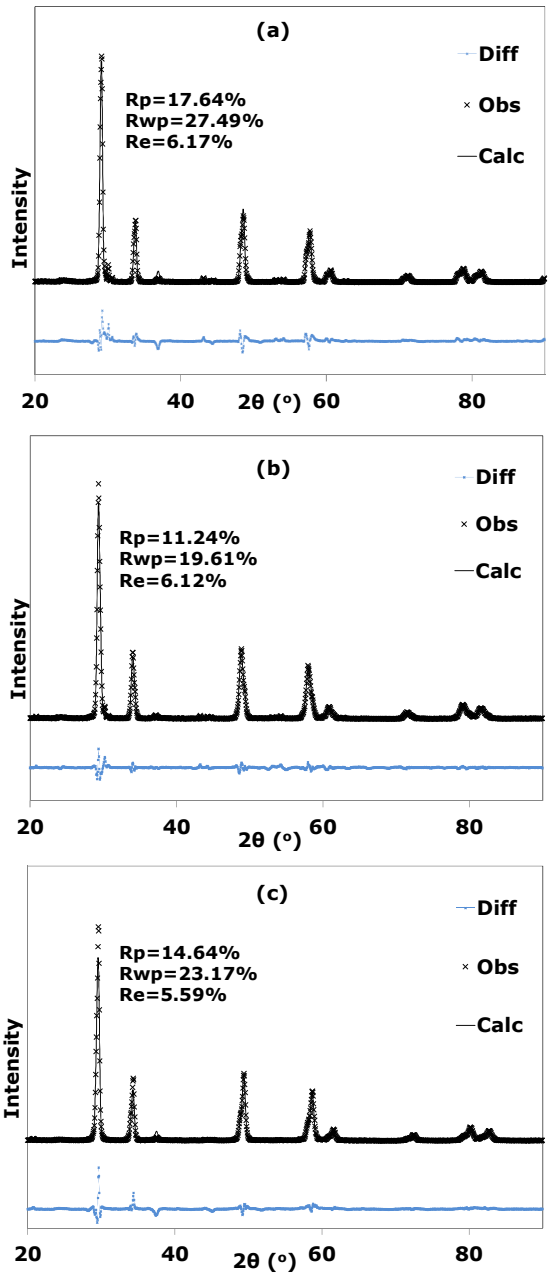

Figure 4-3: The good agreement between the calculative XRD data and the experimental XRD pattern for samples $(La_{0.7}Yb_{0.3})_2Sn_2O_7$ **(a)**, $(La_{0.5}Yb_{0.5})_2Sn_2O_7$ **(b)** and $(La_{0.3}Yb_{0.7})_2Sn_2O_7$ **(c)**, where Diff refers to the difference between the calculative (Calc) and observed (Obs) data.

According to a previous study, the lattice constant of $La_2Sn_2O_7$ is 10.631 Å [177] and 10.276 Å for $Yb_2Sn_2O_7$ [178]. Figure 4-4 demonstrates that the lattice constants of $(La_xYb_{1-x})_2Sn_2O_7$ (x = 0.3, 0.5 and 0.7) solid solution obtained from Rietveld refinement, are almost linearly increasing with the increase of the La^{3+} ions (mol%), because the radius of La^{3+} ion (0.118 nm) is larger than that of Yb^{3+} ion (0.098 nm) [174]. Therefore, for $(La_{0.7}Yb_{0.3})_2Sn_2O_7$, $(La_{0.5}Yb_{0.5})_2Sn_2O_7$ and $(La_{0.3}Yb_{0.7})_2Sn_2O_7$ solid solutions, the La^{3+} ion contents in C1, C3 and C5 would be slightly higher than those in the corresponding compositions (C2, C4 and C6). Meanwhile, their linear slopes have similar values and the lattice constants are decreasing with reducing the contents of dopant La^{3+} ions. From microstructure level, the difference between these lattice constants could cause strain and stress in materials, which can also be observed in the following TEM images and might also contribute to phonon scattering for reducing their thermal conductivities, because strain and stress can produce difficulty for phonons to travel through the lattice.

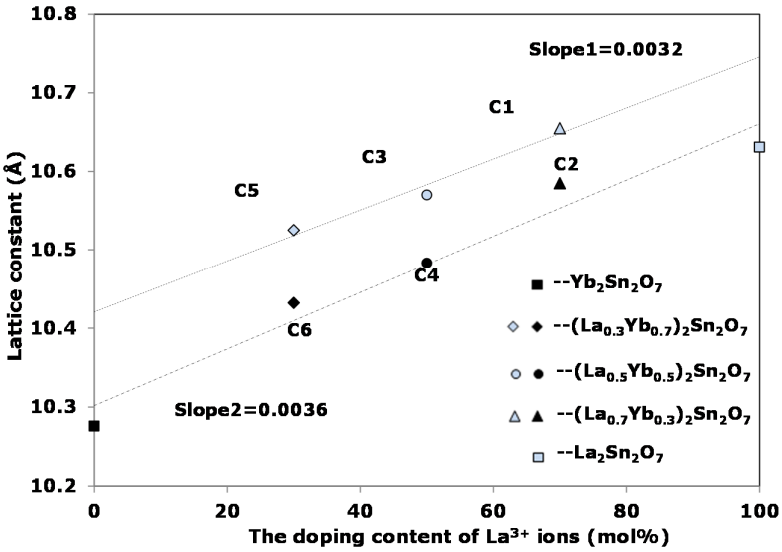

Figure 4-4: The linear changes of lattice constants of $(La_xYb_{1-x})_2Sn_2O_7$ (x = 0.3, 0.5 and 0.7) solid solution with the increasing contents of La^{3+} dopants.

4.2.3 TEM and SEM Characterizations

Bright field TEM images and electron diffraction patterns of $Yb_2Sn_2O_7$, $(La_{0.5}Yb_{0.5})_2Sn_2O_7$, $(La_{0.7}Yb_{0.3})_2Sn_2O_7$, and $(La_{0.3}Yb_{0.7})_2Sn_2O_7$ ceramics are presented in Figure 4-5 **(a)**-**(d)**, respectively. The crystal sizes of $Yb_2Sn_2O_7$, $(La_{0.7}Yb_{0.3})_2Sn_2O_7$, $(La_{0.5}Yb_{0.5})_2Sn_2O_7$ and $(La_{0.3}Yb_{0.7})_2Sn_2O_7$ powders range from 30 nm to 100 nm. Crystals of $Yb_2Sn_2O_7$ in Figure 4-5 **(a)** have uniform diffraction contrast. But in **(b)**, **(c)** and **(d)**, TEM images of $(La_{0.7}Yb_{0.3})_2Sn_2O_7$, $(La_{0.5}Yb_{0.5})_2Sn_2O_7$ and $(La_{0.3}Yb_{0.7})_2Sn_2O_7$ ceramics have diffraction contrast variation, indicating the existence of strain and stress within the particles that might result from two different compositions or caused by the displacement of

48*f* oxygen ions in the pyrochlore crystal structure [109]. The *d*-spacing values of ceramic $Yb_2Sn_2O_7$ are in agreement with the Powder Diffraction File (PDF) data reported by Kennedy [179]. In addition, from the electron diffraction patterns inserted in Figure 4-5, $(La_xYb_{1-x})_2Sn_2O_7$ (x = 0.3, 0.5 and 0.7) solid solutions have smaller *d*-spacing values if compared with the standard $Yb_2Sn_2O_7$, as also being observed according to the peak shift to lower 2θ in XRD results, which might be due to the replacement of Yb^{3+} ions by larger La^{3+} ions or stain/stress in crystallites. Moreover, the electron diffraction patterns further indicate that all particles have the pyrochlore crystal structure, as there are two weak diffraction rings corresponding to (3,3,1) and (5,1,1) peaks, which matches well with XRD results (two diffraction rings noted in each diffraction pattern). The ceramics exhibit clear diffraction rings generated by diffraction spots due to their nano-sized particles and different crystal orientations.

SEM surface morphology of as-sintered pellet $Yb_2Sn_2O_7$, $(La_xYb_{1-x})_2Sn_2O_7$ (x = 0.3, 0.5 and 0.7) and $La_2Sn_2O_7$ are shown in Figure 4-6. There are many small pores that are uniformly distributed in all specimens. The grain boundaries in these images are slightly blurry, due to the grain growth. However, the grains can be easily distinguished.

From the TEM images (Figure 4-5), it is observed that the grain size of as-synthesised powder is from 30 nm to 100 nm. The grain size of as-sintered pellet increases but does not exceed 500 nm after sintering.

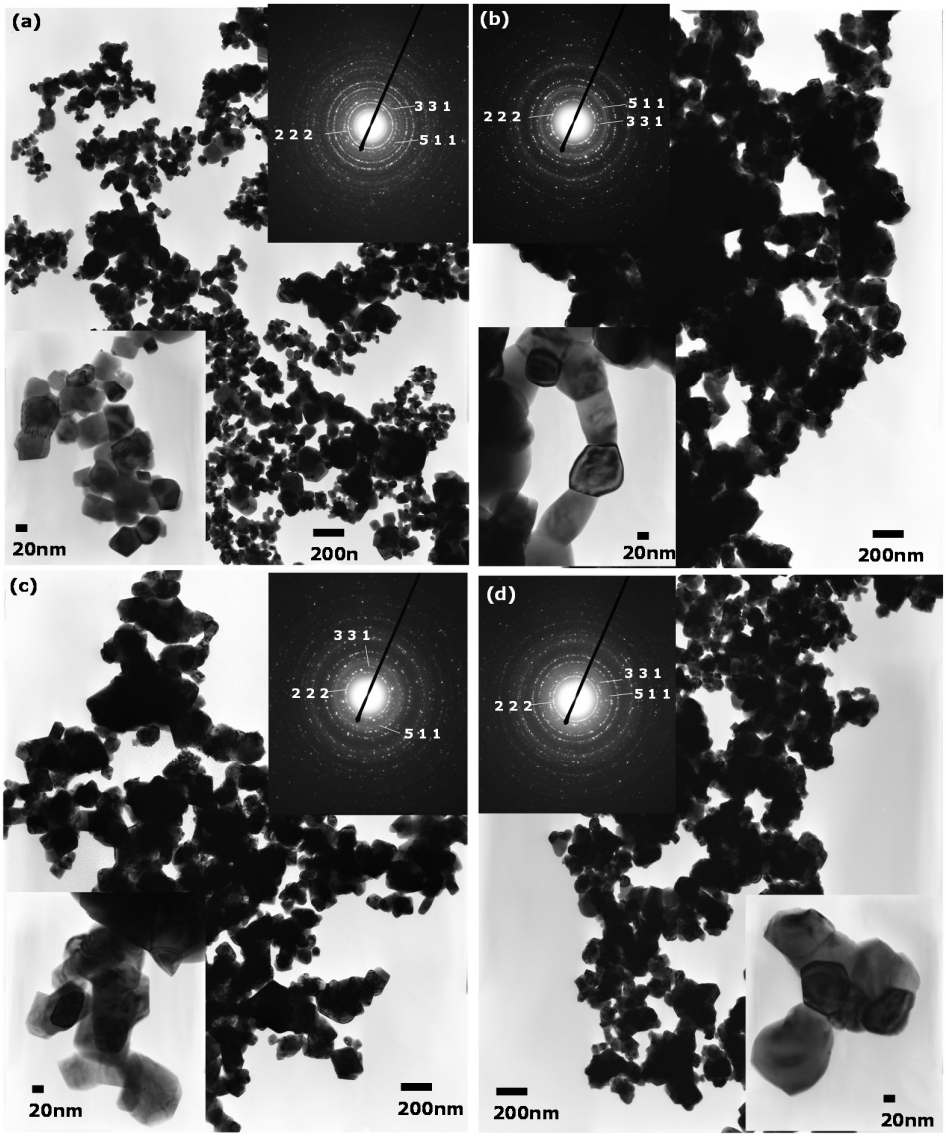

Figure 4-5: Bright field TEM images of **(a)** $Yb_2Sn_2O_7$, **(b)** $(La_{0.3}Yb_{0.7})_2Sn_2O_7$, **(c)** $(La_{0.7}Yb_{0.3})_2Sn_2O_7$ and **(d)** $(La_{0.5}Yb_{0.5})_2Sn_2O_7$ powders. The insert images are the higher magnification TEM images and electron diffraction patterns at selected area for each sample, respectively.

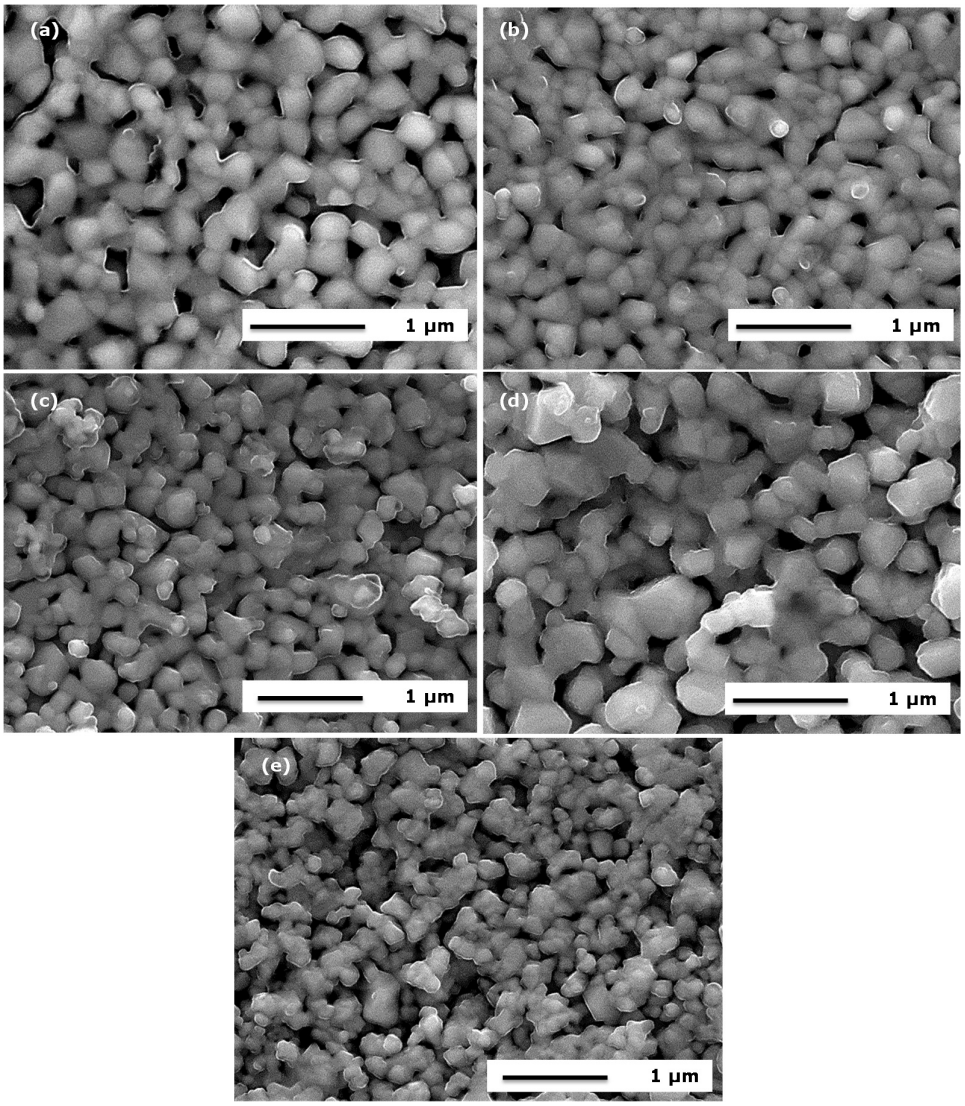

Figure 4-6: SEM images of bulk surface of un-doped stannate and $(La_xYb_{1-x})_2Sn_2O_7$ (x = 0.3, 0.5 and 0.7).solid solution: **(a)** $Yb_2Sn_2O_7$; **(b)** $(La_{0.3}Yb_{0.7})_2Sn_2O_7$; **(c)** $(La_{0.5}Yb_{0.5})_2Sn_2O_7$; **(d)** $(La_{0.7}Yb_{0.3})_2Sn_2O_7$; **(e)** $La_2Sn_2O_7$.

4.2.4 Thermal Properties

4.2.4.1 Thermal Conductivity

The thermal conductivities of stannate ceramics and 8YSZ are compared in Figure 4-7. The thermal conductivities of $La_2Sn_2O_7$, $(La_{0.7}Yb_{0.3})_2Sn_2O_7$, $(La_{0.5}Yb_{0.5})_2Sn_2O_7$, $(La_{0.3}Yb_{0.7})_2Sn_2O_7$ and $Yb_2Sn_2O_7$ pellets are 1.471 $W{\cdot}m^{-1}{\cdot}K^{-1}$, 1.063 $W{\cdot}m^{-1}{\cdot}K^{-1}$, 0.851 $W{\cdot}m^{-1}{\cdot}K^{-1}$, 1.069 $W{\cdot}m^{-1}{\cdot}K^{-1}$ and 1.736 $W{\cdot}m^{-1}{\cdot}K^{-1}$, respectively. All thermal conductivity values were corrected by their porosities, which are from 30% to 40%. Additionally, it can be seen that the thermal conductivities do not always decrease with the increase of the doping content of La^{3+} ions. The lowest point of thermal conductivity appears in $(La_xYb_{1-x})_2Sn_2O_7$ (x = 0.3, 0.5 and 0.7) solid solution when x = 0.5. However, compared with that of 8 wt% YSZ (1.353 $W{\cdot}m^{-1}{\cdot}K^{-1}$, produced in this work following the same procedure as the reference material) and $La_2Zr_2O_7$ (1.154 $W{\cdot}m^{-1}{\cdot}K^{-1}$) ceramic pellets, all doped stannates have relatively lower thermal conductivities, which is the key advantage for TBCs application. A similar thermal conductivity value (around 1.4 $W{\cdot}m^{-1}{\cdot}K^{-1}$) was reported for 8YSZ produced by sol-gel method at room temperature [111], by Rauf *et al*.

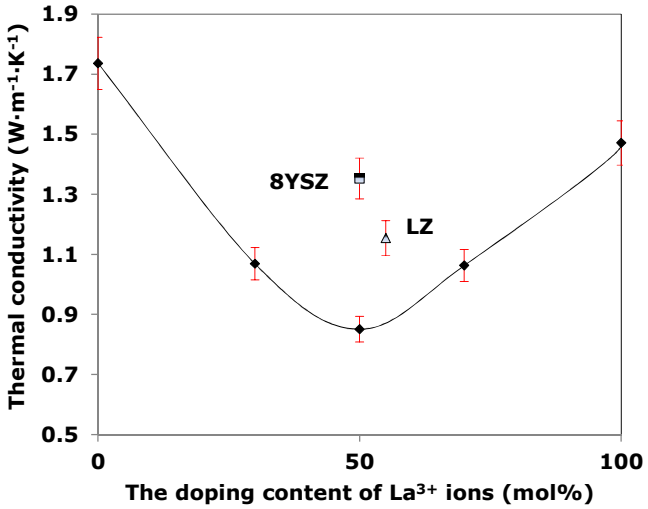

Figure 4-7: Thermal conductivity versus doping content of La^{3+} ions in $(La_xYb_{1-x})_2Sn_2O_7$ (x = 0.3, 0.5 and 0.7) solid solution.

In crystalline solids, phonons are the main heat carriers [180]. Stannate pellets with such low thermal conductivity cannot be just simply explained by one or two phonon scattering mechanisms. In this present work, a combination of the following factors could have led to low thermal conductivities of doped and un-doped stannates: (1) grain boundaries can scatter phonons in nano-crystalline materials. (2) stannates have layered and complex pyrochlore crystal structure that can efficiently scatter phonons; (3) oxygen vacancies existing in this crystal structure would also play a role in scattering phonons.

However, in $(La_xYb_{1-x})_2Sn_2O_7$ (x = 0.3, 0.5 and 0.7) solid solution, their thermal performance might be governed by more complex mechanisms. If observed from the [0,1,0] direction, pyrochlore exhibits a layer-structure, alternating by cation layers and oxygen

layers; while in each oxygen layer, some oxygen atoms are displaced from their centre positions, because of the oxygen vacancies. This is one possibility to cause a decrease of thermal conductivity. It is known that there are no extra oxygen vacancies created by replacing host cations with different rare earth ions due to the same valence charge, so the phonons are possibly scattered from the substitution defects and structure disorders created by the difference of ionic radius or atomic mass.

However, the cations could stabilise in new positions when the doping concentration is high enough. Therefore, when doping La^{3+} ions in Yb^{3+} sites, the radius difference could cause the disorder in cation layers, and then would also affect the arrangement in oxygen layers. These disorders could have a huge effect on further scattering phonons to reduce thermal conductivity. Furthermore, $(La_{0.5}Yb_{0.5})_2Sn_2O_7$ exhibits the lowest thermal conductivity, which could be explained by the maximum disorder achieved by replacing 50 mol% Yb^{3+} ions by La^{3+} ions. When the doping concentration of La^{3+} ions increases to 70 mol%, the thermal conductivity rises to a similar value as that of the 30 mol% doped specimen. So when x equals 0.7, there is a new stable state for La^{3+} ions, which seems that they are newly ordered in the crystal structure again. Moreover, these disorders might also weaken the Sn-O interatomic bonding, which could not just reduce thermal conductivity but also improve CTEs. Finally, two different compositions in each $(La_xYb_{1-x})_2Sn_2O_7$ solid solution could also contribute to phonon scattering for reducing their thermal

conductivities, due to the different lattice parameters and interfaces between them.

4.2.4.2 Coefficients of Thermal Expansion

It has been reported that CTEs of un-doped stannates are $7\sim9\times10^{-6}$ K^{-1} [181], in good agreement with the values measured for $La_2Sn_2O_7$ and $Yb_2Sn_2O_7$ ceramic pellets in this work, which are 3.819×10^{-6} K^{-1} and 7.355×10^{-6} K^{-1} at 50 ^oC; 7.560×10^{-6} K^{-1} and 9.035×10^{-6} K^{-1} at 950 ^oC, respectively (Figure 4-8). The CTEs increase with increasing temperature but they level off at high temperatures. In Figure 4-8, it is shown that ceramic $La_2Sn_2O_7$ has the lowest CTE even at high temperatures. The CTE of $(La_{0.5}Yb_{0.5})_2Sn_2O_7$ pellet shows a dramatic increase from 7.082×10^{-6} K^{-1} at 50 ^oC to 13.530×10^{-6} K^{-1} at 950 ^oC, while the CTE values of 8YSZ are 9.860×10^{-6} $K^{-1}\sim$ 13.310×10^{-6} K^{-1} from 50 ^oC to 950 ^oC. Moreover, $(La_{0.7}Yb_{0.3})_2Sn_2O_7$, $(La_{0.3}Yb_{0.7})_2Sn_2O_7$ and $Yb_2Sn_2O_7$ ceramic pellets have similar CTE values, approximately $7\sim9\times10^{-6}$ K^{-1}.

In term of microscopic scale, the atoms never vibrate symmetrically around their equilibrium positions in imperfect crystals, so the volume expansion happens and is dependent on temperature. From previous studies, lower CTEs in stannates might generally result from the stronger bonding of Sn-O present in stannates than that of Zr-O in zirconates [181]. Lian *et al.* reported that $La_2Sn_2O_7$ has stronger covalent bonding of Sn-O than other stannates, because of larger La^{3+} ions [182].

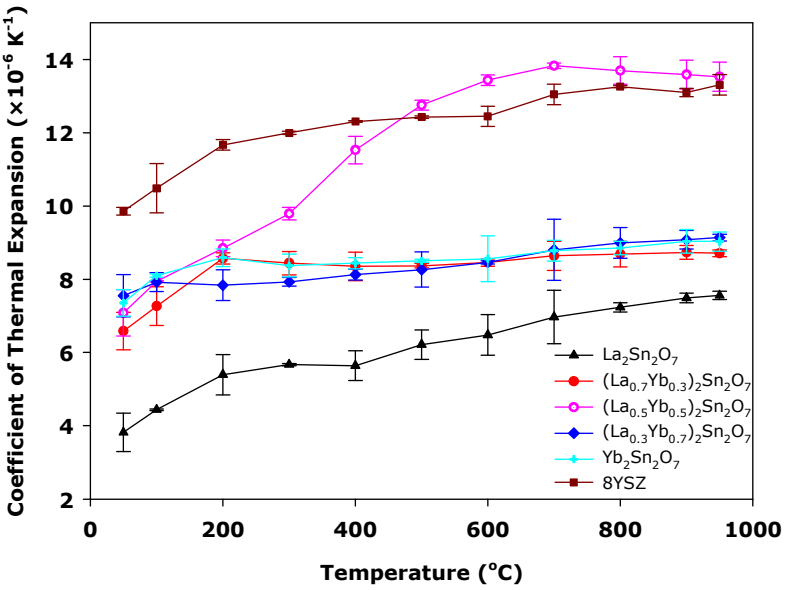

Figure 4-8: Coefficients of thermal expansion versus temperature for $La_2Sn_2O_7$, $(La_{0.7}Yb_{0.3})_2Sn_2O_7$, $(La_{0.5}Yb_{0.5})_2Sn_2O_7$, $(La_{0.3}Yb_{0.7})_2Sn_2O_7$ and $Yb_2Sn_2O_7$ pellets.

Pyrochlore structure is usually considered as an ordered defect fluorite structure with the ordered two cations and 8a anion vacancy. However, these order structures could be changed by doping different cations on A sites, so the disorder could be created in cation layers, then these disorders would affect the bonding length between cation atoms and coordinated oxygen atoms. Therefore, the strong bonding of Sn-O would be weakened, leading to increased CTEs. Especially for $(La_{0.5}Yb_{0.5})_2Sn_2O_7$ pellet, the maximum disorders may be entirely activated at high temperatures, which leads to the highest CTE values in solid solution $(La_xYb_{1-x})_2Sn_2O_7$ (x = 0.3, 0.5 and 0.7). At low

temperatures, the level of atom vibration is limited, thus thermal expansion is increasing with the increase of temperature. After 500 °C, due to the saturation of atom vibrations, CTE values increase very slowly, nearly being temperature independent.

4.2.5 Chemical Compatibility with Alumina

4.2.5.1 Thermogravimetry and Differential Scanning Calorimetry (TG-DSC)

In order to identify whether the synthesised ceramic materials react with alumina, and the reaction temperature if it happens, Thermogravimetry and Differential Scanning Calorimetry (TG-DSC) has been performed on the mixture of as-synthesised ceramic powder and alumina powder.

Figure 4-9 and Figure 4-10 display the changes of the mass and heat flow from 200 °C to 1400 °C. The TG curves maintain the level off during this temperature range, which indicates that there is no weight loss and gain. There is an endothermal peak around 450 °C from DSC curves in each mixed powder in Figure 4-9 **(b-c)** and Figure 4-10 **(a-b)**. This peak can also be observed from DSC data of pure Al_2O_3 powder in Figure 4-9 **(a)**, which is the phase transformation from boehmite to γ-Al_2O_3 [183]. More heat has been absorbed from 1000 °C, which could be related to the phase transformation from δ-Al_2O_3 to α-Al_2O_3 [183].

In the TG-DSC curve of $La_2Sn_2O_7$ mixed with Al_2O_3 powder [Figure 4-9 **(b)**], there are two extra endothermic peaks around

320 °C and 668 °C. The corresponding total mass loss until 700 °C is very small (less than 1%), which might be related to the La_2O_3 phase transformations (hexagonal to cubic phase) because of the existing impure La_2O_3 phase [184]. Without regard to impure La_2O_3 phase, an endothermal peak at 1300 °C indicates the reaction temperature to generate the $LaAlO_3$ phase. In Figure 4-9 **(c)**, TG-DSC data of mixture powder of $Yb_2Sn_2O_7$ and Al_2O_3 is presented, in which there is an endothermic peak at 1275 °C, indicating the formation of $YbAlO_3$ phase at high temperatures.

In Figure 4-10 **(a)**, the mixture between 8YSZ and Al_2O_3 has a very similar DSC curve to pure Al_2O_3, and does not show an obvious reaction temperature. For the mixture of $(La_{0.5}Yb_{0.5})_2Sn_2O_7$ and Al_2O_3, the TG-DSC results are shown in Figure 4-10 **(b)**, where a sharp endothermic peak appears around 1360 °C. This reaction temperature is higher than that of either un-doped $Yb_2Sn_2O_7$ or $La_2Sn_2O_7$, and is also higher than the maximum application temperature of 8YSZ.

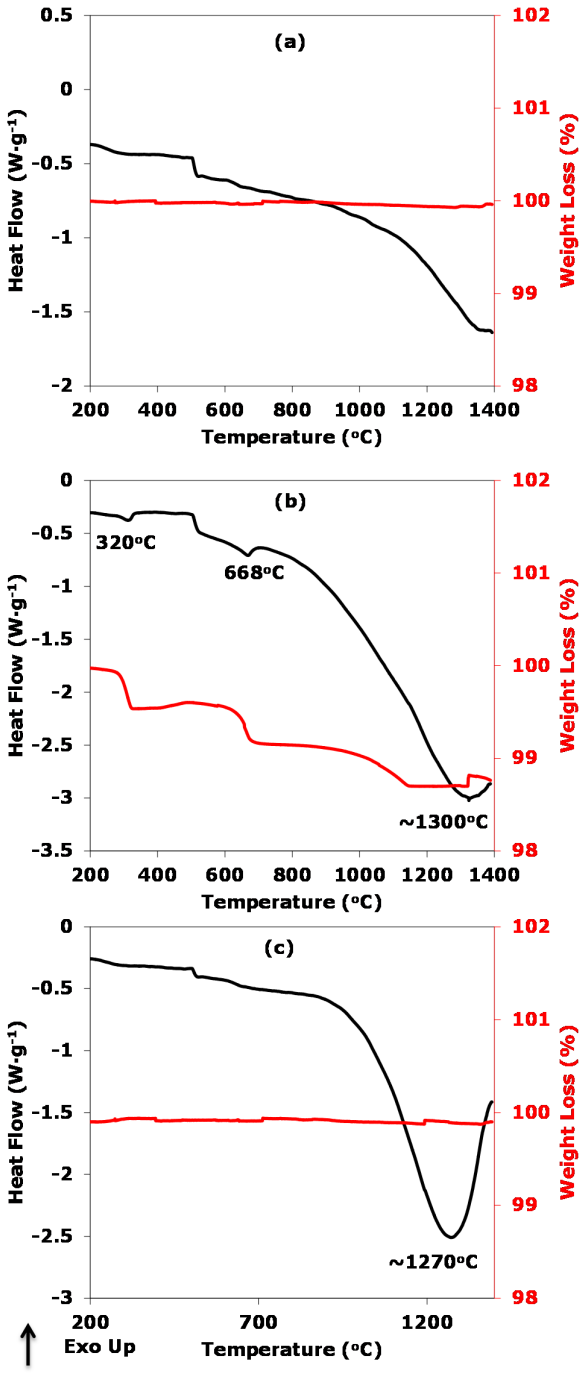

Figure 4-9: TG-DSC curves of pure Al_2O_3 **(a)**, the mixed powders of $La_2Sn_2O_7$ and Al_2O_3 **(b)** and the mixed powder of $Yb_2Sn_2O_7$ and Al_2O_3 **(c)**.

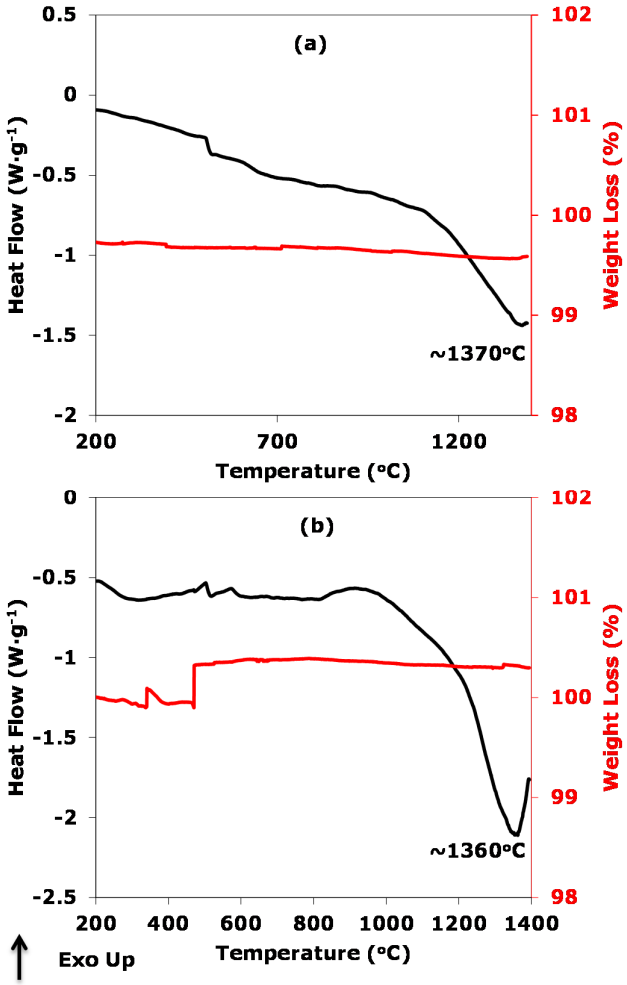

Figure 4-10: **(a)** TG-DSC curves of the mixture of 8YSZ with Al_2O_3 and **(b)** the mixed powder of $(La_{0.5}Yb_{0.5})_2Sn_2O_7$ and Al_2O_3.

4.2.5.2 Heat-Treatment of $(La_{0.5}Yb_{0.5})_2Sn_2O_7$ Mixed with Al_2O_3

In last section, the TG-DSC results indicate that the chemical compatibility with Al_2O_3 of $(La_{0.5}Yb_{0.5})_2Sn_2O_7$ is better than un-doped $Yb_2Sn_2O_7$ or $La_2Sn_2O_7$ without long heat duration. The isothermal heating is performed to further test the chemical compatibility, so the mixture of $(La_{0.5}Yb_{0.5})_2Sn_2O_7$ and Al_2O_3 has

been compressed into a pellet, and heat-treated at different temperatures for certain heating durations.

When the heating temperature and duration are 1200 °C and 6 h, respectively, there is no chemical reaction observed from the XRD results in Figure 4-11. When the pellet is treated at relatively high temperatures (*e.g.* 1250 °C), being held for another 6 h, the $LaAlO_3$ phase is detected. But the $YbAlO_3$ phase is observed when the heating temperature increases to 1300 °C; at that time, the pellet has undergone 18 h heat treatment. Meanwhile, the peak intensities of $LaAlO_3$ and $YbAlO_3$ phases increase after further heat treatment.

The $LaAlO_3$ phase observed at 1250 °C could result from the reaction between the impure phase La_2O_3 and Al_2O_3, which is shown in Reaction (4-1). From XRD results, both $LaAlO_3$ and $YbAlO_3$ phases are obtained at 1300 °C, which is due to Reactions (4-2) and (4-3). The temperature (1300 °C) is slightly smaller than that obtained from DSC data (1360 °C). The slight difference of reaction temperature is possibly related to the accelerated cation diffusion, as a result of long heating durations.

$$La_2O_3 + Al_2O_3 \rightarrow 2LaAlO_3 \qquad \text{Reaction (4-1)}$$

$$La_2Sn_2O_3 + Al_2O_3 \rightarrow 2LaAlO_3 + 2SnO_2 \qquad \text{Reaction (4-2)}$$

$$Yb_2Sn_2O_3 + Al_2O_3 \rightarrow 2YbAlO_3 + 2SnO_2 \qquad \text{Reaction (4-3)}$$

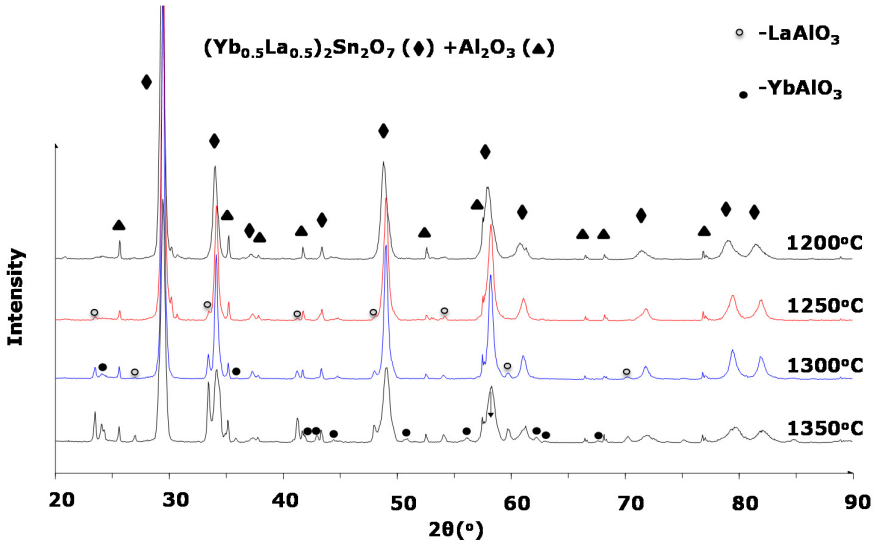

Figure 4-11: XRD patterns of the mixed pellet of $(La_{0.5}Yb_{0.5})_2Sn_2O_7$ and Al_2O_3 after heat treatment at 1200 °C, 1250 °C, 1300 °C and 1350 °C for 6 h, separately.

4.3 Molecular Dynamics Simulations

In section 4.2, it is experimentally found that doping La^{3+} ions in $Yb_2Sn_2O_7$ can dramatically reduce thermal conductivity and increase coefficient of thermal expansion, when the doping concentration is 50 mol%. However, there are many external factors that can also influence thermal conductivity, such as grain boundary, porosity, and grain size. In order to eliminate these external factors, Molecular Dynamics (MD) simulations have been performed on $(La_xYb_{1-x})_2Sn_2O_7$ (x = 0.3, 0.5 and 0.7) solid solution to investigate the variation of thermal conductivity with different doping concentrations.

4.3.1 Simulation Parameters

4.3.1.1 Buckingham Potential Parameters for Sn-O

In simulations, Buckingham potential $\emptyset(r)$ is applied for the short ranged interaction, as presented in Eq. (4-1):

$$\emptyset(r) = A\exp\left(-\frac{r}{B}\right) - \frac{C}{r^6} \qquad \text{Eq. (4-1)}$$

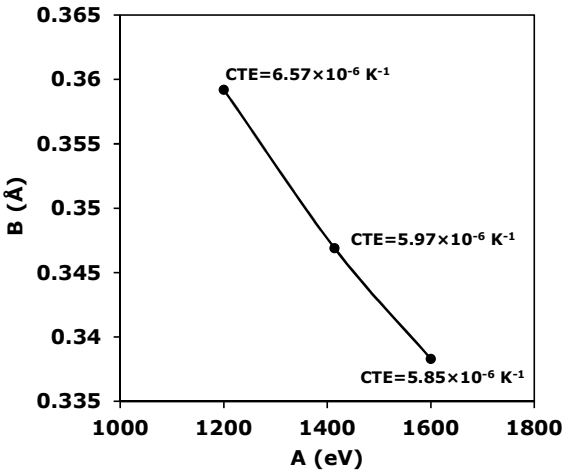

Figure 4-12: The relationship between of Buckingham potential parameters *A* and *B* with linear coefficient of thermal expasion of $Yb_2Sn_2O_7$ at 1700K.

The Buckingham parameters (*A, B* and *C*) for La-O, Yb-O and O-O are taken from previous work [168-170]. *C* value for Sn-O is obtained elsewhere [169], but the parameters *A* and *B* are slightly modified for this calculation work. In Figure 4-12, it is suggested that CTE value increases with lower *A* and higher *B* values. The final Buckingham parameters for La-O, Yb-O, O-O and Sn-O are listed in Table 4-2.

Table 4-2: Buckingham potential parameters used for La^{3+} doped $Yb_2Sn_2O_7$ and un-doped stannates (Represented from Table 3-3 for conventional reading).

Pairs	*A* (eV)	*B* (Å)	*C* (eVÅ^6)
Yb-O	1649.80	0.3386	16.57
La-O	2088.79	0.3460	23.25
Sn-O	1200.00	0.3592	13.66
O-O	9547.96	0.2192	32.0

4.3.1.2 The Heat Plate Power

In the calculation of thermal conductivity, it is found that thermal conductivity is dependent on the values of thermal power used in the simulation program. In Figure 4-13, the thermal conductivity slightly increases to a maximum point and then decreases a bit. After 250 nW, the thermal conductivity starts to be stabilised. In order to reduce the calculation time, 300 nW is selected as the final heating power for the simulation of La^{3+} ions doped $Yb_2Sn_2O_7$.

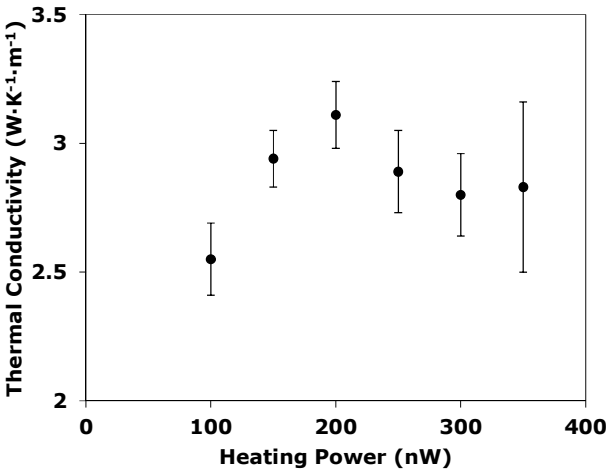

Figure 4-13: The effect of heating power on thermal conductivity of $(La_{0.5}Yb_{0.5})_2Sn_2O_7$ at 300K.

4.3.2 Thermal Properties

4.3.2.1 Thermal Conductivity

Figure 4-14 shows the simulated thermal conductivities of all studied materials. In general, thermal conductivity decreases with increasing temperature. At room temperature, Figure 4-14 **(a)** and **(e)** show that un-doped $Yb_2Sn_2O_7$ and $La_2Sn_2O_7$ exhibit the largest thermal conductivities, both around 4.55 $W \cdot m^{-1} \cdot K^{-1}$. When x = 0.3 and 0.7 in $(La_xYb_{1-x})_2Sn_2O_7$ solid solution, the thermal conductivity is reduced to 3.41 $W \cdot m^{-1} \cdot K^{-1}$, and $(La_{0.5}Yb_{0.5})_2Sn_2O_7$ shows the lowest thermal conductivity of 3.13 $W \cdot m^{-1} \cdot K^{-1}$ at room temperature. This simulation result agrees with experimental data at room temperature [15] and suggests that the change of thermal conductivity of $(La_xYb_{1-x})_2Sn_2O_7$ solid solution is determined by the

disorder of cation layer resulting from the doping concentration, rather than porosity, particle size and grain boundary.

When the temperature increases to 1400 ^{o}C, the thermal conductivity of doped and un-doped materials decreases to a similar value, 1.5 $W \cdot m^{-1} \cdot K^{-1}$, indicating that it is becoming less dependent on the doping concentration at high temperatures. This observation is possibly related to the minimum thermal conductivity of materials, which is independent of intrinsic defects of materials at high temperatures [108, 158].

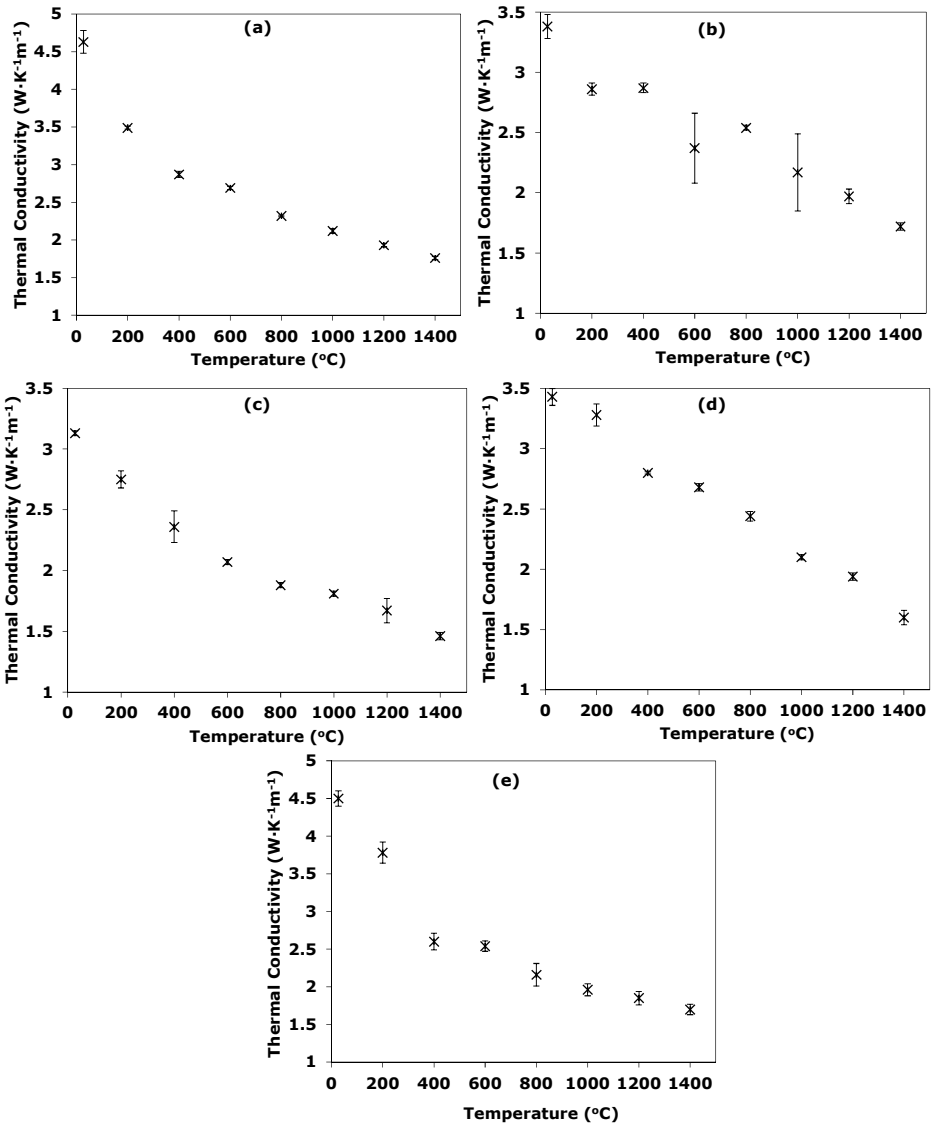

Figure 4-14: Thermal conductivities of $Yb_2Sn_2O_7$ **(a)**, $(La_{0.3}Yb_{0.7})_2Sn_2O_7$ **(b)**, $(La_{0.5}Yb_{0.5})_2Sn_2O_7$ **(c)**, $(La_{0.7}Yb_{0.3})_2Sn_2O_7$ **(d)** and $La_2Sn_2O_7$ **(e)** calculated by MD method from room temperature to 1400 °C.

4.3.2.2 Linear Coefficients of Thermal Expansion

Figure 4-15 shows the lattice constant *a'* of $Yb_2Sn_2O_7$, $La_2Sn_2O_7$ and $(La_xYb_{1-x})_2Sn_2O_7$ solid solution, which increases almost linearly against temperature. The lattice constants of pure $Yb_2Sn_2O_7$ and $La_2Sn_2O_7$ are 10.3438 Å and 10.6628 Å at room temperature, respectively. Due to the larger ionic size of the La^{3+} ion to replace the host cation Yb^{3+}, the lattice constant is 10.4421 Å, 10.5069 Å and 10.5704 Å for $(La_xYb_{1-x})_2Sn_2O_7$ when the *x* is 0.3, 0.5 and 0.7, respectively.

The linear coefficient of thermal expansion (CTE) is obtained according to Eq. (4-2):

$$\mathrm{CTE} = \frac{1}{a'}\frac{da'}{dT} = \frac{d\ ln(a')}{dT} \qquad \text{Eq. (4-2)}$$

The first derivative of $\mathrm{Ln}(a')$ with respect to dT is calculated by using the cubic spline interpolation method.

Figure 4-16 **(a)** to **(d)** show the linear CTE results of pure $Yb_2Sn_2O_7$, $La_2Sn_2O_7$ and $(La_xYb_{1-x})_2Sn_2O_7$ solid solution. The overall linear CTE values are around 6×10^{-6} K^{-1}. Meanwhile, the CTEs almost keep constant and independent of the doping concentration of La^{3+} ions, but slightly increase with increasing temperature. The data fluctuate at low temperatures, probably resulting from low ionic speed.

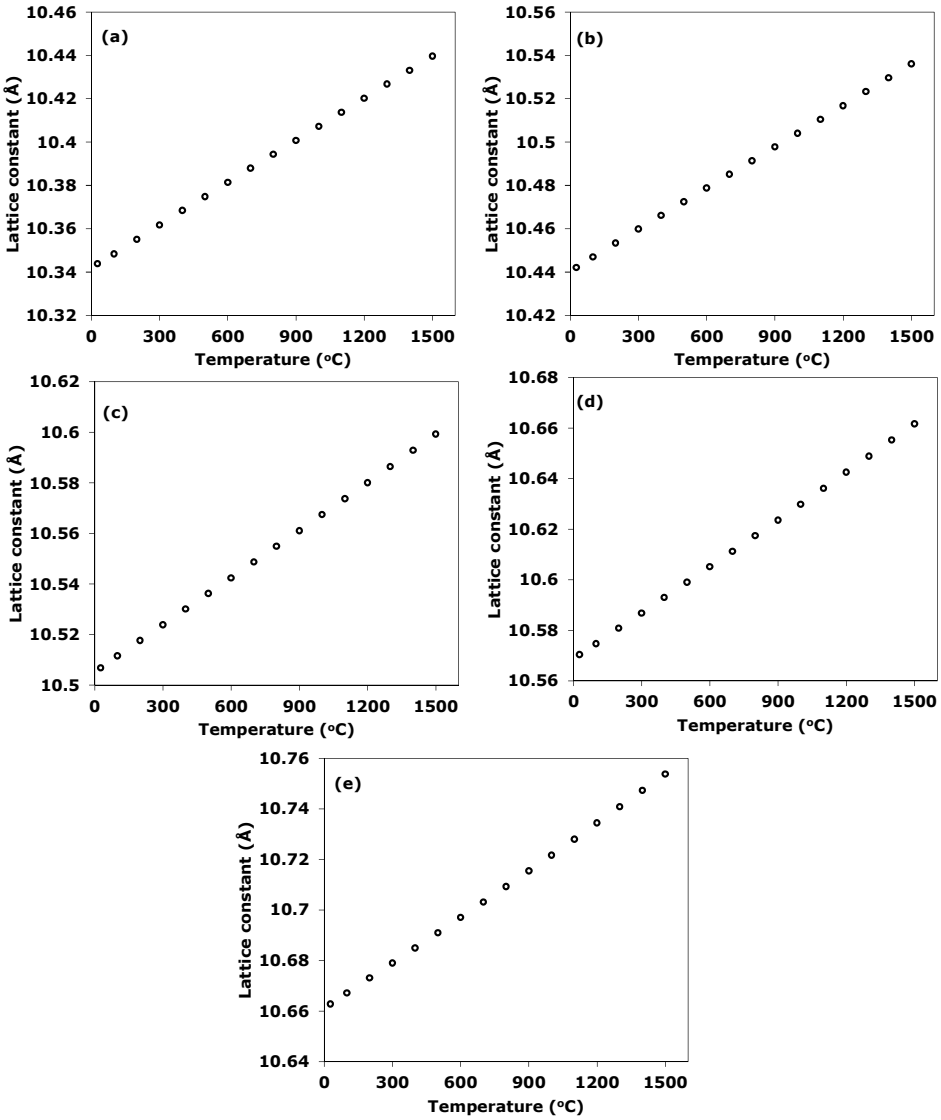

Figure 4-15: The increase of lattice constants of $Yb_2Sn_2O_7$ **(a)**, $(La_{0.3}Yb_{0.7})_2Sn_2O_7$ **(b)**, $(La_{0.5}Yb_{0.5})_2Sn_2O_7$ **(c)**, $(La_{0.7}Yb_{0.3})_2Sn_2O_7$ **(d)** and $La_2Sn_2O_7$ **(e)** against the temperature.

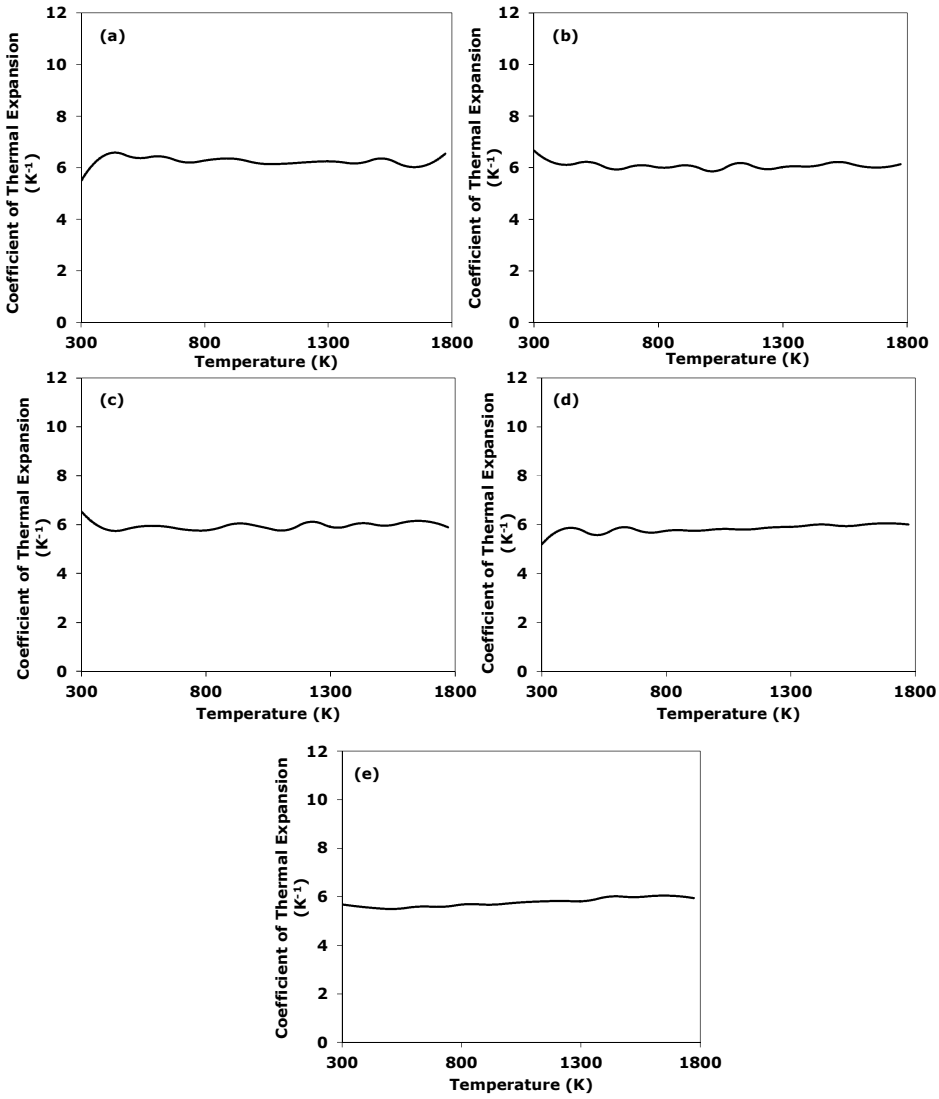

Figure 4-16: Linear coefficients of thermal expansion of $Yb_2Sn_2O_7$ **(a)**, $(La_{0.3}Yb_{0.7})_2Sn_2O_7$ **(b)**, $(La_{0.5}Yb_{0.5})_2Sn_2O_7$ **(c)**, $(La_{0.7}Yb_{0.3})_2Sn_2O_7$ **(d)** and $La_2Sn_2O_7$ **(e)** calculated from 200 °C to 1500 °C.

Therefore, the thermal conductivity and linear coefficient of thermal expansion are obtained by using the dedicated simulation programs. The thermal conductivities of pure $Yb_2Sn_2O_7$, $La_2Sn_2O_7$

and $(La_xYb_{1-x})_2Sn_2O_7$ solid solution at the room temperature have a similar tendency to experimental results. Moreover, the thermal conductivities of pure $Yb_2Sn_2O_7$, $La_2Sn_2O_7$ and $(La_xYb_{1-x})_2Sn_2O_7$ solid solution at high temperatures trend toward a similar value (1.5 $W \cdot m^{-1} \cdot K^{-1}$), becoming independent of intrinsic defects. Furthermore, the linear coefficient of thermal expansion does not have significant change with different doping concentrations.

4.4 Summary

Based on the study of crystal structure and ion radii, La^{3+} ions have been introduced to produce crystal disorders by replacing Yb^{3+} ions in $Yb_2Sn_2O_7$. La^{3+} Doped $Yb_2Sn_2O_7$ materials with pyrochlore crystal structure were synthesised by the sol-gel method, demonstrating lower thermal conductivity and good phase stability at higher temperatures.

The XRD results and TEM diffraction pattern indicate their pyrochlore crystal structure. The simulation XRD results had good agreement with experimental data. Lattice constants and relative phase contents of two different compositions in each solid solution $(La_xYb_{1-x})_2Sn_2O_7$ (x = 0.3, 0.5 and 0.7) were obtained, and the lattice constants change linearly with the increase of La^{3+} ions. Moreover, the TEM images indicate that the grain size of as-synthesised powder does not exceed 100 nm, and it increases to more than 500 nm when the synthesised powders are sintered.

In addition, $(La_{0.7}Yb_{0.3})_2Sn_2O_7$, $(La_{0.5}Yb_{0.5})_2Sn_2O_7$ and $(La_{0.3}Yb_{0.7})_2Sn_2O_7$ show lower thermal conductivities than that of 8YSZ. $(La_xYb_{1-x})_2Sn_2O_7$ (x = 0.3, 0.5 and 0.7) solid solution have much lower thermal conductivity values, around 1 $W \cdot m^{-1} \cdot K^{-1}$ at the room temperature. However, most stannates, $La_2Sn_2O_7$, $(La_{0.7}Yb_{0.3})_2Sn_2O_7$, $(La_{0.3}Yb_{0.7})_2Sn_2O_7$ and $Yb_2Sn_2O_7$, exhibit relatively lower coefficients of thermal expansion, $7 \sim 9 \times 10^{-6}$ K^{-1}, compared with that of 8YSZ.

As ceramic $(La_{0.5}Yb_{0.5})_2Sn_2O_7$ pellet has the lowest thermal conductivity value (0.851 $W \cdot m^{-1} \cdot K^{-1}$) in stannates at room temperature, and higher coefficient of thermal expansion (13.530×10^{-6} K^{-1}) at 950 ^oC, compared with standard 8YSZ ceramic, the chemical compatibility of ceramic $(La_{0.5}Yb_{0.5})_2Sn_2O_7$ with Al_2O_3 is studied and also the reaction temperature between them is detected. It is found that $LaAlO_3$ and $YbAlO_3$ phases are formed at around 1360 ^oC. With the consideration of temperature gradient resulting from its low thermal conductivity, the application temperature of the top-coat surface may reach up to 1500 ^oC, which is much higher than the maximum application temperature (1250 ^oC) of 8YSZ.

Molecular Dynamics (MD) simulation verifies that the thermal conductivity of $(La_xYb_{1-x})_2Sn_2O_7$ (x = 0.3, 0.5 and 0.7) solid solution is mainly affected by the doping concentration of La^{3+} ions, not porosity, grain size and grain boundary. The lowest thermal conductivity from the simulations is 3.13 $W \cdot m^{-1} \cdot K^{-1}$ at room temperature when x is 0.5. This value is higher than the experimental result since the latter is also affected by the phonon

scattering from grain boundary, grain size and porosity. Additionally, the simulations show that the thermal conductivities of all studied materials decrease with increasing temperature and reach similar values (around 1.5 $W \cdot m^{-1} \cdot K^{-1}$) at 1400 ^oC.

Chapter 5. Rare Earth Oxides Doped Erbia-Stabilised Zirconia

5.1 Introduction

There is an imperative demand of increasing the application temperature of turbine blade, but 8 wt% yttria stabilised zirconia (8YSZ) with the maximum application temperature (1250 ^{o}C) cannot be applied for new generation gas engines [12-15]. When temperature is above 1250 ^{o}C, the phase decomposition of 8YSZ can cause 3.5% volume change and then produce serious strain in the ceramic [16], leading to the failure of ceramic coating. The phase transformations mainly result from the dramatically increased diffusivity of Y^{3+} ions. Therefore, a new stabilised zirconia with high thermal phase stability at elevated temperatures (above 1250 ^{o}C) is highly desirable. The main topic of this Chapter is to find new stabilisers for zirconia, which can replace 8YSZ for application temperatures above 1250 ^{o}C.

Figure 5-1 presents the phase diagram between ZrO_2 and Er_2O_3. When the mole percentage of Er_2O_3 is between 4 mol% to 6 mol%, the composition exhibits a pure non-transformable metastable (t') phase without monoclinic (m) and second metastable tetragonal phase (t''-phase) by avoiding T_o^{t-m} (boundary of tetragonal to monoclinic phase transformation), which is desired for thermal barrier materials. Moreover, Khor and Yand [126] found that Er_2O_3 could be a good phase stabiliser. However, there is no specific

report on the phase stability, thermal conductivity and coefficient of thermal expansion of erbia-stabilised zirconia.

Therefore, this chapter mainly studies the crystal structure, phase stability, thermal conductivity and coefficient of thermal expansion of erbia stabilised zirconia, and also mono- or bi-rare earth oxides doped erbia stabilised zirconia. In order to further reduce thermal conductivity, some other rare earth oxides are introduced to form cluster defects, which can lead to more phonon scattering. The difference of atomic mass and radius can also contribute to low thermal conductivity. Moreover, the relationship between crystal structure and thermal phase stability are also investigated in this chapter.

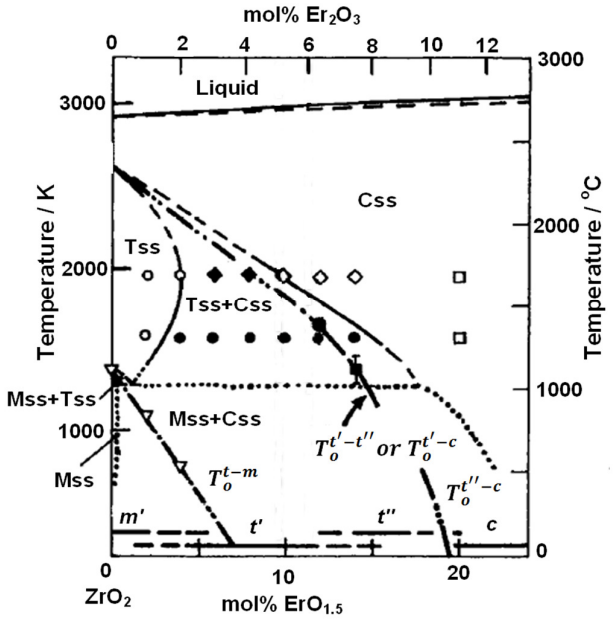

Figure 5-1: The metastable-stable phase diagram Er_2O_3-ZrO_2 (the subscript 'ss' means solid solution) [51].

5.2 Erbia-stabilised Zirconia

The crystalline phase, thermal conductivity and thermal phase stability of erbia-stabilised zirconia are studied, with the doping contents of 4 mol% (E4Z), 5 mol% (E5Z) and 6 mol% (E6Z) erbia, according to the ZrO_2-Er_2O_3 phase diagram. The substituting mechanism is described in Eq. (5-1):

$$xEr_2O_3 \xrightarrow{ZrO_2} 2xEr'_{Zr} + 3xO_O{}^X + xV_O^{\cdot\cdot} \qquad \text{Eq. (5-1)}$$

5.2.1 Crystalline Phase of Erbia-Stabilised Zirconia

The crystalline phases of as-synthesised powders are shown in Figure 5-2. The non-transformable tetragonal phase (t'-phase) is obtained in all specimens produced by sol-gel method, which is distinguished by peaks (004) and (400) [185, 186]. The (004)t' and (400)t' peaks tend to overlap when the doping concentration increases, which is related to the variation of crystal structure, closely to the boundary of $T_o^{t'-t''}$ or $T_o^{t'-c}$. Furthermore, there is very small amount of monoclinic phase observed in E4Z.

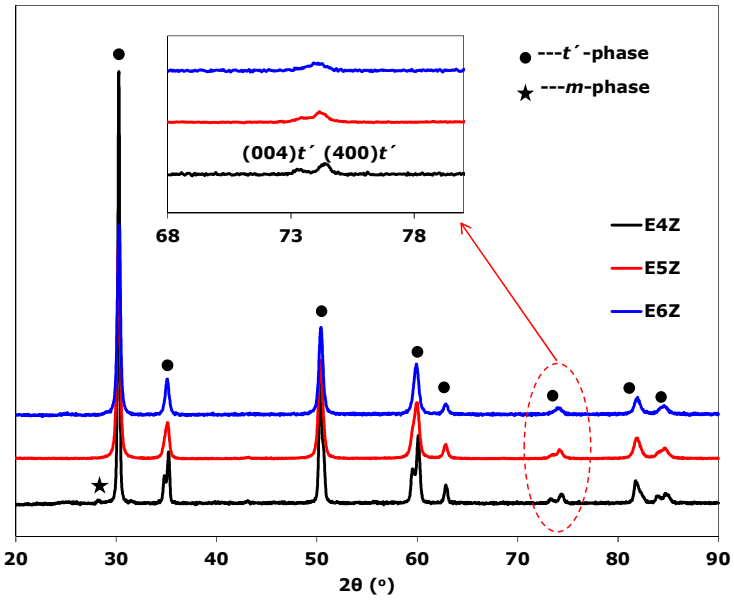

Figure 5-2: XRD patterns of 4 mol%, 5 mol% and 6 mol% erbia-stabilised zirconia.

5.2.2 Thermal Conductivity, Thermal Phase Stability and Chemical Compatibility with Alumina

The thermal conductivity and theoretical density of E4Z, E5Z and E6Z are shown in Figure 5-3. The theoretical density increases linearly with the increase of erbia content from 4 mol% to 6 mol%. The thermal conductivity of erbia-stabilised zirconia decreases with increasing the doping concentration of erbia.

Furthermore, the thermal phase stability of E4Z, E5Z and E6Z is presented in Figure 5-4, as well as the chemical compatibility with alumina. There is no chemical reaction observed at 1400 °C after 50 h heat treatment. Additionally, no monoclinic phase (*m*-phase) is found in E6Z during this process. A very small amount of *m*-

phase in E5Z appears after 50 h. But the content of *m*-phase in E4Z increases dramatically during isothermal duration. So E5Z and E6Z have better thermal phase stability than E4Z. Therefore, the stabilised zirconia with high doping content of erbia shows better thermal phase stability during the isothermal heat treatment.

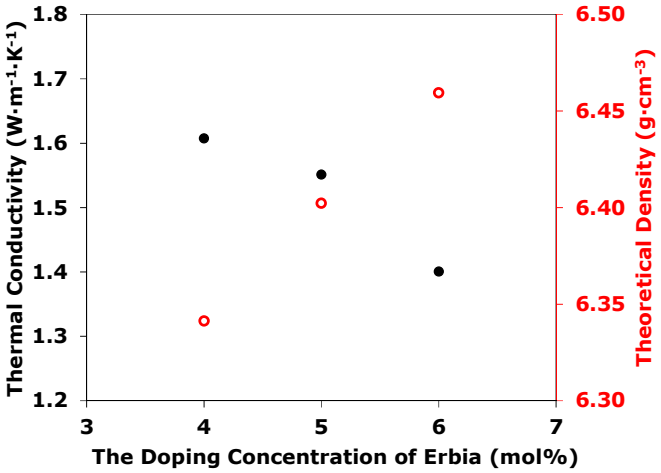

Figure 5-3: The thermal conductivity and theoretical density of erbia-stabilised zirconia against the doping concentration. The black solid circle indicates thermal conductivity and the red hollow circle refers to theoretical density.

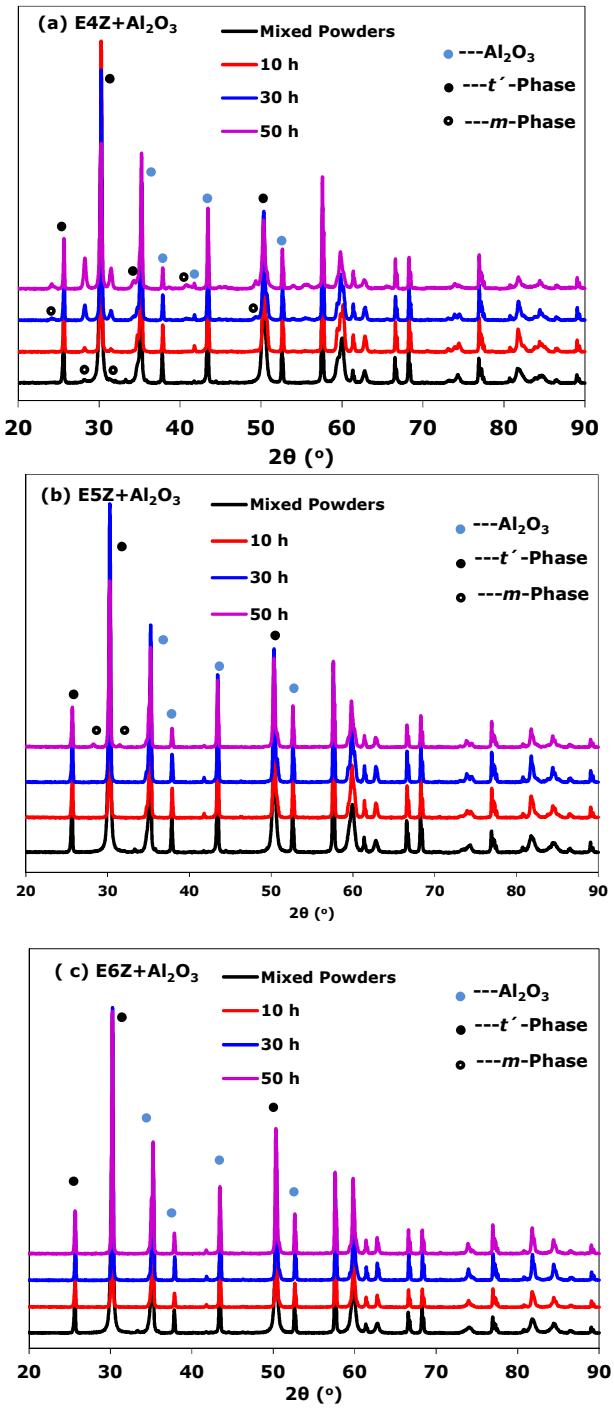

Figure 5-4: XRD patterns of the mixed powder of as-synthesised erbia-stabilised zirconia powder and alumina, and the mixed pellets at 1400 °C for different durations.

5.3 Mono-Rare Earth Oxide Doped Erbia-Stabilised Zirconia

As discussed in section 5.2, the thermal phase stability of erbia-stabilised zirconia is improved by increasing the doping concentration of erbia from 4 mol% to 6 mol%. In this section, the main study involves the crystalline phase, thermal phase stability, thermal conductivity and coefficient of thermal expansion of mono-rare earth oxides doped erbia-stabilised zirconia. The total doping content including erbia is fixed at 5 mol%. For mono-rare earth oxide doped erbia-stabilised zirconia, the doping is described Eq. (5-2):

$$xEr_2O_3 + yR_2O_3 \xrightarrow{ZrO_2} 2xEr'_{Zr} + 2yR'_{Zr} + (3x+3y){O_O}^X + (x+y)V_O^{\cdot\cdot}$$

Eq. (5-2)

where *x* and *y* are the mole percentage and they are equal, 2.5 mol%; R_2O_3 refers to Er_2O_3 (E5Z), Yb_2O_3 (E2.5Y2.5Z), Gd_2O_3 (E2.5G2.5Z) or Dy_2O_3 (E2.5D2.5Z). So the chemical formula is $Er_{0.05}R_{0.05}Zr_{0.9}O_{1.95}$. The average doping radius is listed in Table 5-1.

Table 5-1: The doping radius of rare earth ions in mono-rare earth oxides doped erbia-stabilised zirconia, from database of Shannon radii [187].

Second Stabiliser	Average Doping Radius (Å)
Yb_2O_3	0.985
Er_2O_3	1.004
Dy_2O_3	1.027
Gd_2O_3	1.053

5.3.1 XRD and Lattice Parameter Refinement of Synthesised Powder

5.3.1.1 Phase Analysis and Grain Size of as-Synthesised Powder

In most cases, rare earth oxides doped 7-8YSZ ceramics usually show multi-phases due to inhomogeneous dopant distribution, though the non-transformable tetragonal phase is desirable to minimise some unexpected phase transformation. If zirconia is doped with high level rare earth oxides, it forms the cubic phase, which is unstable when cooling down to room temperature. So it is very important to characterise the crystal phase of the stabilised zirconia. Generally, there are three types of tetragonal phases: the first metastable tetragonal phase *t* (also known as normal tetragonal), the second metastable tetragonal phase *t''* and the non-transformable tetragonal phase *t'*. Both *t'*- and *t''*-phases belong to the space group $P4_2/nmc$. In *t'*-phase, the parameter *c*

is larger than *a* and *b* (*a*=*b*), but the parameter *c* is equal to *a* (*a*=*b*) in *t*''-phases [51]. Yashima studied the metastable-stable ZrO_2-Er_2O_3 phase diagram by changing tetragonality *c/a* [51]. It is suggested that, if the doping content of Er_2O_3 is in the range of 4~6 mol%, the crystal should present *t*'-phase without *m* and *t*''-phases (second metastable tetragonal phase).

Figure 5-5 presents XRD patterns of as-synthesised powders of mono-rare earth oxides doped erbia-stabilised zirconia and there is no extra peak observed in Figure 5-5 **(a)**. Both Figure 5-5 **(a)** and Figure 5-5 **(b)** exhibit the non-transformable tetragonal phase, distinguishing from the peaks (004) nearly 73.4^o and (400) nearly 73.9^o [50, 188] and (006) and (600) peaks.

In Figure 5-6, TEM images (**a**), (**b**), (**c**) and (**d**) were acquired from the as-synthesised powder of E5Z, E2.5Y2.5Z, E2.5D2.5Z and E2.5G2.5Z, respectively. The grain sizes do not exceed 50 nm when the ceramic powders are synthesised via the sol-gel method.

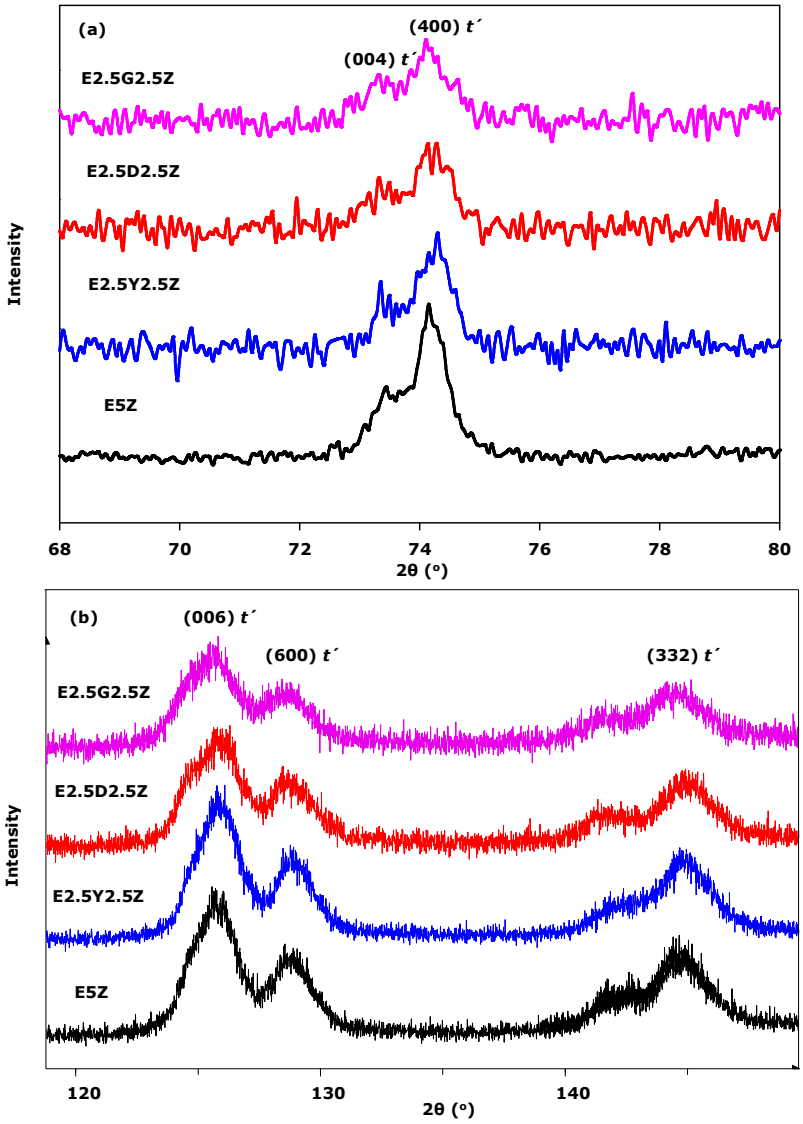

Figure 5-5: XRD patterns of mono-rare earth oxide doped erbia-stabilised zirconia powders (total doping content, 5 mol%): **(a)** no extra peak observed at low 2θ; **(b)** indicating their tetragonal phases by (006) and (600) peaks.

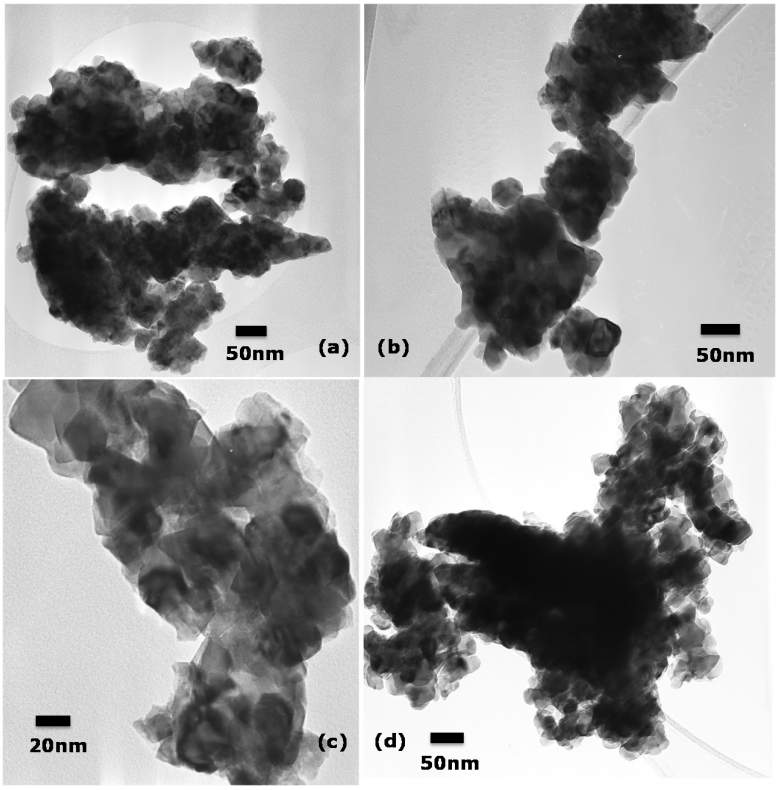

Figure 5-6: TEM images stabilised zirconia, where image (**a**) was taken from ceramic E5Z, image (**b**) was from ceramic E2.5Y2.5Z; image (**c**) was from ceramic E2.5D2.5Z; image (**d**) was from ceramic E2.5G2.5Z.

5.3.1.2 Rietveld Refinement

Rietveld refinement has been applied on the measured XRD patterns, where the 2θ collected from 25^{o} to 150^{o} to simulate the lattice parameters, a ($a=b$) and c. Figure 5-7 indicates that the simulation results have good agreement with XRD patterns collected from the as-synthesised powders. The lattice parameters are obtained from this simulation and listed in Table 5-2, in which the $c/a\sqrt{2}$ ratio is also calculated.

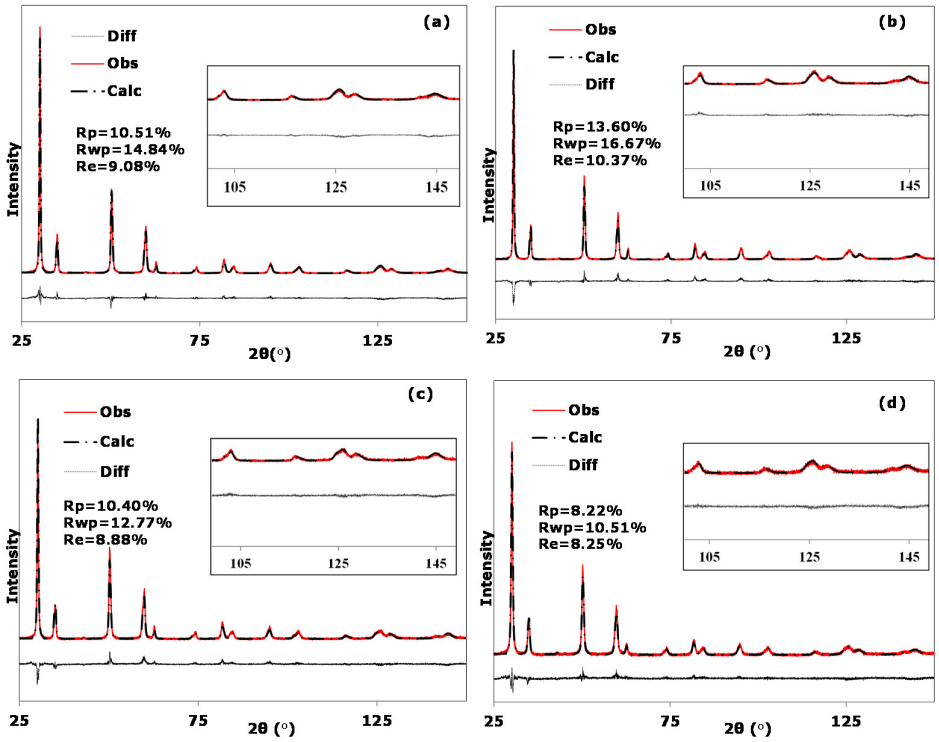

Figure 5-7: The good agreement between the simulation results and the experimental XRD data, especially at high 2-theta for refining unit cell of ceramics **(a)** E5Z, **(b)** E2.5Y2.5Z, **(c)** E2.5D2.5Z and **(d)** E2.5G2.5Z, where Diff refers to the difference between the calculated (Calc) and observed (Obs) data.

From Table 5-2, it is found that the lattice constant *a* decreases from 3.6187 to 3.6151Å and lattice constant *c* decreases from 5.1671 to 5.1551Å. If compared with pure erbia-stabilised zirconia (E5Z), the $c/a\sqrt{2}$ ratio of E2.5Y2.5Z is very close to E5Z, due to the similar radius between Er^{3+} (1.004 Å) and Yb^{3+} ions (0.985 Å) But the $c/a\sqrt{2}$ ratio becomes larger when the dopants are Dy^{3+} (1.027 Å) and Gd^{3+} ions (1.053 Å), which indicates that the doping enlarges the lattice constant in the *c*-direction.

Table 5-2: Lattice constants of mono-rare earth oxide doped erbia-stabilised zirconia obtained from the refinement.

Ceramics	Lattice constants (Å)		$c/a\sqrt{2}$ ratio
	$a=b$	c	
E2.5Y2.5Z	3.6151	5.1551	1.0083±0.0002
E5Z	3.6163	5.1577	1.0085±0.0002
E2.5D2.5Z	3.6147	5.1644	1.0102±0.0002
E2.5G2.5Z	3.6187	5.1671	1.0097±0.0001

5.3.2 Thermal Phase Stability and Chemical Compatibility with Alumina

The as-synthesised powders are mixed with alumina powder and compressed into pellets, which are heat-treated at 1400 °C for different durations to investigate their chemical compatibility with alumina and thermal phase stability at this high temperature. Figure 5-8 and Figure 5-9 present the XRD patterns collected after each heat treatment. From Figure 5-8 **(a)** to **(d)**, no chemical reaction with alumina is observed during the heat treatment, but the *m*-phase appears in pellets after 30 h or 50 h heat-treatment at 1400 °C. Meanwhile, the chemical compatibility with alumina and thermal phase stability of 8YSZ is exhibited in Figure 5-9, where the *m*-phase is found after 30 h heat treatment.

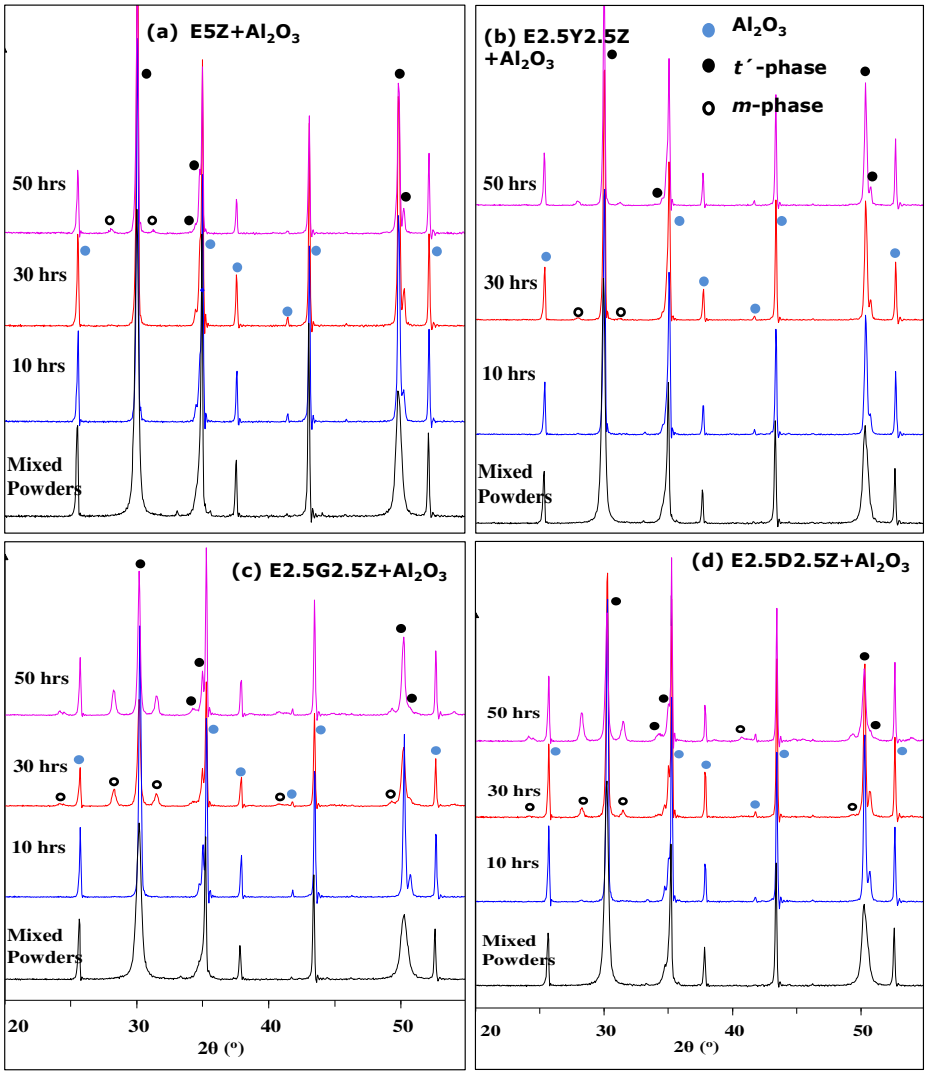

Figure 5-8: XRD patterns of mixed powders without heat-treatment and the pellets of stabilised zirconia mixed with Al_2O_3 sintered at 1400 ºC for different heating times: **(a)**, E5Z mixed with Al_2O_3; **(b)**, E2.5Y2.5Z mixed with Al_2O_3; **(c)**, E2.5G2.5Z mixed with Al_2O_3; **(d)**, E2.5D2.5Z mixed with Al_2O_3.

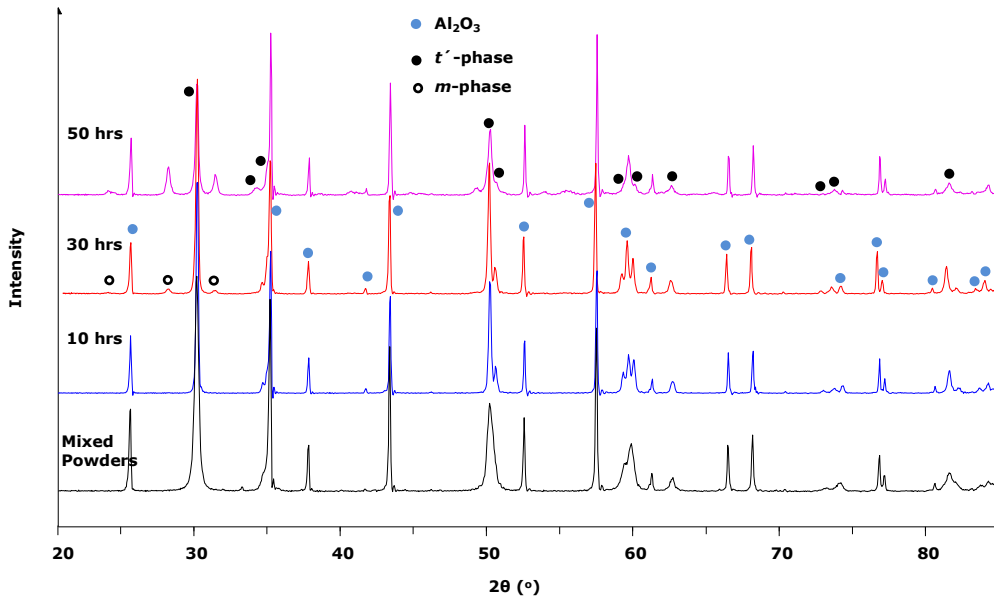

Figure 5-9: XRD patterns of mixed powders without heat-treatment and the pellet of 8YSZ mixed with Al_2O_3 sintered at 1400 °C after different heating durations.

The content of *m*-phase formed in the stabilised zirconia after different heating durations is shown in Table 5-3. It is observed that the *m*-phase is firstly detected in E2.5Y2.5Z, E2.5D2.5Z and E2.5G2.5Z after 30 h heat-treatment. The content of *m*-phase in E2.5D2.5Z rises dramatically from 6.07% to 26.28% when the heating duration increases from 30 h to 50 h. A similar increase is observed in E2.5G2.5Z (19.24% to 23.06%). Furthermore, the conventional 8YSZ shows poor thermal phase stability, the content of *m*-phase of which increases from 4.35% to 28.67%. For E5Z, *m*-phase appears after longer heating duration (50 h) with the content about 2.84%. In contrast, the *m*-phase is found in E2.5Y2.5Z after 30 h, but it increases very slowly from 1.40% to

3.35%. So E5Z and E2.5Y2.5Z show lower phase transformation rates than E2.5D2.5Z and E2.5G2.5Z.

It is known that the $c/a\sqrt{2}$ ratio of 8YSZ is around 1.012 [50], and the $c/a\sqrt{2}$ ratios of E2.5D2.5Z and E2.5G2.5Z are around 1.01, which are very close to that of 8YSZ. But in E5Z and E2.5Y2.5Z, the dopant (erbia or ytterbia) has relatively small radius, which contributes to the smaller $c/a\sqrt{2}$ ratio if compared with E2.5D2.5Z and E2.5G2.5Z. Therefore, it is assumed that the thermal phase stability might be also dependent on $c/a\sqrt{2}$ ratio.

Table 5-3: Evolution of phase composition of E5Z and bi-doped zirconia when heating at 1400 °C for different heating times.

Samples	30 h		50 h	
	m-phase (mol%)	*t′*-phase (mol%)	*m*-phase (mol%)	*t′*-phase (mol%)
E5Z	-	-	2.84	97.16
E2.5Y2.5Z	1.40	98.60	3.35	96.65
E2.5D2.5Z	6.07	93.93	26.28	73.72
E2.5G2.5Z	19.24	80.76	23.06	76.94
8YSZ	4.35	95.65	28.67	71.33

The non-transformable tetragonal structure of stabilised zirconia is shown in Figure 5-10. The oxygen vacancy is produced by the trivalent dopant for electron compensation. When the $c/a\sqrt{2}$ ratio becomes large, *c*-axis length can be enlarged. This crystal change

can cause the dopant ions or Zr^{4+} ions easily to diffuse from one unit cell to the other one. This explains why E2.5D2.5Z and E2.5G2.5Z exhibit worse thermal phase stability than E2.5Y2.5Z and E5Z.

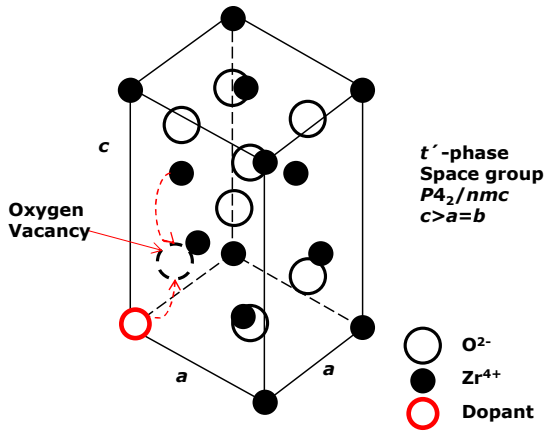

Figure 5-10: The non-transformable tetragonal phase of stabilised zirconia, where the oxygen vacancy is produced by the trivalent dopant.

5.3.3 Thermal Conductivity and Coefficient of Thermal Expansion

5.3.3.1 Thermal Conductivity

The as-synthesised powders of stabilised zirconia are compressed into pellets and sintered for thermal conductivity measurement. Thermal conductivity and theoretical density of stabilised zirconia are shown in Figure 5-11. The densities of E5Z, E2.5Y2.5Z, E2.5D2.5Z, E2.5G2.5Z and 8YSZ are 6.40, 6.42, 6.39, 6.36 and 6.41 $g \cdot cm^{-3}$ respectively. The stabilised zirconia has higher

densities than that of 8YSZ, due to the heavy dopants, *e.g.* Er_2O_3, Yb_2O_3, Gd_2O_3 or Dy_2O_3.

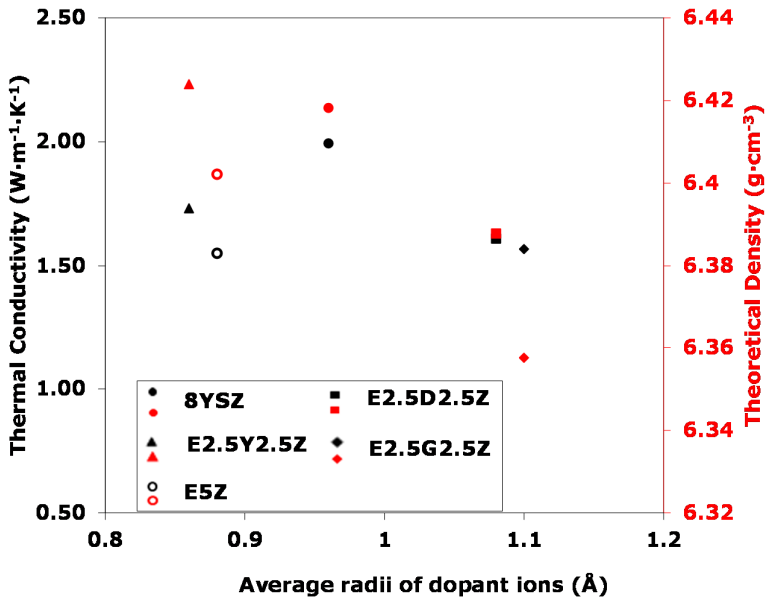

Figure 5-11: The thermal conductivity and theoretical density of erbia based oxides stabilised zirconia against with average radii of dopant ions.

In addition, the thermal conductivity of conventional 8YSZ is 1.99 $W \cdot m^{-1} \cdot K^{-1}$ at room temperature, and the values for E5Z, E2.5Y2.5Z, E2.5D2.5Z and E2.5G2.5Z are 1.55 $W \cdot m^{-1} \cdot K^{-1}$, 1.73 $W \cdot m^{-1} \cdot K^{-1}$, 1.61 $W \cdot m^{-1} \cdot K^{-1}$ and 1.57 $W \cdot m^{-1} \cdot K^{-1}$, respectively. The thermal conductivity of stabilised zirconia is smaller than that of conventional 8YSZ. The theoretical density increases due to the rare earth elements with the heavy atomic weights. Meanwhile, the relative densities are calculated, to be approximately 65% for all ceramic pellets.

According to Debye's phonon theory, thermal conductivity is defined in Eq. (5-3) [189]:

$$k^* = \frac{1}{3}\int C_p(\omega)\, l(\omega)\; v(\omega)\; d(\omega) \qquad \text{Eq. (5-3)}$$

where C_p, l and v represent the heat capacity per unit volume, the phonon mean free path and the sound speed, respectively. Using this approach, the corrected thermal conductivity, k_o, can be expressed in Eq. (5-4).

$$k_o = k_i - (k_U + k_v + k_c + k_{gb} + k_m + k_r) \qquad \text{Eq. (5-4)}$$

where k_i is intrinsic thermal conductivity; k_U, k_v and k_c are thermal conductivity reduction by Umklapp phonon-phonon scattering, oxygen vacancy scattering and cluster defect scattering, respectively; k_{gb} is the thermal conductivity reduction by gain boundary in nanostructured materials; k_m and k_r are thermal conductivities reduction by the difference of atomic mass and ionic radius, respectively.

The Umklapp phonon-phonon scattering is usually the dominant factor for thermal conductivity, and strongly dependent on the anharmonicity of bonding, the average mass and temperature [30]. Because the anharmonicity of bonding and the average mass are similar in stabilised zirconia, the effect of Umklapp process is assumed the same on all specimens at room temperature. So the phonon-defect scattering plays the main role in decreasing thermal conductivity, including oxygen vacancy, cluster defect, mass difference and radius difference scattering. Because the total doping concentration in stabilised zirconia is fixed at 5 mol%, the

contents of oxygen vacancy produced by dopants (all 3+ charges) are the same in all materials. Thus the partial reduction of thermal conductivity resulting from the oxygen vacancies should be equal for all stabilised zirconia, due to the fixed total doping concentration (5 mol%).

In rare earth stabilised zirconia, another theory for further reducing thermal conductivity is oxide defect clusters produced by dopants, which can decrease the mean free path of phonons. Oxide defect clusters are usually formed by the aggregation of dopant cations, which can effectively scatter lattice phonon waves and radiative photon waves at a wide range of frequencies [190, 191]. Furthermore, the minor difference of thermal conductivity between E5Z, E2.5Y2.5Z, E2.5D2.5Z and E2.5G2.5Z could result from the mass difference and radius difference between the dopants.

5.3.3.2 Coefficients of Thermal Expansion

The coefficients of thermal expansion (CTEs) of mono-rare earth oxide doped erbia-stabilised zirconia (5 mol%) are plotted in the range of 100 ^{o}C-900 ^{o}C in Figure 5-12, which are the average values obtained from three measurements. E5Z, E2.5D2.5Z and E2.5G2.5Z have similar CTEs from 100 ^{o}C up to 900 ^{o}C, 9.0~11.0 × 10^{-6} K^{-1}. But E2.5Y2.5Z shows slightly higher CTEs than the others, especially above 300 ^{o}C. The reason for this change could be related to lattice distortion due to the different radius of dopants. Additionally, the CTEs of stabilised zirconia are

similar to that of conventional 8YSZ (10.5~11.45 × 10^{-6} K^{-1}). The CTEs of 8YSZ in this thesis is also very close to the reported value (10.5~11.0 × 10^{-6} K^{-1}) [192].

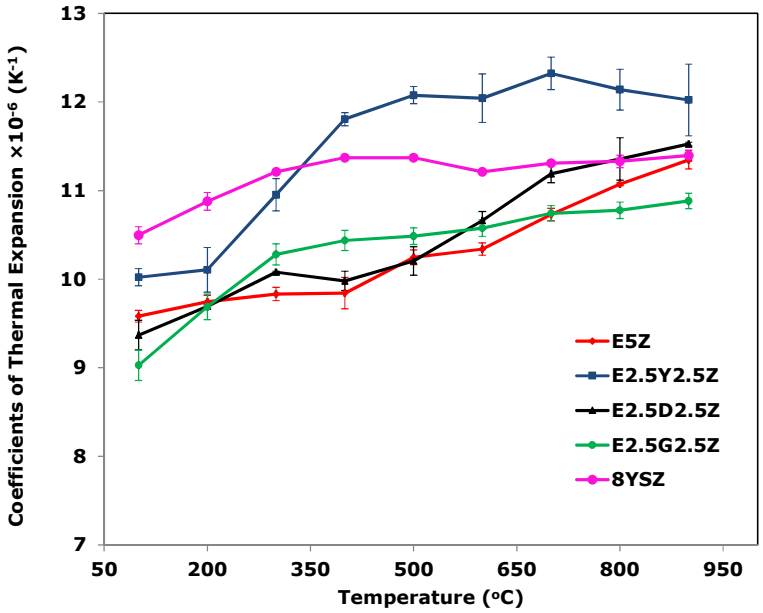

Figure 5-12: The coefficients of thermal expansion of stabilised zirconia versus temperature.

5.4 Bi-Rare Earth Oxides Doped Erbia-Stabilised Zirconia

The main topic of this section is to investigate crystalline phase, thermal phase stability, thermal conductivity and coefficient of thermal expansion of bi-rare earth oxides doped erbia-stabilised zirconia, in which the total doping content is 6 mol%. For bi-rare earth oxides doped erbia-stabilised zirconia, the substituting equation is described in Eq. (5-5):

$$xE_{r_2}O_3 + yR_2O_3 + zR^*{}_2O_3 \xrightarrow{ZrO_2} 2xE_{r_{Z_r}}{}' + 2yR'_{Z_r} + 2zR^{*\prime}{}_{Z_r} + (3x + 3y + 3z){O_O}^X + (x + y + z)V_O^{\cdot\cdot} \quad \text{Eq. (5-5)}$$

where *x*, *y* and *z* are the mole percentage and have the same value, 2 mol%; R_2O_3 and $R^*{}_2O_3$ are rare earth oxides, *e.g.* Er_2O_3 and Er_2O_3 (E6Z), Yb_2O_3 and Dy_2O_3 (E2Y2D2Z), Yb_2O_3 and Gd_2O_3 (E2Y2G2Z) or Dy_2O_3 and Gd_2O_3 (E2D2G2Z), respectively. The chemical formula is $Er_{0.04}R_{0.04}\ R^*{}_{0.04}Zr_{0.88}O_{1.94}$. The average doping radius is calculated and listed in Table 5-4.

Table 5-4: The average doping radius of bi-rare earth oxide doped erbia-stabilised zirconia.

First Dopant (2 mol%)	Second Dopant (2 mol%)	Average Doping Radius (Å)
Er_2O_3	Er_2O_3	1.004
Yb_2O_3	Dy_2O_3	1.006
Yb_2O_3	Gd_2O_3	1.019
Dy_2O_3	Gd_2O_3	1.040

5.4.1 XRD and Lattice Parameter Refinement of Synthesised Powder

5.4.1.1 Phase Analysis

Figure 5-13 presents XRD patterns of as-synthesised powders of bi-rare earth oxides doped erbia-stabilised zirconia and there is no extra peak as shown in Figure 5-13 **(a)**. Additionally,

Figure 5-13 **(a)** and **(b)** indicate the non-transformable tetragonal phase distinguished from (004)t', (400)t', (006)t' and (600)t' peaks. With increasing average radius of dopants (as listed in Table 5-4), the peak (600) slightly shifts to low 2θ, but peak (006) almost keeps the same position, which indicates that the distance between the two peaks is getting closer with the increase of the average doping radius. For the tetragonal system, the d-space between the lattice planes is expressed in Eq. (5-6):

$$d_{hkl} = \frac{1}{\sqrt{\frac{h^{*2}+k^{*2}}{a^2}+(\frac{l^*}{c})^2}} \qquad \text{Eq. (5-6)}$$

where h^*, k^* and l^* are the Miller indices of the Bragg plane; *a* and *c* are the lattice parameters. When $d_{h^*k^*l^*}$ decreases, the lattice parameter *a* and/or *c* increases.

In Figure 5-14, TEM images (**a**), (**b**), (**c**) and (**d**) present the microstructure of as-synthesised powders of E6Z, E2Y2D2Z, E2Y2G2Z and E2D2G2Z. The grain sizes of specimens do not exceed 50 nm which are also similar to mono-rare earth oxides doped erbia-stabilised zirconia.

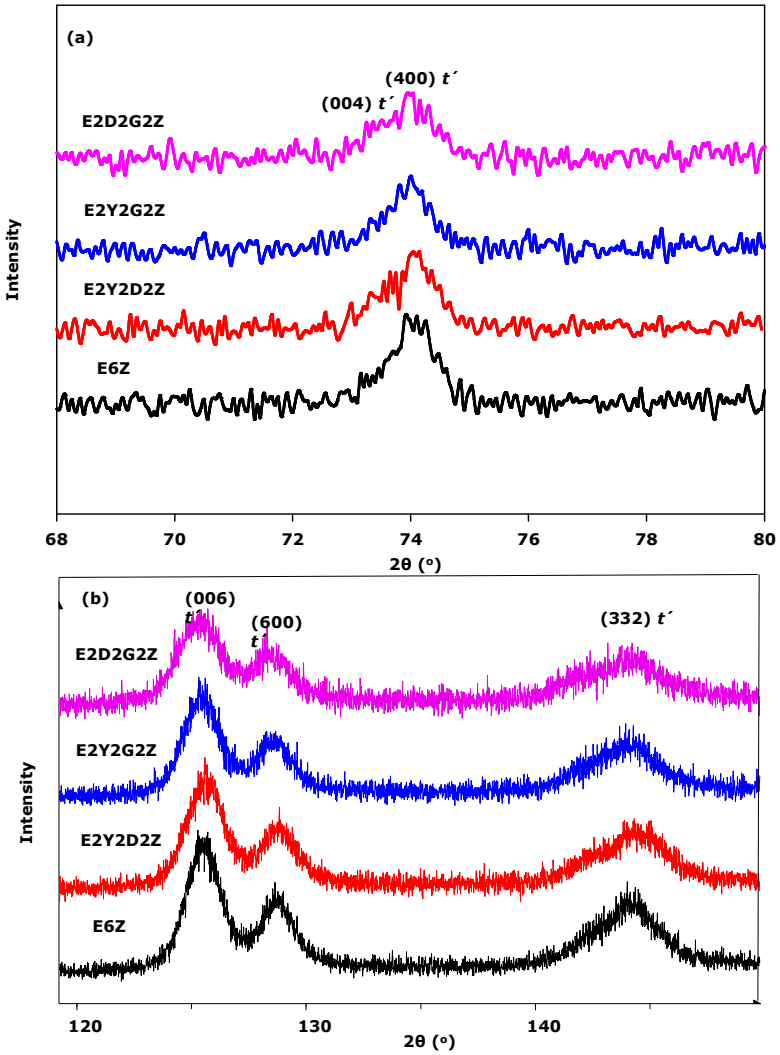

Figure 5-13: XRD patterns of rare earth oxides doped erbia-stabilised zirconia powders: **(a)** no extra peaks observed at low 2θ; **(b)** indicating their tetragonal phases by (006) and (600) peaks.

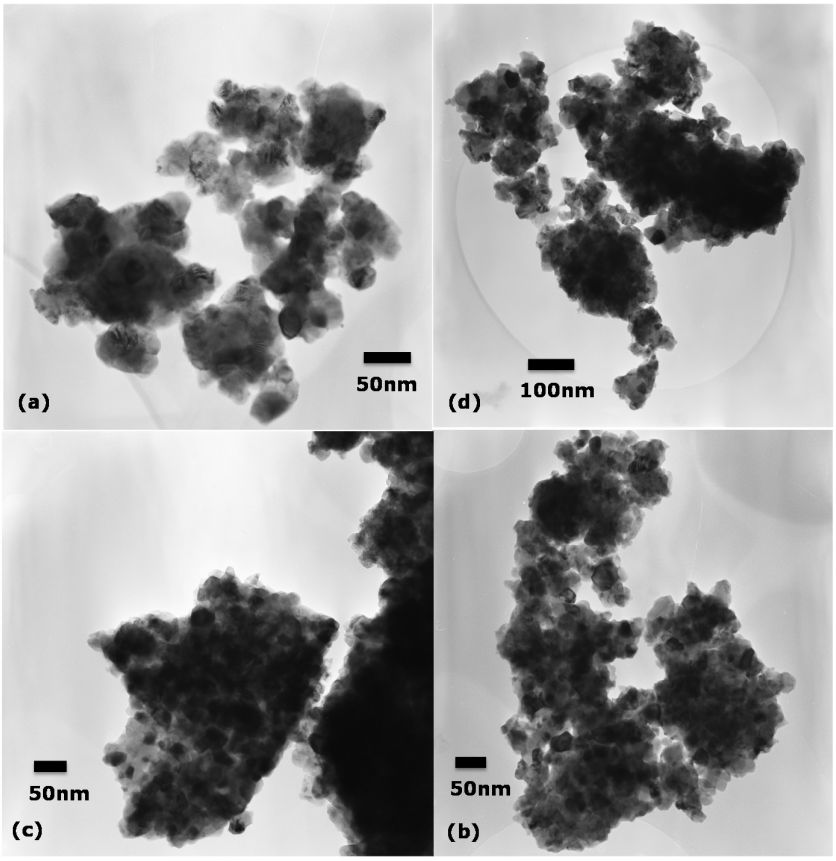

Figure 5-14: TEM images of stabilised zirconia, where image (**a**) was taken from ceramic E6Z, image (**b**) was from ceramic E2Y2D2Z; image (**c**) was from ceramic E2Y2G2Z; image (**d**) was from ceramic E2D2G2Z.

5.4.1.2 Rietveld Refinement

In Figure 5-15, the simulation results obtained by Rietveld refinement show very good agreement with the experimental data, especially at high 2θ. The lattice constants of E2D2G2Z, E2Y2G2Z, E2Y2D2Z and E6Z are listed in Table 5-5. For ceramic E2D2G2Z, E2Y2G2Z and E6Z, the lattice parameter *a* (*a*=*b*) almost keeps constant, around 3.62 Å, while the lattice parameter *c* decreases

from 5.1645 Å to 5.1507 Å, respectively. It is suggested that the doping oxides have greater impact on the *c*-direction rather than *a*/*b*-direction. Furthermore, comparing ceramics E2Y2G2Z and E2Y2D2Z, both lattice parameters reasonably change with different radii of Gd^{3+} and Dy^{3+} ions.

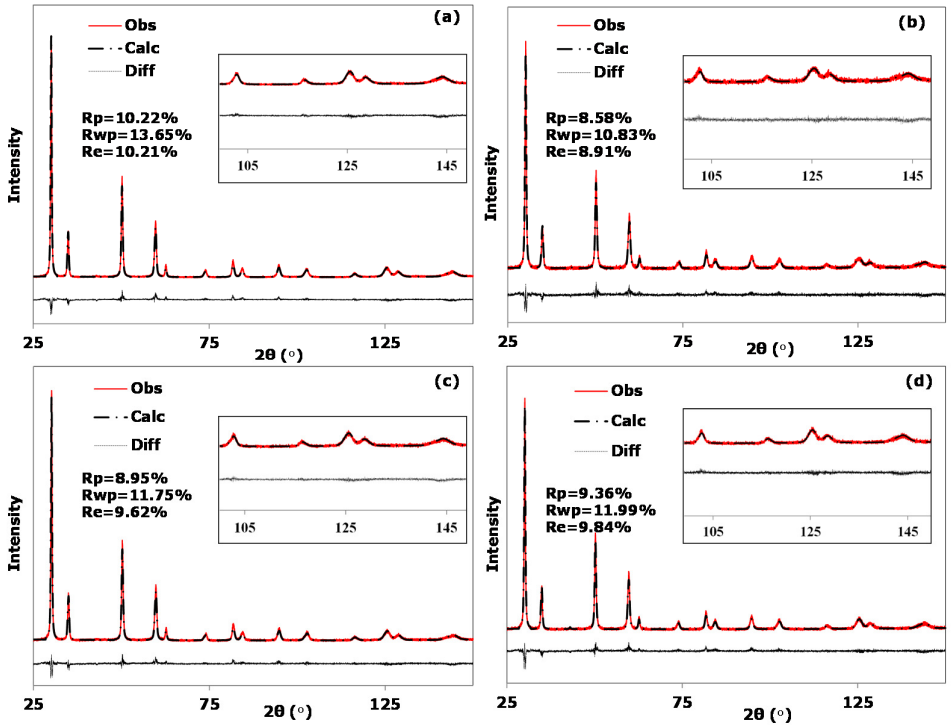

Figure 5-15: The good agreement between the calculated simulation results and the experimental XRD data, especially at high 2-theta for refining unit cell of ceramics **(a)** E6Z, **(b)** E2D2G2Z, **(c)** E2Y2D2Z and **(d)** E2Y2G2Z, where Diff refers to the difference between the calculated (Calc) and observed (Obs) data.

In Table 5-5, E6Z exhibits the smallest $c/a\sqrt{2}$ ratio, followed by E2Y2G2Z, E2Y2D2Z and E2D2G2Z, and their $c/a\sqrt{2}$ ratios are smaller than those of mono-rare earth oxide doped erbia-stabilised zirconia in section 5.2.1.2. The smaller $c/a\sqrt{2}$ ratio of E6Z than that of E5Z was also found by Viazz *et al.* [50], where the $c/a\sqrt{2}$ ratio moves to small value if the doping concentration increases.

Table 5-5: Lattice constants of bi-rare earth oxides doped erbia-stabilised zirconia obtained from the refinement.

Ceramics	Lattice constants (Å)		$c/a\sqrt{2}$ ratio
	$a=b$	c	
E2D2G2Z	3.6224	5.1645	1.0083±0.0002
E2Y2G2Z	3.6227	5.1546	1.0063±0.0002
E2Y2D2Z	3.6194	5.1526	1.0068±0.0001
E6Z	3.6215	5.1507	1.0059±0.0002

5.4.2 Thermal Phase Stability and Chemical Compatibility with Alumina

The thermal phase stability of the mixed pellets and their chemical compatibility with alumina has been studied, by heat treating at 1400 °C for different durations. The related XRD patterns have been recorded, as presented in Figure 5-16. Apparently, they do not have chemical reaction with alumina even after 130 h. However, the *t*-phase begins to transform into *m*-phase after heat treatment. In Figure 5-16 **(a)**, very minor *m*-phase is detected in

E6Z when the heating duration is 90 h. While the *m*-phase forms much earlier (30 h) in E2D2G2Z, and its peak intensities increase rapidly with increased heating time in XRD patterns, which indicates poor thermal phase stability of E2D2G2Z.

In Figure 5-16 **(b)**-**(d)**, E2Y2D2Z and E2Y2G2Z exhibit better phase stability than E2D2G2Z, and the phase transformations occur after relatively longer heating duration, which is 50 h at 1400 ^{o}C versus 30 h for E2D2G2Z. E6Z presents the highest thermal stability in this work. The percentage of monoclinic phase is only 1.88% after 90 h thermal heat treatment. When heating duration increases to 130 h, this value just reaches 4.16%. E2D2G2Z has relatively poor phase stability, due to the high percentage of *m*-phase (6.41% after 30 h). For conventional 8YSZ, 4.35% of monoclinic phase is found after 30 h heat treatment (as shown in Figure 5-9).

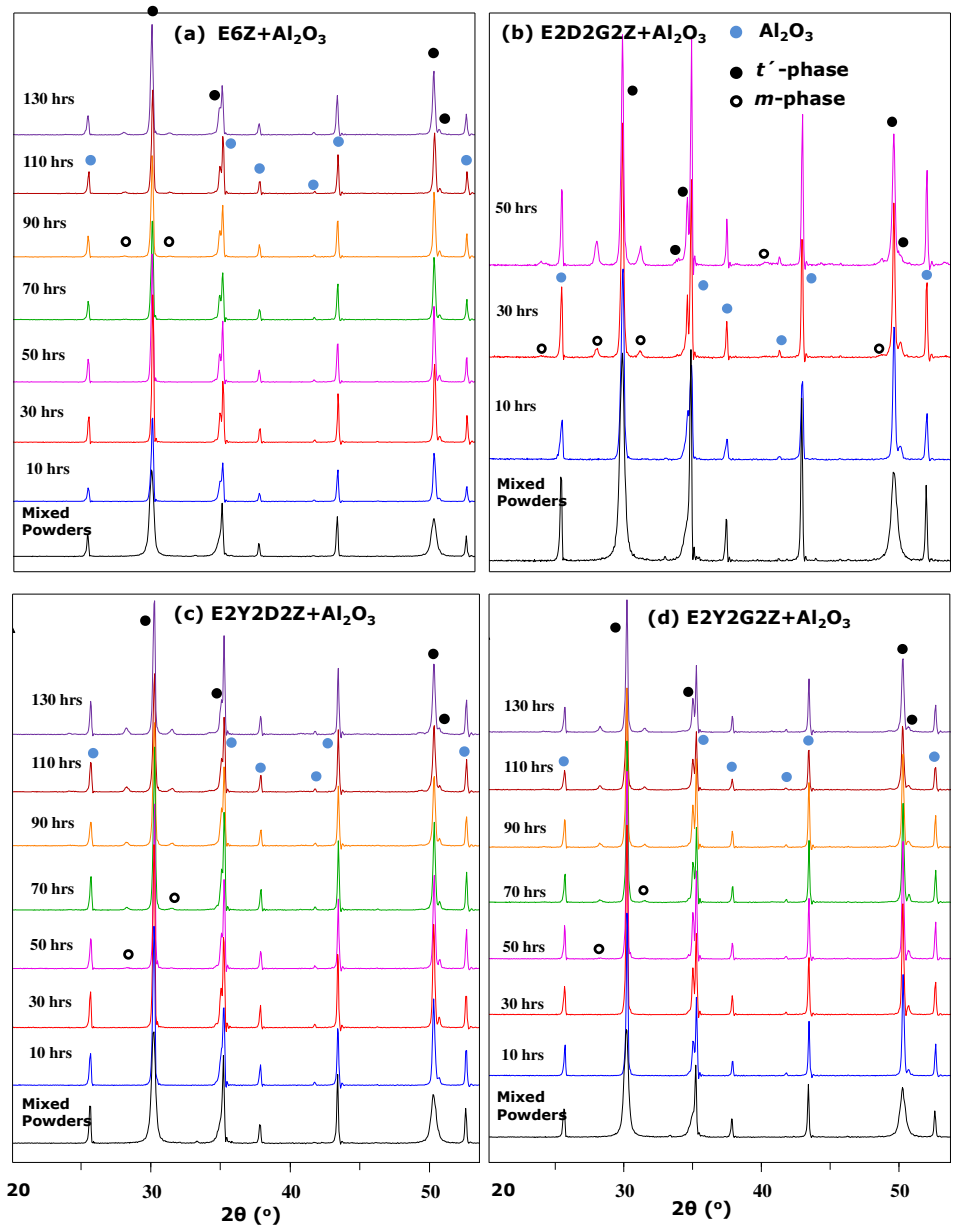

Figure 5-16: XRD patterns of mixed powders without heat-treatment and the pellet of stabilised zirconia mixed with Al_2O_3 sintered at 1400 °C after different heating durations: **(a)**, E6Z mixed with Al_2O_3; **(b)**, E2D2G2Z mixed with Al_2O_3; **(c)**, E2Y2D2Z mixed with Al_2O_3; **(d)**, E2Y2G2Z mixed with Al_2O_3.

As it is found that the thermal phase stability may be also related to the $c/a\sqrt{2}$ ratio in mono-rare earth oxide doped erbia-stabilised zirconia in section 5.3.2, the same relation is also proved in bi-rare earth oxides doped erbia-stabilised zirconia. In Table 5-5, E6Z has the lowest $c/a\sqrt{2}$ ratio among all specimens, so it presents the best thermal phase stability. In contrast, E2D2G2Z has the highest $c/a\sqrt{2}$ ratio, which shows the worst thermal phase stability.

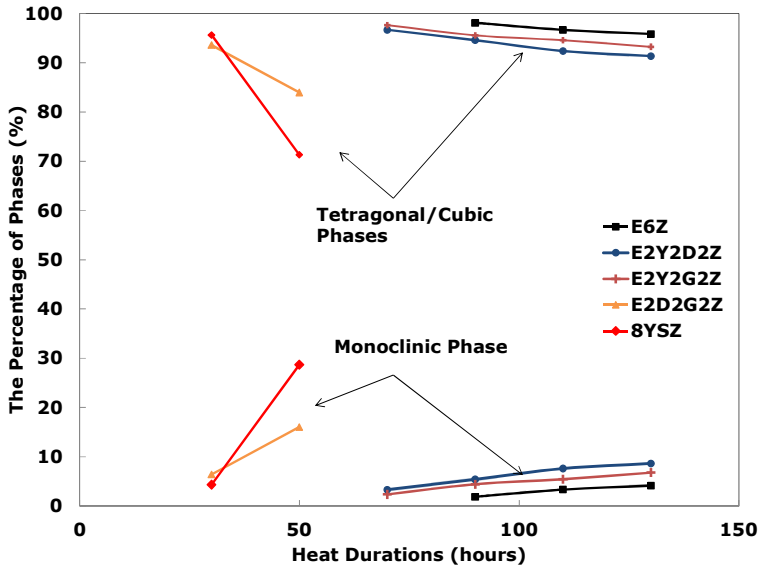

Figure 5-17: The ratios of tetragonal/cubic and monoclinic phases with different heating durations.

Furthermore, for rare earth oxides stabilised zirconia, cation diffusion cannot be independent of the defects in the crystal structure, which determines the activation energy of the diffusion process required. Generally, the cluster defects (substitutional defects and oxygen vacancies) in zirconia can suppress the movability of atoms, but in this work, the influence from oxygen

vacancies can be excluded, because the content of oxygen vacancies is fixed for all specimens as shown in Eq. (5-5).

Excluding the influence from oxygen vacancy, the diffusivities of dopants are mainly determined by the lattice distortion in crystal structure, which is caused by the difference in atomic mass and radius. Rebollo [193] suggested that increasing atomic size can raise the local distortion in crystals. The larger size the dopant ion is, the more local distortion it creates, and then it is much easier for dopant to diffuse to form the cubic phase. Therefore, it is found that E6Z with the lowest local distortion exhibits the best thermal phase stability. As Gd^{3+} and Dy^{3+} have relatively larger radii, the thermal phase stability of Gd_2O_3 and Dy_2O_3 doped Er_2O_3-stabilised ZrO_2 is the worst. But by introducing the small Yb^{3+} ions to minimise the local distortion of oxygen lattice, the thermal phase stabilities of E2Y2G2Z and E2Y2D2Z are similar but much better than that of E2D2G2. Therefore, zirconia stabilised by dopants with small radii could be applied at temperatures above 1250 ^{o}C, when the crystal phase is the non-transformable tetragonal phase *t'*.

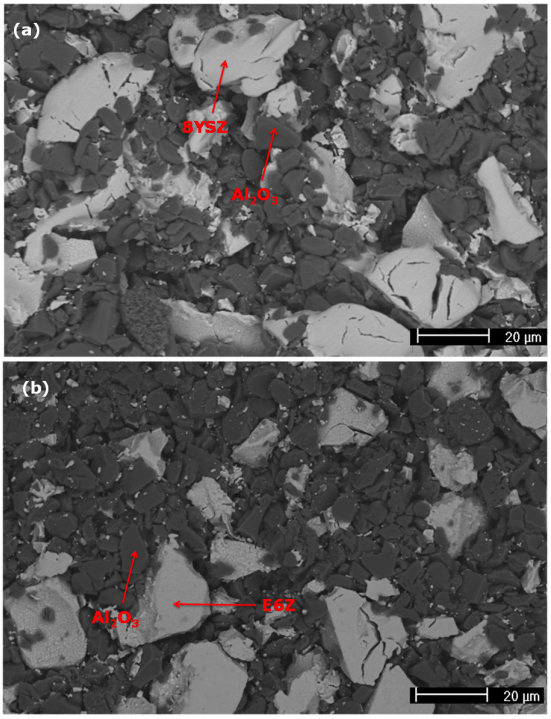

Figure 5-18: The microstructure of 8YSZ+Al_2O_3 **(a)** and E6Z+Al_2O_3 **(b)** sintered at 1400 ^oC for 10 h.

Moreover, the grain size of stabilised zirconia can also be used to understand the diffusion rates of cations. Figure 5-18 **(a)** and **(b)** exhibit the microstructure of 8YSZ and E6Z with Al_2O_3, respectively. The alumina particles are distributed around stabilised zirconia particles and the pellets are relatively porous. The particle size of Al_2O_3 is smaller than the stabilised zirconia, so the alumina particle can barely affect the grain growth of stabilised zirconia. Therefore, it is very important to study the grain size of stabilised zirconia before and after heat-treatment.

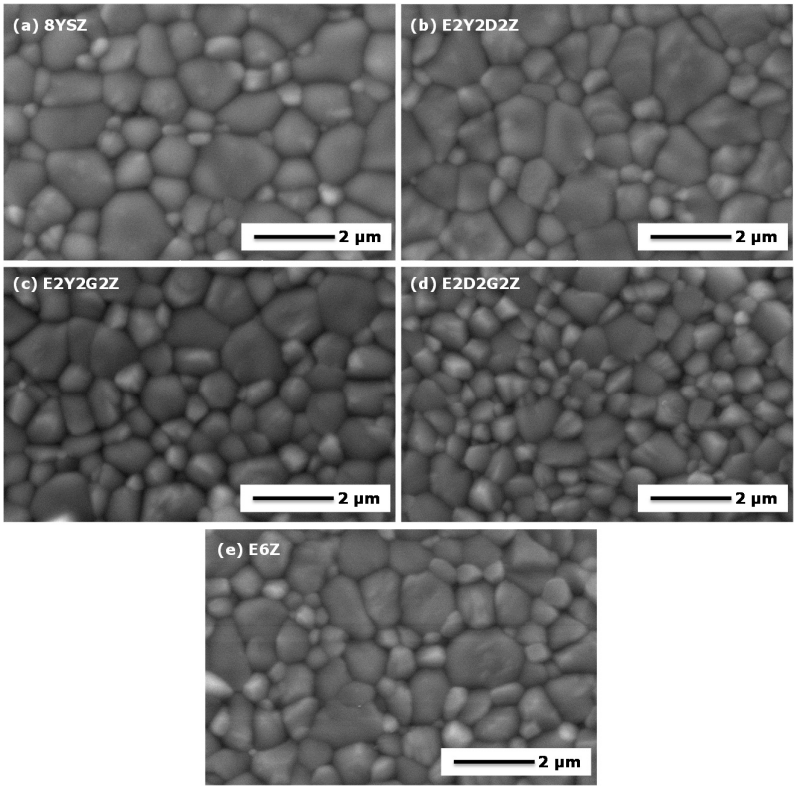

Figure 5-19: The SEM images taken from the surface of pellet 8YSZ **(a)**, E2Y2D2Z **(b)**, E2Y2G2Z **(c)**, E2D2G2Z **(d)** and E6Z **(e)** without alumina sintered at 1400 ^{o}C for 6 h.

The grain sizes of stabilised zirconia without alumina and with alumina heat-treated at 1400 ^{o}C for different durations are demonstrated from Figure 5-19 to Figure 5-21. In Figure 5-19, SEM images of specimen 8YSZ, E2Y2D2Z, E2Y2G2Z, E2D2G2Z and E6Z without alumina show similar average grain size, around 1.3 µm. E2D2G2Z has slightly smaller grain size than other materials, but this minor difference in grain size may not have significant influence on the phase stability. From Figure 5-20 and Figure 5-21, it is found that the average grain sizes of E6Z and 8YSZ in mixed pellets increase with the increased heating

durations at 1400 °C. When the stabilised zirconia in mixed pellets are heat treated at 1400 °C for 10 h, the average grain sizes of 8YSZ and E6Z in mixed pellets are quite similar to those heated for 6 h without alumina [Figure 5-19 **(a)** and **(e)**].

Additionally, the grain sizes of both E6Z and 8YSZ in mixed pellets are quite similar to each other, either from the short heat treatment (*i.e.* 10 h), or long heat treatment (50 h). It could be deduced that, with similar grain size after 6 h heating [Figure 5-19 **(b)** and **(c)**], E2Y2D2Z and E2Y2G2Z could also exhibit similar grain sizes after the same heating durations. E2D2G2Z shows slightly smaller grain size, which may influence the diffusivity of cations. Overall, the effect of grain size on cation diffusion could not be a governing factor in this particular case.

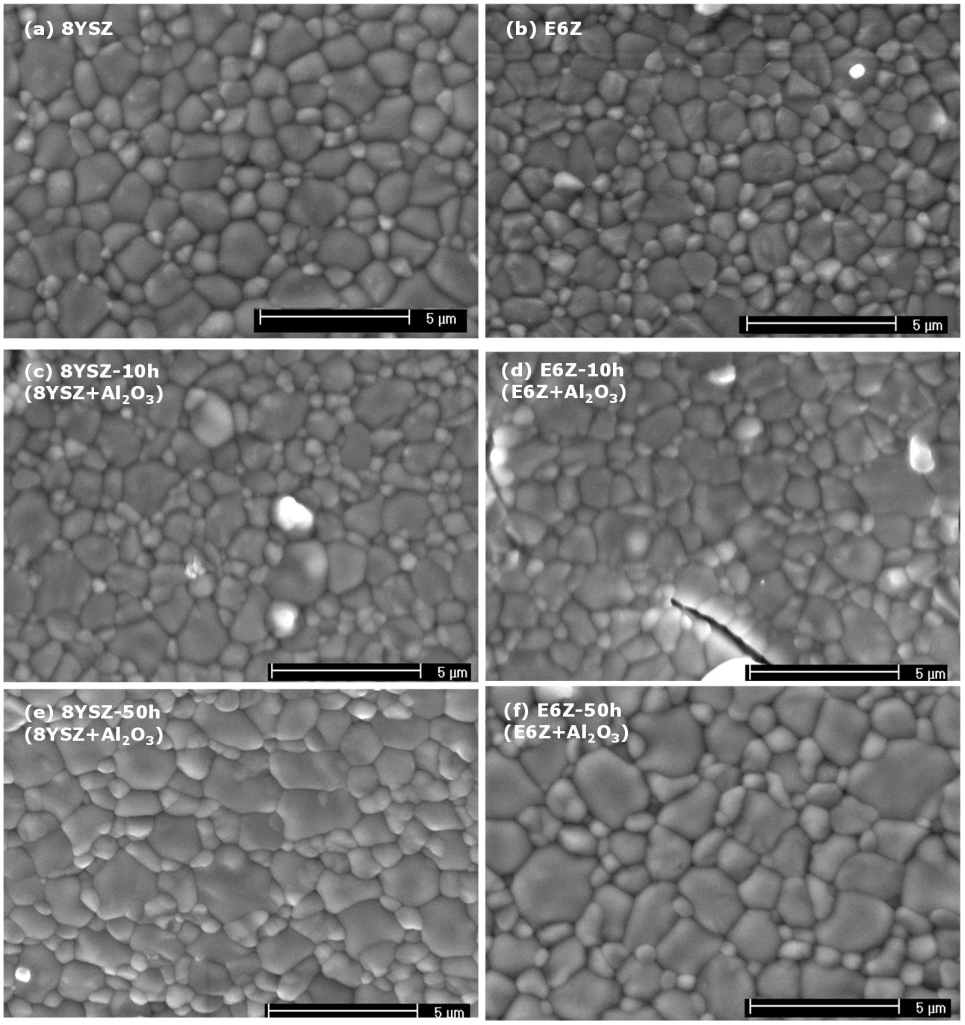

Figure 5-20: SEM images of 8YSZ **(a)** and E6Z **(b)** sintered at 1400 °C for 6 h, and also the images of 8YSZ and E6Z in the mixed pellet, where **(c)** and **(e)** are the grain sizes of 8YSZ at 1400 °C for 10 and 50 h; **(d)** and **(f)** are the grain sizes of E6Z at 1400 °C for 10 and 50 h.

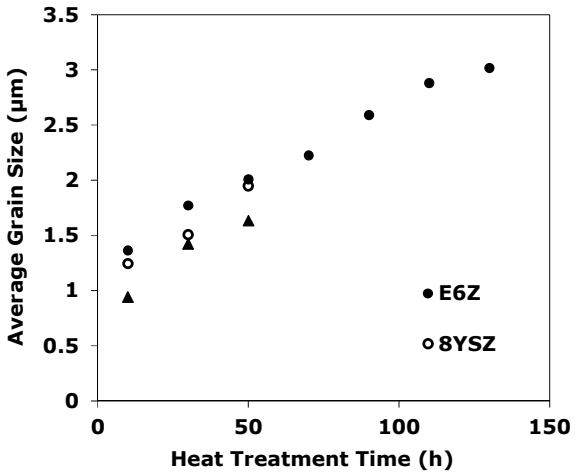

Figure 5-21: The average size of E6Z and 8YSZ versus the different heating durations at 1400 °C.

5.4.3 Thermal Conductivity and Coefficient of Thermal Expansion

5.4.3.1 Thermal Conductivity

Thermal conductivity and theoretical density of stabilised zirconia are presented in Figure 5-22. The densities of E6Z, E2Y2D2Z, E2Y2G2Z and E2D2G2Z are 6.46, 6.47, 6.44 and 6.41 $g \cdot cm^{-3}$, respectively. The thermal conductivity of E6Z, E2Y2D2Z, E2Y2G2Z and E2D2G2Z are 1.40 $W \cdot m^{-1} \cdot K^{-1}$, 1.31 $W \cdot m^{-1} \cdot K^{-1}$, 1.60 $W \cdot m^{-1} \cdot K^{-1}$ and 1.34 $W \cdot m^{-1} \cdot K^{-1}$, respectively, which is lower than that of conventional 8YSZ.

As mentioned in section 5.3.3, Eq. (5-4) is applied to understand the decrease of thermal conductivity in mono-rare earth oxide doped erbia-stabilised zirconia, and it also can be used for bi-rare earth oxide doped erbia-stabilised zirconia. But for bi-rare earth

oxide doped erbia-stabilised zirconia, because k_v, k_c, k_m and k_r are relatively different, this difference causes the variation of thermal conductivity.

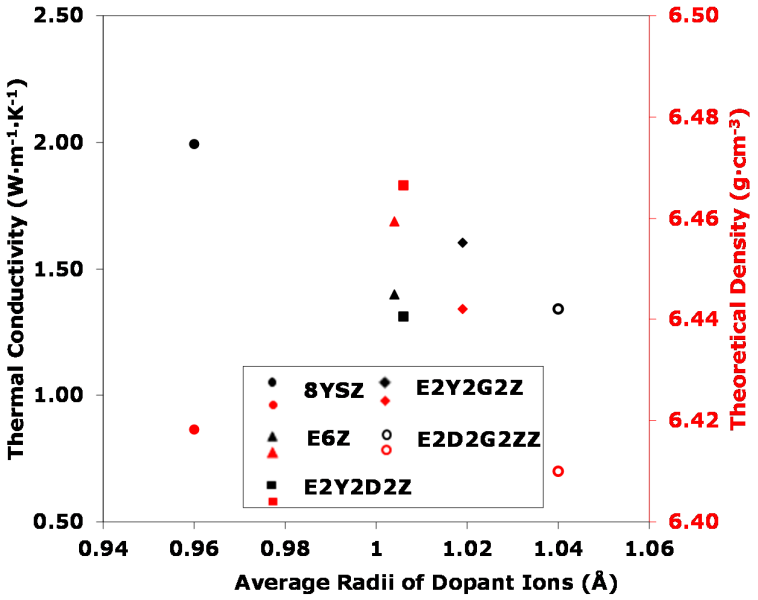

Figure 5-22: The thermal conductivity (in black) and theoretical density (in red) of bi-rare earth doped erbia-stabilised zirconia against average radii of dopant ions.

The thermal conductivity of bi-rare earth doped erbia-stabilised zirconia is slightly smaller than that of mono-rare earth erbia-stabilised zirconia. For the bi-rare earth doped erbia-stabilised zirconia, there is relatively higher content of oxygen vacancy than that in mono-rare earth erbia-stabilised zirconia, which can further reduce k_v. But this decrement is same for E6Z, E2Y2D2Z, E2Y2G2Z and E2D2G2Z, because the total doping concentration is fixed at 6 mol%. The variant thermal conductivity of E6Z, E2Y2D2Z,

E2Y2G2Z and E2D2G2Z is mainly related to k_c, k_m and k_r. The difference of atomic mass and radius can decrease thermal conductivity, accordingly.

5.4.3.2 Coefficients of Thermal Expansion

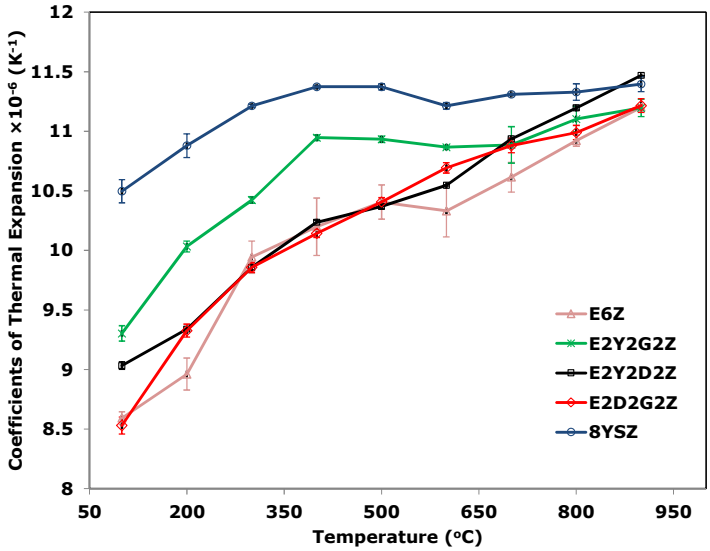

Figure 5-23: The coefficients of thermal expansion of bi-rare earth oxide doped erbia-stabilised zirconia against temperature.

Figure 5-23 presents the coefficients of thermal expansion (CTEs) of bi-rare earth doped erbia-stabilised zirconia in the range of 100 °C-900 °C. There is no significant difference between E6Z, E2Y2D2Z, E2Y2G2Z and E2D2G2Z, and the CTEs are in the range of 9.0-11.5 × 10^{-6} K^{-1} at the temperature range of 100 °C-900 °C. In addition, their CTEs are very similar to that of mono-rare earth doped erbia-stabilised zirconia in section 5.2.3.2.

5.5 Summary

For the consideration of increasing potential operational temperature and engine power efficiency, erbia-stabilised zirconia, and mono- and bi-rare earth doped erbia-stabilised zirconia (the range of total doping content is from 4 mol% to 6 mol%) were investigated at 1400 ^{o}C to replace the conventional 7-8YSZ. For erbia-stabilised zirconia, thermal conductivity decreases with the increase of doping concentration of erbia and also good thermal phase stability is found with high content of erbia.

For mono- and bi-rare earth doped erbia-stabilised zirconia, the TEM images indicate the grain sizes of as-synthesised powders do not exceed 50 nm. The XRD results confirm that the powders have the non-transformable tetragonal phase distinguished from (004) and (400) peaks. Moreover, good thermochemical compatibility with alumina is confirmed at 1400 ^{o}C. Additionally, all specimens exhibit much lower thermal conductivities than conventional 8YSZ and also they have comparable coefficients of thermal expansion with 8YSZ.

In addition, the thermal phase stability of E6Z, E2Y2D2Z and E2YE2G2Z are much better than the other studied materials. Most materials show better thermal phase stability than conventional 8YSZ, especially E6Z. Meanwhile, the mole percentage of monoclinic phase in 4 mol% Er_2O_3 doped erbia-stabilised zirconia is only 1.88% after heat treatment at 1400 ^{o}C for 90 h, and it just rises to 4.16% after 130 h. Because the transforming rates to

monoclinic phase are very slow, it indicates that Er^{3+} and Yb^{3+} ions have relatively lower diffusivities than Y^{3+} ion in 8YSZ.

Furthermore, it is found that the thermal phase stabilities of these candidate materials are mainly related to the $c/a\sqrt{2}$ ratio, which indicates that the cation diffusion is also dependent on crystal structure of stabilised zirconia. When the lattice parameter *c* increases more quickly than lattice parameter *a* (*a*=*b*), the $c/a\sqrt{2}$ ratio also increases, which can promote the diffusion of cations in *t´*-phase; otherwise, slightly decreased $c/a\sqrt{2}$ ratio can slow down cation diffusivity. When the $c/a\sqrt{2}$ ratio is around 1.01, such as E2.5D2.5Z and E2.5G2.5Z, they show the worst thermal phase stability. When the $c/a\sqrt{2}$ ratio decreases to around 1.006, like E2Y2D2Z, E2YE2G2Z and E6Z, they have much better thermal phase stability. The best $c/a\sqrt{2}$ ratio investigated in R_2O_3+Er_2O_3 stabilised zirconia is around 1.006.

Chapter 6. The Effects of Rare Earth Elements on Thermal Conductivity and Thermal Expansion of Yttrium Aluminium Garnet

6.1 Introduction

The thickness of thermally grown oxides (TGO) increases when thermal barrier coatings (TBCs) are exposed in oxidizing thermal environment during operation. It is suggested that the thickness of TGO is usually in the range of 6 to 7 μm and certainly cannot exceed 10 μm to avoid the spallation of ceramic top-coat [7]. The oxygen for growing TGO usually comes from ceramic material as top-coat, which means that a new TBCs candidate is better to have low oxygen diffusivity. Low oxygen diffusion can slow down the growing rate of TGO layer and increase thermal cycling life time. Yttrium aluminium garnet [$Y_3Al(1)_2Al(2)_3O_{12}$, YAG] has extremely low oxygen diffusivity (10^{-25} $m^2 \cdot s^{-1}$), which is about 10 orders of magnitude lower than that of yttria stabilised zirconia (10^{-10}~10^{-11} $m^2 \cdot s^{-1}$) [17]. Meanwhile, YAG shows excellent phase stability after long term exposure, and has only slightly higher thermal conductivity and lower coefficient of thermal expansion than conventional yttria stabilised zirconia [17, 135-139]. So far, the study of YAG for TBCs application is mainly based on un-doped YAG, to construct TBCs bilayer consisting of porous YSZ with YAG top layer [17, 137, 194]. Liu *et al*. found that Er doped YAG on dodecahedral sites can reduce thermal conductivity although there is a decrease in CTE [143]. Overall, YAG could be a good candidate for TBCs application.

In $Y_3Al(1)_2Al(2)_3O_{12}$, there are three type polyhedrons, dodecahedra, octahedra and tetrahedra shown in Figure 6-1, where Y^{3+} ions are on dodecahedral sites (24c), $Al^{3+}(1)$ and $Al^{3+}(2)$ ions are on octahedral (16a) and tetrahedral sites (24d), respectively [142]. The purpose of this chapter is to investigate the effects of dodecahedron and octahedron on thermal conductivity and thermal expansion in YAG.

Because the space inside the octahedra is relatively small, Yb^{3+} with the smallest ionic radial size in the lanthanide series has been selected to be doped on dodecahedral and octahedral sites to investigate the effects on thermal conductivity and thermal expansion. In YAG, if the doping site is different, the ionic radius of Yb^{3+} changes with the numbers of neighbouring oxygens, called coordination numbers. When the coordination number is 8 for a dodecahedron, the ionic radius of Yb^{3+} (0.985 Å) is to replace host Y^{3+} ion with the small ionic radius of (1.019 Å) [155, 195]. For a octahedron, the coordination number is 6, so Yb^{3+} with larger ionic radius (0.868 Å) is to replace host Al^{3+} ion (0.535 Å) [187, 196]. Therefore, it is expected that this radial difference will significantly influence thermal conductivity and thermal expansion by causing the distortion of polyhedrons (section 6.2).

Furthermore, La^{3+} ions will be introduced on dodecahedral sites to understand the influences from the difference in atomic mass and ionic radius (section 6.3). The radius of La^{3+} ions (1.16 Å) is larger than that of Y^{3+} ions [196] and also they have large difference in atomic mass, which may increase the coefficient of thermal expansion, not just reduce thermal conductivity.

Moreover, the difference of atomic mass can also strongly scatter phonons to reduce thermal conductivity [197]. In order to study the influence caused by the difference in atomic mass, it is necessary to find a dopant that has similar radius to host Y^{3+} ion, but big atomic mass difference. So Er^{3+} ion is chosen due to its similar radius (1.004 Å) as Y^{3+} ion, and heavier atom mass (167.26 u) than that of Y^{3+} ion (88.906 u). Therefore, the thermal properties of Er^{3+} ions doped YAG are investigated in section 6.4.

Overall, rare earth elements doped YAGs on dodecahedral sites or octahedral sites are investigated in this chapter, in order to understand the reduction of thermal conductivity and the increase or decrease of coefficient of thermal expansion.

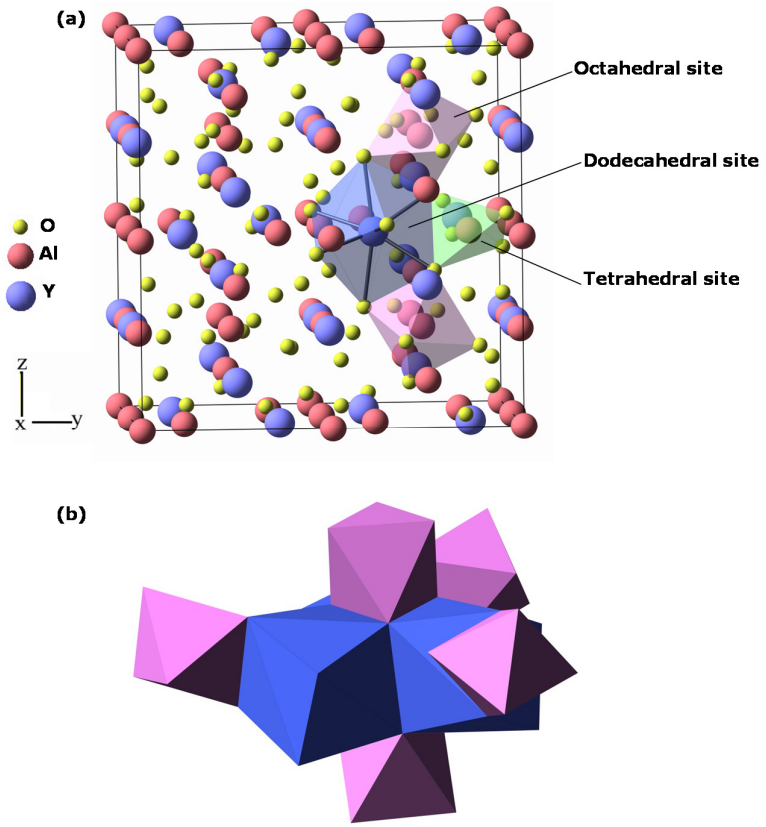

Figure 6-1: **(a)** Crystal structure of Yttrium aluminium garnet, in which there are three type polyhedrons: dodecahedra, octahedra and tetrahedra; **(b)** one octahedron sharing its three edges with three different shared-edge dodecahedra.

6.2 Yb^{3+} Ions Doped on Dodecahedral or Octahedral Sites in YAG

This section mainly involves studies of the effect on thermal conductivity and coefficient of thermal expansion by introducing the small Yb^{3+} ions in dodecahedra to replace host Y^{3+} ions or in octahedra to replace host Al^{3+} ions. The mole ratios of chemical

elements and the descriptions of the compositions are exhibited in Table 6-1.

Table 6-1: The mole ratios of chemical elements in stoichiometric composition.

Stoichiometric composition	Chemical element (mole ratio: Y/Al/Al/Yb)			
	Y	Al (in octahedra)	Al (in tetrahedra)	Yb
$Y_3Al_2Al_3O_{12}$ (YAG)	3	2	3	0
$(Yb_{0.05}Y_{0.95})_3Al_2Al_3O_{12}$ (A1)	2.85	2	3	0.15
$(Yb_{0.15}Y_{0.85})_3Al_2Al_3O_{12}$ (A2)	2.55	2	3	0.45
$(Yb_{0.20}Y_{0.80})_3Al_2Al_3O_{12}$ (A3)	2.40	2	3	0.60
$Y_3(Yb_{0.005}Al_{0.995})_2Al_3O_{12}$ (B1)	3	1.99	3	0.01
$Y_3(Yb_{0.015}Al_{0.985})_2Al_3O_{12}$ (B2)	3	1.97	3	0.03
$Y_3(Yb_{0.020}Al_{0.980})_2Al_3O_{12}$ (B3)	3	1.96	3	0.04

6.2.1 Thermogravimetry and Differential Scanning Calorimetry (TG-DSC)

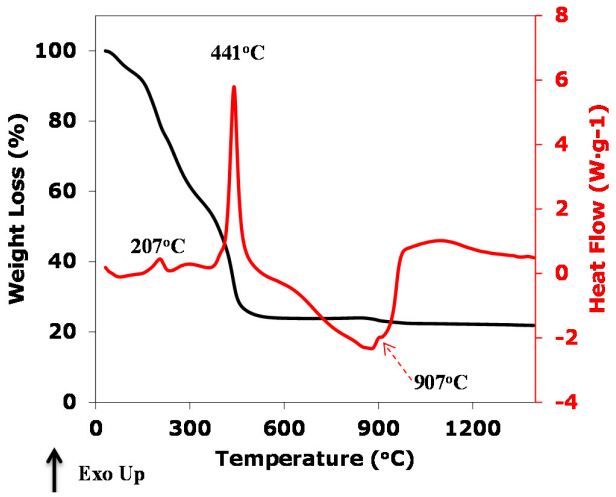

Figure 6-2: TG-DSC curves of dried synthesised gel heat-treated from room temperature to 1400 °C.

Figure 6-2 presents Thermogravimetry and Differential Scanning Calorimetry (TG-DSC) of the dried precursor from room temperature to 1400 °C with heating rate of 5 °C/min. The total weight loss is about 79.5% up to 900 °C. 78.0% mass loss occurs from around 100 °C to 490 °C, indicating the vaporization of absorbed water and the decompositions of C-and N-containing precursors. The corresponding DSC curve displays a relatively small exothermic peak and a sharp exothermic peak at 207 °C and 441 °C, respectively, which results from the release of molecular water and the pyrolysis of the precursor. Moreover, there is a small exothermic peak at 907 °C, which can be described as the crystallization of YAG from the amorphous phase.

6.2.2 Phase Analysis

6.2.2.1 XRD Results

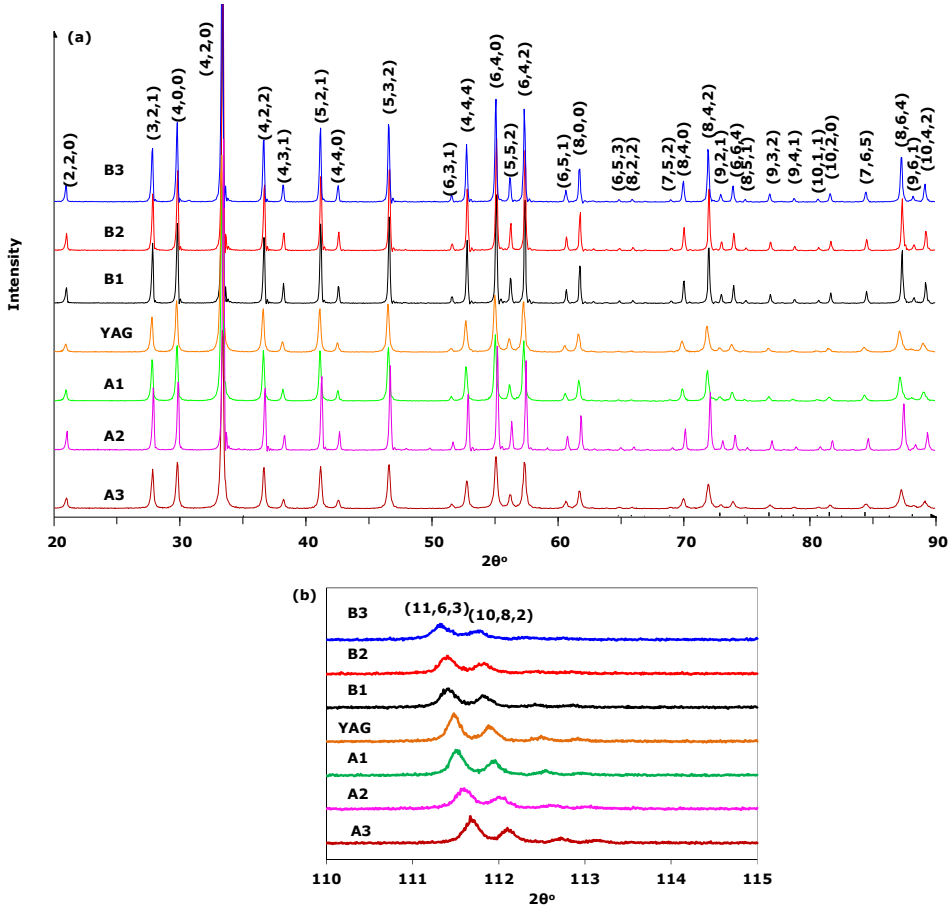

Figure 6-3: XRD patterns of Yb^{3+} ions doped on dodecahedral and octahedral sites in YAG and un-doped YAG powders **(a)** 2θ from 20 to 90°; **(b)** 2θ from 110 to 115°.

The XRD patterns of un-doped and doped YAG powders are presented in Figure 6-3. Figure 6-3 **(a)** demonstrates that no extra phase is observed and all materials exhibit a single cubic phase with space group Ia3d [166]. The peak shift is much easier to be

observed at high 2θ for Yb doped YAG, as shown in Figure 6-3 **(b):** peak (11,6,3) and (10,8,2) shift to higher 2θ from A1 to A3, when doping concentration x increases from 0.05 to 0.2 in $(Yb_xY_{1-x})_3Al_2Al_3O_{12}$ solid solution, which indicates that Yb^{3+} ions locate on the dodecahedral site and cause shrinkage of the crystal structure, due to the replacement of Y^{3+} ions in dodecahedra with relatively small Yb^{3+} ions. On the contrary, peaks (11,6,3) and (10,8,2) slightly shift to lower 2θ from B1 to B3 when doping concentration x increases from 0.005 to 0.02 in $Y_3(Yb_xAl_{1-x})_2Al_3O_{12}$ solid solution. Therefore, it is confirmed that Yb^{3+} ions are doped on the octahedral site which results in the expansion of the crystal structure, due to the replacement of Al^{3+} ions in octahedra with the relatively large Yb^{3+} ions.

6.2.2.2 Rietveld Refinement

In Figure 6-4 and Figure 6-5, the calculated results are well fitted with experimental XRD patterns after the Rietveld Refinement, and the obtained lattice constant is shown in Figure 6-6. As YAG has the cubic phase, *a* equals to *b* and *c*. The lattice constant of un-doped YAG is 12.0116 Å in this work, which is slightly larger than the value (12.0089 Å) reported by Carda *et al.* (JCPDS 33–40) [166]. If the Yb^{3+} ions occupy sites in dodecahedra, due to the slightly smaller ionic radius compared with Y^{3+} ions, distortion would occur in the dodecahedra, and generate shrinkage in order to achieve a stabilised crystal structure. The lattice constant *a* decreases from 12.0088 to 11.9968 Å with the increased doping

concentration, which further confirms that Yb^{3+} ions enter dodecahedral sites in $(Yb_xY_{1-x})_3Al_2Al_3O_{12}$ solid solution. Conversely, the crystal structure expands when the dopant is located on octahedral sites due to its relatively large radius, and *a* increases from 12.0164 to 12.0220 Å, which also proves that Yb^{3+} ions are doped in octahedral sites in $Y_3(Yb_xAl_{1-x})_2Al_3O_{12}$ solid solution.

For specimen B2 with 1.5 mol% doping concentration on octahedral sites, its lattice constant slightly increases compared with the specimen with 0.5 mol% doping concentration. The result indicates that a very small amount of Yb^{3+} ions may enter dodecahedral sites then cause the shrinkage of crystal structure.

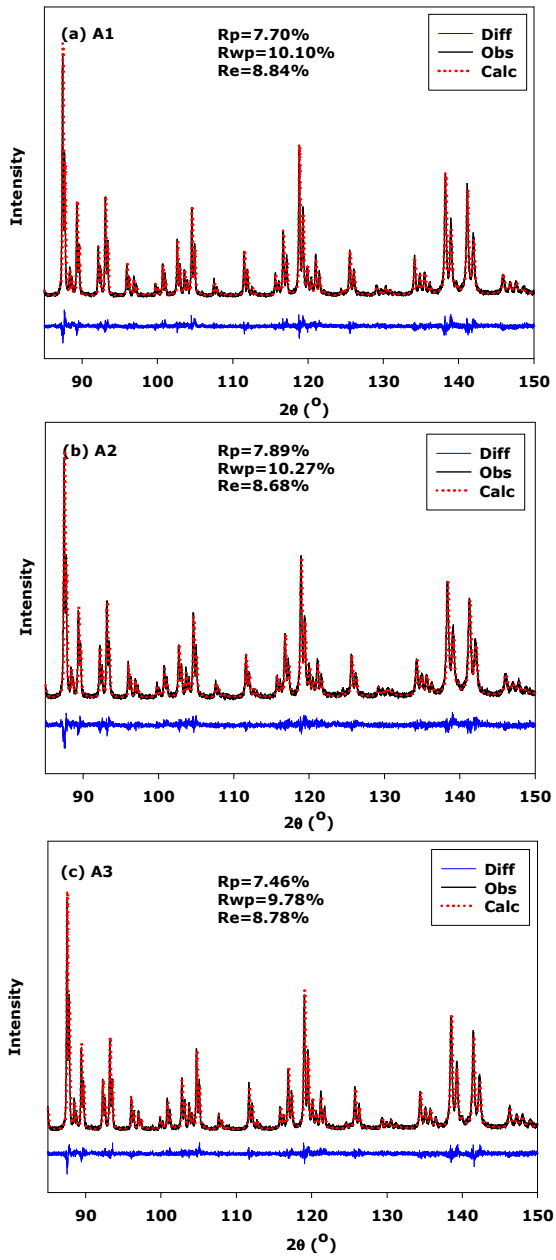

Figure 6-4: Good agreement between the calculative simulation results and the experimental XRD data for refining unit cell of ceramics $(Yb_{0.05}Y_{0.95})_3Al_2Al_3O_{12}$ **(a)**, $(Yb_{0.15}Y_{0.85})_3Al_2Al_3O_{12}$ **(b)** and $(Yb_{0.20}Y_{0.80})_3Al_2Al_3O_{12}$ **(c)**, where Diff refers to the difference between the calculative (Calc) and observed (Obs) data.

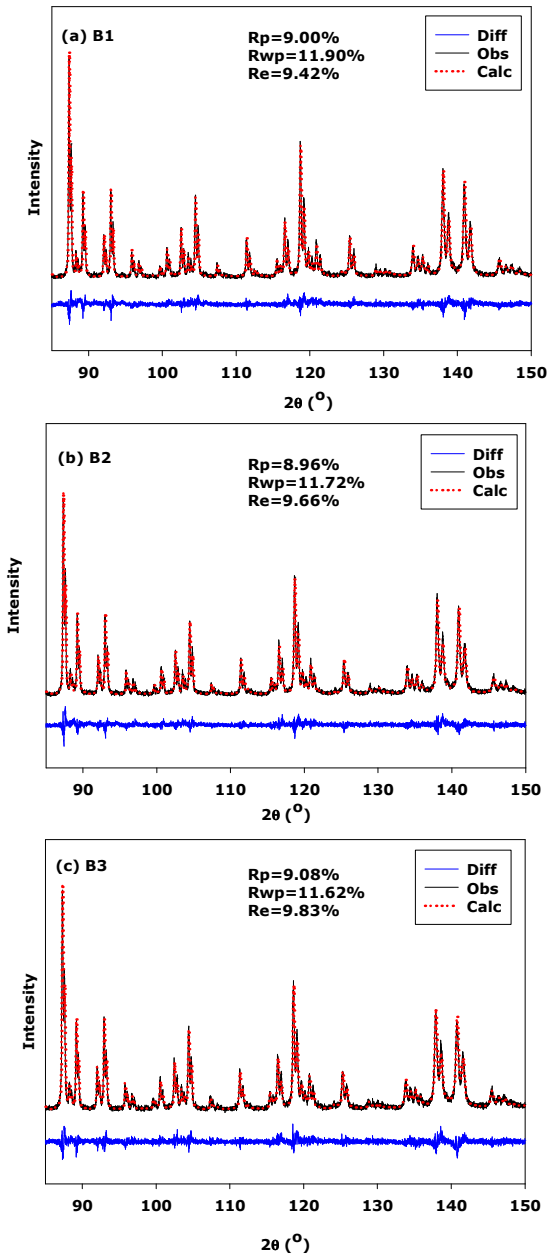

Figure 6-5: Good agreement between the calculative simulation results and the experimental XRD data for refining unit cell of ceramics $Y_3(Yb_{0.005}Al_{0.995})_2Al_3O_{12}$ **(a)**, $Y_3(Yb_{0.015}Al_{0.985})_2Al_3O_{12}$ **(b)** and $Y_3(Yb_{0.020}Al_{0.980})_2Al_3O_{12}$ **(c)**, where Diff refers to the difference between the calculative (Calc) and observed (Obs) data.

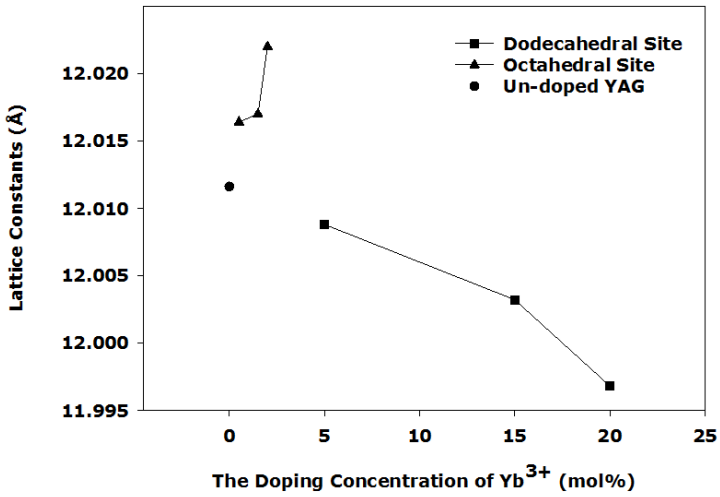

Figure 6-6: The change of lattice constant with Yb^{3+} doping concentration in YAG.

6.2.3 Microstructure of As-Sintered Pellets

The grain sizes of doped YAG pellets are investigated from their SEM images as shown in Figure 6-7. The grain sizes in all studied pellets are in the range of 100 nm to 600 nm. The calculated porosities from Eq. (3-4) and Eq. (3-5) in Chapter 3 are around 35%, and pores have been observed in each material. The recrystallization (marked as the red circled regions) also occurs in these materials, which would result from the diffusion of ions. Additionally, more regions of gain growth appear in the specimens with higher doping concentrations either on dodecahedral or octahedral sites.

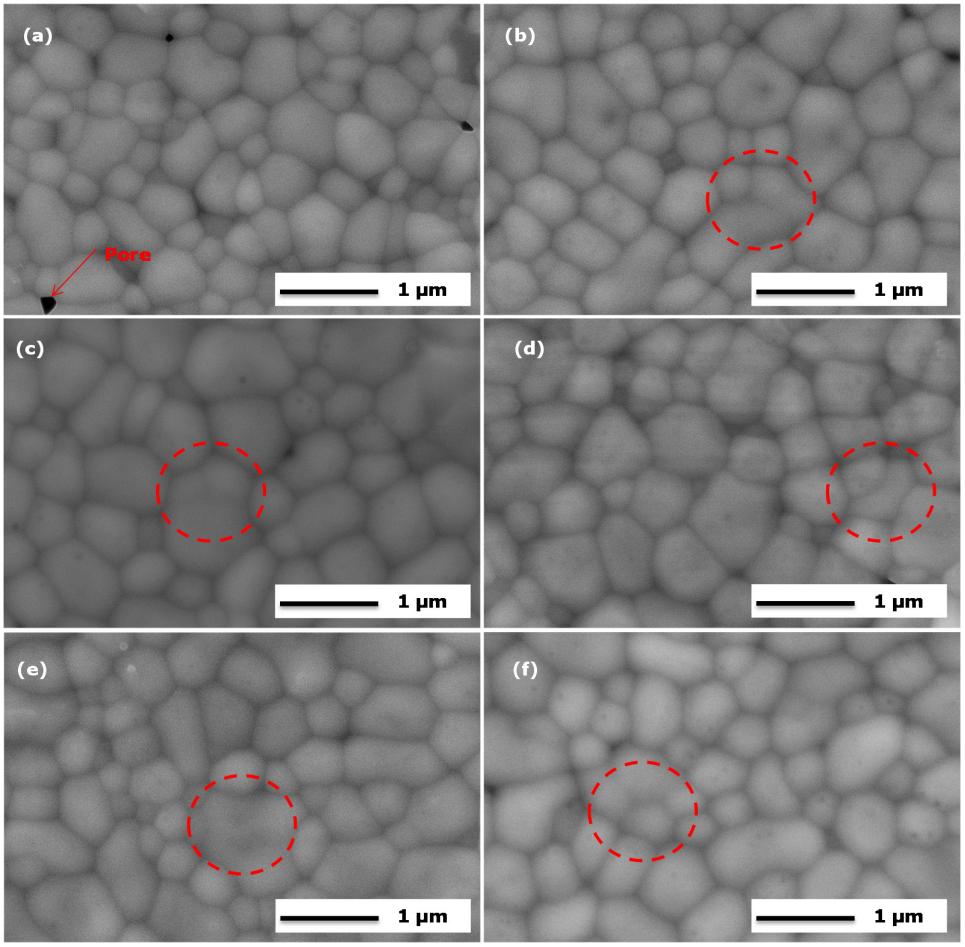

Figure 6-7: The SEM images of Yb^{3+} ions doped on dodecahedral and octahedral sites in YAG and YAG pellets: **(a)** $(Yb_{0.05}Y_{0.95})_3Al_2Al_3O_{12}$; **(b)** $(Yb_{0.15}Y_{0.85})_3Al_2Al_3O_{12}$; **(c)** $(Yb_{0.2}Y_{0.8})_3Al_2Al_3O_{12}$; **(d)** $Y_3(Yb_{0.005}Al_{0.095})_2Al_3O_{12}$; **(e)** $Y_3(Yb_{0.015}Al_{0.085})_2Al_3O_{12}$; **(f)** $Y_3(Yb_{0.02}Al_{0.08})_2Al_3O_{12}$.

6.2.4 Thermal Properties

6.2.4.1 Thermal Conductivity

The thermal conductivities and theoretical densities of doped and un-doped YAG are shown in Figure 6-8. The theoretical density of

un-doped YAG (4.55 $g \cdot cm^{-3}$) is very close to the reported data (4.56~4.57 $g \cdot cm^{-3}$) [198, 199]. Furthermore, the theoretical density of doped YAG increases with the increasing doping concentration of Yb^{3+} ions which have a relatively heavy atomic mass compared with Y^{3+} ions. In addition, the thermal conductivity of un-doped YAG is 3.28 $W \cdot m^{-1} \cdot K^{-1}$ at room temperature, similar to the value reported by Padture (3.2 $W \cdot m^{-1} \cdot K^{-1}$) [70] and it is relatively high for thermal barrier application. When the doping concentration of Yb^{3+} ion in dodecahedra is in the range of 5 mol% to 20 mol%, the thermal conductivity decreases from 2.31 $W \cdot m^{-1} \cdot K^{-1}$ to 2.09 $W \cdot m^{-1} \cdot K^{-1}$, which is much lower than un-doped YAG. Furthermore, the thermal conductivity is reduced from 2.38 $W \cdot m^{-1} \cdot K^{-1}$ to 2.11 $W \cdot m^{-1} \cdot K^{-1}$, when the doping concentration increases from 0.5 mol% to 2 mol% in octahedra. It is suggested that the thermal conductivity is efficiently reduced by introducing Yb^{3+} ions in octahedra rather than in dodecahedra.

The thermal conductivity Eq. (6-1) for doped YAG is optimised from Eq. (5-2), by adding substituting defect scattering (k_d) instead of oxygen vacancy scattering and defect cluster scattering.

$$k_o = k_i - (k_U + k_{gb} + k_d + k_m + k_r) \qquad \text{Eq. (6-1)}$$

In a dodecahedral site, one Y atom is surrounded by 8 oxygen atoms, so the ionic radius of Y^{3+} is 1.019 Å [155], while the radius of Yb^{3+} ion with 8 coordination is 0.985 Å [155], which is slightly smaller than that of the host Y^{3+} ion. Because the Yb^{3+} ions are relatively small to stay in the centre of dodecahedra, it could lead to the distortion of the dodecahedra for the structural stabilisation.

Nevertheless, this radial difference between Yb^{3+} and Y^{3+} ions is only 0.034 Å, thus the distortion is indistinct and does not have strong influence on the structures of neighbouring dodecahedra and octahedra. Therefore, with higher doping concentration than that doped on octahedral sites, Yb^{3+} ions doped on dodecahedra only exhibits a slight decrease of thermal conductivity.

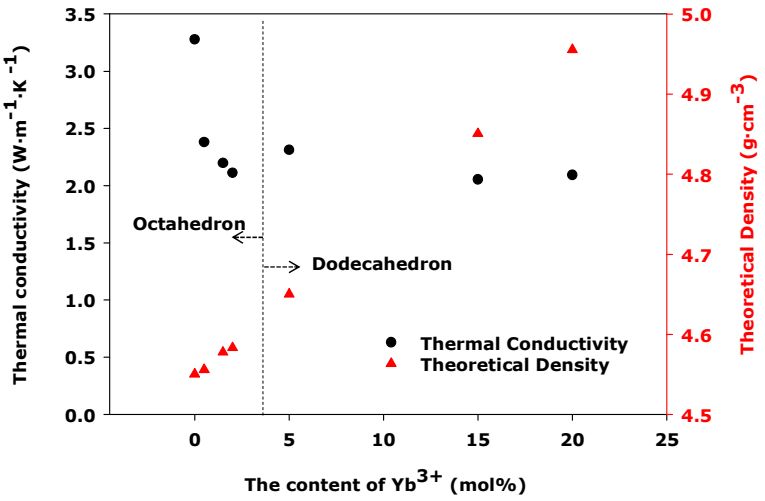

Figure 6-8: Thermal conductivities of Yb^{3+} ions doped on dodecahedra and octahedra in YAG and un-doped YAG at room temperature and the theoretical densities of ceramic pellets.

However on an octahedral site, the radial difference between Yb^{3+} and Al^{3+} ions is 0.333 Å, which is much larger compared with the difference (0.034 Å) between Yb^{3+} and Y^{3+} ions. The large size difference causes the octahedra to expand significantly due to the relatively large radius of Yb^{3+} ions. Moreover, this expansion can also compress the adjacent dodecahedra structures. Therefore, it

is found that doping Yb^{3+} ions in octahedra can more effectively reduce thermal conductivity than those in dodecahedra.

6.2.4.2 Coefficients of Thermal Expansion

The coefficients of thermal expansion of un-doped and doped YAGs are plotted in Figure 6-9. It is observed that the dopants do not have significant effect on thermal expansion below 300 ^{o}C whether they are in dodecahedra or octahedra. In Figure 6-9 **(a)**, the coefficient of thermal expansion of un-doped YAG is $7\sim10\times10^{-6}$ K^{-1} from 100 ^{o}C to 950 ^{o}C and the CTEs at low temperatures are very similar to the value reported by Klein ($\sim8\times10^{-6}$ K^{-1}) [199]. When introducing relatively small Yb^{3+} ions in dodecahedra, the structure can generate distortion and slightly shrink simultaneously, which creates variation of the interatomic spacing and has a negative effect on thermal expansion of YAG. When the doping concentration is 5 mol%, the values of CTEs are dramatically reduced to 8.5×10^{-6} K^{-1} at high temperatures. With the increasing doping concentration, CTEs increase and become comparative to that of un-doped YAG. Additionally, it is also observed that the CTEs increase quickly below 300 ^{o}C, whereas they change very slowly from 300 to 950 ^{o}C.

Figure 6-9 **(b)** gives the CTEs of Yb^{3+} doped on octahedral site, which increase with the increase of the Yb^{3+} doping concentration. When the doping concentrations are 0.5 mol% and 1.5 mol%, the CTE shows slightly lower values than that of un-doped YAG at high temperatures. The CTEs of specimen B2 only slightly increase

compared with specimen B1, which could result from some Yb^{3+} ions occupying different sites or interstitial space.

When the doping concentration increases to 2.0 mol%, CTEs of ceramic B3 are over 10×10^{-6} K^{-1} at temperatures above 800 ^{o}C, which is higher than that of un-doped YAG. The doping concentration in octahedra is much lower than that in dodecahedra, but the dopants in octahedral sites have a significant effect on increasing the coefficient of thermal expansion.

Therefore, Yb^{3+} ions as dopant in octahedra can effectively reduce thermal conductivity and also increase the coefficient of thermal expansion, rather than in dodecahedra. Similarly in future work, if doping in dodecahedral sites, it is suggested to select a dopant with ionic radius larger than the host Y^{3+} ion to effectively reduce thermal conductivity and increase the coefficient of thermal expansion of YAG.

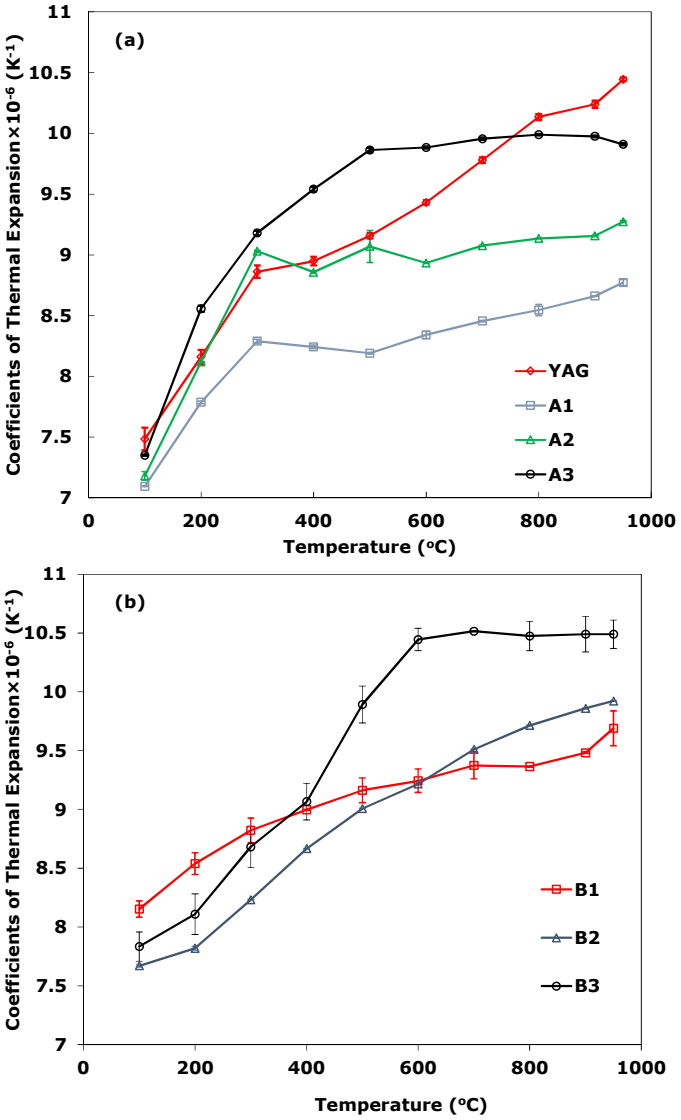

Figure 6-9: The change of CTEs with different doping content of Yb^{3+} ions on dodecahedral or octahedral sites: **(a)** The CTEs of A1, A2, A3 and YAG from 100 °C to 950 °C; **(b)** The CTEs of B1, B2 and B3 from 100 °C to 950 °C.

6.3 La^{3+} Ions on Dodecahedral Sites in YAG

In the previous section, it is found that Yb^{3+} ions doped in dodecahedra or octahedra in YAG can significantly reduce thermal conductivity, but the coefficients of thermal expansion only increase when Yb^{3+} ions are on dodecahedral sites. The increase of CTE is related to the larger radial size of Yb^{3+} ions compared with Al^{3+} ions in octahedra. Therefore, it is also assumed that if a dopant has larger radius than Y^{3+} ions, it may increase the coefficients of thermal expansion and also decrease thermal conductivity.

Therefore, La^{3+} ions (1.16 Å) are selected as a dopant on dodecahedral site, as they have the largest ionic radius in the lanthanides group, which is larger than host Y^{3+} ions and can be used for investigating whether it could increase the coefficients of thermal expansion for YAG.

6.3.1 Phase Analysis

The synthesised powders are characterised to investigate the crystal structure of La^{3+} ions doped YAG on the dodecahedral sites. Figure 6-10 shows the XRD patterns of La^{3+} ions doped YAG. The second phase $LaAlO_3$ with perovskite crystal structure is clearly observed when the doping concentration is 0.05 mol% and the content of $LaAlO_3$ phase rises with increasing the doping concentration.

Because the ratio of Y(La)/Al in YAG is 3/5 and the ratio of La/Al in $LaAlO_3$ is 1/1, some Al^{3+} ions have been left even after the formation of YAG and $LaAlO_3$ (as shown in Table 6-2), but there is no peak to indicate the possible phase of residual Al^{3+} ions. From the enlarged image in Figure 6-10, the peak of specimen with La^{3+} ions shifts to high 2θ compared with un-doped YAG, which means that the crystal structure shrinks for stabilisation. Therefore, these residual Al^{3+} ions may enter into dodecahedra or the interstice between dodecahedra due to their small radial sizes. Meanwhile, it is confirmed that most La^{3+} ions do not enter dodecahedra to form $(La_xY_{1-x})_3Al_2Al_3O_{12}$ solid solution.

Table 6-2: The mole percentage of La^{3+} ions and Al^{3+} ions.

M (La^{3+} ions)	M′ (Al^{3+} ions)	M′′ (Al^{3+} ions)
0.15	0.25	0.10
0.45	0.75	0.30
0.60	1.00	0.40

Note: **M:** The total doping concentration of La^{3+} ions (mol%); M′: The total residual percentage of Al^{3+} ions after forming YAG (mol%); M′′: The residual percentage of Al^{3+} ions after forming YAG and $LaAlO_3$ (mol%).

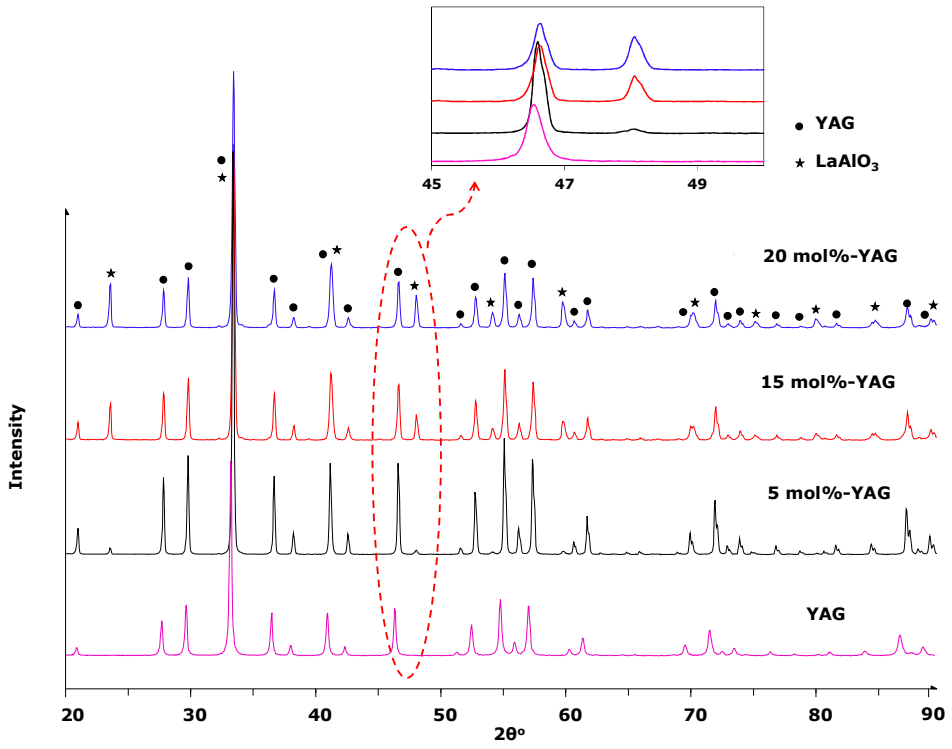

Figure 6-10: XRD patterns of La^{3+} ions doped on dodecahedral sites in YAG, where the slight shift of peaks to high 2θ is observed from the enlarged image.

Figure 6-11 and Figure 6-12 show phase diagrams of La_2O_3-Al_2O_3 and Y_2O_3-Al_2O_3 [200, 201]. In Figure 6-11, $LaAlO_3$ exists from low temperature until its melting point. In Figure 6-12, YAG is stable up to its melting point, and $YAlO_3$ can only be formed above 1800 °C. In the La_2O_3-Al_2O_3 phase diagram, there is no $La_3Al_2Al_3O_{12}$ phase at the La_2O_3/Al_2O_3 ratio of 3/5, which is the mixed region of $LaAlO_3$ and $(La, Y)_2O_3$ [202]. From XRD results, La^{3+} ions prefer to form $LaAlO_3$ rather than $(La_xY_{1-x})_3Al_2Al_3O_{12}$ solid solution, resulting from the fact that the activation energy to form $LaAlO_3$ is smaller than to form $(La_xY_{1-x})_3Al_2Al_3O_{12}$ solid solution.

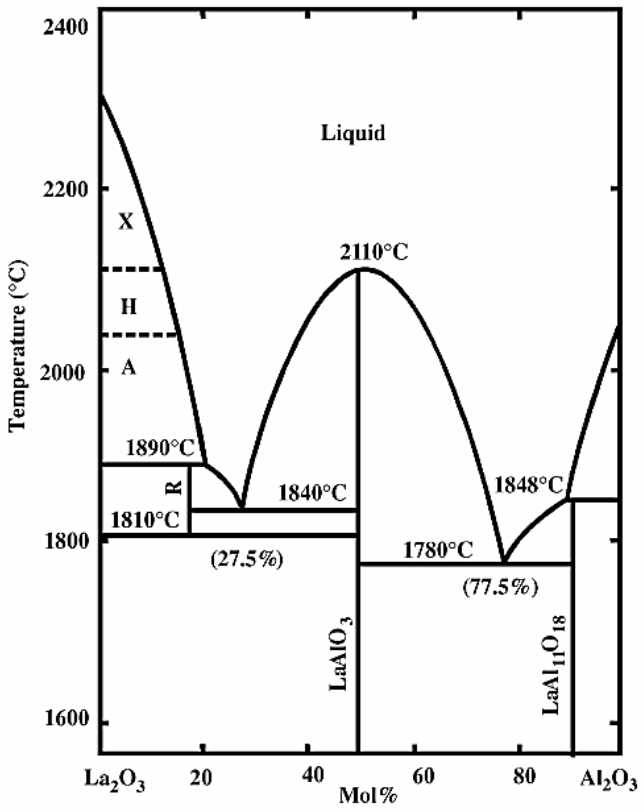

Figure 6-11: The phase diagram of La_2O_3-Al_2O_3 (H-Hexagonal high-temperature structure; A-Hexagonal low-temperature structure; X-Another hexagonal high-temperature structure) [201].

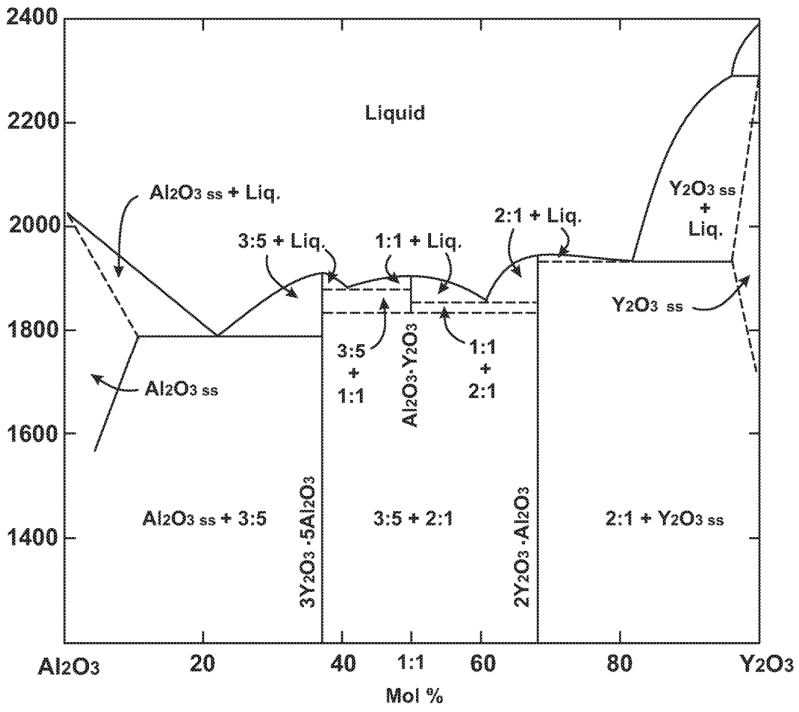

Figure 6-12: The phase diagram of Y_2O_3-Al_2O_3, where $3Y_2O_3{\cdot}5Al_2O_3$ is YAG (the subscript 'ss' means solid solution) [200].

6.3.2 Microstructure of As-Sintered Pellets

Figure 6-13 shows the microstructure of YAG with La^{3+} doped on dodecahedral site. The grain size of main YAG phase does not exceed 1 μm in all specimens. But inhomogeneous microstructures are observed and $LaAlO_3$ as second phase is confirmed, the content of which rises with increasing the doping concentration of La^{3+} ions. In Figure 6-13, the second $LaAlO_3$ phase shows light colour and grows near grain boundaries.

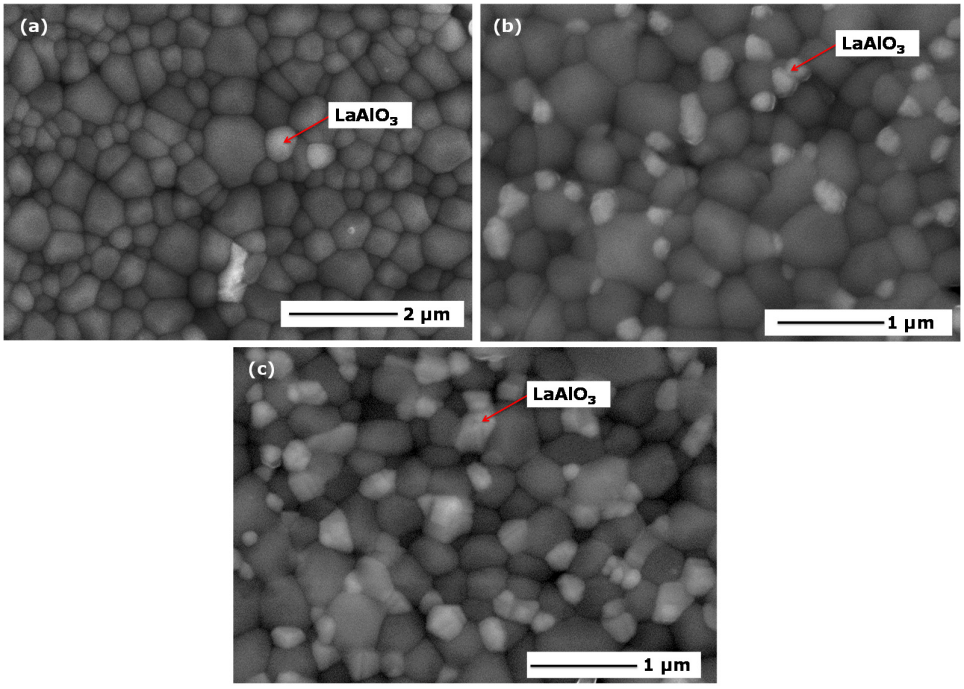

Figure 6-13: The SEM images of La^{3+} doped on dodecahedral site in YAG: **(a)**, 5 mol% La^{3+} doped YAG; **(b)** 15 mol% La^{3+} doped YAG; **(c)** 20 mol% La^{3+} doped YAG, where $LaAlO_3$ phase is observed in all of them.

Thus, it can be seen that La^{3+} ions doped YAG do not show a single phase, which means La^{3+} ions do not enter dodecahedral sites, so it could have extremely small influence on thermal properties. Therefore, if doping on dodecahedral sites, dopants should be able to stabilise in dodecahedra.

6.4 Er^{3+} Ions on Dodecahedral Sites in YAG

In section 6.2, the partial reduction of thermal conductivity of Yb^{3+} ions doped YAG results from the differences of atomic mass and ionic radius. Because it has been found that the difference in atomic mass can also significantly decrease thermal conductivity [197], it would be very interesting to investigate which one (atomic mass difference or ionic radial difference) has more influence on reducing thermal conductivity.

Therefore, Er^{3+} ion is chosen, due to the similar radius as host Y^{3+} ion and heaver atomic mass. Er^{3+} ions doped YAG can be used to study the influence from atomic mass difference scattering.

6.4.1 Phase Analysis

The XRD patterns in Figure 6-14 exhibit that the $(Er_xY_{1-x})_3Al_2Al_3O_{12}$ solid solution (x = 0.05, 0.15, 0.20) has single phase without extra peaks. XRD results show cubic phase of $(Er_xY_{1-x})_3Al_2Al_3O_{12}$ solid solution. Because the radius of Er^{3+} ion (1.004 Å) is very similar to that of the host Y^{3+} ion (1.019 Å), there is no significant peak shift observed, which is confirmed from peak (10, 2, 0) and (7,6,5) at higher 2θ in Figure 6-14 **(b)**.

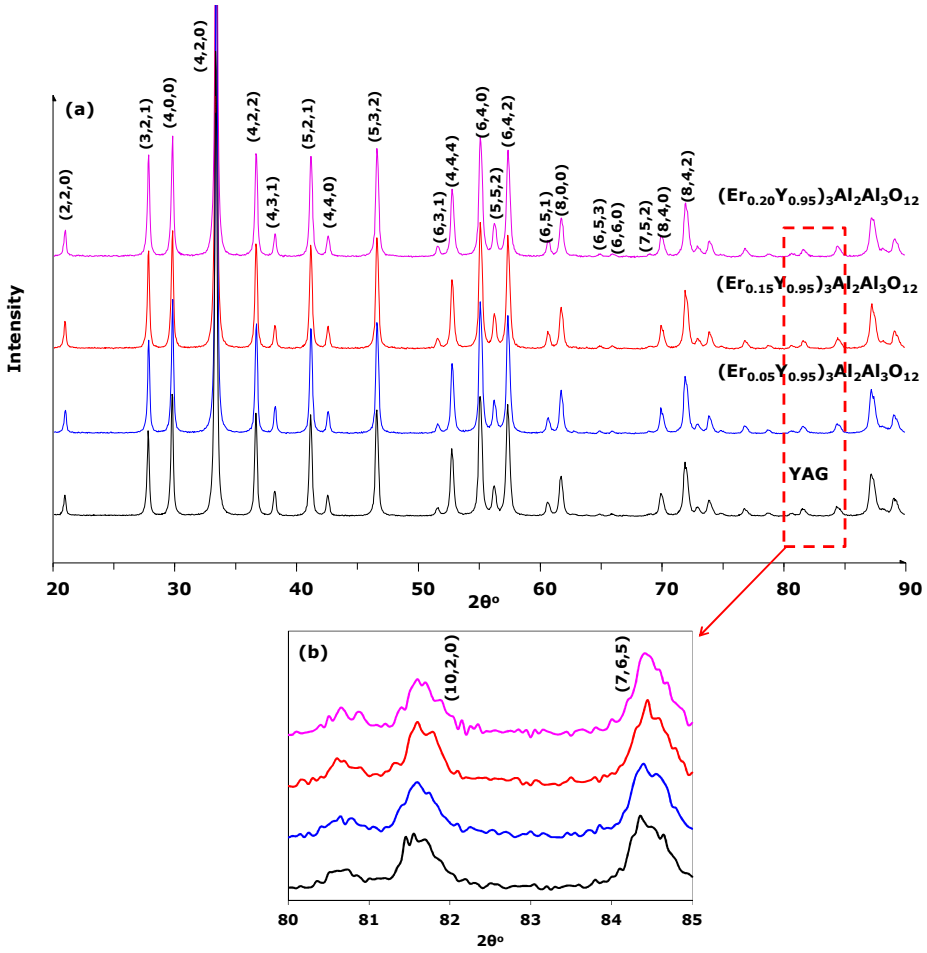

Figure 6-14: **(a)** The XRD patterns of un-doped YAG and Er^{3+} ions doped on dodecahedral site in YAG; **(b)** The enlarged peaks (10, 2, 0) and (7,6,5).

6.4.2 Microstructure of As-Sintered Pellets

SEM micrographs of as-sintered pellets provide the surface morphology of $(Er_xY_{1-x})_3Al_2Al_3O_{12}$ solid solution (x = 0.05, 0.15, 0.20) sintered at 1400 °C, as shown in Figure 6-15. The $(Er_xY_{1-x})_3Al_2Al_3O_{12}$ solid solution exhibits homogeneous microstructure and the grain size slightly increases when the

doping concentration increases from 5 mol% to 20 mol%. The increase of grain size is related to the recrystallization due to the diffusion of ions accelerated by increasing the doping concentration. The slight increase of grain size is also discovered in $(Yb_xY_{1-x})_3Al_2Al_3O_{12}$ solid solution (x = 0.05, 0.15, 0.20) and the recrystallization regions are observed in SEM images (Figure 6-7 in section 6.2.3). Moreover, more regions of grain growth are found in the specimen with high doping concentration.

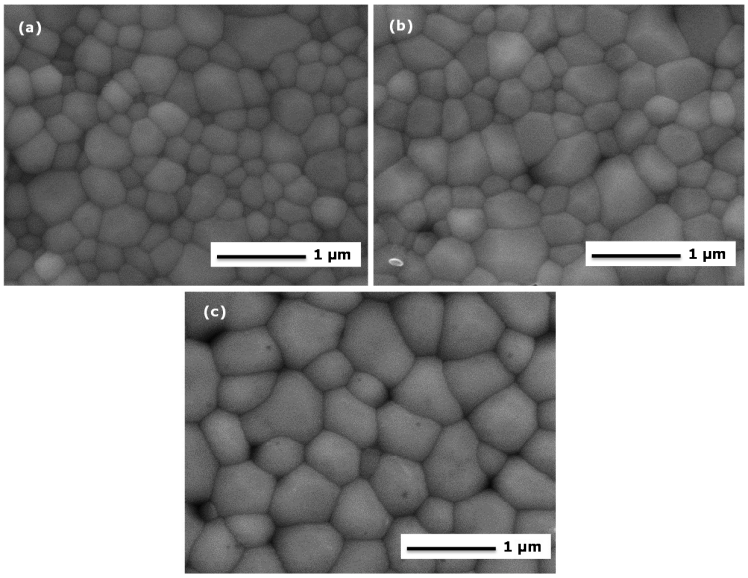

Figure 6-15: The SEM images of Er^{3+} doped in dodecahedra in YAG: **(a)** $(Er_{0.05}Y_{0.95})_3Al_2Al_3O_{12}$; **(b)** $(Er_{0.15}Y_{0.85})_3Al_2Al_3O_{12}$; **(c)** $(Er_{0.20}Y_{0.80})_3Al_2Al_3O_{12}$.

6.4.3 Thermal Conductivity

Er^{3+} ion has a similar ionic radius to host Y^{3+} ion, but they have a big difference in atomic mass. Yan *et al.* found that phonons can

be strongly scattered by large differences in atomic mass and size [197]. So the thermal conductivity of $(Er_xY_{1-x})_3Al_2Al_3O_{12}$ solid solution (x = 0.05, 0.15, 0.20) is expected to be dramatically reduced by the larger atomic mass difference between Er^{3+} ion and Y^{3+} ion.

Figure 6-16 exhibits thermal conductivity and theoretical density of $(Er_xY_{1-x})_3Al_2Al_3O_{12}$ solid solution (x = 0.05, 0.15, 0.20) at room temperature. The theoretical density increases from 4.64 to 4.89 $g \cdot cm^{-3}$ when the doping concentration rises from 5 mol% to 20 mol%, slightly higher than the value of un-doped YAG (4.55 $g \cdot cm^{-3}$), as shown in Figure 6-8. The thermal conductivities of $(Er_{0.05}Y_{0.95})_3Al_2Al_3O_{12}$, $(Er_{0.15}Y_{0.85})_3Al_2Al_3O_{12}$ and $(Er_{0.20}Y_{0.20})_3Al_2Al_3O_{12}$ are 2.28 $W \cdot m^{-1} \cdot K^{-1}$, 2.13 $W \cdot m^{-1} \cdot K^{-1}$ and 2.10 $W \cdot m^{-1} \cdot K^{-1}$, respectively, which are much smaller than that of un-doped YAG, 3.28 $W \cdot m^{-1} \cdot K^{-1}$ as shown in Figure 6-8.

Also in Figure 6-8, the reduction of thermal conductivity of $(Yb_xY_{1-x})_3Al_2Al_3O_{12}$ solid solution (x = 0.05, 0.15, 0.20) is from 2.31 $W \cdot m^{-1} \cdot K^{-1}$ to 2.09 $W \cdot m^{-1} \cdot K^{-1}$, which is almost as same as the decrement of $(Er_xY_{1-x})_3Al_2Al_3O_{12}$ solid solution. This similar change could result from the very similar size difference between Yb^{3+}-Y^{3+} and Er^{3+}-Y^{3+}. Therefore, the big atomic mass difference mainly contributes to the decrement of thermal conductivity in both $(Yb_xY_{1-x})_3Al_2Al_3O_{12}$ and $(Er_xY_{1-x})_3Al_2Al_3O_{12}$ solid solution.

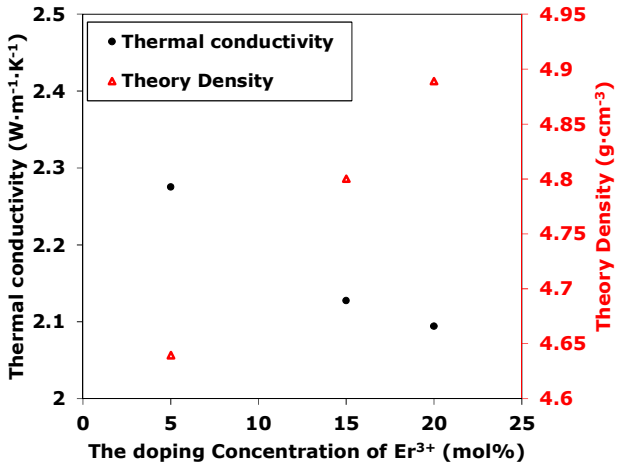

Figure 6-16: Thermal conductivity and theoretical density of $(Er_xY_{1-x})_3Al_2Al_3O_{12}$ solid solution (x = 0.05, 0.15, 0.20) at room temperature.

6.4.4 Coefficients of Thermal Expansion

Figure 6-17 shows the CTEs of $(Er_xY_{1-x})_3Al_2Al_3O_{12}$ solid solution (x = 0.05, 0.15, 0.20), which is in the range of 7.0~9.5×10^{-6} K^{-1} from 100 °C to 900 °C. It is found that the CTE slightly decreases by replacing Y^{3+} ions with Er^{3+} ions, but the CTE value increases with increasing the doping concentration. When x is 0.05 and 0.15, the CTE keeps in a similar range, 7.0~9.2×10^{-6} K^{-1}. But the CTE increases from 8.2 to 9.5×10^{-6} K^{-1} when x is 0.20. Because Er^{3+} ion (1.004 Å) has a similar radius to Y^{3+} ion (1.004 Å), introducing Er^{3+} ions does not influence the CTE values of YAG materials. However, the CTEs are higher than those of $(Yb_xY_{1-x})_3Al_2Al_3O_{12}$ solid solution (x = 0.05, 0.15, 0.20) as shown in Figure 6-9.

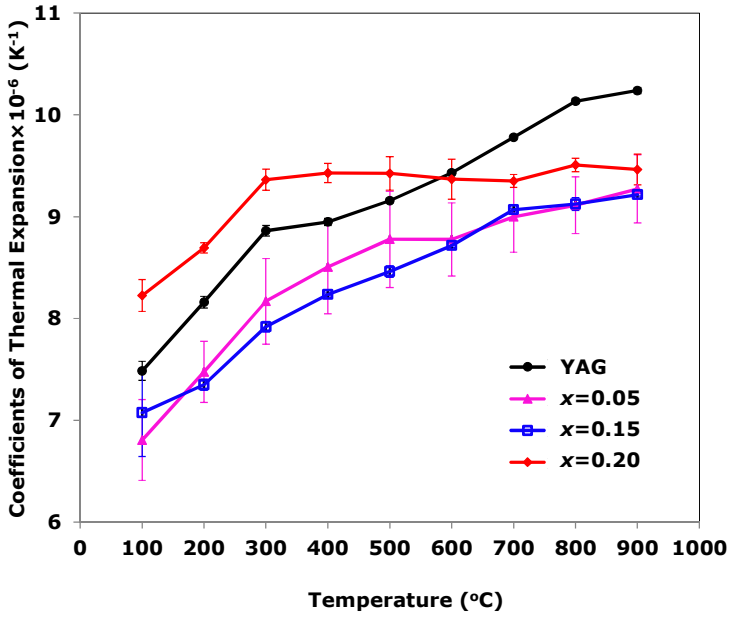

Figure 6-17: The change of CTEs with different doping contents of Er^{3+} ions on dodecahedral sites in YAG and the CTE values of YAG from 100 °C to 900 °C.

6.5 Summary

YAG becomes an attractive candidate for thermal barrier application, due to good phase stability and very low oxygen diffusivity, but its drawbacks are relatively high thermal conductivity and too low coefficient of thermal expansion. In order to further reduce thermal conductivity and slightly increase coefficient of thermal expansion, rare earth ions doped YAG are studied in this chapter. As they have the smallest radius in the lanthanide series, Yb^{3+} ions are introduced into dodecahedra or octahedra in YAG, and distortion could be generated in the crystal structure that affects the thermal properties. The shifts of XRD

peaks and changes of lattice constant indicate that dopants are occupying dodecahedral or octahedral sites, except for ceramic B2, in which some Yb^{3+} ions may occupy different sites or interstitial space. In addition, the thermal conductivity at room temperature can be reduced with the dopant on either site, though the reduction is much more remarkable when the dopant is an octahedral site. The decrease of CTE is observed when doping on dodecahedral sites, due to the small radius of Yb^{3+} ions causing the contraction of dodecahedra. However, the coefficient of thermal expansion increases when the dopants occupy in octahedra. The CTE value is over 10×10^{-6} K^{-1} above 800 ^{o}C, with doping concentration at 2 mol%. Therefore, Yb^{3+} ions doped on octahedral sites can efficiently reduce thermal conductivity and increase the coefficient of thermal expansion, which is mainly attributed to the larger ionic radial size of Yb^{3+} and the larger radial difference between Yb^{3+} and Al^{3+} ions. In future work, it is suggested that a dopant with larger radius occupy either dodecahedral or octahedral sites to further reduce thermal conductivity and increase coefficient of thermal expansion for YAG as thermal barrier coating material.

By comparing the results of $(Yb_xY_{1-x})_3Al_2Al_3O_{12}$ solid solution with $(Er_xY_{1-x})_3Al_2Al_3O_{12}$ solid solution (x = 0.05, 0.15, 0.20), it is found that big atomic mass difference mainly contributes to the reduction of thermal conductivity, which can also apply to Yb^{3+} ions doped YAG. Meanwhile, in order to increase coefficient of thermal expansion, La^{3+} ion is selected due to its large ionic radius and atomic mass. However, it is difficult for La^{3+} ions to enter

dodecahedral site to form $(La_xY_{1-x})_3Al_2Al_3O_{12}$ solid solution, but $LaAlO_3$ phase is preferred instead of $(La_xY_{1-x})_3Al_2Al_3O_{12}$ solid solution, which may be related to small activation energy of $LaAlO_3$ phase.

Overall, in octahedra, it is found that Yb^{3+} ions can effectively reduce thermal conductivity and also increase CTE even with very low doping concentration. For doping on dodecahedral sites, it is only found that both Yb^{3+} ions and Er^{3+} ions can dramatically reduce thermal conductivity, mainly due to the big difference in atomic mass, but their CTEs do not have a significant change. Therefore, it is assumed that if a dopant has larger radius than Y^{3+} ions and also larger atomic mass, to be doped on dodecahedral sites, this strategy might effectively reduce thermal conductivity as well as increase coefficient of thermal expansion. In addition, the same idea can be applied for doping in octahedra.

Chapter 7. Conclusion and Future Work

With increasing the demands on operating temperatures to improve the thermal efficiency of gas engines, new ceramics applied as top-coat in thermal barrier coatings (TBCs) are expected to replace conventional 7-8 wt% yttria-stabilised zirconia (7-8YSZ). 7-8YSZ is not capable to be applied above 1250 ^{o}C, due to its poor thermal phase stability, relatively high thermal conductivity and slightly small coefficient of thermal expansion. Through critical literature review and analysis, three ceramic systems are identified and studied in this thesis, which are stannate (pyrochlore), erbia-stabilised zirconia and yttrium aluminium garnet (YAG). Sol-gel method has been used to synthesise nano-sized ceramic powders. Furthermore, thermal conductivity, coefficient of thermal expansion and thermal phase stability of these candidate materials are also investigated. In addition molecular dynamics (MD) simulations have also been used to calculate thermal conductivity and coefficient of thermal expansion to exclude the influences from external factors, such as porosity, grain size and grain boundary.

Pyrochlore has very good phase stability up to its melting point (> 2000 ^{o}C) [107] and stannate system is expected to have much lower thermal conductivity than either Mo- or Zr-based systems [108]. La^{3+} Doped $Yb_2Sn_2O_7$ and un-doped $Yb_2Sn_2O_7$ or $La_2Sn_2O_7$ are studied as potential TBCs materials in chapter 4. XRD patterns and TEM diffraction results indicate their pyrochlore crystal

structure. Thermal conductivity of $(La_xYb_{1-x})_2Sn_2O_7$ (x = 0.3, 0.5 and 0.7) solid solution is much lower (around 1.0 $W \cdot m^{-1} \cdot K^{-1}$ at room temperature) than those of 8YSZ and $La_2Zr_2O_7$. Moreover, $(La_{0.5}Yb_{0.5})_2Sn_2O_7$ exhibits the lowest thermal conductivity (0.85 $W \cdot m^{-1} \cdot K^{-1}$ at room temperature) and highest coefficient of thermal expansion (13.530×10^{-6} K^{-1} at 950 ^oC). The decrement of thermal conductivity could mainly result from the disorder scattering of cation layer. In order to further verify this conjecture, molecular dynamics simulation is carried out to calculate thermal conductivity from atomic-level, to avoid the influence from porosity, grain boundary, and grain size *etc*.

According to the simulation, the thermal conductivity decreases to a minimum value (3.13 $W \cdot m^{-1} \cdot K^{-1}$ at room temperature) when x is 0.5, then increases with further increase of x, showing good agreement with the experimental result. This discovery indicates that the disorder of cation layers can effectively scatter phonons to reduce thermal conductivity. The simulation values are larger than experimental values, mainly as there is no consideration on grain boundary scattering, grain scattering and porosity. Furthermore, the thermal conductivity of $(La_xYb_{1-x})_2Sn_2O_7$ (x = 0.3, 0.5 and 0.7) solid solution tends to reach a similar value, around 1.5 $W \cdot m^{-1} \cdot K^{-1}$ at 1400 ^oC.

One main disadvantage of 7-8YSZ is that it has very high diffusivity of Y^{3+} ions to cause phase instability above 1250 ^oC. Erbia is chosen as a new stabiliser to replace yttria and erbia-stabilised zirconia is investigated at 1400 ^oC in chapter 5. XRD patterns indicate non-transformable phase (t'-phase) of erbia

based rare earth oxides stabilised zirconia. Thermal conductivity decreases and thermal phase stability can be improved when the content of Er_2O_3 is increased from 4 mol% to 6 mol%.

Creating cluster defects in stabilised zirconia can effectively reduce thermal conductivity and might also improve thermal phase stability. Thus, mono- and bi-rare earth oxides doped erbia-stabilised zirconia are also studied. Their thermal conductivities are smaller than that of 8YSZ, which is an outstanding advantage to be TBCs candidates. The main factor for reducing thermal conductivity is the larger difference of atomic mass between rare earth elements and zirconium. Additionally, for erbia-stabilised zirconia, it is found that thermal phase stability is related to the tetragonality, $c/a\sqrt{2}$ ratio. When the $c/a\sqrt{2}$ ratio is in the range of 1.006 to 1.010, the crystalline phase is *t′*-phase. Moreover, the thermal phase stability increases when the $c/a\sqrt{2}$ ratio decreases to 1.006. The best composition is 6 mol% erbia-stabilised zirconia and its $c/a\sqrt{2}$ ratio is around 1.006. On the other hand, when the $c/a\sqrt{2}$ ratio increases, cations could diffuse more easily, due to the enlarged *c*-direction.

YAG is also considered as a TBCs candidate, due to its good phase stability and very low oxygen diffusivity, where the oxygen diffusion determines the growth rate of thermally grown oxides layer between ceramic coat and bond coat. In YAG, there are three type polyhedrons in its structure, dodecahedra, octahedra and tetrahedra. To understand the relationship between doping on different polyhedrons and thermal conductivity or coefficient of thermal expansion, Yb^{3+} ions with the smallest radius in the

lanthanide series are introduced onto dodecahedral or octahedral sites. It is found that Yb^{3+} ions in octahedra can effectively reduce thermal conductivity and increase coefficient of thermal expansion rather than in dodecahedra. The main influence on thermal conductivity and coefficient of thermal expansion is contributed to the ionic radial difference, which is related to the distortion level of dodecahedra or octahedra. In octahedra, the radial difference between Yb^{3+} and host Al^{3+} ion is 0.333 Å, which is much larger than that of Yb^{3+} and host Y^{3+} ion (0.034 Å).

Additionally, in order to introduce larger radial difference on dodecahedral site to increase coefficient of thermal expansion, La^{3+} ions doped YAG has also been studied. However, La^{3+} ions cannot be completely stabilised in dodecahedra. Second phase $LaAlO_3$ is found in all specimens of La^{3+} ions doped YAG, the content of which increases with the increase of doping concentration of La^{3+} ions.

For doped YAG, the decrement of thermal conductivity is related to a number of factors, typically phonon-phonon scattering, defect scattering, grain boundary scattering, atomic mass difference scattering and radial difference scattering. For doping on the same polyhedron sites, the effects from phonon-phonon scattering, defect scattering, grain boundary scattering are similar, so atomic mass difference scattering and radial difference scattering play important roles on reducing thermal conductivity.

For $(Er_xY_{1-x})_3Al_2Al_3O_{12}$ solid solution (x = 0.05, 0.15, 0.20), it is found that their thermal conductivities are very similar to those of

$(Yb_xY_{1-x})_3Al_2Al_3O_{12}$ solid solution. Because Er^{3+} ion has very similar ionic radius to Y^{3+} ion, it indicates that the decrease of thermal conductivity mainly results from the difference of atomic mass either in $(Er_xY_{1-x})_3Al_2Al_3O_{12}$ solid solution or $(Yb_xY_{1-x})_3Al_2Al_3O_{12}$ solid solution.

From the above summary, different ceramic systems have their own advantages and disadvantages. Their limitations can be further improved through introducing dopants to modify the crystal structure or creating defects. In a future study, the synthesised materials may be applied on superalloy substrate using air plasma spray (APS) or electron beam physical vapour deposition (ED-PVD) to study thermophysical properties.

On the other side, there are still some specific drawbacks for different systems. For stannate, the chemical compatibility with alumina (main phase in thermally grown oxide layer in TBCs) needs to be further improved, which is mainly dependent on the diffusion rate of cations. The disorder of crystal structure produced by dopants can decrease thermal conductivity, but also can accelerate the diffusivity of cations. Thus, the main work for stannate system may focus on its chemical compatibility. For stabilised zirconia, the thermal conductivity has been further reduced but has not reached the minimum value. Moreover, thermal phase stability needs to be further improved after much longer thermal cycling time (usually above one thousand hours). Additionally, because YAG has very complex crystal structure, it can provide good phase stability and low thermal conductivity. However, its relatively small coefficient of thermal expansion

needs to be increased. In the next step, the work will need to find a suitable dopant which is stable on dodecahedral site and can also increase the coefficient of thermal expansion. Thus the future work can be summarised as following these directions:

(1) To better understand the relationship between crystal structure and thermal conductivity, coefficient of thermal expansion and phase stability, when introducing different dopants into materials;

(2) Based on the outcomes from (1), to optimise the crystal structure by introducing suitable dopants and then to improve suboptimal properties of different systems;

(3) If potential compositions are confirmed, coating process will be carried out to study the thermophysical properties of the whole TBCs system.

References:

[1] W. Beele, G. Marijnissen, and A. V. Lieshout, "The Evolution of Thermal Barrier Coatings — Status and Upcoming Solutions for Today's Key Issues," *Surface and Coatings Technology,* vol. 120–121, pp. 61-67, 1999.

[2] M. Yuri, J. Masada, K. Tsukagoshi, E. Ito, and S. Hada, "Development of 1600 C-Class High-Efficiency Gas Turbine for Power Generation Applying J-Type Technology," *Mitsubishi Heavy Industries Technical Review,* vol. 50, pp. 1-10, 2013.

[3] D. R. Clarke, M. Oechsner, and N. P. Padture, "Thermal-Barrier Coatings for More Efficient Gas-Turbine Engines," *MRS bulletin,* vol. 37, pp. 891-898, 2012.

[4] U. Schulz, C. Leyens, K. Fritscher, M. Peters, B. Saruhan-Brings, O. Lavigne*, et al.*, "Some Recent Trends in Research and Technology of Advanced Thermal Barrier Coatings," *Aerospace Science and Technology,* vol. 7, pp. 73-80, 2003.

[5] J. T. DeMasi-Marcin and D. K. Gupta, "Protective coatings in the gas turbine engine," *Surface and Coatings Technology,* vol. 68, pp. 1-9, 1994.

[6] S. Bose and J. DeMasi-Marcin, "Thermal barrier coating experience in gas turbine engines at Pratt & Whitney," *Journal of thermal spray technology,* vol. 6, pp. 99-104, 1997.

[7] S. Bose, *High Temperature Coatings*: Butterworth-Heinemann, 2011.

[8] S. Stecura, "Thermal barrier coating system," ed: Google Patents, 1985.

[9] X. Q. Cao, R. Vassen, and D. Stoever, "Ceramic materials for thermal barrier coatings," *Journal of the European Ceramic Society,* vol. 24, pp. 1-10, 2004.

[10] N. P. Padture, M. Gell, and E. H. Jordan, "Thermal Barrier Coatings for Gas-Turbine Engine Applications," *Science,* vol. 296, pp. 280-284, 2002.

[11] C. U. Hardwicke and Y. C. Lau, "Advances in Thermal Spray Coatings for Gas Turbines and Energy Generation: A

Review," *Journal of Thermal Spray Technology,* vol. 22, pp. 564-576, Jun 2013.

[12] S. Bose, "Thermal Barrier Coatings (TBCs)," in *High Temperature Coatings*, ed Burlington: Butterworth-Heinemann, 2007, p. 183.

[13] J. Ilavsky and J. K. Stalick, "Phase Composition and Its Changes During Annealing of Plasma-Sprayed YSZ," *Surface and Coatings Technology,* vol. 127, pp. 120-129, 2000.

[14] R. L. Jones, R. F. Reidy, and D. Mess, "Scandia, Yttria-Stabilized Zirconia for Thermal Barrier Coatings," *Surface and Coatings Technology,* vol. 82, pp. 70-76, 1996.

[15] J. Wang, F. Xu, R. J. Wheatley, K.-L. Choy, N. Neate, and X. Hou, "Investigation of La^{3+} Doped $Yb_2Sn_2O_7$ as New Thermal Barrier Materials," *Materials & Design,* vol. 85, pp. 423-430, 2015.

[16] H. S. Zhang, S. Q. Yan, and X. G. Chen, "Preparation and Thermophysical Properties of Fluorite-Type Samarium-Dysprosium-Cerium Oxides," *Journal of the European Ceramic Society,* vol. 34, pp. 61-67, Jan 2014.

[17] Y. J. Su, R. W. Trice, K. T. Faber, H. Wang, and W. D. Porter, "Thermal Conductivity, Phase Stability, and Oxidation Resistance of $Y_3Al_5O_{12}$ (YAG)/Y_2O_3-ZrO_2 (YSZ) Thermal-Barrier Coatings," *Oxidation of Metals,* vol. 61, pp. 253-271, 2004.

[18] M. Belmonte, "Advanced Ceramic Materials for High Temperature Applications," *Advanced engineering materials,* vol. 8, pp. 693-703, 2006.

[19] J. Gao, Y. He, and D. Wang, "Preparation of YSZ/Al_2O_3 Micro-Laminated Coatings and Their Influence on the Oxidation and Spallation Resistance of MCrAlY Alloys," *Journal of the European Ceramic Society,* vol. 31, pp. 79-84, 2011.

[20] J. Wang, F. Xu, R. J. Wheatley, N. Neate, and X. Hou, "Yb^{3+} Doping Effects on Thermal Conductivity and Thermal Expansion of Yttrium Aluminium Garnet," *Ceramics International,* vol. 42, pp. 14228-14235, 2016.

[21] T. M. Tritt, *Thermal Conductivity: Theory, Properties, and Applications*: Springer, 2004.

[22] M. J. Kelly, D. E. Wolfe, J. Singh, J. Eldridge, D. M. Zhu, and R. Miller, "Thermal Barrier Coatings Design with Increased

Reflectivity and Lower Thermal Conductivity for High-Temperature Turbine Applications," *International Journal of Applied Ceramic Technology,* vol. 3, pp. 81-93, 2006.

[23] J. Meyer, F. Bartoli, and M. Kruer, "Optical Heating in Semiconductors," *Physical Review B,* vol. 21, p. 1559, 1980.

[24] A. J. McGaughey and M. Kaviany, "Phonon Transport in Molecular Dynamics Simulations: Formulation and Thermal Conductivity Prediction," *Advances in Heat Transfer,* vol. 39, pp. 169-225, 2006.

[25] X. Huang and Asme, *Effect of Co-Doping on Microstructure, Thermal and Mechanical Properties of Ternary Zirconia-Based Thermal Barrier Coating Materials*, 2009.

[26] Unknown. (2013, 20,Dec). *Phonon Scattering*. Available: http://en.wikipedia.org/wiki/Phonon_scattering

[27] M. J. Kelly, D. E. Wolfe, J. Singh, J. Eldridge, D. M. Zhu, and R. Miller, "Thermal Barrier Coatings Design with Increased Reflectivity and Lower Thermal Conductivity for High - Temperature Turbine Applications," *International Journal of Applied Ceramic Technology,* vol. 3, pp. 81-93, 2006.

[28] W. D. Kingery, H. K. Bowen, and D. R. Uhlmann, *Introduction to Ceramics*. New York: Jhon Willey & Sons, 1976.

[29] D. R. Clarke and S. R. Phillpot, "Thermal Barrier Coating Materials," *Materials Today,* vol. 8, pp. 22-29, 2005.

[30] E. S. Toberer, A. Zevalkink, and G. J. Snyder, "Phonon Engineering Through Crystal Chemistry," *Journal of Materials Chemistry,* vol. 21, pp. 15843-15852, 2011.

[31] M. R. Winter and D. R. Clarke, "Oxide Materials with Low Thermal Conductivity," *Journal of the American Ceramic Society,* vol. 90, pp. 533-540, 2007.

[32] D. R. Clarke, "Materials Selection Guidelines for Low Thermal Conductivity Thermal Barrier Coatings," *Surface and Coatings Technology,* vol. 163, pp. 67-74, 2003.

[33] R. Peterson, "Direct Simulation of Phonon-Mediated Heat Transfer in A Debye Crystal," *Journal of Heat Transfer,* vol. 116, pp. 815-822, 1994.

[34] M. Black, "Thermal Conductivity and Anharmonic Forces," *American Journal of Physics,* vol. 41, pp. 691-696, 1973.

[35] J. Dugdale and D. MacDonald, "Lattice Thermal Conductivity," *Physical Review,* vol. 98, p. 1751, 1955.

[36] P.G.Klemens, "Theory of Thermal Condcutivity in Solids," in *Thermal Conductivity*. vol. 1, R.P.Tye, Ed., ed London: Academic Press, 1969.

[37] M. Roufosse and P. G. Klemens, "Thermal Conductivity of Complex Dielectric Crystals," *Physical Review B,* vol. 7, pp. 5379-5386, 1973.

[38] G. A. Slack and S. Galginaitis, "Thermal Conductivity and Phonon Scattering by Magnetic Impurities in CdTe," *Physical Review,* vol. 133, p. A253, 1964.

[39] H. Goldsmid and A. Penn, "Boundary Scattering of Phonons in Solid Solutions," *Physics Letters A,* vol. 27, pp. 523-524, 1968.

[40] P. Klemens and M. Gell, "Thermal Conductivity of Thermal Barrier Coatings," *Materials Science and Engineering: A,* vol. 245, pp. 143-149, 1998.

[41] J. Chung, A. McGaughey, and M. Kaviany, "Role of Phonon Dispersion in Lattice Thermal Conductivity Modeling," *Journal of heat transfer,* vol. 126, pp. 376-380, 2004.

[42] P. G. Klemens, "The Scattering of Low-Frequency Lattice Waves by Static Imperfections," *Proceedings of the Physical Society. Section A,* vol. 68, p. 1113, 1955.

[43] W. Pan, S. R. Phillpot, C. Wan, A. Chernatynskiy, and Z. Qu, "Low Thermal Conductivity Oxides," *MRS bulletin,* vol. 37, pp. 917-922, 2012.

[44] Unknown. (Unknown, January 15). *Thermal Properties*. Available: http://people.virginia.edu/~lz2n/mse209/Chapter19.pdf

[45] H. S. Zhang, Z. J. Li, Q. Xu, F. C. Wang, and L. Liu, "Preparation and Thermophysical Properties of $Sm_2(Ce_{0.3}Zr_{0.7})_2O_7$ Ceramic," *Advanced Engineering Materials,* vol. 10, pp. 139-142, 2008.

[46] M. Dietrich, R. Vaßen, and D. Stöver, "$LaYbO_3$, A candidate for thermal barrier coating materials," in *27th Annual Cocoa Beach Conference on Advanced Ceramics and Composites: A: Ceramic Engineering and Science Proceedings*, ed: John Wiley & Sons, Inc., 2008, pp. 637-643.

[47] V. Lughi and D. R. Clarke, "High Temperature Aging of YSZ Coatings and Subsequent Transformation at Low Temperature," *Surface and Coatings Technology,* vol. 200, pp. 1287-1291, 2005.

[48] H. G. Scott, "Phase Relationships in The Zirconia-Yttria System," *Journal of Materials Science,* vol. 10, pp. 1527-1535, 1975.

[49] I. Askestad, "Ceramic Thermal Barrier Coatings of Yttria Stabilized Zirconia Made by Spray Pyrolysis," 2011.

[50] C. Viazzi, J. P. Bonino, F. Ansart, and A. Barnabé, "Structural Study of Metastable Tetragonal YSZ Powders Produced via a Sol–Gel Route," *Journal of Alloys and Compounds,* vol. 452, pp. 377-383, 2008.

[51] M. Yashima, M. Kakihana, and M. Yoshimura, "Metastable-Stable Phase Diagrams in The Zirconia-Containing Systems Utilized in Solid-Oxide Fuel Cell Application," *Solid State Ionics,* vol. 86–88, Part 2, pp. 1131-1149, 1996.

[52] Wikipedia. (14th Dec.). *Yttria-Stabilized Zirconia*. Available: http://en.wikipedia.org/wiki/Yttria-stabilized_zirconia

[53] W. Ma, S. Gong, H. Xu, and X. Cao, "On Improving the Phase Stability and Thermal Expansion Coefficients of Lanthanum Cerium Oxide Solid Solutions," *Scripta Materialia,* vol. 54, pp. 1505-1508, 2006.

[54] H. Eaton, J. Linsey, and R. Dinwiddie, "The Effect of Thermal Aging on The Thermal Conductivity of Plasma Sprayed Fully Stabilized Zirconia," *Thermal conductivity,* vol. 22, pp. 289-289, 1993.

[55] P. Bengtsson and T. Johannesson, "Characterization of Microstructural Defects in Plasma-Sprayed Thermal Barrier Coatings," *Journal of Thermal Spray Technology,* vol. 4, pp. 245-251, 1995.

[56] D. E. Wolfe, J. Singh, R. A. Miller, J. I. Eldridge, and D.-M. Zhu, "Tailored Microstructure of EB-PVD 8YSZ Thermal Barrier Coatings with Low Thermal Conductivity and High Thermal Reflectivity for Turbine Applications," *Surface and Coatings Technology,* vol. 190, pp. 132-149, 2005.

[57] P. Meyer and S. Muehlberger, "Historical Review and Update to the State of the Art of Automation for Plasma Coating Processes," *Thin Solid Films,* vol. 118, pp. 445-456, 1984.

[58] A. Wank. (17-05-2016). *Basics of Thermal Spray Technology Processes*. Available: http://www.gtv-mbh.com/_old/gtv-mbh-englisch/www.gtv-mbh.de/cms/upload/publikat/Wank/thermal_spray_basics_processes.pdf

[59] S. Safai and H. Herman, "Microstructural Investigation of Plasma-Sprayed Aluminum Coatings," *Thin Solid Films,* vol. 45, pp. 295-307, 1977.

[60] J. R. Davis, *Handbook of Thermal Spray Technology*: ASM international, 2004.

[61] R. B. Dinwiddie, S. C. Beecher, W. D. Porter, and B. A. Nagaraj, "The Effect of Thermal Aging on the Thermal Conductivity of Plasma Sprayed and EB-PVD Thermal Barrier Coatings," in *ASME 1996 International Gas Turbine and Aeroengine Congress and Exhibition*, p. 006, 1996.

[62] M. Seraffon, "Performance of Air Plasma Sprayed Thermal Barrier Coatings for Industrial Gas Turbines," PhD Thesis, School of Applied Sciences, Cranfield University, Cranfield, 2012.

[63] N. Curry, N. Markocsan, X.-H. Li, A. Tricoire, and M. Dorfman, "Next Generation Thermal Barrier Coatings for The Gas Turbine Industry," *Journal of thermal spray technology,* vol. 20, pp. 108-115, 2011.

[64] N. Curry, N. Markocsan, L. Östergren, X.-H. Li, and M. Dorfman, "Evaluation of The Lifetime and Thermal Conductivity of Dysprosia-Stabilized Thermal Barrier Coating Systems," *Journal of thermal spray technology,* vol. 22, pp. 864-872, 2013.

[65] U. Schulz, O. Bernardi, A. Ebach-Stahl, R. Vassen, and D. Sebold, "Improvement of EB-PVD Thermal Barrier Coatings by Treatments of a Vacuum Plasma-Sprayed Bond Coat," *Surface and coatings technology,* vol. 203, pp. 160-170, 2008.

[66] W. Pan, Q. Xu, L. H. Qi, J. D. Wang, H. Z. Miao, K. Mori*, et al.*, "Novel Low Thermal Conductivity Ceramic Materials for Thermal Barrier Coatings," *Key Engineering Materials,* vol. 280-283, pp. 1497-1500, 2005.

[67] H. Ibégazène, S. Alpérine, and C. Diot, "Yttria-Stabilized Hafnia-Zirconia Thermal Barrier Coatings: The Influence of Hafnia Addition on TBC Structure and High-Temperature Behaviour," *Journal of Materials Science,* vol. 30, pp. 938-951, 1995.

[68] J. R. Nicholls, K. J. Lawson, A. Johnstone, and D. S. Rickerby, "Methods to Reduce The Thermal Conductivity of EB-PVD TBCs," *Surface and Coatings Technology,* vol. 151–152, pp. 383-391, 2002.

[69] L. G. Kong, I. Karatchevtseva, D. J. Gregg, M. G. Blackford, R. Holmes, and G. Triani, "A Novel Chemical Route to Prepare $La_2Zr_2O_7$ Pyrochlore," *Journal of the American Ceramic Society,* vol. 96, pp. 935-941, 2013.

[70] N. P. Padture and P. G. Klemens, "Low Thermal Conductivity in Garnets," *Journal of the American Ceramic Society,* vol. 80, pp. 1018-1020, 1997.

[71] X. Xie, H. Guo, S. Gong, and H. Xu, "Lanthanum–Titanium–Aluminum Oxide: A Novel Thermal Barrier Coating Material for Applications at 1300°C," *Journal of the European Ceramic Society,* vol. 31, pp. 1677-1683, 2011.

[72] B. Jiang, M. H. Fang, Z. H. Huang, Y. G. Liu, P. Peng, and J. Zhang, "Mechanical and Thermal Properties of $LaMgAl_{11}O_{19}$," *Materials Research Bulletin,* vol. 45, pp. 1506-1508, 2010.

[73] B. V. Beznosikov and K. S. Aleksandrov, "Perovskite-like Crystals of the Ruddlesden-Popper Series," *Crystallography Reports,* vol. 45, pp. 792-798, 2000.

[74] L. Guo, H. Guo, G. Ma, S. Gong, and H. Xu, "Phase Stability, Microstructural and Thermo-Physical Properties of $BaLn_2Ti_3O_{10}$ (Ln=Nd and Sm) Ceramics," *Ceramics International,* vol. 39, pp. 6743-6749, 2013.

[75] K. E. Sickafus, L. Minervini, R. W. Grimes, J. A. Valdez, M. Ishimaru, F. Li*, et al.*, "Radiation tolerance of complex oxides," *Science,* vol. 289, pp. 748-751, 2000.

[76] R. Vassen, X. Cao, F. Tietz, D. Basu, and D. Stöver, "Zirconates as New Materials for Thermal Barrier Coatings," *Journal of the American Ceramic Society,* vol. 83, pp. 2023-2028, 2000.

[77] X. Q. Cao, R. Vassen, W. Jungen, S. Schwartz, F. Tietz, and D. Stöver, "Thermal Stability of Lanthanum Zirconate Plasma-Sprayed Coating," *Journal of the American Ceramic Society,* vol. 84, pp. 2086-2090, 2001.

[78] E. P. Busso, J. Lin, and S. Sakurai, "A Mechanistic Study of Oxidation-Induced Degradation in A Plasma-Sprayed Thermal Barrier Coating System: Part II: Life Prediction Model," *Acta Materialia,* vol. 49, pp. 1529-1536, 2001.

[79] M. A. Subramanian, Aravamudan, G. and Subba Rao, *Oxide Pyrochlores* vol. 15, 1983.

[80] X. Wang, S. Guo, L. Zhao, Y. Zhu, and L. Ai, "A Novel Thermal Barrier Coating for High-Temperature Applications," *Ceramics International,* vol. 42, pp. 2648-2653, 2016.

[81] J. Wu, X. Z. Wei, N. P. Padture, P. G. Klemens, M. Gell, E. Garcia*, et al.*, "Low-Thermal-Conductivity Rare-Earth Zirconates for Potential Thermal-Barrier-Coating Applications," *Journal of the American Ceramic Society,* vol. 85, pp. 3031-3035, 2002.

[82] P. S. L. F. L. Michael J. Maloney, "Thermal Barrier Coating Systems and Materials," US Patent US 6117560, 2000.

[83] A. M. Alper, *Phase Diagrams in Advanced Ceramics*: Academic Press, Inc, 1995.

[84] S. Raghavan, H. Wang, R. B. Dinwiddie, W. D. Porter, and M. J. Mayo, "The Effect of Grain Size, Porosity and Yttria Content on The Thermal Conductivity of Nanocrystalline Zirconia," *Scripta Materialia,* vol. 39, pp. 1119-1125, 1998.

[85] A. Rouanet, "CONTRIBUTION TO STUDY OF ZIRCONIUM-OXIDES SYSTEMS OF LANTHANIDES CLOSE TO MELTING POINT," *Revue Internationale Des Hautes Temperatures Et Des Refractaires,* vol. 8, pp. 161, 1971.

[86] X. Ren, C. Wan, M. Zhao, J. Yang, and W. Pan, "Mechanical and Thermal Properties of Fine-Grained Quasi-Eutectoid $(La_{1-x}Yb_x)_2Zr_2O_7$ Ceramics," *Journal of the European Ceramic Society,* vol. 35, pp. 3145-3154, 2015.

[87] D. Shin, H.-G. Shin, and H. Lee, "Thermodynamic Investigation of The $(La_{1-x}Gd_x)_2Zr_2O_7$ Pyrochlore Phase," *Calphad,* vol. 45, pp. 27-32, 2014.

[88] Y. Zhang, M. Xie, F. Zhou, X. Cui, X. Lei, X. Song*, et al.*, "Influence of Er Substitution for La on The Thermal Conductivity of $(La_{1-x}Er_x)_2Zr_2O_7$ Pyrochlores," *Materials Research Bulletin,* vol. 64, pp. 175-181, 2015.

[89] H. Lehmann, D. Pitzer, G. Pracht, R. Vassen, and D. Stöver, "Thermal Conductivity and Thermal Expansion Coefficients of The Lanthanum Rare-Earth-Element Zirconate System," *Journal of the American Ceramic Society,* vol. 86, pp. 1338-1344, 2003.

[90] L. Guo, Y. Zhang, X. Zhao, C. Wang, and F. Ye, "Thermal Expansion and Fracture Toughness of $(RE_{0.9}Sc_{0.1})_2Zr_2O_7$ (RE=La, Sm, Dy, Er) Ceramics," *Ceramics International,* vol. 42, pp. 583-588, 2016.

[91] C. L. Wan, W. Pan, Q. Xu, Y. X. Qin, J. D. Wang, Z. X. Qu*, et al.*, "Effect of Point Defects on The Thermal Transport Properties of $(La_xGd_{1-x})_2Zr_2O_7$: Experiment and Theoretical Model," *Physical Review B,* vol. 74, p. 144109, 2006.

[92] C. Wan, Z. Qu, A. Du, and W. Pan, "Influence of B Site Substituent Ti on The Structure and Thermophysical Properties of $A_2B_2O_7$-Type Pyrochlore $Gd_2Zr_2O_7$," *Acta Materialia,* vol. 57, pp. 4782-4789, 2009.

[93] W. Ma, D. Mack, J. Malzbender, R. Vaßen, and D. Stöver, "Yb_2O_3 and Gd_2O_3 Doped Strontium Zirconate for Thermal Barrier Coatings," *Journal of the European Ceramic Society,* vol. 28, pp. 3071-3081, 2008.

[94] M. R. Winter and D. R. Clarke, "Thermal Conductivity of Yttria-Stabilized Zirconia–Hafnia Solid Solutions," *Acta Materialia,* vol. 54, pp. 5051-5059, 2006.

[95] H. Zhang, K. Sun, Q. Xu, F. Wang, and L. Liu, "Thermal Conductivity of $(Sm_{1-x}La_x)_2Zr_2O_7$ (x=0, 0.25, 0.5, 0.75 and 1) Oxides for Advanced Thermal Barrier Coatings," *Journal of Rare Earths,* vol. 27, pp. 222-226, 2009.

[96] J. Xiang, S. Chen, J. Huang, W. Liang, Y. Cao, R. Wang*, et al.*, "Synthesis Kinetics and Thermophysical Properties of $La_2(Zr_{0.7}Ce_{0.3})_2O_7$ Ceramic for Thermal Barrier Coatings," *Journal of Rare Earths,* vol. 30, pp. 228-232, 2012.

[97] J. Fenech, M. Dalbin, A. Barnabe, J. P. Bonino, and F. Ansart, "Sol-Gel Processing and Characterization of (RE-Y)-Zirconia Powders for Thermal Barrier Coatings," *Powder Technology,* vol. 208, pp. 480-487, 2011.

[98] Z. Hong-song, X. Qiang, W. Fu-chi, L. Ling, W. Yuan, and C. Xiaoge, "Preparation and Thermophysical Properties of $(Sm_{0.5}La_{0.5})_2Zr_2O_7$ and $(Sm_{0.5}La_{0.5})_2(Zr_{0.8}Ce_{0.2})_2O_7$ Ceramics for Thermal Barrier Coatings," *Journal of Alloys and Compounds,* vol. 475, pp. 624-628, 2009.

[99] H. Zhang, S. Liao, X. Dang, S. Guan, and Z. Zhang, "Preparation and Thermal Conductivities of $Gd_2Ce_2O_7$ and $(Gd_{0.9}Ca_{0.1})_2Ce_2O_{6.9}$ Ceramics for Thermal Barrier Coatings," *Journal of Alloys and Compounds,* vol. 509, pp. 1226-1230, 2011.

[100] J. Xiang, S. Chen, J. Huang, H. Zhang, and X. Zhao, "Phase Structure and Thermophysical Properties of Co-Doped $La_2Zr_2O_7$ Ceramics for Thermal Barrier Coatings," *Ceramics International,* vol. 38, pp. 3607-3612, 2012.

[101] H. Liu, S. Li, Q. Li, and Y. Li, "Investigation on The Phase Stability, Sintering and Thermal Conductivity of Sc_2O_3–Y_2O_3–ZrO_2 for Thermal Barrier Coating Application," *Materials & Design,* vol. 31, pp. 2972-2977, 2010.

[102] Z. Hong-song, W. Yuan, L. Gang, C. Xiao-ge, and W. Xin-Li, "Investigation About Thermal Conductivities of $La_2Ce_2O_7$ Doped with Calcium or Magnesium for Thermal Barrier Coatings," *Journal of Alloys and Compounds,* vol. 537, pp. 141-146, 2012.

[103] J. Wu, N. P. Padture, and M. Gell, "High-Temperature Chemical Stability of Low Thermal Conductivity ZrO_2–$GdO_{1.5}$ Thermal-Barrier Ceramics in Contact With α-Al_2O_3," *Scripta Materialia,* vol. 50, pp. 1315-1318, 2004.

[104] Z. Hong-song, C. Xiao-ge, L. Gang, W. Xin-Li, and D. Xu-dan, "Influence of Gd_2O_3 Addition on Thermophysical Properties of $La_2Ce_2O_7$ Ceramics for Thermal Barrier Coatings," *Journal of the European Ceramic Society,* vol. 32, pp. 3693-3700, 2012.

[105] Z. Xu, X. Zhou, R. Mu, and L. He, "Structure, Phase Stability and Thermophysical Properties of $(Yb_{0.1}La_{0.9})_2(Zr_{0.7}Ce_{0.3})_2O_7$ Ceramics," *Materials Letters,* vol. 135, pp. 162-164, 2014.

[106] Z. Xu, L. He, R. Mu, and X. Zhou, "$(Y_{0.05}La_{0.95})_2(Zr_{0.7}Ce_{0.3})_2O_7$ Ceramics as A Thermal Barrier Coating Material for High-Temperature Applications," *Materials Letters,* vol. 116, pp. 182-184, 2014.

[107] L. Wang, Y. Wang, X. G. Sun, J. Q. He, Z. Y. Pan, and C. H. Wang, "A Novel Structure Design Towards Extremely Low Thermal Conductivity for Thermal Barrier Coatings–Experimental and Mathematical Study," *Materials & Design,* vol. 35, pp. 505-517, 2012.

[108] P. K. Schelling, S. R. Phillpot, and R. W. Grimes, "Optimum pyrochlore compositions for low thermal conductivity," *Philosophical Magazine Letters,* vol. 84, pp. 127-137, 2004.

[109] Z. Qu, C. Wan, and W. Pan, "Thermophysical properties of rare-earth stannates: Effect of pyrochlore structure," *Acta Materialia,* vol. 60, pp. 2939-2949, 2012.

[110] B.-K. Jang, S. Kim, Y.-S. Oh, H.-T. Kim, Y. Sakka, and H. Murakami, "Effect of Gd_2O_3 on The Thermal Conductivity of ZrO_2–4mol.% Y_2O_3 Ceramics Fabricated by Spark Plasma Sintering," *Scripta Materialia,* vol. 69, pp. 165-170, 2013.

[111] A. Rauf, Q. Yu, L. Jin, and C. Zhou, "Microstructure and thermal properties of nanostructured lanthana-doped yttria-stabilized zirconia thermal barrier coatings by air plasma spraying," *Scripta Materialia,* vol. 66, pp. 109-112, 2012.

[112] A. A. Bukaemskiy, D. Barrier, and G. Modolo, "Physical Properties of 8mol% Ceria Doped Yttria Stabilised Zirconia Powder And Ceramic And Their Behaviour During Annealing And Sintering," *Journal of the European Ceramic Society,* vol. 26, pp. 1507-1515, 2006.

[113] M. Zhao, X. Ren, J. Yang, and W. Pan, "Thermo-Mechanical Properties of ThO_2-Doped Y_2O_3 Stabilized ZrO_2 For Thermal Barrier Coatings," *Ceramics International,* vol. 42, pp. 501-508, 2016.

[114] D. Zhu and R. A. Miller, "Development of Advanced Low Conductivity Thermal Barrier Coatings," *International Journal of Applied Ceramic Technology,* vol. 1, pp. 86-94, 2004.

[115] X. Huang, D. Wang, M. Lamontagne, and C. Moreau, "Experimental Study of The Thermal Conductivity of Metal Oxides Co-Doped Yttria Stabilized Zirconia," *Materials Science and Engineering: B,* vol. 149, pp. 63-72, 2008.

[116] R. L. Jones and D. Mess, "Improved Tetragonal Phase Stability at 1400°C with Scandia, Yttria-Stabilized Zirconia," *Surface and Coatings Technology,* vol. 86–87, Part 1, pp. 94-101, 1996.

[117] M. Leoni, R. L. Jones, and P. Scardi, "Phase Stability of Scandia–Yttria-Stabilized Zirconia TBCs," *Surface and Coatings Technology,* vol. 108–109, pp. 107-113, 1998.

[118] Y. L. Zhang, L. Guo, Y. P. Yang, H. B. Guo, H. J. Zhang, and S. K. Gong, "Influence of Gd_2O_3 and Yb_2O_3 Co-Doping on Phase Stability, Thermo-Physical Properties and Sintering of 8YSZ," *Chinese Journal of Aeronautics,* vol. 25, pp. 948-953, 2012.

[119] L. Guo, H. B. Guo, S. K. Gong, and H. B. Xu, "Improvement on The Phase Stability, Mechanical Properties And Thermal Insulation of Y_2O_3-Stabilized ZrO_2 by Gd_2O_3 And Yb_2O_3 Co-

Doping," *Ceramics International,* vol. 39, pp. 9009-9015, 2013.

[120] L. Guo, M. Li, and F. Ye, "Phase Stability and Thermal Conductivity of RE_2O_3 (RE=La, Nd, Gd, Yb) and Yb_2O_3 Co-Doped Y_2O_3 Stabilized ZrO_2 Ceramics," *Ceramics International,* vol. 42, pp. 7360-7365, 2016.

[121] K. Bobzin, L. Zhao, M. Öte, and T. F. Linke, "Deposition and Characterization of Thermal Barrier Coatings of ZrO_2–4 mol.% Y_2O_3–1 mol.% Gd_2O_3–1 mol.% Yb_2O_3," *Surface and Coatings Technology,* vol. 268, pp. 205-208, 2015.

[122] S. Raghavan, H. Wang, R. B. Dinwiddie, W. D. Porter, R. Vaβen, D. Stöver*, et al.*, "Ta_2O_5/Nb_2O_5 and Y_2O_3 Co-doped Zirconias for Thermal Barrier Coatings," *Journal of the American Ceramic Society,* vol. 87, pp. 431-437, 2004.

[123] E. Y. Lee, Y.-h. Sohn, S. K. Jha, J. W. Holmes, and R. D. Sisson, "Phase Transformations of Plasma-Sprayed Zirconia–Ceria Thermal Barrier Coatings," *Journal of the American Ceramic Society,* vol. 85, pp. 2065-2071, 2002.

[124] S. Sodeoka, M. Suzuki, K. Ueno, H. Sakuramoto, T. Shibata, and M. Ando, "Thermal and Mechanical Properties of ZrO_2-CeO_2 Plasma-Sprayed Coatings," *Journal of Thermal Spray Technology,* vol. 6, pp. 361-367, 1997.

[125] K. A. Khor and J. Yang, "Rapidly Solidified Neodymia-Stabilised Zirconia Coatings Prepared by DC Plasma Spraying," *Surface and Coatings Technology,* vol. 96, pp. 313-322, 1997.

[126] K. A. Khor and J. Yang, "Lattice Parameters, Tetragonality (c/a) and Transformability of Tetragonal Zirconia Phase in Plasma-Sprayed ZrO_2-Er_2O_3 Coatings," *Materials Letters,* vol. 31, pp. 23-27, 1997.

[127] K. A. Khor and J. Yang, "Plasma Sprayed ZrO_2-Sm_2O_3 Coatings: Lattice Parameters, Tetragonality (c/a) and Transformability of Tetragonal Zirconia Phase," *Journal of Materials Science Letters,* vol. 16, pp. 1002-1004, 1997.

[128] U. Schulz, P. Moretto, B. Saint-Ramond, A. Vanlieshout, O. Lavigne, and A. Börger, "Low Thermal Conductivity Ceramics for Turbine Blade Thermal Barrier Coating Application," in *28th International Conference on Advanced Ceramics and Composites B: Ceramic Engineering and Science Proceedings*, ed: John Wiley & Sons, Inc., pp. 375-380, 2008.

[129] M. Nejati, M. R. Rahimipour, I. Mobasherpour, and A. H. Pakseresht, "Microstructural Analysis And Thermal Shock Behavior of Plasma Sprayed Ceria-Stabilized Zirconia Thermal Barrier Coatings With Micro And Nano Al_2O_3 as a Third Layer," *Surface and Coatings Technology,* vol. 282, pp. 129-138, 2015.

[130] J. Brandon and R. Taylor, "Phase Stability of Zirconia-Based Thermal Barrier Coatings Part II. Zirconia-Ceria Alloys," *Surface and coatings technology,* vol. 46, pp. 91-101, 1991.

[131] J. Feng, X. Ren, X. Wang, R. Zhou, and W. Pan, "Thermal Conductivity of Ytterbia-Stabilized Zirconia," *Scripta Materialia,* vol. 66, pp. 41-44, 2012.

[132] A. Imran, S. Alam, M. Irfan, and M. Farooq, "Micro Structural Study of Plasma-sprayed Zirconia-CaO Thermal Barrier Coatings," *Materials Today: Proceedings,* vol. 2, pp. 5318-5323, 2015.

[133] M. Baig, F. Khalid, F. Khan, and K. Rehman, "Properties and Residual Stress Distribution of Plasma Sprayed Magnesia Stabilized Zirconia Thermal Barrier Coatings," *Ceramics International,* vol. 40, pp. 4853-4868, 2014.

[134] R. H. Piva, D. H. Piva, and M. R. Morelli, "Synthesis by Coprecipitation of India-Stabilized Zirconia and Codoping with MoO_3, WO_3, $TaO_{2.5}$, or $NbO_{2.5}$ for Application as Thermal Barrier Coatings," *Materials Research,* vol. 19, pp. 31-39, 2016.

[135] J. S. Abell, I. R. Harris, B. Cockayne, and B. Lent, "An Investigation of Phase Stability in the Y_2O_3-Al_2O_3 System," *Journal of Materials Science,* vol. 9, pp. 527-537, 1974.

[136] Y. J. Su, R. W. Trice, K. T. Faber, H. Wang, and W. D. Porter, "Thermal Conductivity, Phase Stability, and Oxidation Resistance of $Y_3Al_5O_{12}$ (YAG)/Y_2O_3–ZrO_2 (YSZ) Thermal-Barrier Coatings," *Oxidation of Metals,* vol. 61, pp. 253-271, 2004.

[137] L. J. Gu, S. M. Zhao, H. Y. Xu, Y. Hui, X. Z. Fan, B. L. Zou, *et al.*, "Phase Stability of Plasma Sprayed YAG-YSZ Composite Beads/Coatings at High Temperature," *Journal of the European Ceramic Society,* vol. 33, pp. 3325-3333, 2013.

[138] T. A. Parthasarathy, T.-I. Mah, and K. Keller, "Creep Mechanism of Polycrystalline Yttrium Aluminum Garnet,"

Journal of the American Ceramic Society, vol. 75, pp. 1756-1759, 1992.

[139] J. French, "High-Temperature Deformation and Fracture Toughness of Duplex Ceramic Microstructures," PhD. Thesis, Lehigh Univ., Bethlehem, PA (United States), 1993.

[140] O. Fabrichnaya, H. J. Seifert, T. Ludwig, F. Aldinger, and A. Navrotsky, "The Assessment of Thermodynamic Parameters in The Al_2O_3-Y_2O_3 System and Phase Relations in The Y-Al-O System," *Scandinavian Journal of Metallurgy,* vol. 30, pp. 175-183, 2001.

[141] R. Vassen, X. Cao, F. Tietz, G. Kerkhoff, and D. Stöver, "$La_2Zr_2O_7$—A New Candidate for Thermal Barrier Coatings," in *Proceedings of the United Thermal Spray Conference-UTSC'99*, pp. 830-834. 1999.

[142] Z. Li, B. Liu, J. Wang, L. Sun, J. Wang, and Y. Zhou, "Mechanism of Intrinsic Point Defects and Oxygen Diffusion in Yttrium Aluminum Garnet: First - Principles Investigation," *Journal of the American Ceramic Society,* vol. 95, pp. 3628-3633, 2012.

[143] Y. G. Liu, P. Peng, M. Fang, and Z. Huang, "$Y_{3-x}Er_xAl_5O_{12}$ Aluminate Ceramics: Preparation, Thermal Properties and Theoretical Model of Thermal Conductivity," *Advanced Engineering Materials,* vol. 14, pp. 170-177, 2012.

[144] A. R. West, "Preparative Methods," in *Solid state chemistry and its applications*, ed: John Wiley & Sons, 2007.

[145] J. D. Corbett, "Synthesis of Solid-State Materials," in *Solid State Chemistry: Techniques*, A. K. Cheetham and P. Day, Eds., ed: Clarendon Press; Oxford University Press, 1991.

[146] T.-H. Cho, Y. Shiosaki, and H. Noguchi, "Preparation and Characterization of Layered $LiMn_{1/3}Ni_{1/3}Co_{1/3}O_2$ as a Cathode Material by an Oxalate Co-Precipitation Method," *Journal of power sources,* vol. 159, pp. 1322-1327, 2006.

[147] M. Godinho, R. Gonçalves, L. S. Santos, J. A. Varela, E. Longo, and E. Leite, "Room Temperature Co-Precipitation of Nanocrystalline CeO_2 and $Ce_{0.8}Gd_{0.2}O_{1.9-\delta}$ Powder," *Materials Letters,* vol. 61, pp. 1904-1907, 2007.

[148] L. Sun, H. Guo, H. Peng, S. Gong, and H. Xu, "Influence of Partial Substitution of Sc_2O_3 with Gd_2O_3 on the Phase Stability and Thermal Conductivity of Sc_2O_3-Doped ZrO_2," *Ceramics International,* vol. 39, pp. 3447-3451, 2013.

[149] H. Chen, Y. Gao, Y. Liu, and H. Luo, "Coprecipitation Synthesis and Thermal Conductivity of $La_2Zr_2O_7$," *Journal of Alloys and Compounds,* vol. 480, pp. 843-848, 2009.

[150] C. J. Brinker and G. W. Scherer, *Sol-Gel Science: The Physics and Chemistry of Sol-Gel Processing*: Academic press, 2013.

[151] L. L. Hench and J. K. West, "The Sol-Gel Process," *Chemical Reviews,* vol. 90, pp. 33-72, 1990.

[152] Wikimedia. (2016, 01/07). *Sol-Gel*. Available: https://en.wikipedia.org/wiki/Sol-gel

[153] M. Veith, S. Mathur, A. Kareiva, M. Jilavi, M. Zimmer, and V. Huch, "Low Temperature Synthesis of Nanocrystalline $Y_3Al_5O_{12}$ (YAG) and Ce-Doped $Y_3Al_5O_{12}$ via Different Sol-Gel Methods," *Journal of Materials Chemistry,* vol. 9, pp. 3069-3079, 1999.

[154] C. Viazzi, J. P. Bonino, and F. Ansart, "Synthesis by Sol-Gel Route and Characterization of Yttria Stabilized Zirconia Coatings for Thermal Barrier Applications," *Surface and Coatings Technology,* vol. 201, pp. 3889-3893, 2006.

[155] D. Lybye and M. Mogensen, "Effect of Transition Metal ions on The Conductivity and Stability of Stabilised Zirconia," in *Advances in Solid Oxide Fuel Cells II: Ceramic Engineering and Science Proceedings*, ed: John Wiley & Sons, Inc., pp. 67-78, 2008.

[156] N. P. Bansal and D. Zhu, "Effects of doping on thermal conductivity of pyrochlore oxides for advanced thermal barrier coatings," *Materials Science and Engineering: A,* vol. 459, pp. 192-195, 2007.

[157] S. Raghavan, H. Wang, W. D. Porter, R. B. Dinwiddie, and M. J. Mayo, "Thermal Properties of Zirconia Co-Doped with Trivalent and Pentavalent Oxides," *Acta Materialia,* vol. 49, pp. 169-179, 2001.

[158] P. K. Schelling, S. R. Phillpot, and P. Keblinski, "Comparison of Atomic-Level Simulation Methods for Computing Thermal Conductivity," *Physical Review B,* vol. 65, p. 144306, 2002.

[159] S. Stackhouse and L. Stixrude, "Theoretical Methods for Calculating the Lattice Thermal Conductivity of Minerals," *Reviews in Mineralogy and Geochemistry,* vol. 71, pp. 253-269, 2010.

[160] E. Wu, "A Method for Treating Thermal Expansion Effects in Molecular Dynamics Simulations for Solids," *Journal of Physics: Condensed Matter,* vol. 2, p. 9335, 1990.

[161] P. K. Schelling and S. R. Phillpot, "Mechanism of Thermal Transport in Zirconia and Yttria-Stabilized Zirconia by Molecular-Dynamics Simulation," *Journal of the American Ceramic Society,* vol. 84, pp. 2997-3007, 2001.

[162] A. R. West, *Solid State Chemistry and its Applications*: John Wiley & Sons, 2007.

[163] L. W. Finger, D. E. Cox, and A. P. Jephcoat, "A Correction for Powder Diffraction Peak Asymmetry Due to Axial Divergence," *Journal of Applied Crystallography,* vol. 27, pp. 892-900, 1994.

[164] T. Hagiwara, H. Yamamura, and H. Nishino, "Relationship Between Oxide-Ion Conductivity and Ordering of Oxygen Vacancy in the $Ln_2Zr_2O_7$ (Ln = La, Nd, Eu) System Having a Pyrochlore Composition," *IOP Conference Series: Materials Science and Engineering,* vol. 18, p. 132003, 2011.

[165] B. Hunter, C. Howard, and D. Kim, "Neutron Diffraction Study of Tetragonal Zirconias Containing Tetravalent Dopants," *Australian journal of physics,* vol. 51, pp. 539-546, 1998.

[166] J. Carda, M. A. Tena, G. Monros, V. Esteve, M. M. Reventos, and J. M. Amigo, "A Rietveld Study of the Cation Substitution Between Uvarovite and Yttrium-Aluminum Synthetic Garnets, Obtained by Sol-Gel Method," *Crystal Research and Technology,* vol. 29, pp. 387-391, 1994.

[167] D. Wolf, P. Keblinski, S. R. Phillpot, and J. Eggebrecht, "Exact Method for the Simulation of Coulombic Systems by Spherically Truncated, Pairwise r−1 Summation," *The Journal of Chemical Physics,* vol. 110, pp. 8254-8282, 1999.

[168] Z.-P. Li, T. Mori, J. Zou, and J. Drennan, "Optimization of Ionic Conductivity in Solid Electrolytes Through Dopant-Dependent Defect Cluster Analysis," *Physical Chemistry Chemical Physics,* vol. 14, pp. 8369-8375, 2012.

[169] L. Minervini, R. W. Grimes, and K. E. Sickafus, "Disorder in Pyrochlore Oxides," *Journal of the American Ceramic Society,* vol. 83, pp. 1873-1878, 2000.

[170] T. Pramananda Perumal, V. Sridhar, K. P. N. Murthy, K. S. Easwarakumar, and S. Ramasamy, "Molecular Dynamics

Simulations of Oxygen Ion Diffusion and Superionic Conduction in Ytterbia-Stabilized Zirconia," *Computational Materials Science,* vol. 38, pp. 865-872, 2007.

[171] P. Jund and R. Jullien, "Molecular-Dynamics Calculation of the Thermal Conductivity of Vitreous Silica," *Physical review B,* vol. 59, p. 13707, 1999.

[172] A. Mashreghi, "Determining the Volume Thermal Expansion Coefficient of TiO_2 Nanoparticle by Molecular Dynamics Simulation," *Computational Materials Science,* vol. 62, pp. 60-64, 2012.

[173] M. Omini and A. Sparavigna, "Effect of phonon scattering by isotope impurities on the thermal conductivity of dielectric solids," *Physica B: Condensed Matter,* vol. 233, pp. 230-240, 1997.

[174] S. Zouari, R. Ballou, A. Cheikh-Rouhou, and P. Strobel, "Synthesis and structure of new pyrochlore-type oxides Ln_2ScNbO_7(Ln = Pr, Nd, Eu, Gd, Dy)," *Mater Lett,* vol. 62, pp. 3767-3769, 2008.

[175] H. Zhu, D. Jin, L. Zhu, H. Yang, K. Yao, and Z. Xi, "A general hydrothermal route to synthesis of nanocrystalline lanthanide stannates: $Ln_2Sn_2O_7$ (Ln=Y, La–Yb)," *Journal of Alloys and Compounds,* vol. 464, pp. 508-513, 2008.

[176] J. Matejicek, S. Sampath, P. C. Brand, and H. J. Prask, "Quenching, thermal and residual stress in plasma sprayed deposits: NiCrAlY and YSZ coatings," *Acta Materialia,* vol. 47, pp. 607-617, 1999.

[177] Z. Fu, H. K. Yang, B. K. Moon, B. C. Choi, and J. H. Jeong, "$La_2Sn_2O_7$: Eu^{3+} Micronanospheres: Hydrothermal Synthesis and Luminescent Properties," *Crystal Growth and Design,* vol. 9, pp. 616-621, 2008.

[178] M. G. Brik and A. M. Srivastava, "Pyrochlore structural chemistry: predicting the lattice constant by the ionic radii and electronegativities of the constituting ions," *Journal of the American Ceramic Society,* vol. 95, pp. 1454-1460, 2012.

[179] B. J. Kennedy, B. A. Hunter, and C. J. Howard, "Structural and bonding trends in tin pyrochlore oxides," *Journal of Solid State Chemistry,* vol. 130, pp. 58-65, 1997.

[180] G. A. Slack and D. W. Oliver, "Thermal conductivity of garnets and phonon scattering by rare-earth ions," *Physical Review B,* vol. 4, pp. 592-609, 1971.

[181] J. Feng, B. Xiao, R. Zhou, and W. Pan, "Thermal expansion and conductivity of $RE_2Sn_2O_7$ (RE=La, Nd, Sm, Gd, Er and Yb) pyrochlores," *Scripta Materialia,* vol. 69, pp. 401-404, 2013.

[182] J. Lian, K. B. Helean, B. J. Kennedy, L. M. Wang, A. Navrotsky, and R. C. Ewing, "Effect of structure and thermodynamic stability on the response of lanthanide stannate pyrochlores to ion beam irradiation," *The Journal of Physical Chemistry B,* vol. 110, pp. 2343-2350, 2006/02/01 2006.

[183] I. Levin and D. Brandon, "Metastable Alumina Polymorphs: Crystal Structures and Transition Sequences," *Journal of the American Ceramic Society,* vol. 81, pp. 1995-2012, 1998.

[184] A. Bahari, A. Anasari, and Z. Rahmani, "Low Temperature Synthesis of La_2O_3 and CrO_2 By Sol–Gel Process," *J. Eng. Technol. Res,* vol. 3, pp. 203-208, 2011.

[185] M. Yashima, K. Ohtake, M. Kakihana, H. Arashi, and M. Yoshimura, "Determination of Tetragonal-Cubic Phase Boundary of $Zr_{1-x}RxO_{2-x/2}$ (R= Nd, Sm, Y, Er and Yb) BY Raman Scattering," *Journal of Physics and Chemistry of Solids,* vol. 57, pp. 17-24, 1996.

[186] M. Hajizadeh-Oghaz, R. S. Razavi, and M. R. Loghman-Estarki, "Synthesis and Characterization of Non-Transformable Tetragonal YSZ Nanopowder by Means of Pechini Method for Thermal Barrier Coatings (TBCs) Applications," *Journal of sol-gel science and technology,* vol. 70, pp. 6-13, 2014.

[187] I. College. Database of Ionic Radii [Online]. Available: http://abulafia.mt.ic.ac.uk/shannon/ptable.php

[188] I. R. Gibson and J. T. S. Irvine, "Qualitative X-ray Diffraction Analysis of Metastable Tetragonal (t') Zirconia," *Journal of the American Ceramic Society,* vol. 84, pp. 615-618, 2001.

[189] R. Berman, *Thermal Conduction in Solids*: Clarendon Press, 1976.

[190] D. Zhu and R. A. Miller, "Thermal Conductivity and Sintering Behavior of Advanced Thermal Barrdxr Coatings," in *26th Annual Conference on Composites, Advanced Ceramics,*

Materials, and Structures: B: Ceramic Engineering and Science Proceedings, ed: John Wiley & Sons, Inc., pp. 457-468, 2008.

[191] "Theories of Dissolution and Etch-Pit Formation," in *Defects in Solids*. vol. 15, S. Keshra, Ed., ed: Elsevier, pp. 87-160, 1987.

[192] D. Zhu, J. A. Nesbitt, C. A. Barrett, T. R. McCue, and R. A. Miller, "Furnace Cyclic Oxidation Behavior of Multicomponent Low Conductivity Thermal Barrier Coatings," *Journal of Thermal Spray Technology,* vol. 13, pp. 84-92, 2004.

[193] N. R. Rebollo, A. S. Gandhi, and C. G. Levi, "Phase Stability Issues in Emerging TBC Systems," *High temperature corrosion and materials chemistry iv,* pp. 431-442, 2003.

[194] C. Ren, Y. D. He, and D. R. Wang, "Cyclic Oxidation Behavior and Thermal Barrier Effect of YSZ–(Al_2O_3/YAG) Double-Layer TBCs Prepared by the Composite Sol–Gel Method," *Surface and Coatings Technology,* vol. 206, pp. 1461-1468, 2011.

[195] N. B. I. Ftema W. Aldbea, "An Overview about the Garnet Thin Films (Terbium Yttrium Iron Garnet and Aluminum Terbium Yttrium Iron Garnet) Structural and Magnetic Properties," *Journal of Materials Sciences and Applications,* vol. 1, pp. 185-194, 2015.

[196] R. Shannon, "Revised Effective Ionic Radii and Systematic Studies of Interatomic Distances in Halides and Chalcogenides," *Acta Crystallographica Section A,* vol. 32, pp. 751-767, 1976.

[197] X. Yan, W. Liu, H. Wang, S. Chen, J. Shiomi, K. Esfarjani*, et al.*, "Stronger Phonon Scattering by Larger Differences in Atomic Mass and Size in p-Type Half-Heuslers $Hf_{1-x}Ti_xCoSb_{0.8}Sn_{0.2}$," *Energy & Environmental Science,* vol. 5, pp. 7543-7548, 2012.

[198] R. Boulesteix, A. Maître, J. F. Baumard, C. Sallé, and Y. Rabinovitch, "Mechanism of the Liquid-Phase Sintering for Nd:YAG Ceramics," *Optical Materials,* vol. 31, pp. 711-715, 2009.

[199]P. H. Klein and W. J. Croft, "Thermal Conductivity, Diffusivity, and Expansion of Y_2O_3, $Y_3Al_5O_{12}$, and LaF_3 in the Range 77°–300°K," *Journal of Applied Physics,* vol. 38, pp. 1603-1607, 1967.

[200] J. H. Harris, F. J. Polese, R. J. Tesch, S. P. Nootens, S. Dinescu, and W. L. Bradbury, "Transient Liquid Phase, Pressureless Joining of Aluminum Nitride Components," ed: Google Patents, 2013.

[201] A. Navrotsky, "Thermodynamics of Solid Electrolytes and Related Oxide Ceramics Based on the Fluorite Structure," *Journal of Materials Chemistry,* vol. 20, pp. 10577-10587, 2010.

[202] O. Fabrichnaya, M. Zinkevich, and F. Aldinger, "Thermodynamic Assessment of the Systems La_2O_3–Al_2O_3 and La_2O_3–Y_2O_3," *International Journal of Materials Research,* vol. 97, pp. 1495-1501, 2006.